Changes in Global and Regional Precipitation Patterns under the Impact of Climate Warming: Human Influences, Extremes and Seasonality

by

Jin Zhao

A thesis submitted in partial fulfillment of the requirements for the degree of

Doctor of Philosophy

in

Water Resources Engineering

Department of Civil and Environmental Engineering
University of Alberta

Abstract

Climate variability and human activities exert significant influences on various components of the hydrologic cycle worldwide. Changes to the global climate system may affect the magnitude and frequency of both mean and extreme hydrological events, thereby changing the risk to critical infrastructure. To mitigate the potential damage, it is crucial to elucidate why and how high-impact precipitation events could develop, to predict representative future precipitation events under a changing climate, and to assess their potential societal impacts. These insights will provide the scientific basis essential for decision-makers in developing effective mitigation policies and adaptation strategies against the impacts of global warming on future precipitation events.

This dissertation aims to fill this research gap by 1) investigating the spatiotemporal changes in observed extreme precipitation over the Northern Hemisphere land and possible human influences to observed changes; 2) projecting changes in ten extreme precipitation indices under the impact of global warming, and 3) quantifying changes in precipitation seasonality across the global land under the influence of climate warming, and the impact of seasonal precipitation changes on future water availability.

Chapter 1 - General Introduction

Chapter 2 - Detection and attribution analysis is conducted on seasonal precipitation extremes using HadEX3 datasets and simulations from five CMIP6 Global Climate Models (GCMs) in 1950-2014 over the Northern Hemisphere land (NHL), two risk regions (LR and HR) and 16 CMIP6 domains. Results indicate that GHG forcing dominates the increase in observed

Rx1day indices across most NHL. Positive trends are more pronounced in fall and winter than in spring and summer. However, due to the cooling effect of anthropogenic aerosols, a weakened Rx1day is evident in the winter of India and southern China. Using the optimal fingerprinting method, results show that anthropogenic forcing is detectable in at least one season over 80% of CMIP6 domains, with more than 60% of attributable contribution, especially in northern Eurasia. Individual AER signal is most detectable in East Asia. Even though seasonal natural forcings are undetectable in one-signal analysis, they contribute to observed changes in certain regions in the two- and three-signal analysis, which suggest the combined impact of anthropogenic and natural forcings on extreme precipitation patterns.

Chapter 3 - Ten extreme precipitation indices based on datasets of CMIP6 global climate models and two observed datasets over North America (NA) are evaluated, and their projected changes are assessed (e.g., temporal variations, spatial distributions, seasonal patterns, and model agreement) over the 21st century under different climate warming scenarios of the Intergovernmental Panel on Climate Change (IPCC). Results indicate that the CMIP6 ensemble median (CMIP6-EnM) generally performs better than individual GCMs across most regions of NA and more accurately captures observed patterns of extreme precipitation in NA. The frequency and severity of extreme precipitation events are predominantly projected to increase, particularly in latitudes above 55°N and coastal areas of NA. In contrast, dry conditions in southern NA are projected to intensify throughout the 21st century. Seasonal changes are projected to be more pronounced in winter compared to summer in northern NA, while in Central America, precipitation extremes will likely be less severe in both seasons. However, unlike strong model agreements in high (100%) and mid-latitudes (80%) of NA, there is a wide disparity between the signs of projected changes between GCMs in southern NA.

Chapter 4 - A non-parametric precipitation seasonality index (SI) is used to evaluate changes in precipitation seasonality across global land monsoon regions (GLM) and its subregions under a warmer climate, and the impact of SI variations on the seasonal water availability (AW). By conducting a detection and attribution analysis, observed changes in SI are shown to be attributable to anthropogenic influence with high confidence. Anthropogenic aerosol contributed to decreased SI before the 1980s, while greenhouse gas forcing led to an increase in SI after the 1980s at about 5.67%/K. Future changes in SI are projected to increase across most global monsoon regions, indicating an increased contrast in the AW between wet and dry seasons, largely attributed to the wet seasons projected to be wetter. SI changes in the 2080s are expected to affect seasonal water availability (AW) across the GLM, with 'wet (dry) get wetter ' mechanism in regions projecting a higher (lower) SI and more AW, while with dry (wet) get drier ' mechanism in regions projecting a higher (lower) SI and lower AW.

Chapter 5 - Conclusions are summarized and recommendations for future work are proposed to better understand the impact of climate warming on future precipitation extremes globally.

Preface

This dissertation, an original work authored by Jin Zhao and guided by Dr. Thian Yew Gan, is structured into five main chapters.

Chapter 1, titled "General Introduction", establishes a comprehensive context for the research by outlining its background, problem statement and research objectives.

Chapters 2 to 4, formatted individually as journal articles, constitute the crux of this thesis. Each of these chapters is crafted to be self-contained, furnished with introductions, methodologies, results and with supporting material presented in the "Appendix" section.

Chapter 2, titled "Detection and Attribution of Human Influence on Seasonal Extreme Precipitation in Northern Hemisphere", will be submitted to the journal Science of The Total Environment, which will be cited as Zhao, J., Gan, T. Y., Zhang, S., Oki, T. & Tan, X. (2023), Detection and Attribution of Human Influence on Seasonal Extreme Precipitation in Northern Hemisphere, submitted to *Science of The Total Environment*.

Chapter 3, titled "Projected Changes of Precipitation Extremes in North America Using CMIP6 Multi-Climate Model Ensembles," has been published in the Journal of Hydrology (2023). The citation for this publication is Zhao, J., Gan, T. Y., Zhang, G., & Zhang, S. (2023). Projected changes of precipitation extremes in North America using CMIP6 multi-climate model ensembles. *Journal of Hydrology*, **621**, 129598. DOI: https://doi.org/10.1016/J.JHYDROL.2023.129598.

Chapter 4, "Increased Precipitation Seasonality over Global Land Monsoon Affecting Seasonal Water Availability" will be submitted to the journal npj Climate and Atmospheric

Science, which will be cited as Zhao, J. & Gan, T. Y. (2023), Increased Precipitation Seasonality over Global Land Monsoon Affecting Seasonal Water Availability, submitted to *npj Climate and Atmospheric Science*.

Chapter 5 integrates and synthesizes the research findings from all previous chapters and concluded with recommendations for future research.

In addition to the main content, supplementary materials, instrumental for a deeper understanding of the dissertation, are included in the "Appendix" section. This applies to Chapters 2 to 4. Items such as figures and tables, associated with the appendix, are indexed with an "A." prefix. For instance, Figure A.2-1 and Table A.2-1, and these have been submitted as part of the appendix to the respective journals.

Given the overlapping nature of references across chapters, a consolidated bibliography has been appended, providing a comprehensive list of references pertinent to the entire dissertation.

Moreover, I also contributed the following publications:

Zhang, G., Wang, H., Gan, T. Y., Zhang, S., Shi, L., Zhao, J., et al. (2022). Climate change determines future population exposure to summertime compound dry and hot events. *Earth's Future*, **10**, e2022EF003015. https://doi.org/10.1029/2022EF003015

Gan, T. Y, Serreze, M., Gan, K. E., Zhao, J., and Huang, L. (2023). Climate warming Impact to Permafrost of Alaska, Western Arctic of Canada and Arctic Infrastructure, submitted to *International Journal of Climatology.*

Dedication

This thesis is dedicated to my family, for their endless love, support, and encouragement.

Acknowledgments

First, I want to give a heartfelt thanks to my supervisor, Professor Thian Yew Gan. His constant support during my Ph.D. study and research have been nothing short of remarkable. Over the last four years, his patience, motivation, and guidance have been critical to my progress and achievements. Without his dedicated mentorship, I would not have reached this point. He has been an amazing guide during my Ph.D. journey, always ready with advice and encouragement. His love for learning and his excitement for our field of study has always inspired me. Thank you, Professor Gan. My sincere thanks also go to the rest of my thesis committee for their valuable comments and suggestions.

In addition, I would like to express my thanks to the China Scholarship Council (CSC). Their financial support has been crucial to my study, providing me with the resources needed to focus on my research. This financial aid has allowed me to delve into my work without any undue worries, and for that, I am extremely grateful.

Moreover, I would like to thank the University of Alberta for their continued support. The university has created a nurturing environment for my research, making it possible for me to pursue my Ph.D. without any roadblocks. Their dedication to research and commitment to supporting students has made my journey smoother and more fulfilling.

In closing, I reflect on this journey with a sense of deep appreciation for the constellation of individuals and institutions that have illuminated my path. As I step forward into the next chapter of my academic journey, I carry with me the immeasurable knowledge, inspiration, and resilience imparted by those whom I have been fortunate enough to encounter on this journey.

Table of Contents

List of Tables

List of Figures

Chapter 1 General Introduction

1.1. Background and Problem Statement

Climate warming attributed to human activities is rapidly altering the hydrologic cycle worldwide. These changes have far-reaching implications for ecosystems, societies and economies worldwide and are becoming a pressing issue of global concern (Stocker et al., 2013). According to the Clausius–Clapeyron relationship, rising global mean temperature increases the atmospheric moisture holding capacity by approximately 7% per degree Celsius (Wehner, 2020; Westra et al., 2013). This rise in moisture availability fuels storm systems, which results in more intensive precipitation events and potentially more severe weather disturbances (Dong et al., 2021; Li et al., 2021). Concurrently, an upsurge in thermal energy also leads to enhanced evaporation rates, which tends to intensify the duration and severity of droughts (Dai, 2013). The intensification of both hydrologic processes - increased precipitation and heightened evaporation - means an amplification of the global hydrological cycle, which can significantly affect the spatial and temporal distribution of precipitation (Chou et al., 2009; Held & Soden, 2006) at regional to global scale, with significant repercussions on the intensity and frequency of extreme weather events, seasonal climatic patterns and water availability (Trenberth, 2011; Zhang et al., 2007).

Two recent extreme events likely demonstrate the influence of these hydrological changes. On July 21, Halifax, Canada, experienced unprecedented extreme precipitation, receiving three months' worth of rainfall within 24 hours (Weber, 2023). This extreme rainfall event resulted in severe flooding that affected an estimated 80,000 residents of Halifax. In addition to displacing many, the floods caused substantial infrastructural damage, including severe damage to several

roads and bridges. Concurrently, in August 2023, Beijing was hit by the Typhoon 'Doksuri'. Accompanied by torrential rainfall, the typhoon caused widespread flooding across the megacity of China. According to the municipal government, the typhoon significantly damaged nearly 150,000 homes. Additionally, roughly 37,000 acres of agricultural land were submerged. The concurrent occurrences of disasters of such magnitudes on different continents emphasize the importance of understanding the reasons behind the extreme precipitation events, likely amplified by anthropogenic influences (Kirchmeier-Young & Zhang, 2020; Paik et al., 2020; Zhang et al., 2007).

Under the influence of rising concentrations of greenhouse gases attributed to human activities, there is high confidence that the global mean precipitation will increase with the rise in global surface air temperature (GSAT) (IPCC, 2021). In high-latitude areas and tropical regions, annual mean precipitation is very likely to increase, especially under severe climate projections of high warming levels, with many monsoon regions expected to experience higher precipitation in the future (IPCC, 2021). Major potential changes in the regional mean precipitation are inevitably crucial for us to better understand future precipitation extremes, given their significant social and economic impact to our societies when they occur (Duan et al., 2019b; Ge et al., 2021; Rao et al., 2020; Xu et al., 2019). Therefore, there is an urgent need to better understand future patterns of regional precipitation extremes, which are essential for us to develop effective strategies to mitigate potential impacts of climate warming.

The human-induced warming not only alters the amount of precipitation but also varies the spatial and temporal patterns of precipitation (Chou et al., 2009; Held & Soden, 2006). For example, research indicates that more than 62% of terrestrial ecosystems have experienced a decline in regional precipitation during the wet season but the dry season has become wetter

(Murray-Tortarolo et al., 2017). Further research has demonstrated generally wetter wet seasons since the 1980s, with the changes largely attributed to human activities (Chou et al., 2013; Lan et al., 2019; Polson & Hegerl, 2017). The implications of such changes are significant, as they directly affect the availability of water - a key factor for water supply essential to maintain the agriculture, ecosystems, and biodiversity (Deng et al., 2020; Feng et al., 2013; Konapala et al., 2020).

Global Climate Models (GCMs) have been widely used in simulating historical climate statistics and projecting future climate (Agel & Barlow, 2020; Akinsanola et al., 2020a; Zhan et al., 2020; Zhu & Yang, 2020). The Coupled Model Intercomparison Project Phase 6 (CMIP6) represents the latest generations of global climate models. Compared to CMIP5, CMIP6 offers GCMs with finer spatial resolution, more comprehensive physical processes, and improved representations of human and natural systems, which specifically target critical scientific gaps identified in CMIP5 (Gidden et al., 2019; Priestley et al., 2020; Stouffer et al., 2017a). As a result of these enhancements, CMIP6 models show a stronger capability in reproducing observed climatic patterns (Agel & Barlow, 2020; Chen et al., 2020; Roberts et al., 2018). The more representative simulations of CMIP6 compared to CMIP5 provide a clearer distinction between natural climate variability and anthropogenic influences. Recent studies have reinforced the attribution of warming to extreme events by analyzing CMIP6 simulations under different forcings (e.g., anthropogenic forcing, greenhouse gas forcing, anthropogenic aerosol forcing, natural external forcing, etc.), and there is high confidence (medium confidence in CMIP5 GCMs) that human influence has contributed to observed changes in annual mean and extreme precipitation at global, hemispheric and continental scales (Kirchmeier-Young & Zhang, 2020; Paik et al., 2020; Zhang et al., 2007).

Moreover, in the CMIP6 framework, the introduction of Shared Socioeconomic Pathways (SSPs) provides a foundation for designing future climate scenarios, where models are given a common set of future concentrations of greenhouse gases, aerosols and other climate forcings to construct potential future climates (O'Neill et al., 2014; Riahi et al., 2017). Therefore, CMIP6 GCMs have been designed to simulate various societal futures, each characterized by distinct greenhouse gas emission levels, land-use changes, and population growth paths (Eyring et al., 2016). CMIP6 GCMs under different SSPs offer comprehensive insights into both climate change adaptation and mitigation (van Vuuren et al., 2014). As shown in Zelinka et al. (2020), CMIP6 GCMs show a notably higher climate sensitivity, contributing to projections of greater warming and severe extremes than models in CMIP5. Furthermore, scientific advancements in CMIP6 have contributed to our understanding of precipitation seasonality - a critical parameter for agricultural and water management. For example, Roberts et al. (2018) found that CMIP6 models accurately predict monsoonal patterns, especially in regions that heavily rely on seasonal monsoon rainfall for water supply.

Given the growing concern regarding warming-induced changes in global and regional precipitation events, the results simulated by the latest GCMs of CMIP6 present a valuable and relevant research opportunity. Recognizing the extensive and potentially severe impact of changes in precipitation patterns due to climate change, this doctoral research attempts to address three questions: (1) How does human activity influence observed extreme precipitation? (2) How are precipitation extremes projected to change in the future? and (3) What impact could change in precipitation seasonality have on human society?

1.2. Research Objectives

Under a warmer climate, extreme precipitation events have drawn significant attention to the scientific community and have raised major societal concerns. Investigating the impact of these changes in precipitation on human life will provide us with better insights for developing policymaking and adaptation strategies that will be effective. Therefore, the primary objective of this doctoral study is to investigate potential drivers behind observed extreme precipitation events, its future changes, and the socio-environmental impacts of these climatic changes. Specifically, the key objectives of this doctoral research are:

Objective 1: Detection and Attribution of Human Influence on Seasonal Extreme Precipitation in Northern Hemisphere (Chapter 2)

Detect and attribute observed changes in global and regional precipitation extremes to human influence to unravel the extent anthropogenic activities have influenced the severity and frequency of extreme precipitation events (Zhang et al. 2013). By applying the optimal fingerprinting method to assesses the impact of different external forcings on precipitation patterns (Allen & Stott, 2003; Ribes et al., 2013), we can better understand the influence of anthropogenic activities on observed changes to extreme precipitation.

Objective 2: Projected Changes of Precipitation Extremes in North America using CMIP6 Multi-Climate Model Ensembles (Chapter 3)

Project characteristics of future precipitation extremes under the impact of human-induced warming helps us to gain a better understanding of how climate warming influences precipitation extremes which will also enhance our predictive capabilities (Christidis & Stott,

2022; Paik et al., 2020; Sun et al., 2022). As such, this research seeks to provide a comprehensive overview of potential changes in precipitation extreme indices due to global warming, with a particular focus on North America where such extremes can have significant socio-economic implications.

Objective 3: Increased Precipitation Seasonality over Global Land Monsoon Affecting Seasonal Water Availability (Chapter 4)

Analyze observed precipitation seasonality and the impact of precipitation seasonality on water availability under the influence of climate warming. Given interactions between precipitation, evaporation and climate changes significantly shape water availability, we should investigate their interactions in order to gain a more detailed understanding of their dynamics (Konapala et al., 2020). Through a multifaceted approach that integrates changes in both annual mean available water and precipitation seasonality, we aim to provide a more comprehensive perspective on future water availability (Pascale et al., 2016, 2017).

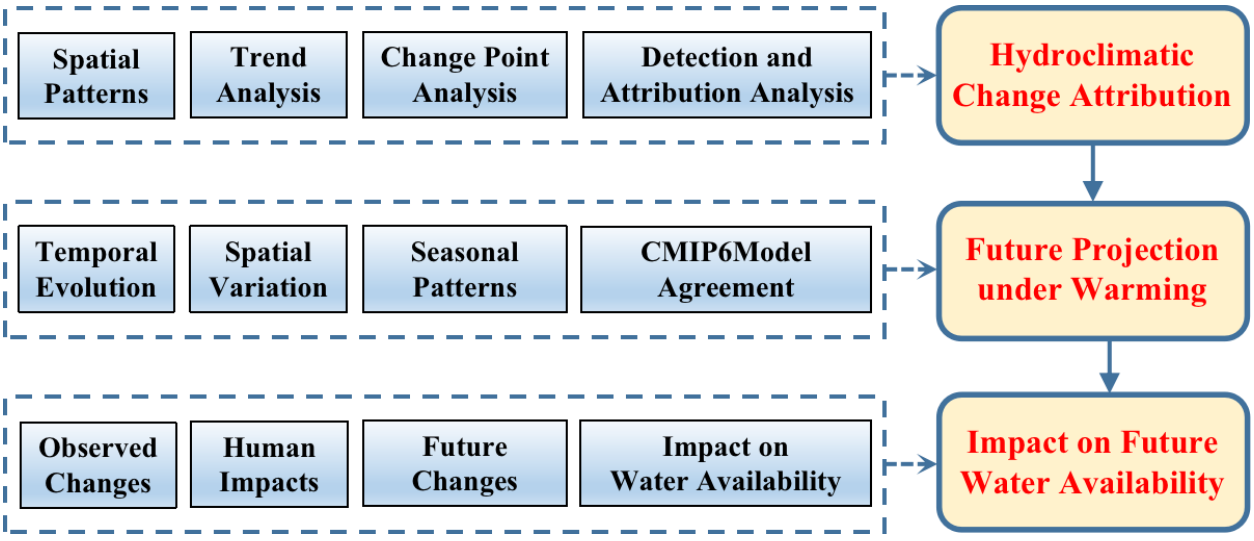

Figure 1-1 Schematic diagram of the research project

Figure 1-1 shows the schematic diagram of this thesis with 3 key chapters (Chapters 2 to 4). Chapter 2 investigates the spatial-temporal changes in annual (in the Appendix) and seasonal extreme precipitation over the Northern Hemisphere land and its subregions and attributes the observed changes to human influences with high confidence. Human activities have been and will continue to be the dominant drivers of recent and future global warming (Cook et al. 2013; IPCC 2013). Daily extreme precipitation has intensified in recent years which is projected to exacerbate as the hydrologic cycle intensifies under the influence of global warming (Kirchmeier-Young & Zhang, 2020; Ma et al., 2020; Zhan et al., 2020; Zhang & Colle, 2017; Zhou et al., 2018). In response to these concerns, Chapter 3 focus on evaluating future extreme precipitation under various SSP climate scenarios of the Sixth Assessment Report (AR6) of the Intergovernmental Panel on Climate Change (IPCC). In this chapter, North America (NA) has been selected as the study site where future changes in extreme precipitation are investigated using ten extreme precipitation indices defined by the Expert Team on Climate Change Detection and Indices (ETCCDI). Apart from the precipitation extremes, precipitation seasonality is also expected to increase under climate change impact since the 1980s (Chou et al., 2013; Lan et al., 2019; Polson & Hegerl, 2017). Even though changes in precipitation seasonality could impact the annual mean water availability (Haddeland et al., 2014; Schewe et al., 2014), there is still a lack of understanding of their relationships. To address this gap, in chapter 4, a non-parametric precipitation seasonality index is introduced to quantify changes in precipitation seasonality across global land regions under a warming climate. Chapter 4 uses the optimal fingerprinting method to attribute observed changes to human activity and assess the impact of the seasonal changes of precipitation on water availability under several SSP scenarios and warming levels. In Chapter 5, all the conclusions from Chapters 2 to 4, the key findings of this

thesis are summarized, and recommendations for future research as an extension to this research are presented.

Chapter 2 Detection and Attribution of Human Influence on Seasonal Extreme Precipitation in Northern Hemisphere

2.1. Introduction

According to the 6th Assessment Report of Working Group 1 of Intergovernmental Panel on Climate Change (IPCC AR6-WG1), the recent four decades have experienced the most significant warming since the 1850s (Pörtner et al., 2022). Between 2010 and 2019, the increase in the global mean surface temperature relative to the baseline period of 1850-1900 has been about 1.06 [0.88-1.21] °C (Pörtner et al., 2022). One of the most relevant consequences of a warmer climate is likely the worsening of extreme precipitation events. It is of high confidence that the increase in extreme precipitation under a warming climate follows the Clausius–Clapeyron rate, that the atmospheric moisture holding capacity increases about 7%/°K increase of warming (Dong et al., 2021; Li et al., 2021; Wehner, 2020; Westra et al., 2013). More frequent and more intensive extreme precipitation have been observed and simulated by climate models ranging from regional to global scales (Bishop et al., 2019; Donat et al., 2016; Kirchmeier-Young & Zhang, 2020; Mukherjee et al., 2018).

Extreme weather events have significant and far-reaching impacts, such as the recent "7·21" extreme precipitation event of Zhengzhou, China which resulted in the loss of at least 350 lives and total economic losses of about 133.7 billion yuan by massive flooding caused by an anomalous moisture transport and a persistent Subtropical High (Tang et al., 2023). In August 2022, the inversion of westerlies had contributed to two atmospheric rivers passing over southern Pakistan, resulting in an extreme precipitation event that led to a displacement of approximately

33 million people (Nanditha et al., 2023). With the intensification of the hydrologic cycle due to global warming (Tabari, 2020), occurrences of more severe extreme precipitation are expected to continue, which will likely increase the risk of major flooding, which would have significant impacts on the ecosystems, human societies, and the economy. Therefore, understanding observed changes in precipitation extremes and their primary drivers are crucial for preparing effective mitigation measures against the impact of extreme weather events.

Attribution studies aim to identify the impact of external or anthropogenic forcings on climatic changes, such as comparative analysis of climate model simulations with and without incorporating the impact of human activities. According to the AR6, human activities have been responsible for an increase that accounts for over 90% of the elevated global mean surface air temperature (Pörtner et al., 2022), which have also significantly impacted precipitation extremes. For example, Donat et al. (2016) reported that human-induced warming is responsible for approximately 40% of heavy precipitation under a 2°C warming, which is expected to increase non-linearly with further warming. Furthermore, recent researches have demonstrated the contribution of warming to climate extremes, indicated as high confidence in the AR6 of IPCC (note: medium confidence in the AR5) that observed changes in extreme precipitation at global and regional scales are largely attributed to human influence (Kirchmeier-Young & Zhang, 2020; Paik et al., 2020; Zhang et al., 2007).

The optimal fingerprint method is commonly used in the detection and attribution (D&A) analysis. This technique involves regressing observed changes of precipitation against different patterns of external forcings (e.g., anthropogenic greenhouse gas forcing, anthropogenic aerosol forcing, natural external forcing, etc.) (Allen & Stott, 2003; Ribes et al., 2013). Past studies have applied this method to examine human-induced changes in annual extreme precipitation and

seasonal mean precipitation (Christidis & Stott, 2022; Paik et al., 2020; Sun et al., 2022; Xu et al., 2022). For example, Paik et al. (2020) robustly detected a human-induced increase in annual extreme precipitation over hemispheric and continental scales by using optimal fingerprinting techniques. By conducting a D&A analysis at global and regional scales, Sun et al. (2022) confirmed that the anthropogenic influences have notably shortened the return period of extreme annual maximum precipitation events. Christidis & Stott (2022) showed that changes in seasonal mean precipitation over Europe are attributed to human activity, which has primarily increased the frequency of high precipitation extremes in most regions of Europe except the Mediterranean basin.

However, a formal D&A analysis of seasonal extreme precipitation in the Northern Hemisphere land (NHL) has not been conducted. Thus, a study is needed to determine whether anthropogenic forcings in the changes of seasonal extreme precipitation is detectable and which season could be most influenced by human activities. Additionally, changes under the anthropogenic influence are more difficult to detect at regional than at global or continental scales because precipitation at smaller spatial scales typically have higher internal variability (Sarojini et al., 2016). As the updated IPCC climate reference regions released in the Coupled Model Intercomparison Project Phase 6 (CMIP6) could better represent consistent regional climate features (Iturbide et al., 2021), a further study is needed to detect the magnitude of human impact on the change of seasonal precipitation extremes at smaller scales, such as the IPCC climate subregions. This could provide information helpful to reduce the vulnerability of communities to climate change impact. Therefore, two main questions are addressed in this chapter: (1) How has seasonal extreme precipitation changed over global and regional scales? (2) To what extent can these changes be attributed to human activities?

To answer these questions, we have analyzed the spatial-temporal changes in seasonal precipitation extremes over the NHL and its subregions. By using the HadEX3 dataset and selected CMIP6 simulations, the optimal fingerprinting method was employed to detect and to attribute changes in seasonal maximum one-day (Rx1day) and consecutive five-day (Rx5day) precipitation from 1950 to 2014. Results are interpreted with plausible mechanistic explanations. The remainder of this chapter is organized as follows: the observed data and CMIP6 model simulations used in this chapter are listed in Section 2.2, followed by a detailed description of the data process and attribution methods. Results, including spatial-temporal changes and D&A analysis of extreme precipitation for all seasons, are explained in section 2.3. Conclusions and discussion are given in section 2.4.

2.2. Data and Methodology

2.2.1. Observation and Climate Model Data

Version 3.0.4 of the Hadley Centre global land-based climate extremes dataset (HadEX3) provides annual and monthly datasets of 29 climate extreme indices on a gride of 1.875°×1.25° longitude/latitude. Furthermore, the precipitation extreme indices estimated from the HadEX3 dataset of 1900 to 2018 are derived from station data distributed over the global land with extensive records over 30 years. To detect long-term changes in extreme precipitation, only those grids data that meet the following two criteria are selected: 1) grids with more than 70% of data for the 1950-2014 study period (45 years); and 2) grids with at least 3-year data in 2010–2014 for estimating extreme precipitation indices.

Simulated daily precipitation data are obtained from the Coupled Model Intercomparison Project Phase 6 (CMIP6) archive. Inner model uncertainties of past studies using limited

ensemble members are likely high (Duan et al., 2019a; Min et al., 2013; Paik et al., 2020). Additionally, unfair comparisons were easily produced by using different ensemble members to detect forcings of a climate model (Xu et al., 2022; Zhang et al., 2013). Only the CMIP6 global climate models (GCMs) that have at least 5 ensemble members forced with historical forcing (ALL, both anthropogenic and natural external forcings), hist-GHG forcing (GHG, greenhouse gases forcing only), his-aer forcing (AER, anthropogenic aerosol forcing only) and hist-nat forcing (NAT, natural external forcing only) are selected to conduct the D&A analysis. Furthermore, for the preindustrial control (CTL) experiment, which is used in D&A analysis to assess the internal variability, a total of 62 chunks of non-overlapping 65-year simulations are used to access the internal variability. Table A.2-1 provides details for the five selected CMIP6 GCMs used in this chapter. Overall, this chapter analyzed 62 chunks of data from preindustrial control experiments (CTL) and 39 runs of data from ALL, GHG, AER, and NAT forcings.

2.2.2. Precipitation Indices

In this chapter, two extreme precipitation indices, maximum one-day (Rx1day) and consecutive five-day (Rx5day) precipitation, are analyzed to detect the human influence on precipitation extremes. High values of Rx1day could result in flash floods, which pose significant threats to urban infrastructure, transportation systems, and others, while high Rx5day may trigger widespread river floods, leading to considerable damage not only to infrastructure and property but also to human lives (Kirchmeier-Young & Zhang, 2020). Rx1day and Rx5day are extreme precipitation indices of an ensemble of the ETCCDI categorized under precipitation amount (mm). Monthly Rx1day and Rx5day for HadEX3 are downloaded from the Centre for Environmental Data Analysis Archive (CEDA). Indices for CMIP6 GCMs are estimated on monthly time scales at their original grids using ClimPACT2.

2.2.3. Probability-based Index

Given the high spatial variability of precipitation across most regions, spatial averages will tend to be influenced predominantly by regions with higher precipitation, Rx1day and Rx5day are standardized ranging from 0 to 1 by calculating a probability-based index (PI) (Min et al., 2011; Zhang et al., 2013). For each grid box, monthly Rx1day and Rx5day from 1950 to 2014 were fitted to a generalized extreme value (GEV) distribution (Kharin & Zwiers, 2005), then quantiles taken from the cumulative density function (CDF) of the adjusted GEV distribution are determined as the PI. The CDF of the GEV distribution is as follows:

$$F(x;\ \mu,\sigma,\xi) = \begin{cases} \exp\left[-exp\left\{-\dfrac{x-\mu}{\sigma}\right\}\right], & \xi = 0 \\ \exp\left[-\left\{1+\xi\dfrac{x-\mu}{\sigma}\right\}^{-\frac{1}{\xi}}\right], & \xi \neq 0, 1+\xi\dfrac{x-\mu}{\sigma} > 0 \end{cases} \qquad (2-1)$$

Where μ, σ, and ξ are the location, scale, and shape parameters, respectively.

Higher PI values correspond to higher Rx1day and Rx5day, indicating significant extreme events. Conversely, lower PI values correspond to lower Rx1day and Rx5day that represent less intensive precipitation events. For the Rx1day and Rx5day derived from CMIP6 simulations, their corresponding PIs are initially estimated at their native grids, then resampled to the HadEx3 1.875°×1.25° grid by using the Climate Data Operators (CDO). Subsequently, the interpolated PIs in CMIP6 GCMs are masked with HadEx3 data where grid points have a record of more than 45 years, as mentioned in 2.2.1.

2.2.4. Data Processing

Only Northern Hemisphere land (0°–90°N, NHL) areas are considered in this chapter because the Rx1day and Rx5day of the HadEx3 dataset are limited in the Southern Hemisphere. The spatial coverage of NHL for Rx5day (Fugure 2-1b) is somewhat greater than that for Rx1day (Figure 2-1a) due to a broader spatial interpolation of the available station values (Min et al., 2011), as shown in Figure 2-1. We define a low-risk region (LR, shown in blue) and a high-risk region (HR, shown in red) as the regions where indices values in an individual grid are smaller or greater than averaged observation climatology during 1961–1990 for Rx1day and Rx5day (Paik et al., 2020). However, partly due to differences in spatial climatology patterns across NHL, there are some differences in the risk regions identified from Rx1day and Rx5day indices. The spatial distribution of the available observational data in NHL is divided into 20 areas referring to the "climate-homogenous" regions in the AR6 of IPCC (Iturbide et al., 2020b), as shown in the colored box of Figure 2-1. To ensure a reasonable representation of diverse regions, each CMIP6 domain is required to have more than 30% of the spatial coverage for Rx1day and Rx5day in the averaged HadEx3 climatology during 1961–1990, which results in 16 CMIP6 domains (show in grey boxes) in NHL as shown in Figure 2-1. HadEX3 data's coverage (in %) for 20 CMIP6 domains in 1961-1990 are listed in Table A.2-2.

We primarily focus on the 1950–2014 period to conduct the D&A analysis on extreme precipitation of NHL because as shown in Figure A.2-1, the percentage change in the spatial coverage for acceptable grid cells of HadEx3 datasets from 1900 to 2020, 1) the spatial coverage for Rx1day and Rx5day from the HadEX3 dataset is relatively sparse over NHL and CMIP6 domains before 1950 and after 2014, and 2) historical simulation (ALL) of most CMIP6 GCMs do not provide data after 2014.

In this chapter, seasonal (spring (MAM - March-April-May), summer (JJA - June-July-August), fall (SON - September-October-November), and winter (DJF - December-January-February)) D&A analysis is conducted for PIs of Rx1day (Rx5day) of observation of HadEX3 and CMIP6 simulations. PI anomalies from 1950 to 2014 are the differences relative to the average of PIs in 1961-1990 at each grid point. Their areally-average means are also estimated. Before conducting the D&A analysis, the dimensionality of data was reduced by computing a five-year non-overlapping average from 65-year annual and seasonal PI anomalies, which produced 13 temporal points for each grid to conduct the optimal fingerprint method.

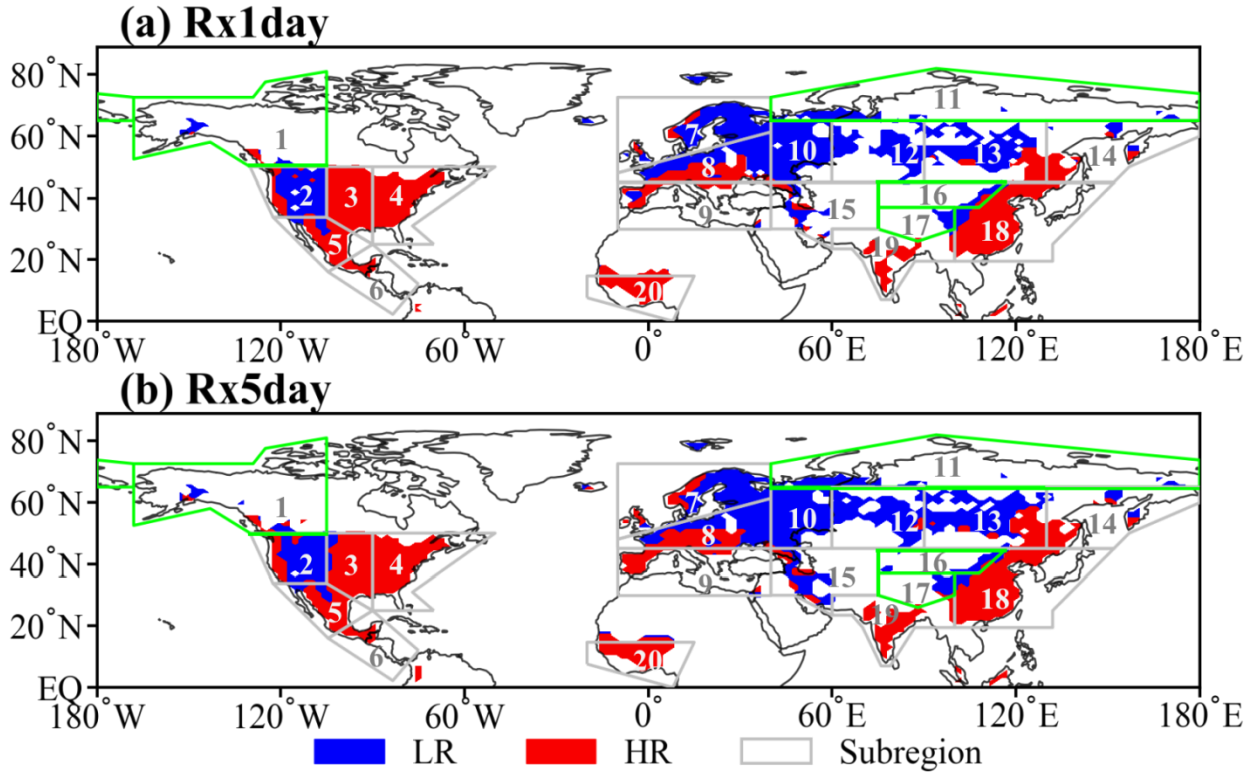

No.	Acronym	Subregion	No.	Acronym	Subregion
1	NWN	northwestern North America	11	RAR	Russian Arctic
2	WNA	western North America	12	WSB	West Siberia
3	CNA	central North America	13	ESB	eastern Siberia

4	ENA	eastern North America	14	RFE	Russian Far East
5	NCA	north Central America	15	WCA	western central Asia
6	SCA	southern Central America	16	ECA	Eastern Central Asia
7	NEU	North Europe	17	TIB	Tibetan Plateau
8	WCE	Western & Central Europe	18	EAS	East Asia
9	MED	Mediterranean	19	SAS	South Asia
10	EEU	eastern Europe	20	WAF	Western Africa

Figure 2-1 The spatial distribution of observational data has more than 70% (45-year) records from 1950 to 2014 for Rx1day (Figure 2-1a) and Rx5day (Figure 2-1b). Grey (Green) boxes are the CMIP6 domains with more (less) than 30% of the spatial coverage. Blue- and red-coloured grids indicate low-risk and high-risk extreme precipitation regions, respectively. Corresponding regions to the number are listed in the table.

2.2.5. Change-Point Analysis

The Pettitt test is a non-parametric method which has been widely used in hydroclimatic research to detect the abrupt change points in a time series (Ogungbenro & Morakinyo, 2014; Pettitt, 1979; Ryberg et al., 2020). We applied the Pettitt test to identify single change points in the time series of Rx1day and Rx5day from 1950 to 2014. The $p - value$ provides the statistical significance at the 5% significant level. The Pettitt statistic U_k is shown as follows:

$$U_k = 2 \times \sum_{i=1}^{n} r_i - k(n+1) \qquad (2-2)$$

Arranged the observed time series $x_1, x_2, \ldots, x_n$ in an ascending order, then r_i represents the rank of the i^{th} observed data; k = 1, 2, …, n.

Then the statistical change point test determined K as the potential change-point where $|U_k|$ is maximized:

$$K = \max_{1 \le k \le n} |U_k| \qquad (2-3)$$

The $p - value$ is determined using Equation (2-4):

$$p - value = 2 \times \exp\left(\frac{-6U^2}{n^3 + n^2}\right) \qquad (2-4)$$

2.2.6. Detection and Attribution Analysis

Ribes et al. (2017), hereafter referred to as 'Ribes17', conducted their D&A analysis for observed extreme precipitation with a new statistical approach that uses a method of hypothesis testing and additive decomposition which is more robust than the traditional linear regression. 'Ribes17' postulates that observed climate changes can be represented as the cumulative effect of scaled fingerprints corresponding to each individual forcing, shown as:

$$Y^* = \sum_{i=1}^{n} X_i^* \qquad (2-5)$$

$$Y = Y^* + \varepsilon_Y \qquad (2-6)$$

$$X_i = X_i^* + \varepsilon_{x_i} \qquad (2-7)$$

Where Y represents the true response to all forcings; X_i represents the true response to individual forcing; n represents the total number of external forcings considered. Y^* and X_i^* are the response to the observed climate and simulated forcing, respectively. $\varepsilon_Y \sim N(0, \sum_Y)$ and $\varepsilon_{x_i} \sim N(0, \sum_{x_i})$ are the observation and model uncertainty (referred as internal variability),

respectively. According to 'Ribes17', the random variables ε_Y and ε_{x_i} are independent and follow a normal distribution. Python code for D&A analysis can be found in the research of de Abreu et al. (2019).

By assuming a linear relationship between the observed change and simulated responses, the ordinary least square method is employed to calculate the scaling factor β. This method is finally expressed as:

$$X_i = X_i^* + \varepsilon_{x_i} \qquad (2-7)$$

To detect the responses of Rx1day and Rx5day changes (fingerprint patterns) under different forcings (e.g., ALL, GHG, AER, NAT), the D&A analysis between observation and the CMIP6 GCMs are conducted in 1950-2014. 1) In one-signal analysis, observed changes in Rx1day (or Rx5day) are regressed against various individual forcings (e.g., ALL, GHG, AER and NAT forcings); 2) in the two-signal analysis, observed changes in Rx1day (or Rx5day) are regressed against NAT forcing and anthropogenic (ANT, corresponding to ALL-NAT) forcing; and 3) in the three-signal analysis, observed changes in Rx1day (or Rx5day) are regressed against three forcings, e.g., GHG, AER and NAT forcings. The fingerprint of a particular forcing is deemed detected when the 90% confidence interval of its associated scaling factor is positive (> 0). Furthermore, observed changes can be attributed to a forcing when its 90% confidence interval is not only positive but also encompasses the value one (Duan et al., 2019a; Min et al., 2011). The attributable contribution of each forcing is estimated by multiplying the linear trend of the observed change in 1950-2014 under this forcing with its corresponding scaling factor.

2.3. Results

2.3.1. Observed and Modeled Trends

Figure 2-2 shows the linear trend in the seasonal spatial distribution of Rx1day (PI) in 1950-2014, comparing observed to modeled trends. Results for Rx5day (PI) are shown in Appendix Figure A.2-2. The CMIP6 multi-model means (MMEs) driven by ALL forcings (Figure 2-2b, g, l, q) generally reproduce the observed trend (Figure 2-2a, f, k, p) of seasonal Rx1day from 1950 to 2014, with more pronounced positive trends in fall and winter than that in spring and summer. However, in JJA (Figure 2-2g), ALL results show a widespread drying in the Mediterranean and western North America, which could be much more severe in the future according to Rowell (2009). Simulated trends are generally less noisy than the observation because MMEs filter out unforced internal variability (Sun et al., 2022). The effects of GHG forcing are like those of ALL forcings but with greater amplitudes and wider impacted regions, which suggests the anthropogenic greenhouse gas emissions play a dominant role in driving the observed changes. Given the enhanced poleward moisture transport under global warming (Zhang et al., 2012), an increased Rx1day is mainly detected in northern high latitudes in winter under GHG forcings. But the impact of GHG emission is reduced by the counter, negative influence of AER forcings, resulted in decreasing trends of ALL results over India and southern China in fall (Figure 2-2l) and winter (Figure 2-2q). Previous studies also widely reported this result for annual changes (Dong et al., 2022; Tan et al., 2022; Undorf et al., 2018b). In DJF, changes in Rx1day under NAT forcing (Figure 2-2t) shows a modest decreasing trend across most regions of Europe, Asia and central North America compared to other seasons. These patterns are likely to result from the volcanic aerosols generated from the Agung eruption in

1963 and the Pinatubo eruption in 1991 (Winter et al., 2015), which have stronger impacts on atmospheric circulation and precipitation patterns during the winter season (Robock, 2000; Stenchikov et al., 2002).

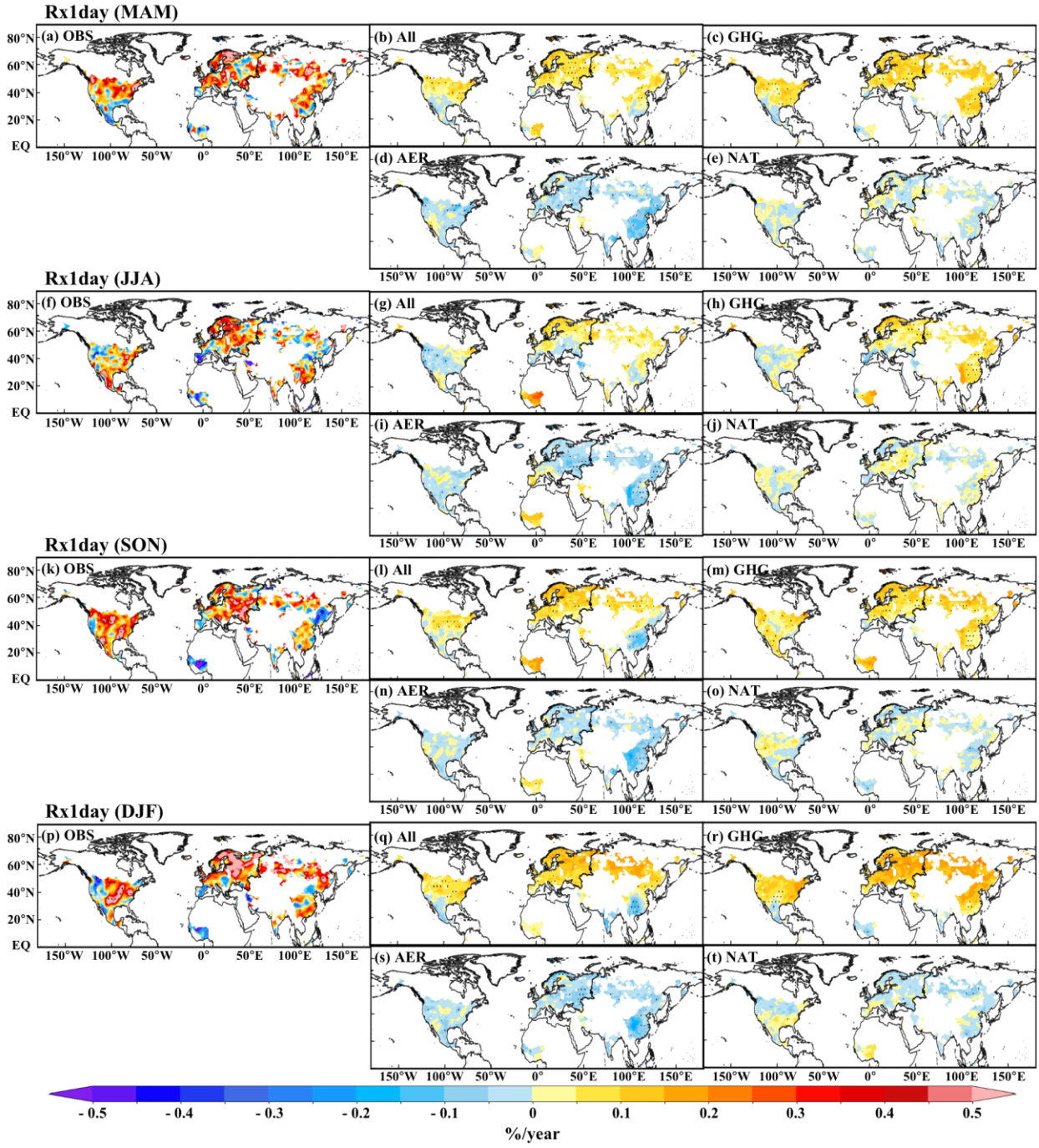

Figure 2-2 Geographical distribution of linear trends (%/yr) in PI of Rx1day during 1950–2014 for MAM, JJA, SON and DJF between observation (HadEX3) and model simulations (anthropogenic plus natural (ALL) forcing, greenhouse gases (GHG) forcing, anthropogenic aerosol (AER) forcing and natural (NAT) forcing). For models, ensemble means of trends from individual simulations are displayed. Black dots indicate grids with significant long-term trends at the 5% level.

2.3.2. Temporal Analysis

The 5-year mean anomalies in Rx1day (PI) during 1950-2014 relative to 1961-1990 between observations and CMIP6 MMEs for JJA and DJF are shown in Figures 3 and 4, respectively. Rx1day anomalies under ALL forcing exhibit consistency with the observations over NHL, HR, LR and almost all the CMIP6 domains, and changes are more evident in winter than that in summer with decreasing trends before the 1980s, followed by rapid recovery, especially over Europe (e.g., WCE, NEU and EEU) and Siberia (e.g., WSB and ESB). However, Rx1day of observation and CMIP6 simulations show negative trends over the Mediterranean area (MED) in JJA. This potential dry trend in the summer MED may result from factors such as the contrast in warming between land and ocean, and thermodynamic and lapse-rate changes (Barcikowska et al., 2020; Tan et al., 2022). Rx1day anomalies in GHG forcing consistently increased over 1950-2014 in both summer and winter over most regions except in central America (e.g., NCA and SCA). Although the cooling effect on Rx1day anomalies by the AER forcing has slowed down since the 1990s in summer and winter over most regions, Rx1day anomalies have been growing in the summer over MED, WCA and WAF since the 1990s. As for the NAT-induced Rx1day anomalies, there is no statistically significant long-term trend over the NHL and subregions. Apparently, based on both observed data and CMIP6 simulations, low-risk regions (LR) tend to experience a greater intensification of Rx1day anomalies than high-risk

regions (HR), especially in winter since the 1980s. This likely means that the risk of low-risk regions has been growing faster than that of high-risk regions, largely attributed to a warmer climate in middle-to-high latitudes (Paik et al., 2020).

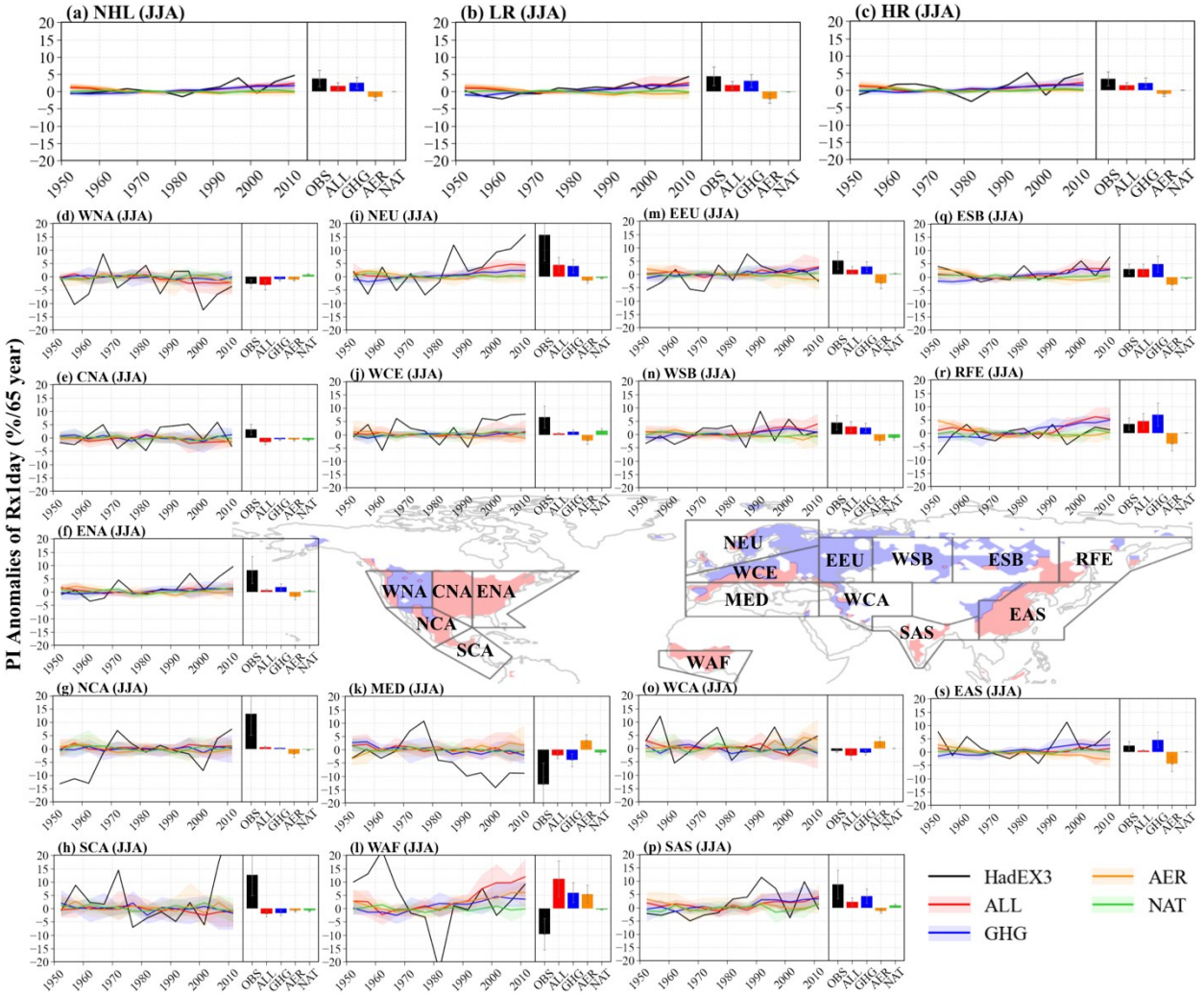

Figure 2-3 Time series of nonoverlapping 5-year mean PI anomalies of Rx1day for JJA from 1950 to 2014 relative to 1961-1990 and their linear trends (bars, %/65yr) with 5%–95% confidence intervals (gray error bars) for OBS (black) and the CMIP6 ensemble means of ALL forcing (red), GHG forcing (blue), AER forcing (orange) and NAT forcing (green). Coloured shadings in the time series indicate model ranges of CMIP6 simulations. Anomalies are averaged over the global (GLB), high-risk region (HR), low-risk region (LR) and 16 CMIP6 subregion domains.

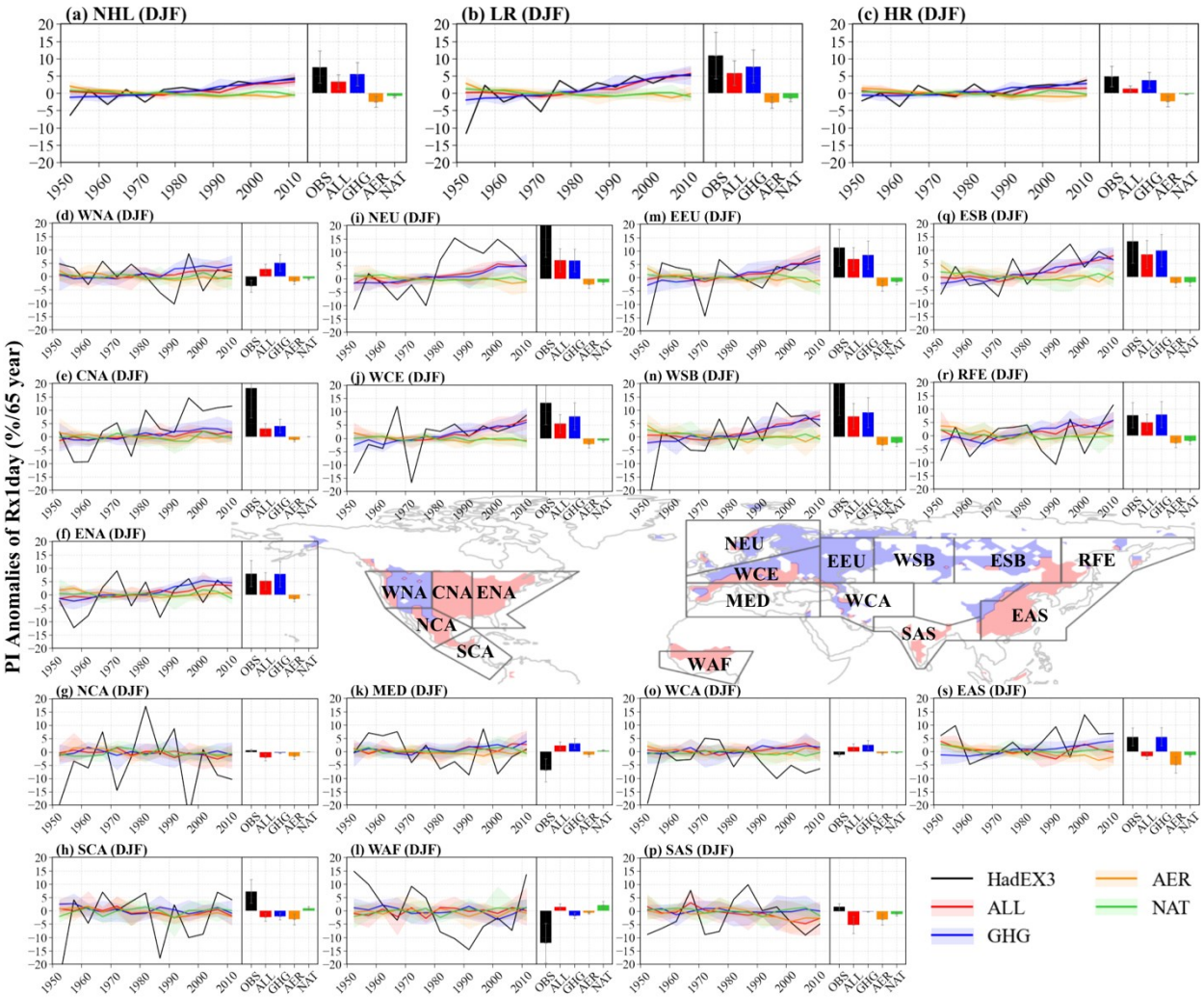

Figure 2-4 Same as Figure 2-3, but for Rx1day in DJF.

Through a change-point analysis, years where detected abrupt change points in Rx1day over 1950-2014 are shown in Figure 2-5. Results show that the statistically significant increase in ALL-induced Rx1day (Figure 2-5a) generally began around the 1990s over NHL and most subregions. Due to the impact of internal variability, change-point detection in the observed Rx1day indices differ widely among regions in the seasonal analysis. However, this internal variability appears to have less influence on the CMIP6 simulations. GHG-induced Rx1day has generally increased faster with statistical significance over most regions since the 1980s. The change points detected in Rx1day are about ten years earlier under GHG responses (since the

1980s) than under ALL responses (since the 1990s) because of the temporal lag between carbon dioxide emissions and their peak warming effects (Ricke and Caldeira, 2014). In Europe and North America, the reduction of aerosol emissions since the 1980s has been found to enhance rainfall due to their radiative activities (Rosenfeld et al., 2008; Undorf et al., 2018a). Thus, decreasing trends of AER-induced Rx1day have generally slowed down over most regions with statistical significance. However, change points detected in Rx1day under NAT forcings are mostly not statistically significant.

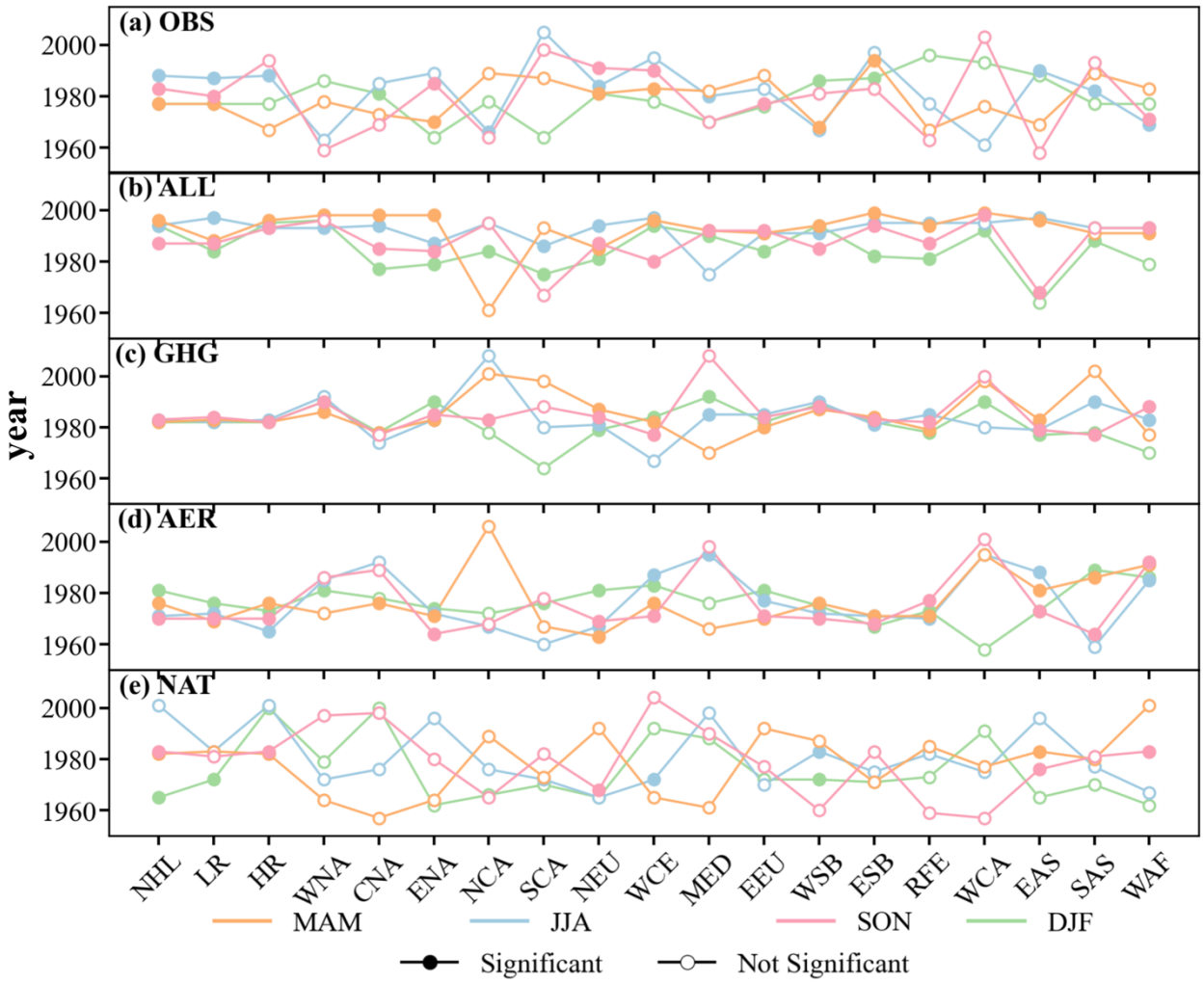

Figure 2-5 Pettitt's test of single change-point detection for the spatial-average Rx1day anomalies during 1950–2014 in MAM (orange), JJA (blue), SON (pink) and DJF (green) over NHL, LR, HR

and CMIP6 subregions. Filled dots indicate the trend is significant at the 5% level, while hollowed dots indicate the trend is not significant at the 5% level.

2.3.3. Detection and Attribution Analysis at Risky Regions

The scaling factors of one-signal analysis (Figure 2-6a, e, i, m) show that the ALL, GHG and AER response patterns are readily detected for seasonal Rx1day over NHL and the two risky regions (HR and LR) in 1950-2014, especially GHG forcings because their uncertainty range of the scaling factor are narrower and closer to one. Anthropogenic forcings mainly drive changes in seasonal extreme precipitation, as ANT fingerprint can be detected over LR and HR in all seasons (Figure 2-6b, f, j, n). The best estimation of the scaling factor and its 90% confidence intervals over HR mostly exceeds 1 during SON and DJF (Figure 2-6j, n), indicating an underestimation of ANT response in the cold season over HR. To better present the observed changes, the results need to be scaled up (Sun et al., 2022). Although GHG forcing is obviously underestimated, D&A results in three-signal analysis (Figure 2-6c, g, k, o) show that GHG fingerprint can be easily detected compared with AER and NAT fingerprints, especially in LR. However, the GHG fingerprint in HR is difficult to be separated from the other two forcings during spring and winter. This is consistent with the results presented in Figure 2-2 that the change of Rx1day can be attributed to AER in India and South China, which occupy a large part of HR. Based on the estimated scaling factors in the three-signal analysis, attributable trends are shown in Figure 2-6d, h, l, p. Results show that the observed increases in Rx1day over LR and HR are primarily explained by GHG forcings. LR tends to have greater GHG-induced Rx1day than HR for all seasons, possibly because LR occupies most of the northern mid-to-high latitudes regions, which exhibit more pronounced warming (Jones et al., 2013; Paik et al., 2020).

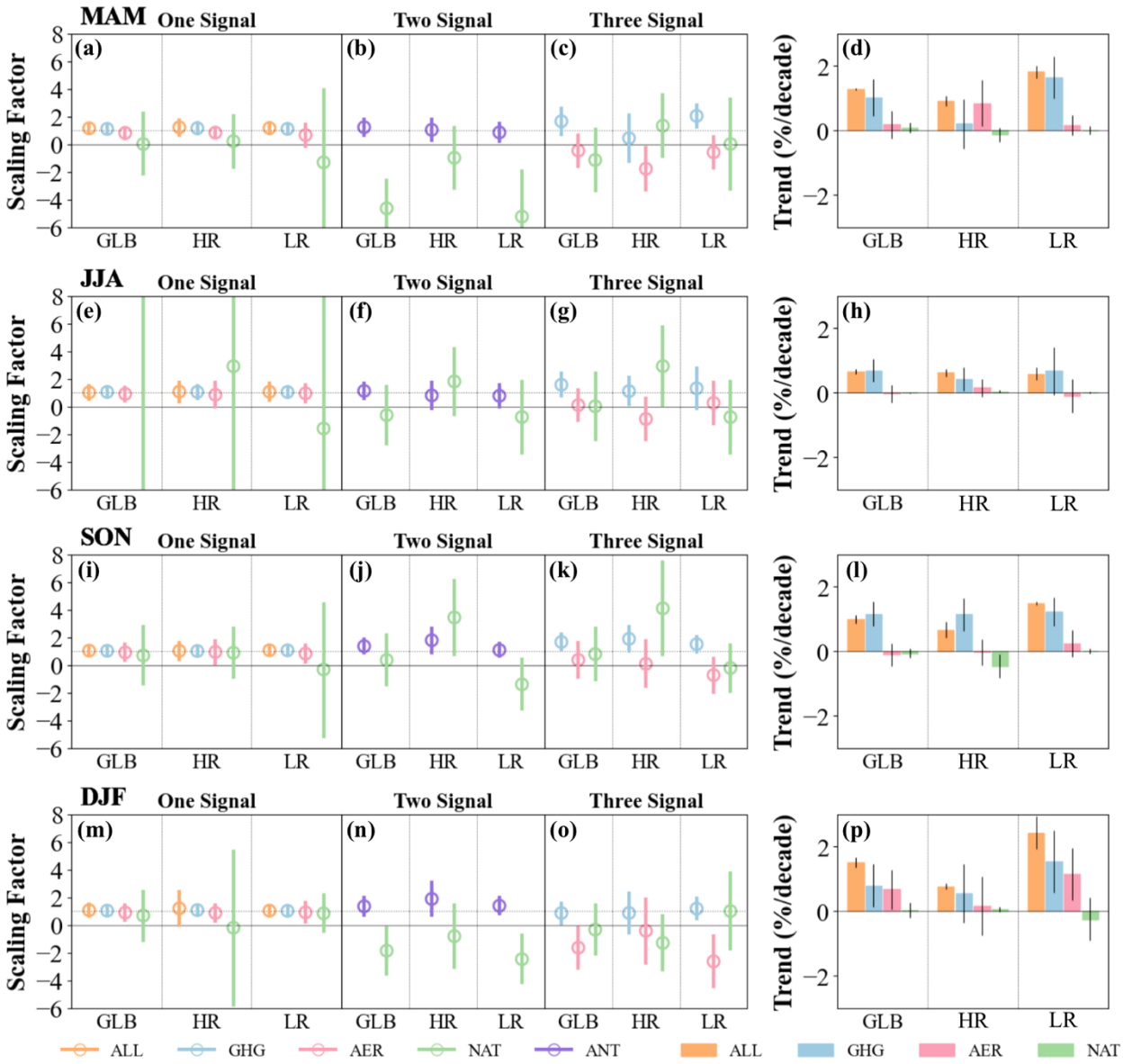

Figure 2-6 Results of the one-, Two- and Three-signal analysis for Rx1day anomalies over NHL, LR and HR in MAM, JJA, SON and DJF are shown in the first three columns. The cycle and vertical line indicate the best estimates of scaling factors and their 10–90% confidence intervals, respectively. The two gray solid and dashed horizontal lines in the first three columns indicate zero and one, respectively. The residual consistency test in one-, two- and three signal analysis are passed at 90% confidence level. The rightmost column is the attributable contribution from GHG, AER, and NAT forcings to observational Rx1day trends during 1950-2014 and their 10–90%

confidence interval (error bars). The attributable contribution is estimated based on three-signal analysis.

2.3.4. Detection and Attribution Analysis for CMIP6 domains

(a) One-Signal Analysis: ALL, GHG, AER and NAT

The one-signal D&A analysis (Figure 2-7 and Table A.2-3) shows that seasonal 90% confidence intervals of 16 CMIP6 domains are broader than the results in the three large scales (Figure 2-6), because the internal variability could raise in smaller regions (Seong et al., 2021). Nevertheless, in 11 out of 16 and 13 out of 16 CMIP6 domains, ALL and GHG forcings are detected in Rx1day in at least one season, respectively. ALL and GHG signals are detectable in five subregions located in North Eurasia (e.g., NEU, EEU, WSB, ESB, REF) in all seasons. In WNA and CNA, GHG signals are detected in all seasons except for JJA, as western North America experienced widespread drying in the summer of 1950-2014. From an aspect of seasonal view, GHG signals are more detectable in fall and winter than that in spring and summer, as GHG forcings are detected in more than half of CMIP6 domains in SON and DJF. The AER forcing is detectable mostly in summer in EAS because its 90% confidence interval of the scaling factor is closer to one compared with other seasons. Although scaling factors are bigger than zero in three seasons of ESB and RFE, the AER signal is not quite detectable as the residual consistency test fails. Because NAT response patterns may not be distinguishable from internal variability, individual NAT forcing cannot be detected in any season over the CMIP6 domains.

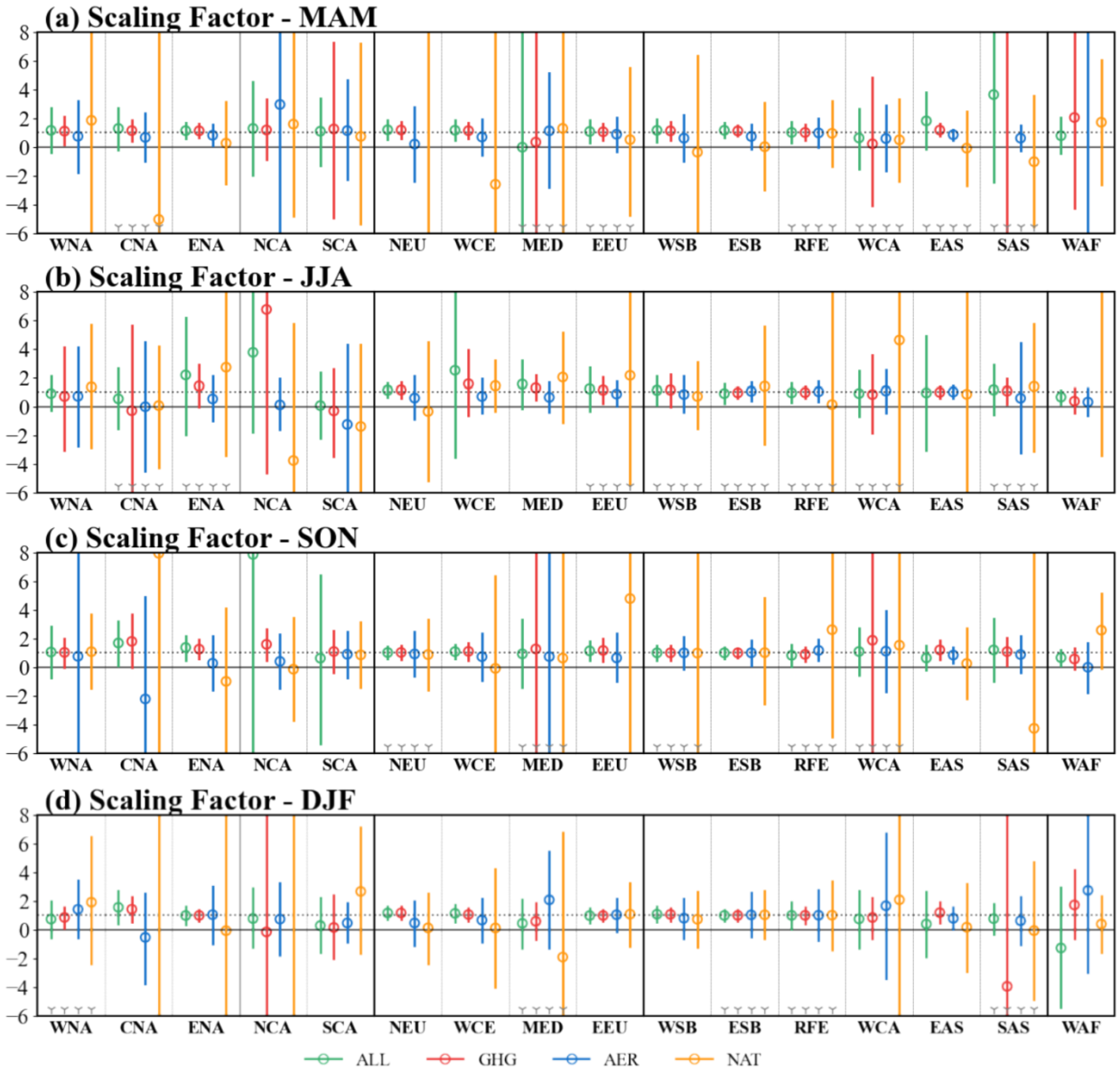

Figure 2-7 Results of the one-signal analysis for Rx1day anomalies over NHL, LR, HR and 16 CMIP6 domains in MAM (a), JJA (b), SON (c) and DJF (d). The best estimates of scaling factors and their 10–90% confidence intervals for ALL (green), GHG (red), ARE (blue) and NAT (yellow) are shown in each subplot. The two gray sloid and dashed horizontal lines indicate zero and one, respectively. The gray triangles in the bottom indicate the failure of the residual consistency test due to too small model variability. Results for continentals are divided by a black vertical line.

(b) Two-Signal Analysis: ANT and NAT

The residual consistency test in two-signal analysis (Figure 2-8 and Table A.2-4) is passed at 90% confidence level over most regions for seasonal analysis. ANT forcings are detected in at least one season over 13 out of 16 CMIP6 domains, which complement results of past annual D&A analysis (e.g., Sun et al. (2022) and Paik et al. (2020)) that both annual and seasonal changes of Rx1day are mainly the result of human influence. Seasonal D&A analysis shows that ANT forcings can be easily distinguished from NAT forcings in colder seasons than that in summer (only NEU and EAS are attributable in JJA). Similar to the results in the individual ALL forcings analysis, in the Eurasia regions (e.g., NEU, WCE, EEU and ESB), Rx1day is more likely to be affected by anthropogenic influence as ANT forcings can be detected in more than two seasons. Detected ANT signals are more likely to be underestimated in winter because, in detected regions (e.g., CAN, NEU, EEU and WSB), the 90% confidence interval of the scaling factor predominantly exceeds one in DJF. It seems that winter precipitation extremes, especially in northern high latitudes, could be potentially more severe than expected. Different from the results in one-signal analysis and many previous annual D&A results, natural external forcings have likely contributed since NAT forcings are detected in 5 regions (e.g., WNA, ENA, SCA, WCA and WAF) in the fall. Therefore, observed changes in seasonal Rx1day should be explained by both anthropogenic and natural external forcings.

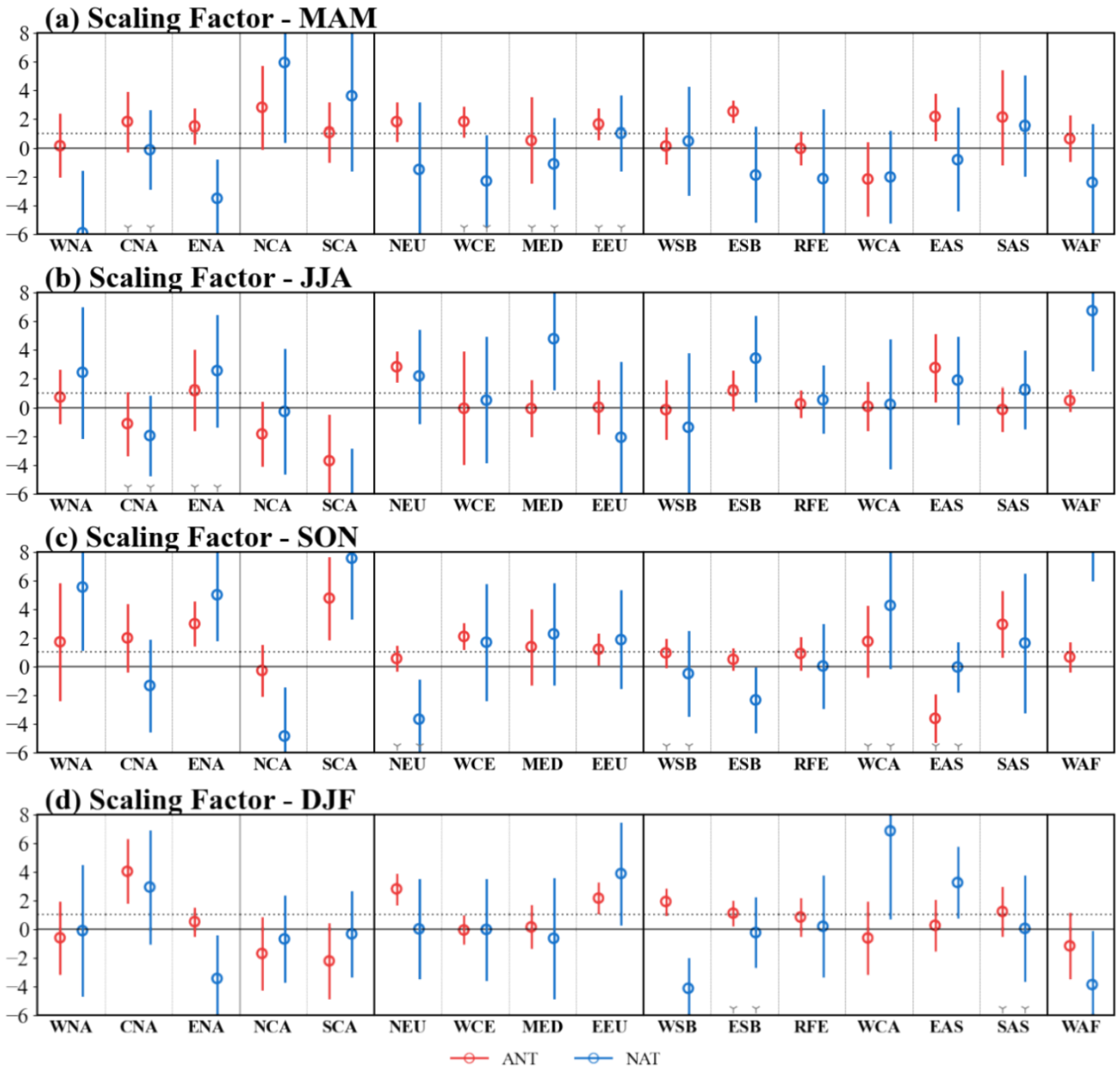

Figure 2-8 Same as Figure 2-7, but for two-signal analysis, ANT (red) and NAT (blue) forcings.

(c) Three-signal Analysis: GHG, AER and NAT

Based on the results presented in Figure 2-9 and Table A.2-5, the three-signal analysis is used to examine whether these forcings, GHG, AER and NAT can be detected and separated from others over CMIP6 domains. Obviously, the detection of GHG signals is season dependent because the increase of Rx1day is stronger in winter than in other seasons. Moreover, GHG

signal is detectable and distinguishable from AER and NAT forcings in winter over high latitudes (e.g., ENA, NEU, WSB, ESB, et al.). A few AER signals are detected in MED and WAF, but their residual consistency tests are negative, indicating the potential underestimation of internal variability. In the two- and three-signal analysis, NAT forcings are detected over similar regions, e.g., WNA, SCA, MED, WCA and WAF. The results contradict the traditional belief that NAT forcings have a limited impact on the changes of precipitation extremes, because seasonal changes in some "climate-homogenous" areas are likely to be attributed to natural external forcings. Apparently, while the anthropogenic GHG forcings are the predominant drivers of the observed intensification in Rx1day, natural external forcings also play a significant role in influencing the seasonal changes of Rx1day in some CMIP6 domains.

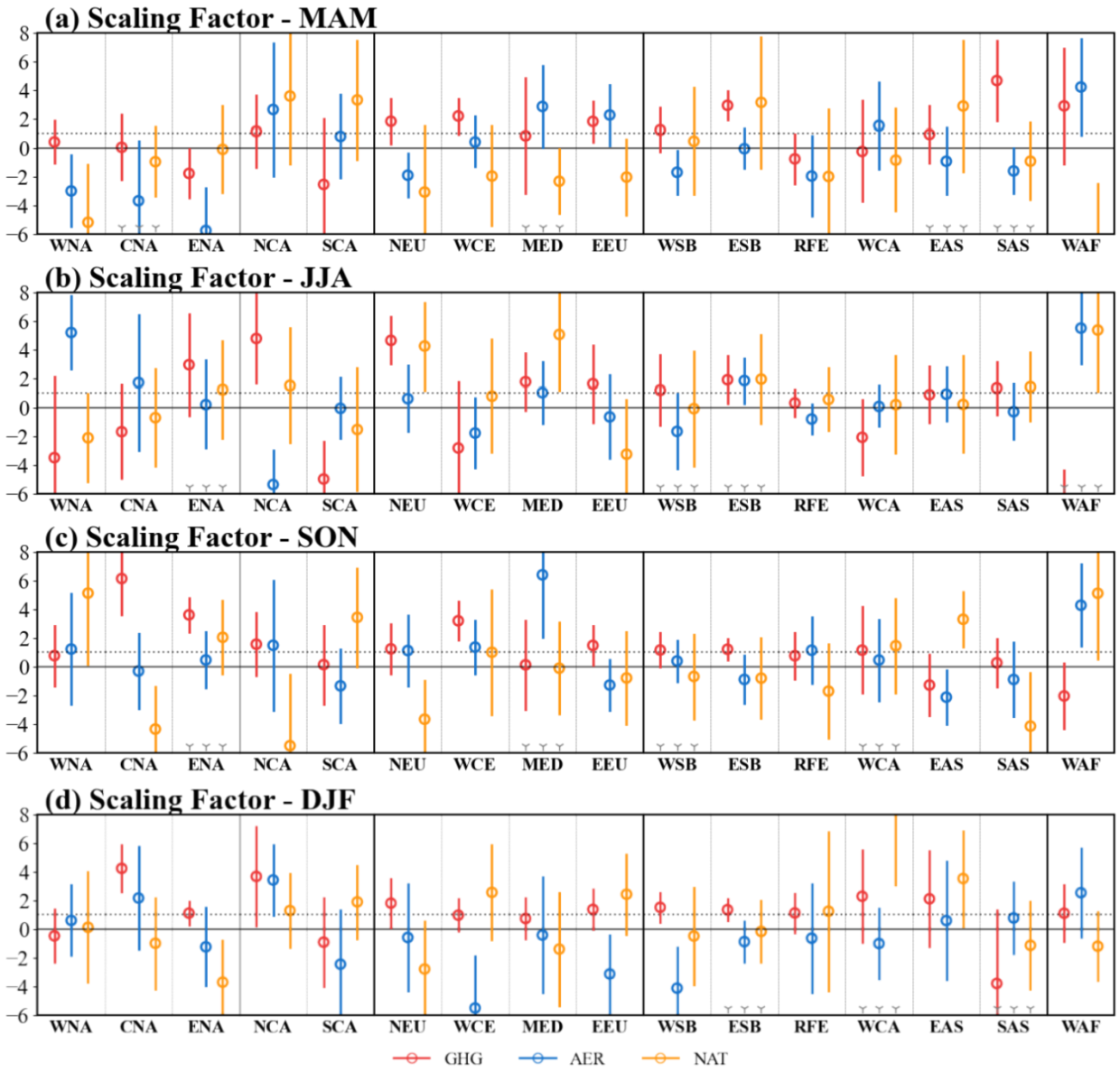

Figure 2-9 Same as Figure 2-7, but for three-signal analysis, GHG (red), AER (blue) and NAT (yellow) forcings.

(d) Attributable Contribution

Figure 2-10 shows the attributable contributions of ANT and NAT forcings to the observed trends. We only analyzed the change in winter as it is likely to be the season when the impact of anthropogenic activities is most detectable. During 1950–2014, observed changes in

Rx1day during winter are mainly found in northern high latitudes, such as CNA, NEU and WSB (Figure 2-10b, f and k). This is expected given the Arctic has been warming much faster than lower latitude regions, commonly known as Arctic amplification (Rantanen et al., 2022), increased temperatures lead to a greater intensification of the hydrological cycle in the above regions (Marvel & Bonfils, 2013). The median values of the attributable contribution of forcing over CNA, NEU and WSB are 67%, 111% and 91%, respectively. In addition, the ANT contributions are explained in more than 2/3 of regions with over 60% detectable contributions. NAT contributions are less than 20% over 2/3 of regions except for WAF (71%) and WSB (43%) (Figure 2-10i and k). Particularly, in EEU and EAS, NAT forcings are detected in two-signal analysis (Figure 2-8d) with a negative contribution in Figure 2-10, while in WCA (Figure 2-10l), NAT is detected with a positive contribution. Therefore, in seasonal D&A analysis, observed changes should not only be explained by anthropogenic forcings because NAT forcings could also have positive or negative contributions.

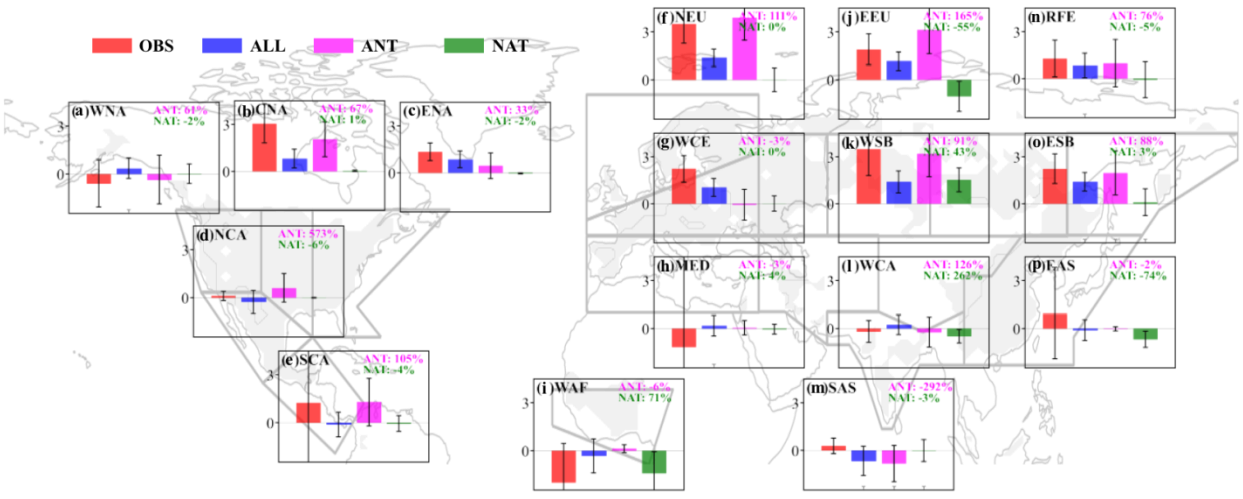

Figure 2-10 Attributable contributions and their 10%–90% confidence intervals for the Rx1day in DJF over 16 CMIP6 domains. The trends for observation (OBS) are estimated by linear least squares regression. The attributable contributions for ALL are estimated based on one-signal

analysis, while those for ANT and NAT are based on two-signal analysis involving ANT and NAT forcings. The magenta and green values in the upright of each subfigure are the percentage of contribution trends for ANT and NAT to observe changes, respectively. The gray triangles at the bottom indicate the failure of the residual consistency test due to too small model variability.

2.4. Discussion and Conclusions

Through the application of an optimal fingerprinting method, we conducted a D&A analysis in the seasonal changes of Rx1day and Rx5day between HadEX3 observations and CMIP6 simulations during 1950–2014 over low-risk (LR) region, high-risk (HR) region and 16 CMIP6 domains. Results show that an increase in the seasonal Rx1day has been confirmed across most of NHL (except for North America and the Mediterranean during JJA) since the mid-twentieth century. The increasing pattern is more significant and widespread in fall and winter but weaker in spring and summer. The dry trend in western North America and the Mediterranean is likely a result of the decreased summer precipitation in midlatitude continents driven by the "warming" mechanism, "spring soil moisture" mechanism and "remote circulation" anomalies (Barcikowska et al., 2020; Brogli et al., 2019; Rowell, 2009). This drying pattern will be more severe in the future as anthropogenic warming increases. The observed changes are predominantly driven by GHG forcing. Due to various feedback mechanisms, such as the ice-albedo feedback, northern Eurasia experiences more significant warming in winter, increasing moisture available for precipitation events (Rantanen et al., 2022). However, Rx1day have mainly decreased during cold seasons in India and southern China because the heavy anthropogenic aerosol loadings in the mid-latitude regions that tend to reflect or to scatter incoming solar radiation, which prevented the increase in surface temperature (Duan et al., 2019a). As anthropogenic aerosol continues to decrease in Europe and North America, the

greenhouse gas influence will become more dominant in future (Seong et al., 2021; Undorf et al., 2018a). Although it is obvious that human influence contributes significantly to higher Rx1day over the study period, the influence of NAT forcing is not negligible as its impact can be detected across regions and in various seasons.

The findings from the regional analysis indicate that response to anthropogenic influence appears more robust in smaller regions when aggregating areas are based on regional climate features instead of geographical delineation. In the one- and two-signal analysis, the anthropogenic influence is detectable for at least one season over more than 80% of CMIP6 domains. Due to the potential collinearity among GHG and AER forcing, GHG signals are less detectable in the three-signal analysis than in the one-signal analysis. Generally, the influence of greenhouse gas emissions in winter is stronger than in other seasons as a large amount of energy is produced from burning fossil fuels in the cold season, leading to a more detectable GHG signal, especially over high-latitude regions like northern Europe (e.g., NEU, WCE and EEU) and northern Asia (e.g., WSB, ESB and REF). Individual AER signal is most attributable in East Asia, particularly in JJA, because its 90% confidence interval of the scaling factor is closer to one in summer compared with the other three detected seasons (MAM, SON, and DJF). The NATs are not detectable in any annual analysis in previous studies (Paik et al., 2020; Sun et al., 2022; Zhang et al., 2013). However, it is not necessarily an indication of no signal when not meeting the D&A condition, and it may state that the signal cannot be distinguishable from the internal variability over this period (Kirchmeier-Young & Zhang, 2020). Interestingly, we cannot detect seasonal NAT forcings in one-signal analysis, but NAT signals are detected over similar regions (e.g., WNA, SCA, MED, WCA and WAF) between the two- and three-signal analysis, implying that human influence alone may not be the only cause for changes in the extreme

precipitation. Volcanic aerosols generated by the Agung eruption in 1963 and the Pinatubo eruption in 1991 (Winter et al., 2015) which had significantly impacted atmospheric circulation and precipitation patterns have been shown to be related to detected changes in extreme precipitation (Robock, 2000; Stenchikov et al., 2002).

If we are not mistaken, our study provides the first D&A analysis of seasonal precipitation changes on global and regional scales. Our results confirm that external anthropogenic forcing has dominated the observed changes at the hemisphere and regional scales since the 1950s, which will contribute to the scientific basis that decision-makers can use to implement effective mitigation policies and adaptation planning against the impact of global warming on extreme precipitation events. Future research should focus on the combined impact of human influence and climate anomalies on annual and seasonal precipitation extremes because anthropogenic GHG forcings and anthropogenic aerosol forcings alone cannot adequately explain observed changes. Natural forcing and internal climate variability are also like to be attributable. New insight into extreme precipitation gained from such studies may give farmers and water resource managers more time to prepare for such major events.

2.5. Notation

AER = His-aer forcing (anthropogenic aerosol forcing only)

ALL = Historical forcing (including both anthropogenic and natural external forcings)

ANT = Anthropogenic forcing, corresponding to ALL-NAT

CEDA = The Centre for Environmental Data Analysis Archive

CDF = Cumulative density function

CDO = The Climate Data Operators

CMIP6 = The Coupled Model Intercomparison Project Phase 6

CTL = The preindustrial control experiment

D&A analysis = The detection and attribution analysis

DJF = Winter (including December, January and February)

ESG = The Earth System Grid data distribution portal

ETCCDI = The Expert Team on Climate Change Detection and Indices

GCMs = Global climate models

GEV = The generalized extreme value distribution

GHG = Hist-GHG forcing (greenhouse gases forcing only)

HadEX3 = The Hadley Centre global land-based climate extremes dataset

HR = High-risk region

IPCC AR6-WG1 = Intergovernmental Panel on Climate Change's Sixth Assessment Report of Working Group 1

JJA = Summer (including June, July and August)

LR = Low-risk region

MAM = Spring (including March, April and May)

MMEs = Multi-model means

NAT = Hist-nat forcing (natural external forcing only)

NHL = The Northern Hemisphere land

OBS = Observation

OLS = Ordinary least square

PI = Probability-based index

Rx1day = Maximum one-day precipitation

RX5day = Maximum five-day precipitation

SON = Fall (including September October and November)

Chapter 3 Projected Changes of Precipitation Extremes in North America using CMIP6 Multi-Climate Model Ensembles

3.1. Introduction

The Intergovernmental Panel on Climate Change Sixth Assessment Report (IPCC, 2021) reported an unprecedented warming in each of the last four decades than any previous decade since 1850, that the global mean surface temperature in 2011–2020 has risen by 1.09 [0.95 to 1.20] ◦C compared to 1850–1900. Unless greenhouse gas emissions are drastically reduced immediately, the world will probably exceed 1.5 ◦C of warming within the next two decades (Allen et al., 2019). The intensification of extreme precipitation is an expected effect of a warming climate (AghaKouchak et al., 2020; Douville et al., 2021): it is of high confidence that the increase of global precipitation extremes is about $7\%K^{-1}$ similar to the moisture increase based on the Clausius - Clapeyron relationship (IPCC, 2021; Li et al., 2021; Wehner, 2020). The intensification of daily extreme precipitation has been observed in North America and high latitudes of the Northern Hemisphere, as well as in many other regions (Kirchmeier-Young & Zhang, 2020; Ma et al., 2020; Zhan et al., 2020; Zhang & Colle, 2017; Zhou et al., 2018), which is expected to worsen as the hydrologic cycle accelerates under global warming impact (Tabari, 2020), leading to a higher risk of major flooding, which will significantly impact the ecosystems, human societies and also the economy.

To investigate the hydroclimatic effect of global warming, a set of indices has been defined by The Expert Team on Climate Change Detection and Indices (ETCCDI) to detect particular characteristics of weather and climate extremes, including frequency, amplitude and

persistency (Zhang et al., 2011). These indices describe extreme meteorological events in a given year or month (Sillmann et al., 2013a; Srivastava et al., 2020), which have been widely used in studies on detection and attribution analysis (Dong et al., 2021; Kirchmeier-Young & Zhang, 2020; Liu et al., 2021a; Zhang & Zhou, 2020), regional studies in observational records and future projections (Akinsanola et al., 2020b; Bai et al., 2021; Duan et al., 2019; Gibson et al., 2019; Kim et al., 2020; Sillmann et al., 2013a; Srivastava et al., 2022), as well as the performance examination among climate models (Fan et al., 2020a; Fan et al., 2020b; Gibson et al., 2019; Srivastava et al., 2022).

Global Climate Models (GCMs) have been widely used in climate studies, and they have been shown to simulate representative historical climate statistics (Agel & Barlow, 2020; Zhan et al., 2020). Moreover, GCMs are critical tools widely used in predicting mean and extreme climate events (Akinsanola et al., 2020a; Knutti et al., 2008; Stouffer et al., 2017b; Zhu & Yang, 2020). Based on GCMs and ETCCDI indices, researchers projected a general increase in global-scale extreme precipitation events (Chen et al., 2020; Li et al., 2021; O'Neill et al., 2016; Wehner, 2020). Recently there have been growing numbers of regional analysis on changes to future precipitation extremes based on GCMs and ETCCDI indices (Duan et al., 2019b; Ge et al., 2021; Rao et al., 2020; Xu et al., 2019). For example, extreme precipitation in California has been projected to increase largely by storms due to "atmospheric river" (Berg & Hall, 2015; Huang et al., 2020; Iturbide et al., 2020b); GCMs were used by Akinsanola et al. (Akinsanola et al., 2020a), Almazroui et al. (2021) and Ning and Bradley (2016) to project an amplification of heavy precipitation over the eastern US; A robust increase in winter precipitation was projected in Canada due to the increase in horizontal water vapor flux (Erler & Richard Peltier, 2016; Zhou et al., 2018) and teleconnections (Tan et al., 2019)

Although some future projections have been conducted on extreme precipitation indices by using GCMs, further study is still needed. Firstly, previous studies of future changes in climate extremes have been based on climate scenarios of the Coupled Model Intercomparison Project 5, but now can be conducted using the most recent simulations from GCMs of CMIP6 and the Shared Socioeconomic Pathway (Eyring et al., 2016; O'Neill et al., 2014). The new generation of GCMs of CMIP6 is developed with finer resolutions and improved dynamical processes that address three critical scientific gaps in CMIP5 (Gidden et al., 2019; Priestley et al., 2020; Stouffer et al., 2017a). Recent studies show an improvement in the CMIP6 ensemble in simulating global climatic extremes (Agel & Barlow, 2020; Chen et al., 2020), with a stronger climate variability than CMIP5 models globally (Fan et al., 2020b; Kim et al., 2020; Zhu & Yang, 2020). Secondly, studies related to the projection of extreme precipitation based on GCMs generally focus on some extreme ETCCDI indices that cannot comprehensively analyze future extreme precipitation in terms of their changes in frequency, amplitude and persistency (Akinsanola et al., 2020b; Bai et al., 2021; Duan et al., 2019b; Gibson et al., 2019; Kim et al., 2020; Sillmann et al., 2013a; Srivastava et al., 2022). Thus, research involving all categories of extreme precipitation indices is needed. Thirdly, previous studies are mainly focused on future changes in sub-regional (e.g., Western NA, Eastern NA and the United States), lacking analysis of extreme precipitation in the whole NA (Almazroui et al., 2021; Ma et al., 2020; McAfee et al., 2011; Zhang & Colle, 2017). Given the strong relationship among regions in the changes of extreme precipitation due to the accelerating hydrologic cycle under global warming impact (Tabari, 2020), it is necessary to assess future extreme precipitation in overall NA to compare the magnitude and sign of changes among subregions. Therefore, in this chapter we analyzed projected changes in ten extreme precipitation indices over NA and its subregions by using

simulations of CMIP6 GCMs. Results may contribute to the scientific basis that decision-makers can use to frame effective mitigation policies and adaptation planning.

This chapter is organized as follows: Section 3.2 describes the CMIP6 multi-model ensembles, two observation datasets and the study area. Section 3.3 defines extreme precipitation indices and the metrics used in this chapter while Section 3.4 evaluates the results based on projections of 18 GCMs of CMIP6, the distributions, temporal evolutions and spatial variabilities of extreme precipitation indices, seasonal patterns, and climate model agreements. Summary of results and conclusions are given in Section 3.5.

3.2. Data

3.2.1. CMIP6 Simulations

Daily precipitation data of CMIP6 simulated by some selected GCMs over 1981–2100 are obtained from the Earth System Grid data distribution portal (ESG, https://esgf-node.llnl.gov/search/cmip6/). The GCMs of CMIP6 are selected for this chapter if (1) the nominal model resolution is between 100 km and 250 km because GCMs of higher resolutions should simulate more representative precipitation extreme events than GCMs of coarser resolutions (Bador et al., 2020; Chen et al., 2020); and (2) model outputs should be available for both historical experiments and three future SSP emissions scenarios (SSP1-2.6, SSP2- 4.5 and SSP5-8.5) to compare the extreme precipitation projected by the selected GCMs under the possible impact of climate warming. In addition, (3) only extreme precipitation data projected by the first ensemble member of each GCM (i.e., r1i1p1f1) is assessed to avoid unfair comparison among the GCMs (Kim et al., 2020; Priestley et al., 2020). In this chapter, we have selected a total of 18 GCMs of CMIP6 based on data available until 2019. Table A.3-1 provides the name,

institutions, nominal model resolution and experimental run information of all the GCMs selected for this chapter.

3.2.2. Observed Precipitation Data

Given uncertainties inevitably exist in most if not all observational products due to different data sources and processing algorithms (Akinsanola et al., 2020b; Herold et al., 2017), an in-situ and a reanalysis observed precipitation datasets are used to comprehensively evaluate the ensemble performance of precipitation extremes simulated by the 18 selected GCMs of CMIP6 over the historical period of 1981–2010. The Daymet (version 4) Data Product is an in situ-based gridded dataset supported by the National Aeronautics and Space Administration of USA (NASA). In Daymet, the latest observed station datasets of daily weather and climatology variables are interpolated to a high, 1-km spatial resolution over NA starting from 1980 (Thornton et al., 2021). The North American Regional Reanalysis (NARR) dataset produced by the National Centers for Environmental Prediction (NCEP) provides daily precipitation data at a 32-km resolution since 1979 (Mesinger et al., 2006). These two datasets have been successfully used in evaluating model-simulated extreme precipitation in certain regions of NA (Ashfaq et al., 2016; Dong et al., 2019; Liu et al., 2017; Srivastava et al., 2022).

1981 to 2010 is chosen as the reference period for evaluating selected GCMs of CMIP6 because this 30-year period is the baseline, “climate normal” period recommended by the World Meteorological Organization (WMO) as the most representative of current climatic conditions (WMO, 2019). Furthermore, many studies (Dosio et al., 2019; Iturbide et al., 2021; Spinoni et al., 2018) based on the Sixth Assessment Report (AR6) of IPCC also choose this period as the baseline “climate normal” period. The projected impact of climate warming relative to the

historical period of 1981–2010 is assessed over two future periods, the 2050s (2041–2070) and the 2080s (2071–2100).

3.2.3. Study Area

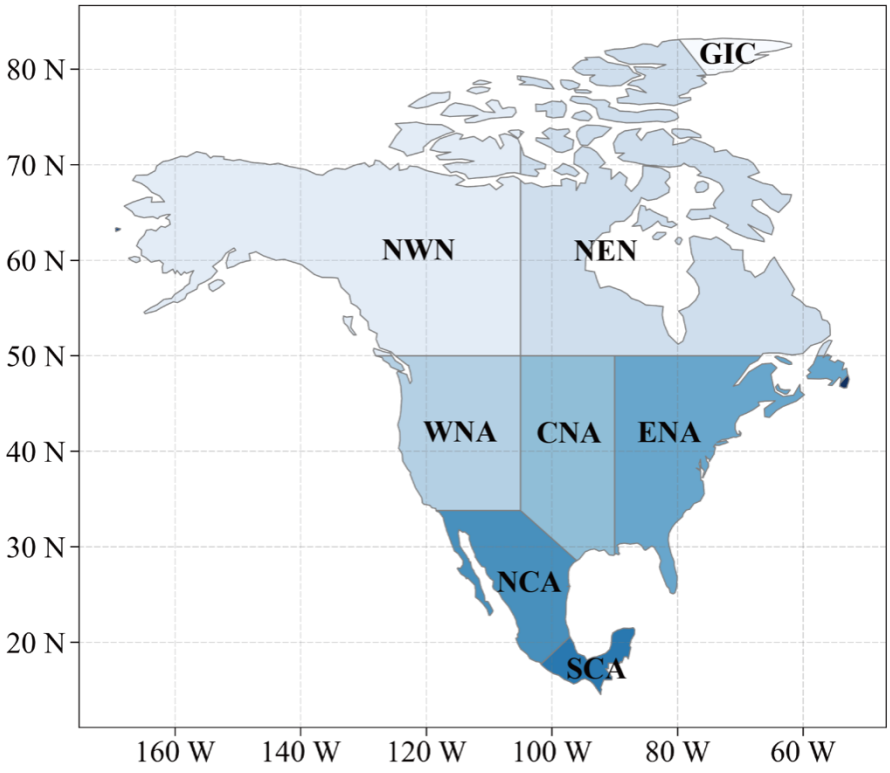

Figure 3-1 Study area (Note: GIC: Greenland/Iceland; NWN: N.W.North-America; NEN: N.E.North-America; WNA: W.North-America; CNA: C.North-America; ENA: E.North-America; NCA: N.Central-America; SCA: S.Central-America; A: S.Central-America).

According to the reference regions in the IPCC AR6 (Iturbide et al., 2020a), North America (NA) is divided into eight "climate-homogenous" areas such as NWN (NW North America), NEN (NE North America), and others, as shown in Figure 3-1. Since these reference regions are widely used in various recent studies on the analysis of CMIP6 simulations, we have

conducted this study using the same reference regions in NA so that we can compare our results with other related studies on AR6 of IPCC (e.g., Kim et al. 2020).

3.3. Research Methodology

The effects of climate warming to the future extreme precipitations of NA are evaluated in terms of ten selected precipitation indices of ETCCDI to assess projected changes in precipitation intensities, maximum rainfall depth over 1 to consecutive 5 days, durations of consecutive wet and dry days, etc. as explained below.

3.3.1. Extreme Climate Indices

Following the ETCCDI, ten precipitation indices are analyzed in this chapter (see Appendix Table A.3-2), which can be grouped under four basic categories:

(1) Absolute precipitation indices are maximum 1-day (Rx1day) or 5-day precipitation (Rx5day) for both annual and monthly time scales. High values of Rx1day could result in flash floods expected to cause damages and hazards to municipal infrastructure, transportation networks, and others, while high Rx5day could lead to large-scale river flooding, resulting in extensive and long-term damages.

(2) Duration indices are consecutive dry (CDD) and wet days (CWD) that respectively represent the maximum number of consecutive days with daily precipitation amount < 1 mm (CDD) or ≥ 1 mm (CWD) in a year. Therefore, CDD and CWD are the indices representing the durations of dry and wet spells.

(3) Threshold indices, R10mm or R20mm, are the number of days with more than 10 mm or 20 mm precipitation, which represent the frequency of heavy precipitation and very heavy precipitation, respectively, at an annual or monthly time scales.

(4) Percentile indices are the R95p and R99p indices that measure the total precipitation per year from wet-day (PR > 1 mm) with precipitation above the 95th and 99th percentile daily precipitation, respectively, for 1981-2010. R95p represents very wet days while R99p represents extremely wet days.

(5) Total wet-day precipitation (PRCPTOT) at annual and monthly time scales, and the simple daily intensity (SDII) index on wet days (PR ≥ 1 mm) at annual time scale.

All indices are computed on an annual basis, but some are also computed on monthly basis (e.g., Rx1day, Rx5day, R10mm, R20mm and PRCPTOT). The extreme precipitation indices are first estimated for the original grids of GCMs using the R package (ClimPACT2) at https://github.com/ARCCSS-extremes/climpact, and then bilinearly interpolated into a common 1°×1° resolution using the Climate Data Operators (CDO) at https://code.mpimet.mpg.de/projects/cdo. Therefore, the CMIP6 ensemble median (CMIP6-EnM) for a specific index is the median at each 1°×1° grid interpolated from the simulations of 18 CMIP6 models over the NA grids.

3.3.2. Model Performance Metrics

The performance of CMIP6 GCMs has been evaluated using the root mean squared error (RMSE) statistics in recent studies at both global and regional scales (Kim et al., 2020; Sillmann et al., 2013a; Srivastava et al., 2020; Xu et al., 2019). The annual, spatially averaged extreme

precipitation index simulated by GCMs is evaluated against corresponding observed datasets (Daymet and NARR) for 1981-2010 using $RMSE_{XY}$ defined as:

$$RMSE_X = \sqrt{< (X - Y)^2 >} \quad (3-1)$$

where X and Y represent the extreme precipitation index simulated by a GCM of CMIP6 and the observed dataset at a grid point, respectively. The angular brackets represent the mean for all grids points over NA.

$RMSE'_{XY}$ is the difference between individual model (including CMIP6-EnM) $RMSE_{XY}$ and $RMSE_{Median}$ (median error of an index for 18 GCMs) that provides an indication of the performance of GCMs of CMIP6 with respect to observations. $RMSE'_{XY}$ is defined as:

$$RMSE'_{XY} = \frac{RMSE_{XY} - RMSE_{Median}}{RMSE_{Median}} \quad (3-2)$$

Thus, for a specific extreme precipitation index, a negative $RMSE'_{XY}$ indicates that the corresponding model performs better than the majority (50%) of CMIP6 GCMs. Similarly, a positive $RMSE'_{XY}$ indicates that the corresponding model performs worse than the majority (50%) of CMIP6 GCMs.

SNR is the signal-to-noise ratio that indicates the credibility of a GCM's projection at a grid point:

$$SNR = \frac{|X_e|}{\sqrt{\frac{1}{n}\sum_{i=1}^{n}(x_i - x_e)^2}} \quad (3-3)$$

Where x_i represents the index simulated by an individual GCM while x_e is the corresponding index of CMIP6-EnM, and n is the ensemble size (n = 18). In a statistical sense, the numerator and denominator represent the signal and the noise, respectively. SNR > 1 implies that the signal is greater than the noise, indicating relatively reliable projections, and vice versa.

3.3.3. Projected Changes in Future Extreme Precipitation

Projected changes of extreme precipitation indices in two periods (the 2050s and the 2080s) relative to the baseline 1981–2010 are calculated as follows:

when indices' units are mm:

$$Relative\ Change\ (\%) = \frac{Index_{future} - Index_{baseline}}{Index_{baseline}} \times 100\% \qquad (3-4)$$

when indices' units are days:

$$Relative\ Change\ (days) = Index_{future} - Index_{baseline} \qquad (3-5)$$

3.4. Results

3.4.1. Performance of Global Climate Models of CMIP6

Portrait diagrams in Figure 3-2 provides an assessment of the performance of 18 CMIP6 GCMs in NA in simulating ten extreme precipitation indices such as CDD, CWD, PRCPTOT, R10mm, etc., with reference to the observed Daymet (Figure 3-2a) and NARR dataset (Figure 3-2b). Model performances in 8 subregions are show in Appendix Figure A.3-2. Negative (Positive) values shown in blue (red) indicate that the GCM performs better (poorer) than the majority (50%) of selected GCMs. The assessment results in the simulations of GCMs are based on the

assumption that the observed dataset is correct even though observed data inevitably has some uncertainty due to the limitations of ground observation. Three GCMs, EC-Earth3, TaiESM1 and NorESM2-MM, perform relatively well, with the most negative $RMSE'_{XY}$ in Figure 3-2. Part of the reason is that higher-resolution climate models generally perform better in simulating observed extreme precipitation than models with coarser resolutions (Agel & Barlow, 2020). In contrast, IPSL-CM6A-LR and FGOALS-g3 show relatively weak performance with many positive $RMSE'_{XY}$ because they generally overestimate the change of extreme precipitation due to their coarser resolution as also found in previous studies (Ge et al., 2021; Srivastava et al., 2020). However, CMIP6-EnM show negative $RMSE'_{XY}$ for all indices, indicating that the CMIP6-EnM is more robust than precipitation events simulated by individual GCMs in both NA and 8 subregions (Figure A.3-2) because as the median at each grid interpolated from the simulations of 18 CMIP6 models over the NA grids, CMIP6-EnM could cancel some of the simulation errors (either over or under simulations) in individual climate models.

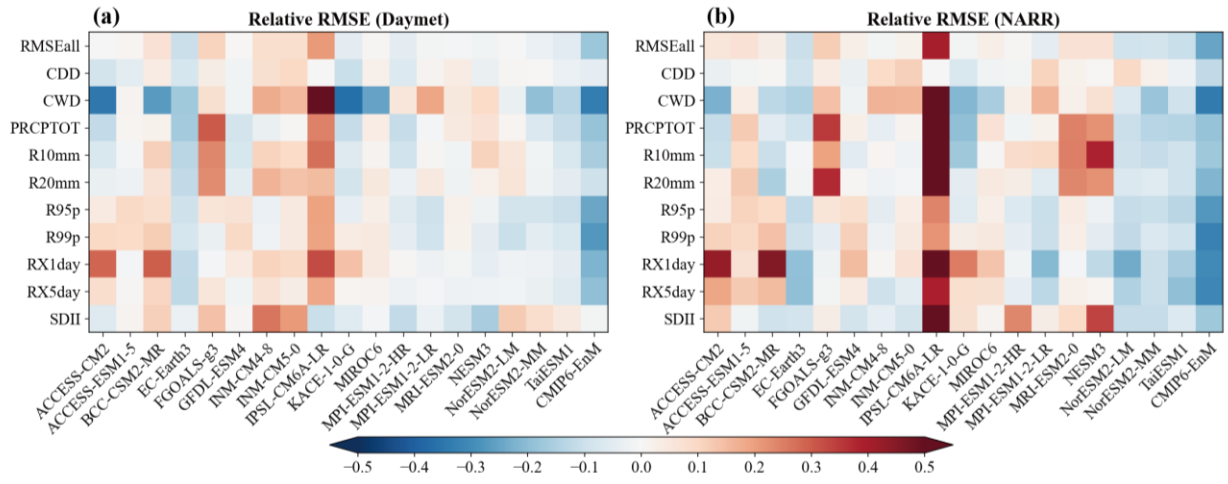

Figure 3-2 The "portrait" diagram of relative spatially averaged $RMSE'_{XY}$ for the 1981–2010 climatology of extreme precipitation indices simulated by the 18 CMIP6 climate models and CMIP6 ensemble median (CMIP6-EnM, in the rightmost of each figure) with respect to the observations,

Daymet (the left figure) and NARR (the right figure). The $RMSE'_{XY}$ are spatially averaged over North America grid points. Each row shows the mean $RMSE'_{XY}$ for one of the ten precipitation indices estimated from the simulation of a particular CMIP6 GCM model. The magnitude of the $RMSE'_{XY}$ is shown as blue-red colors.

Figure 3-3 compares spatial distributions of seven extreme precipitation indices of the CMIP6 ensemble median and observations over NA for 1981–2010, results of R20mm, rx1day and R99p are shown in Appendix Figure A.3-3. The spatial distributions for seven extreme precipitation indices of NA for the historical period are statistically significant (SNR > 1) over almost the entire NA, except for some uncertainty in GIC for R10mm (Figure 3-3b_3), and uncertainty in northern and western NA for R20mm (Figure A.3-3a_3) and R99p (Figure A.3-3c_3). There is an obvious discontinuity between the NARR dataset at the Canada-U.S. border because relatively less number and lower resolution of climate station data is assimilated for Canada than those for the United States (Zhou et al., 2018).

Results show that CMIP6-EnM could well reproduce the historical spatial patterns of observed precipitation events. Precipitation extremes represented by three datasets features a tend to concentrate mainly in the Pacific Northwest, eastern the United States and the Gulf of Mexico which are relatively wet, in contrast to the Arctic (GIC), and central NA (east of the Rocky Mountains) which are relatively dry. On the other hand, Central America, such as NCA and SCA, can experience both dry and wet spells, represented by both high CDD and high CWD, PRCPTOT, R10mm and Rx5day in these regions. As expected, high-latitude regions (e.g., GIC) show dry climatology with high value in CDD and low values in other indices.

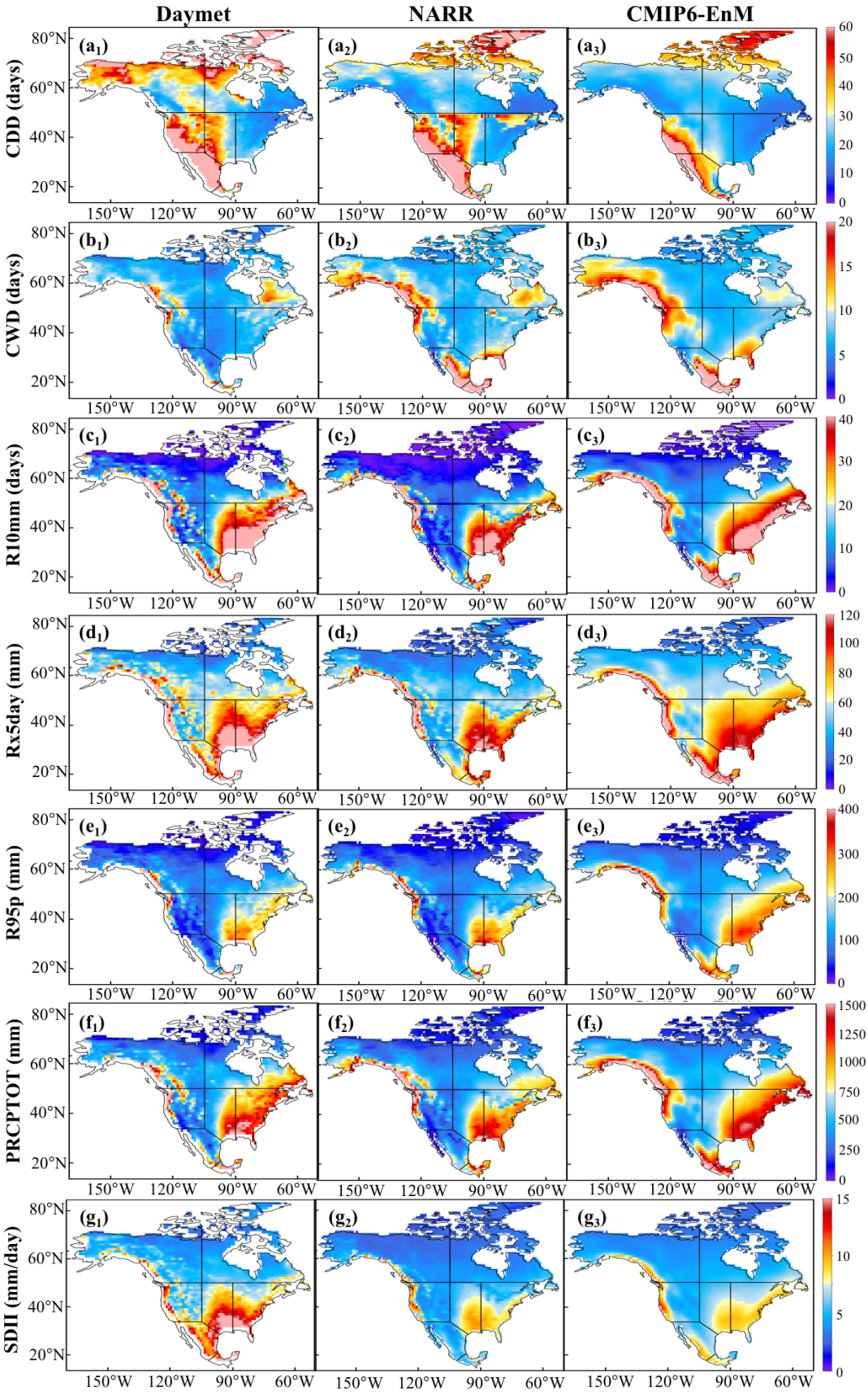
Daymet
NARR
CMIP6-EnM
CDD (days)
CWD (days)
R10mm (days)
Rx5day (mm)
R95p (mm)
PRCPTOT (mm)
SDII (mm/day)
(a1)
(a2)
(a3)
(b1)
(b2)
(b3)
(c1)
(c2)
(c3)
(d1)
(d2)
(d3)
(e1)
(e2)
(e3)
(f1)
(f2)
(f3)
(g1)
(g2)
(g3)
80°N
60°N
40°N
20°N
150°W
120°W
90°W
60°W
0
10
20
30
40
50
60
5
15
100
200
300
400
750
1000
1250
1500
250
500

Figure 3-3 The 30-year (1981–2010) averaged annual spatial distribution of precipitation indices between two observations (Daymet and NARR) and CMIP6-EnM. The white dots (e.g., GIC in Figure 3-4c$_3$) in CMIP6-EnM are where SNR ≤ 1, indicating the simulations are relatively unreliable.

The spatial correlations between the three datasets (CMIP6-EnM-Daymet, CMIP6-EnM-NARR, Daymet-NARR) on precipitation extremes (Figure 3-4) show a strong and consistent agreement between the CMIP6-EnM and two observed data since the statistics R are bigger than 0.8 for most precipitation indices. However, the spatial correlation of the consecutive wet days (CWD) index between CMIP6-EnM (NARR) and Daymet is relatively low (low) may because CMIP6-EnM and NARR are both climate model-based data which tends to simulate more frequent but less intensive precipitation (e.g., drizzle) due to model limitations (i.e., model physics, spatial averaging) compared to the station dataset (Argüeso et al., 2013). This over-simulated light rain in climate models is inevitable and tends to overestimate CWD which is the largest number of consecutive days when daily precipitation is bigger than 1 mm, which has been widely reported in previous studies (Duan et al., 2019b; Stephens et al., 2010).

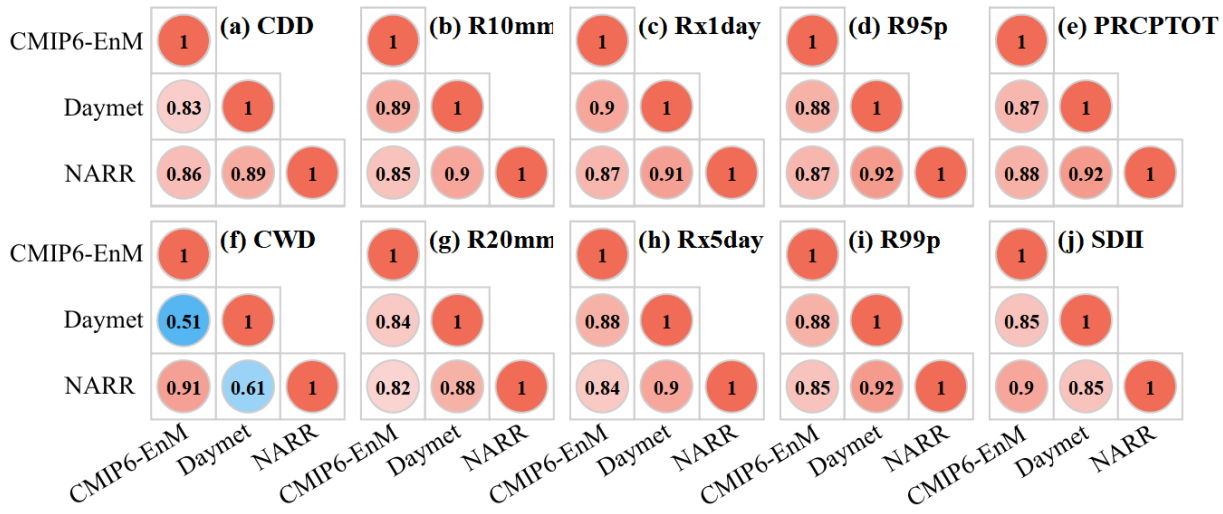

Figure 3-5 The spatial correlations R between the three datasets (CMIP6-EnM-Daymet, CMIP6-EnM-NARR, Daymet-NARR) over NA in 30-year (1981–2010) averaged extreme precipitation indices. The magnitude of the correlation R is shown in blue-red colors.

3.4.2. Temporal Evolution of Precipitation Extremes

Figure 3-5 shows the projected changes of ten spatially averaged extreme precipitation indices from 1981 to 2100. Except for CDD, extreme precipitation indices are projected to consistently increase over the twenty-first century. Rx1day, Rx5day and PRCPTOT are projected to increase by about 10%, 14% and 24% in 2100 under SSP1-2.6, SSP2-4.5 and SSP5-8.5, respectively, indicating a projected increase in the depth of short-duration extreme precipitation. Under SSP5-8.5 scenarios, the largest projected change is found in R99p (170%), followed by R95p (77%), that are far greater than PRCPTOT, implying the growing contributions of extreme precipitation to the total precipitation in the future. Additionally, the projected increase of SDII is relatively smaller than that of PRCPTOT because the frequency of rainy days is also projected to increase. However, projected median changes in the above indices are not distinguishable under three SSP emission scenarios before 2040 but the projections diverge over time after that, with the most significant changes under SSP5-8.5. Furthermore, the 25th-75th quantiles are projected to expand with time and remain overlapped between all SSPs, indicating the growing uncertainty of model simulations as CMIP6-GCMs project the climate to the distant future.

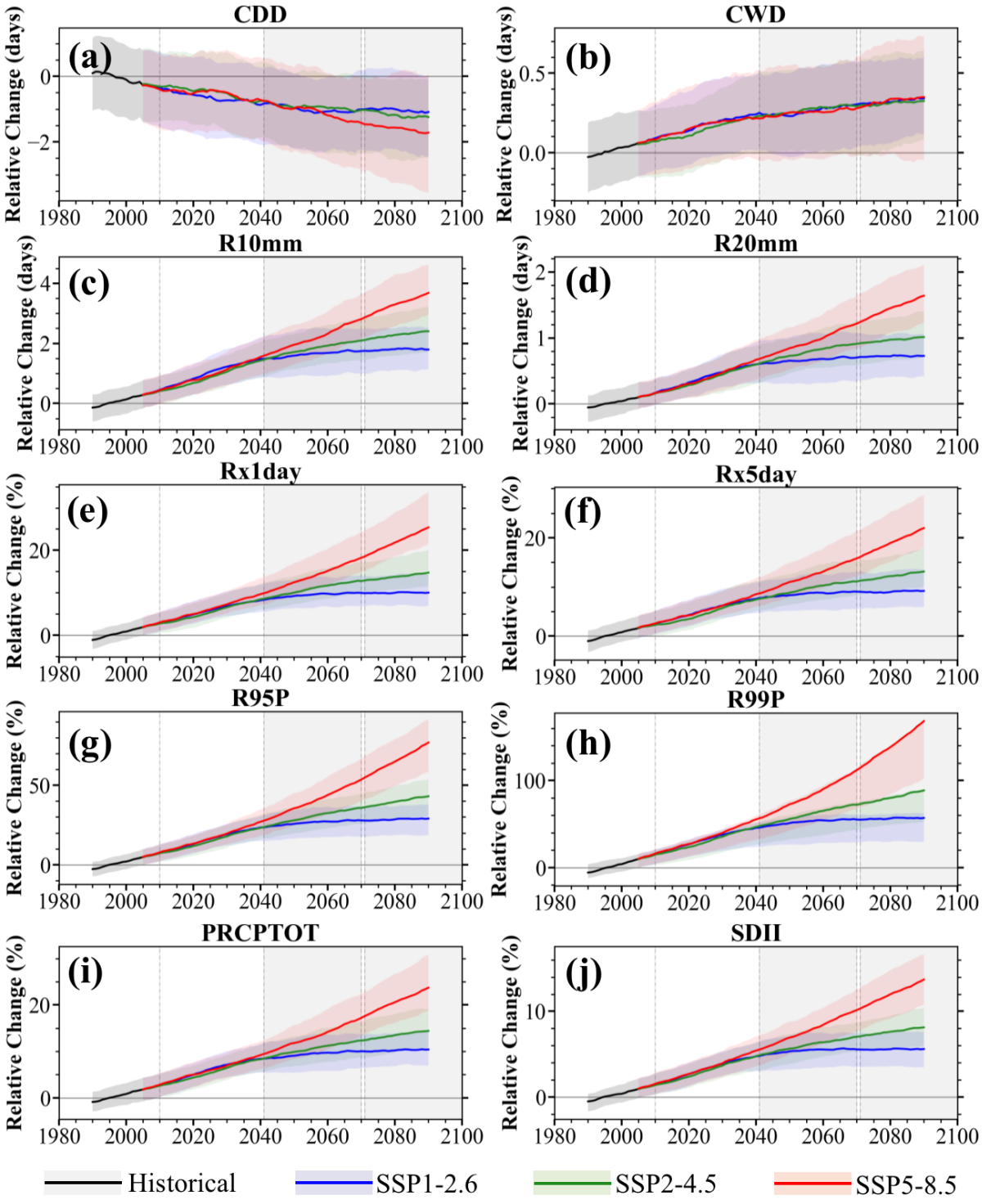

Figure 3-6 Spatial average of ten extreme precipitation indices anomalies over NA as simulated by the CMIP6 models for historical (black), SSP1–2.6 (blue), SSP2–4.5 (green), and SSP5–8.5 (red) relative to the reference period 1981–2010. Solid lines indicate the results of CMIP6-EnM, shadings

show the interquartile spread of 18 models (25th and 75th quantiles). Grey shading along the horizontal x-axis indicates two periods the 2050s and the 2080s. Time series are smoothed with a 20-yr running mean filter from 1981 to 2100.

Figure 3-6 is the distributions of grids showing the projected changes in percentage for ten extreme precipitation indices of CMIP6-EnM over NA for the 2050s (dash line) and 2080s (solid line). Although there are some projected negative changes (< 0), projected positive change dominate most grids for R10mm, R20mm, Rx1day, Rx5day, R95p, R99p, PRCPTOT and SDII for both the 2050s and the 2080s, with a right shift in the distributions of grids under higher SSP emission scenarios. The grids have similar distributions between the 2050s and the 2080s under the SSP1-2.6 scenarios, but the distribution of grids become flatter and spread over wider ranges under SSP5-8.5, likely implying a larger interannual variability under higher projected radiative forcings of higher SSP emission scenarios. In particular, moving from SSP1-2.6 to SSP5-8.5 scenarios, R95p and R99p tends to become more and more skewed towards the right with more elongated upper tails, suggesting a growing projection of extreme events as climate warming worsens.

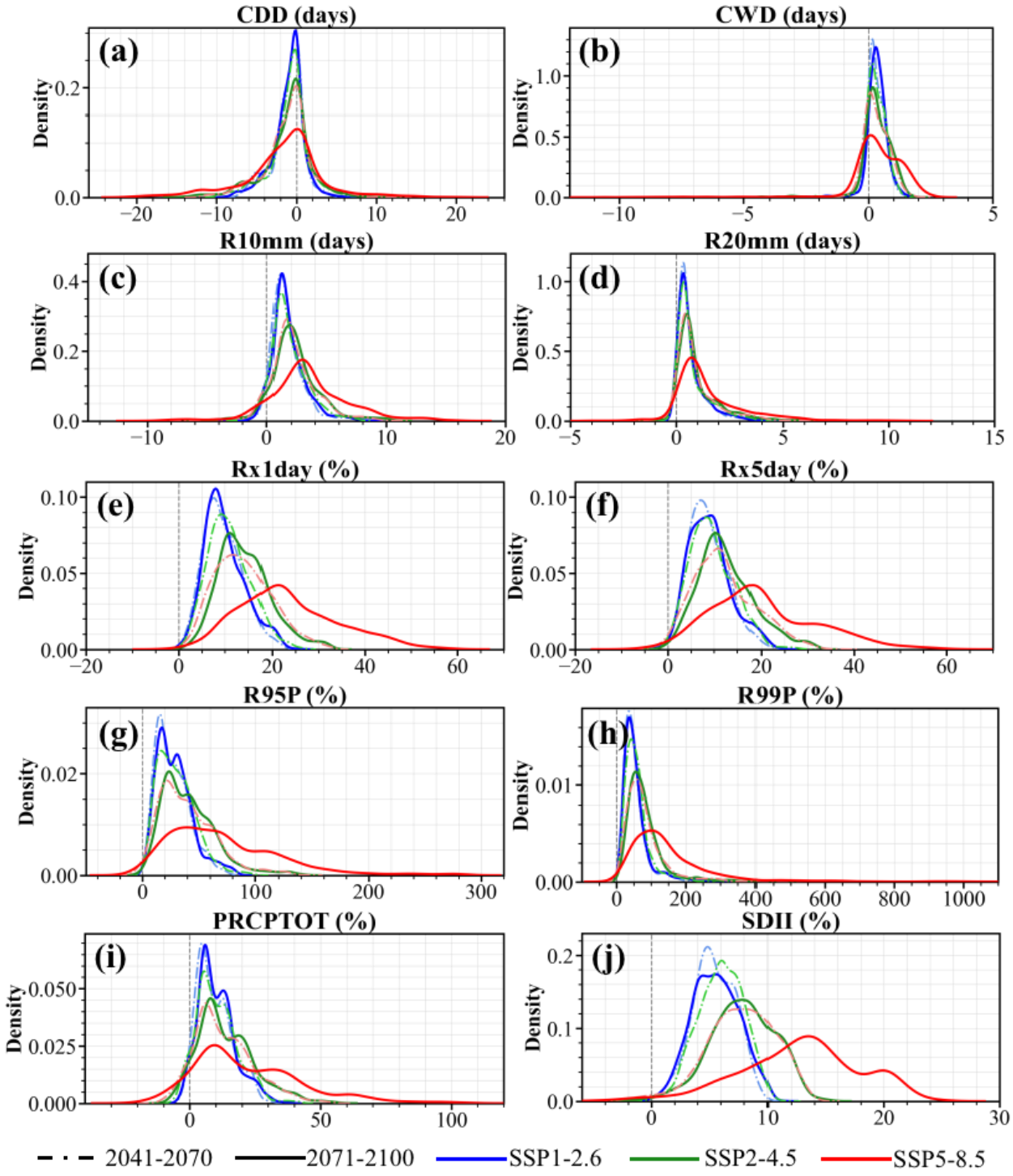

Figure 3-7 The density map of CMIP6-EnM for ten precipitation indices over two periods the 2050s (dash line) and the 2080s (solid line) for SSP1–2.6 (blue), SSP2–4.5 (green) and SSP5–8.5 (red) are displayed as differences (in days or %) relative to the reference period (1981–2010).

Although the projected changes (in Figure 3-5) in CDD and CWD are not as sensitive to the effects of climate warming as the other precipitation indices, the density distributions centered at the zero in Figure 3-6 means are projected to spread over a wider range of CDD and CWD under higher emission scenarios. Partly due to their larger spatial variability, the projected responses of these two indices differ from region to region across NA, but on the whole, they are less sensitive to the effect of climate warming as reported in previous studies (Akinsanola et al., 2020a; Sillmann et al., 2013a).

3.4.3. Projected Spatial Changes in Precipitation Extremes

Relative changes of the spatially distributed extreme precipitation indices and their zonal means of CMIP6-EnM under three SSPs emission scenarios in the 2080s are shown in Figure 3-7. Precipitation extremes are projected to become more severe over most NA in the 2080s relative to the baseline period. All indices are projected to progressively increase in magnitude under the larger radiative forcing of higher emission scenarios, especially the SSP5-8.5 scenarios. The projected percentage increase of CWD, Rx1day (Appendix Figure A.3-4b), Rx5day and R95p, PRCPTOT, SDII, are statistically significant (SNR > 1) over the entire NA, and their zonal-mean increases are higher in latitudes above 55◦N of NA than in lower latitudes. For example, under SSP5-8.5, Rx5day is projected to increase by about 15% between 15◦N and 55◦N, but by about 35% between 55◦N and 80◦N. The change of heavy precipitation, R10mm and R20mm (Appendix Figure A.3-5), are projected to occur more frequently in coastal areas between 40◦N and 70◦ N, as many as 7 days and 3 days zonal mean average under SSP5-8.5 at around 60◦ N of NA.

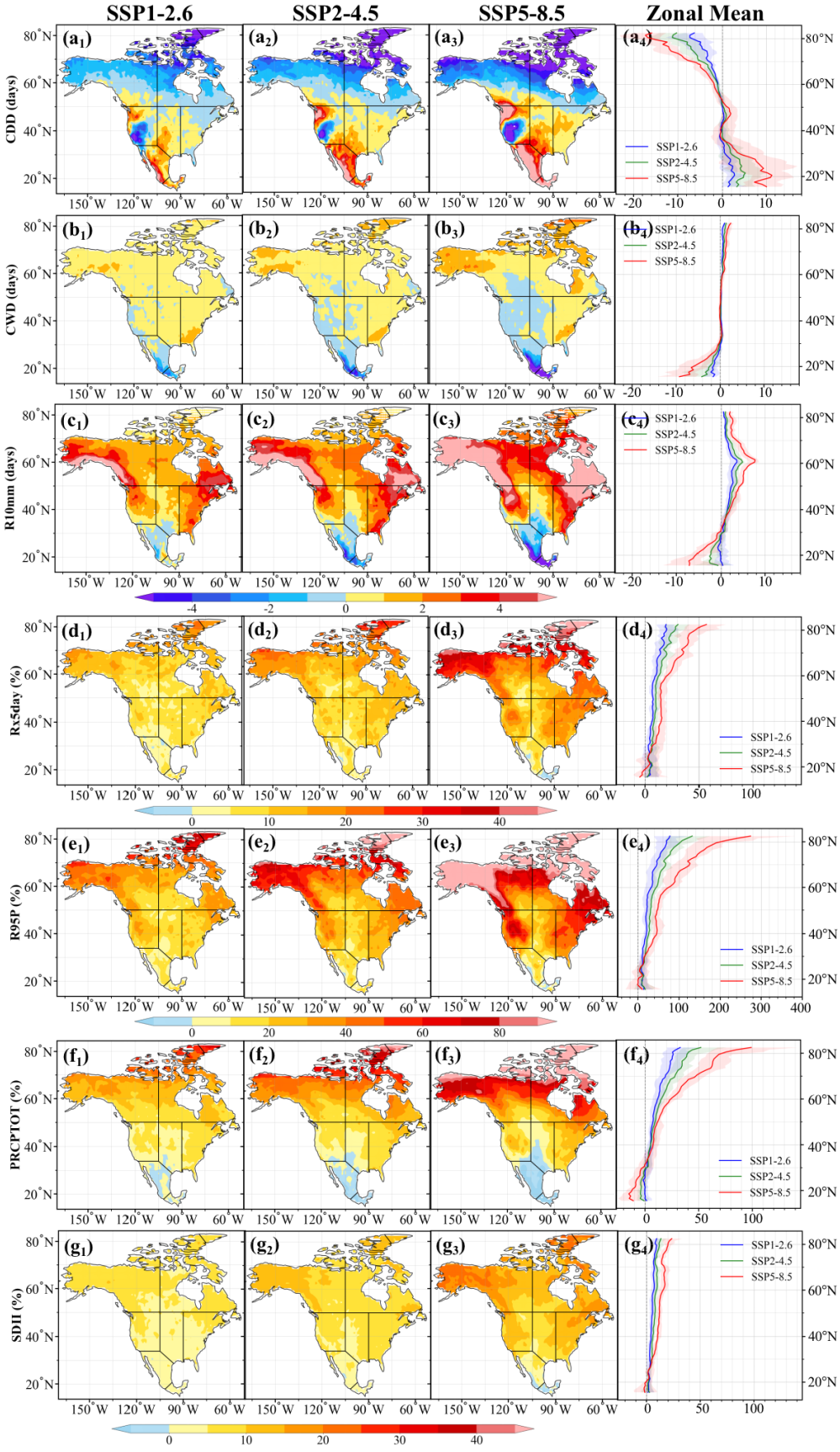
SSP1-2.6
SSP2-4.5
SSP5-8.5
Zonal Mean
CDD (days)
CWD (days)
R10mm (days)
Rx5day (%)
R95P (%)
PRCPTOT (%)
SDII (%)
SSP1-2.6
SSP2-4.5
SSP5-8.5

Figure 3-8 Temporally averaged changes (in the 2080s) of precipitation indices of CMIP6-EnM under SSP1–2.6, SSP2–4.5, and SSP5–8.5 are displayed as differences (in days or %) relative to the reference period (1981–2010). White dots in the left three spatial distribution are where SNR < 1, indicating the projections are relatively unreliable. The rightmost panels show the corresponding zonal mean distribution of each index for SSP1–2.6 (blue), SSP2–4.5 (green) and SSP5–8.5 (red). Solid lines indicate results of CMIP6-EnM, shadings show the interquartile model spread (25th and 75th quantiles).

However, among all the extreme precipitation indices selected for this chapter, the consecutive dry days (CDD) is the only ETCCDI index that is projected to decrease under SSP forcings for zonal mean values in latitudes above 55◦N. In addition, significant decreases in CDD are also detected in California and Nevada, likely attributed to the thermodynamic moistening of air as alpine snowmelt accelerates under climate warming (Huang et al., 2020; Iturbide et al., 2020b; Sun et al., 2019). Southern regions, especially Mexico and Texas, are projected to experience a significant increase in CDD which corresponds to generally projected decrease in other precipitation indices, implying meteorological droughts in these regions will likely intensify. In between WNA and southern NWN of NA (e.g., Oregon, Washington, and southern British Columbia), CDD, R10mm and R95p are all projected to increase, which means that both extreme precipitation events and droughts will become more severe, or hydrologic extremes will worsen under the impact of climate warming (Gaur et al., 2021).

3.4.4. Seasonal Patterns

Using boxplots, Figure 3-8 presents the range of projected changes of 18 GCMs for PRCPTOT, R10mm and Rx5day between summer (JJA) and winter (DJF) over eight subregions of NA in the 2080s, results for R20mm and Rx1day are shown in Appendix Figure A.3-5. In

upper northern latitude regions, such as GIC, NWN and NEN, relative changes of PRCPTOT and Rx5day are projected to be more pronounced in winter than in summer. For example, in GIC, the largest increase of PRCPTOT (Rx5day) in winter is 250% (115%) compared to 55% (50%) in summer. On the other hand, seasonal differences between winter and summer in the relative changes of PRCPTOT and Rx5day in Central America (e.g., NCA and SCA) are minimal because the ensemble median of both indices (CMIP6-EnM) are only projected to decrease marginally in both seasons. However, relative projected changes of R10mm are more homogeneous and positive in winter than in summer, given regional changes in R10mm of CMIP6-EnM ranges from −1 to 1.5 days in DJF, compared with −7 to1.5 days in JJA. In particular, the median R10mm and R20mm (Figure A.3-5c) for winter is virtually unchanged in GIC since in winter the 10 mm and R20mm threshold is rarely exceeded in this region. The most significant change of R10mm (−17 days) is projected in the lowest northern latitude regions (e.g., SCA) in summer under SSP5-8.5. For the middle northern latitude regions of NA, such as WNA, CNA and ENA, PRCPTOT, Rx5 day and R10mm are all projected to increase in winter, but only minor positive change is projected in the summer (5% or even less than zero depending on the SSPs).

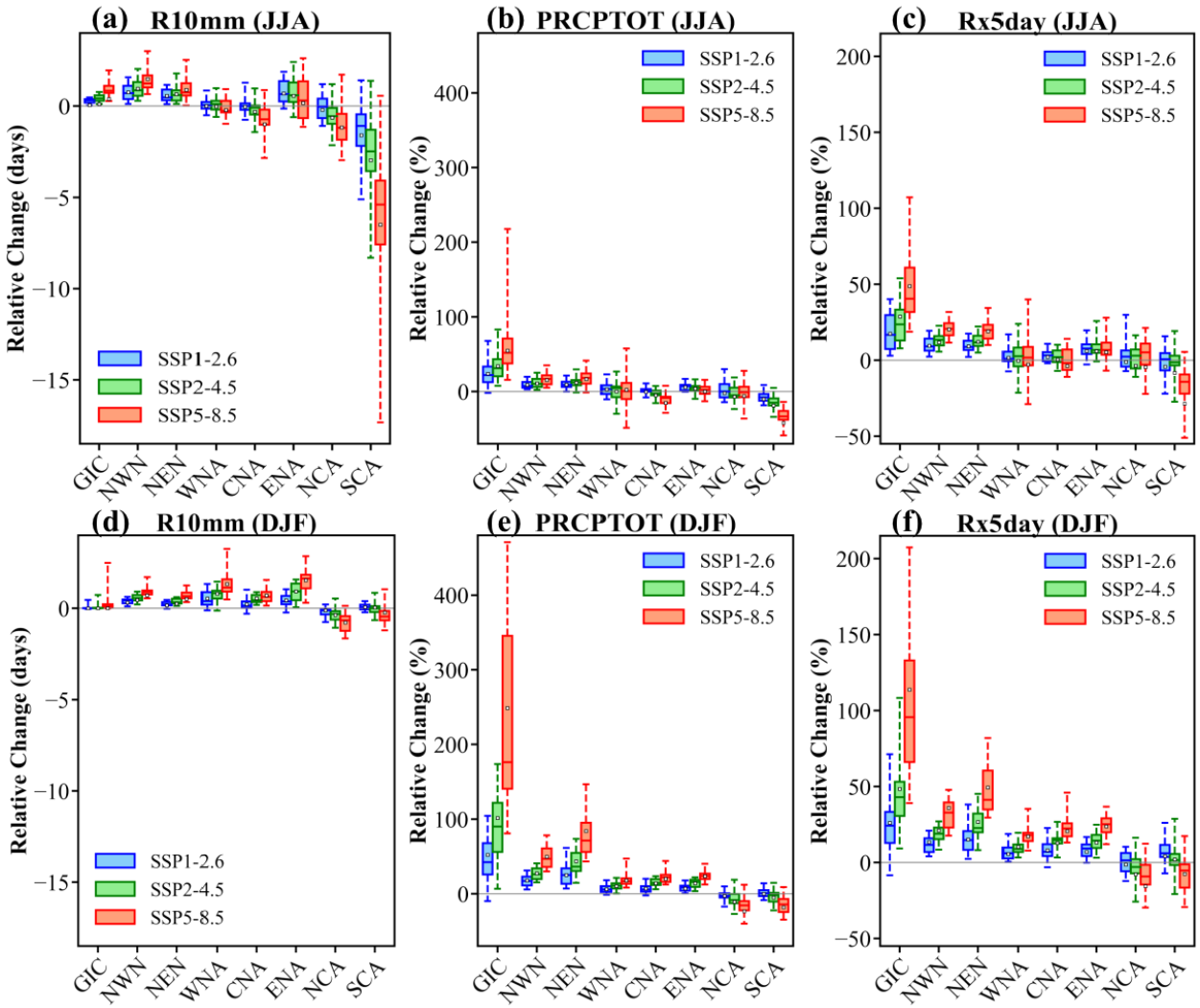

Figure 3-9 Projected spatial averaged changes (in days or %) in summer (JJA) and winter (DJF) of R10mm, PRCPTOT and Rx5day in the 2080s relative to the reference period 1981–2010 under SSP1-2.6 (blue), SSP2-4.5 (green) and SSP5-8.5 (red) over 8 subregions of NA. Boxes indicate the models spread (25th and 75th interquartile), with the horizontal line inside indicating the median of 18 CMIP6 model, while CMIP6-EnM is represented by the small black box inside the boxplot.

3.4.5. Model Agreement

To compare regional responses to different SSP scenarios, annual extreme precipitation indices for the eight sub-regions of NA over the 2080s based on the simulations of 18 individual

GCMs and their ensemble median are presented in Figure 3-9 in terms of data points and bar plots, respectively. Results over the 2050s are shown in Appendix Figure A.3-6. We assess the agreements between the 18 GCMs of CMIP6 by comparing how many GCMs (in %) agree on the sign of ensemble mean changes (CMIP6-EnM) projected for ten indices over the eight sub-regions of NA.

In general, precipitation extremes in CMIP6-EnM are projected to progressively becoming more severe towards the end of the Twenty-First century (the 2080s). The GCMs of CMIP6 unanimously agree (100% agreement) on the increase in precipitation extremes over high latitude regions such as GIC, NWN and NEN. While in WNA, CNA and NCA, model agreements vary between the indices. For example, Rx1day, Rx5day, R95p, R99p that represent thresholds and block-maximum extremes, respectively, are all projected to increase with 100% model agreements in central NA. Given the consistent projections between all 18 GCMs, there is a strong confidence that extreme precipitation events will very likely become more severe under the impact of climate warming in central NA. In comparison, model agreements are about 80% in terms of R10mm, R20mm and PRCPTOT in middle northern latitude of NA. For lower latitude of NA (e.g., NCA and SCA), GCMs disagree on the sign and magnitude of projected changes in extreme precipitation for at least one of the three SSP scenarios, especially for R10mm, R20mm and SDII. Except for some major differences ranging from −2 to −37 days between GCMs in SCA (southern Mexico), it seems that CWD in other parts of NA will only experience minimal changes until the 2080s.

However, the projected increase (decrease) in CDD generally coincides with the projected decrease (increase) in R10mm, R20mm and PRCPTOT, such that CDD is projected to decrease in high latitude regions with 100% model agreement while increasing in Central America, with

only some limited disagreements in NCA (northern Mexico) under SSP1-2.6. On the whole, there is a low confidence that southern NA will become progressively drier over the 21st Century, but as we move north across NA, there is high confidence that NA will become wetter and wetter over the 21st Century (IPCC, 2021).

Among the 18 GCMs of CMIP6 selected in this chapter, some projections deviate significantly from the ensemble medians, which indicate that climate model uncertainties could affect the results on future extreme precipitation for NA obtained from the three SSP scenarios of CMIP6. For example, the GCM IPSL-CM6A-LR of Institute Pierre-Simon Laplace, France projected the largest decrease for CWD, R10mm, PRCPTOT, SDII, Rx5day and R95p over SCA. This could be attributed to the bias in dryness of IPSL-CM6A-LR associated with its negative sea surface temperature bias in the equatorial Pacific (Boucher et al., 2020). In contrast, in GIC, the Ec-Earth3 GCM projected the most severe extreme precipitation indices for the 2080s, including PRCPTOT (+190%), SDII (+39%), Rx5day (+115%) and R95p (+670%) partly because this GCM over simulated the amplitude of global mean precipitation patterns and the volume of Arctic sea ice, resulting in a fast reinforcement in the amplitude of precipitation as warming increases (Döscher et al., 2022).

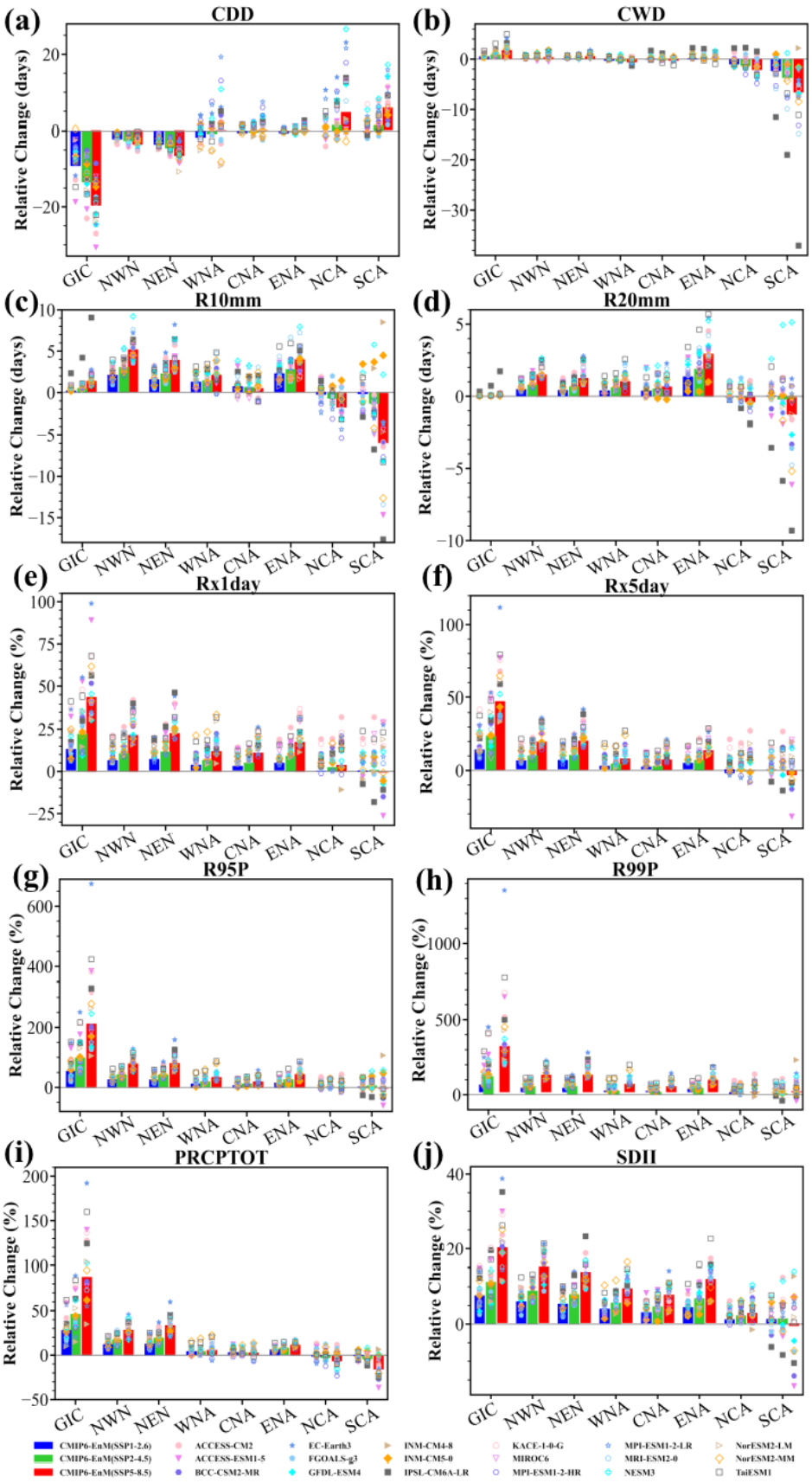
(a)
CDD
Relative Change (days)
(b)
CWD
Relative Change (days)
(c)
R10mm
Relative Change (days)
(d)
R20mm
Relative Change (days)
(e)
Rx1day
Relative Change (%)
(f)
Rx5day
Relative Change (%)
(g)
R95P
Relative Change (%)
(h)
R99P
Relative Change (%)
(i)
PRCPTOT
Relative Change (%)
(j)
SDII
Relative Change (%)
GIC
NWN
NEN
WNA
CNA
ENA
NCA
SCA
CMIP6-EnM(SSP1-2.6)
CMIP6-EnM(SSP2-4.5)
CMIP6-EnM(SSP5-8.5)
ACCESS-CM2
ACCESS-ESM1-5
BCC-CSM2-MR
EC-Earth3
FGOALS-g3
GFDL-ESM4
INM-CM4-8
INM-CM5-0
IPSL-CM6A-LR
KACE-1-0-G
MIROC6
MPI-ESM1-2-HR
MPI-ESM1-2-LR
MRI-ESM2-0
NESM3
NorESM2-LM
NorESM2-MM
TaiESM1

Figure 3-10 Projected spatial averaged changes (in days or %) in annual extreme precipitation indices over the period 2071–2100 as differences relative to the reference period 1981–2010 for SSP1-2.6 (blue), SSP2-4.5 (green) and SSP5-8.5 (red) in 8 subregions of North America. Colored markers are the changes for 18 CMIP6 models, while colors bars represent CMIP6-EnM.

3.5. Summary and Conclusions

In this chapter, we assess the projected spatial and temporal changes in extreme precipitation of NA over the 21st century based on the projections of 18 GCMs of CMIP6, and the performance of these GCMs over the historical period of 1981–2010 over NA with respect to in-situ measurements (Daymet) and reanalysis data (NARR). The analysis of these changes in precipitation extremes is based on the ensemble median of these selected GCMs of CMIP6. The following summarizes the main conclusions:

(1) Compared with previous studies conducted in different regions (Ge et al., 2021; Srivastava et al., 2020), CMIP6-EnM could reasonably reproduce the spatial patterns of observed precipitation events and should be representative and reliable over the future periods because 10 ETCCDI extreme precipitation indices simulated by the CMIP6-EnM out-performs all 18 individual GCMs with negative $RMSE_{XY}$ over NA (Figure 3-2) and 8 subregions (Figure A.3-2), the signal-to-noise ratio (SNR > 1) (Figure 3-3) and higher R statistics (R > 0.8) (Figure 3-4) in most sub-regions of NA. In contrast to results simulated by CMIP5 GCMs (Sillmann et al., 2013a; Srivastava et al., 2020), GCMs of CMIP6 agree better with observations represented by NARR and Daymet. This indicates an improvement in the CMIP6 models in simulating observed precipitation characteristics, partly because CMIP6 GCMs generally are of higher spatial resolutions than CMIP5 models. However, GCMs inevitably oversimulate light rain (e.g., drizzle)

compared to observations, resulting in an overestimated CWD. This is a common problem that has not been significantly improved in CMIP6 models (Duan et al., 2019b; Srivastava et al., 2020; Stephens et al., 2010). The parameterization of physical processes may play a role in improving the model performance which needs to be further investigated (Sillmann et al., 2013a).

(2) Projected changes to extreme precipitation indices in response to a different level of climate warming (SSP1-2.6, SSP2-4.5 and SSP5-8.5) scenarios are similar to each other before 2040 (unanimous agreements between GCMs, especially in high latitude regions), but the difference in projected changes based on the three SSP scenarios progressively become larger and larger towards the end of the Twenty-First century (the 2080s) as expected (Figure 3-5). The temporal changes in extreme precipitation are similar to the changes in global surface air temperature due to increasing radiative forcing patterns as reported in Chapter 4 of AR6 (Lee et al., 2021), which can be assumed that the intensification of extreme precipitation in NA is directly influenced by global warming. The magnitude of changes in extreme precipitation indices depends on the indices' type (Sillmann et al., 2013b). For example, higher increase is projected in the percentile indices (R95p and R99p) compared with PRCPTOT, indicating a projected increase in the future contribution of extreme precipitation to the total precipitation. Moreover, it is of high confidence that the response of extreme precipitation in NA to the impact of global warming will continue to be amplified throughout the 21st century (Figure 3-6), and the magnitude is bigger in CMIP6 ensembles than in CMIP5 models (IPCC, 2021).

(3) Extreme precipitation of NA will likely occur more severely over the 21st century, especially in latitudes above 55◦N of NA and coastal areas under the SSP5-8.5 climate scenarios, represented by larger projected decrease in CDD and larger increase in other indices. This is not a surprise because, according to the Clausius-Clapeyron scaling, atmospheric humidity is

expected to increase at about 7%/◦K of warming, particularly in higher latitude regions where warming is projected to become higher, a phenomenon commonly known as the Arctic amplification (Liu et al., 2021a; Stjern et al., 2019). The spatial patterns shown in Figure 3-7 reveal that at middle latitudes, in between WNA and southern NWN of NA (e.g., Oregon, Washington, and southern British Columbia), where both extreme precipitation events and droughts are projected to become more severe. At lower latitudes, especially in Mexico and Texas, projections of indices imply meteorological droughts in these regions will likely intensify, e.g., projected increase in CDD and decrease in other indices. In addition, coastal regions are also prone to the occurrences of more extreme precipitation. The high elevations of the Rocky Mountains and the Pacific Northwest are mainly fueled by land-falling atmospheric rivers (ARs) that transport more water vapor from the Pacific Ocean (Liu et al., 2021b; Lora et al., 2017; Ma et al., 2020). While precipitation extremes in the eastern coastland are primarily attributed to the higher-intensity, cyclone-relative frontal precipitation (Bishop et al., 2019; Zhang & Colle, 2017).

(4) Seasonal changes in northern latitude (such as GIC, NWN and NEN) and middle latitude regions (e.g., WNA, CNA and ENA) are projected to experience more pronounced changes in precipitation extremes in winter than in summer. This may result from the northward migration storm and expanded subtropical high that contributes to decreasing subtropical precipitation and increasing high-latitude precipitation in summer (Maloney et al., 2014; McAfee et al., 2011; Zhou et al., 2022). Meanwhile, atmospheric rivers, as well as some large climate patterns (e.g., the Madden-Julian Oscillation and the North Atlantic Oscillation), are related to more intensive storms and more precipitation in winter (Dong et al., 2018; Lora et al., 2017; Ma et al., 2020; Ning & Bradley, 2016). On the other hand, changes between winter and summer in lower latitudes of NA (e.g., NCA and SCA) agree with the CMIP5 results that precipitation

seasonality will decrease, with decreasing trends in both winter and summer, suggesting a more severe arid future (Sillmann et al., 2013b).

(5) With regard to model agreement, CMIP6 climate models consistently project that precipitation extremes of NA will progressively become more severe towards the end of the Twenty-First century (the 2080s) with 100% agreement for all indices over high latitude regions such as GIC, NWN and NEN. There is more than 80% agreement between climate models' projections for all indices over middle latitude regions such as WNA, CNA and ENA. However, there is low confidence (less than 60%) that some indices in lower latitudes of NA (such as NCA and SCA) indicate progressively wetter conditions over the 21st Century (IPCC, 2021). Climate models that (e.g., IPSL-CM6A-LR) perform poorly in simulating observed extreme precipitation generally deviate from the ensemble medians in projecting future extreme precipitation indices due to their coarser resolutions. However, models with finer resolutions (e.g., Ec-Earth3) generally project very severe extreme precipitation indices, which may be partly because high values are not easy to smoothen by data resampling (Oubeidillah et al., 2014). Future research is still needed to explore the influence of the GCMs' resolutions in simulating observed climate extremes.

In conclusion, based on results obtained from the projections of 18 GCMs of CMIP6 for NA, there is high confidence that extreme precipitation will likely occur more frequently with greater severity, especially in high latitudes and coastal regions of NA. These variations will contribute to more severe natural hazards such as floods, droughts, and wildfires, which may not only threaten water storage, conveyance and flood control infrastructure but also challenge the regional food supply, which will affect the social stability. CMIP6 results will help us to develop adaptive measures to mitigate the potential impact of these changes in precipitation extremes to

reduce the vulnerability of some parts of North America, such as the Canadian Prairies, against the impact of droughts and floods and possible structural and non-structural measures against future hazards in floods and droughts. Besides the impact of climate warming, the extreme precipitation in some parts of NA has been shown to be related to the effect of climate anomalies such as El Niño Southern Oscillation, Pacific Decadal Oscillation, North Atlantic Oscillation, Arctic Oscillation and others (e.g., Gan et al., 2007; Islam & Gan, 2015; Ning & Bradley, 2016; Tan & Gan 2017; Tan et al., 2017). Future research should investigate the combined impact of climate warming and climate anomalies to the future precipitation extremes of NA.

3.6. Notation

The following symbols are used in this chapter:

AR6 = Sixth Assessment Report

CAN = C.North-America

CDD = Consecutive dry days

CDO = Climate Data Operators

CMIP6 = The International Coupled Model Intercomparison Project 6

CMIP6-EnM = CMIP6 ensemble median

CWD = Consecutive wet days

Daymet = Daily Surface Weather Data on a 1-km Grid for North America

DJF = Winter (including December, January and February)

ENA = E.North-America

ETCCDI = The Expert Team on Climate Change Detection and Indices

GCMs = Global Climate Models

GIC = Greenland/Iceland

IPCC = The Intergovernmental Panel on Climate Change

JJA = Summer (including June, July and August)

NARR = The North American Regional Reanalysis dataset

NASA = National Aeronautics and Space Administration of USA

NCA = N.Central-America

NCEP = National Centers for Environmental Prediction

NEN = N.E.North-America

NWN = N.W.North-America

PRCPTOT = Total wet-day precipitation (PR ≥ 1 mm)

R10mm = Number of days with more than 10 mm precipitation

R20mm = Number of days with more than 20 mm precipitation

R95p = The total precipitation per year from wet-day (PR > 1 mm) with precipitation above the 95th percentile daily precipitation for 1981–2010

R99p = The total precipitation per year from wet-day (PR > 1 mm) with precipitation above the 99th percentile daily precipitation for 1981–2010

RMSE = Root mean squared error

$RMSE_{Median}$= Median root mean squared error for 18 GCMs

$RMSE'_{XY}$ = The difference between individual model $RMSE_{XY}$ and $RMSE_{Median}$

Rx1day = Maximum 1-day precipitation

Rx5day = Maximum 5-day precipitation

SCA = Southern Central-America

SDII = The simple daily intensity index on wet days (PR ≥ 1 mm)

SNR = The signal-to-noise ratio

SSP = Shared socio-economic pathway

the 2050s = 2041–2070

the 2080s = 2071–2100

WMO = The World Meteorological Organization

WNA = Western North-America

Chapter 4 Increased Precipitation Seasonality over Global Land Monsoon Affecting Seasonal Water Availability

4.1. Introduction

According to the Clausius–Clapeyron scaling, the atmospheric water vapor content will increase as the climate warm up by approximately 7%/°K increase in warming (Wehner, 2020; Westra et al., 2013). Under higher atmospheric water vapor content, extreme precipitation events will increase, and precipitation patterns will also change with increased moisture convergence, which can be divided into thermodynamic and dynamic contributions (Lan et al., 2019). Past studies show that shifts in global precipitation patterns exhibit a seasonal disparity, driven thermodynamically by increasing atmospheric moisture content and specific humidity attributed to climate warming induced by rising concentration of greenhouse gases (Giorgi et al., 2011; Lan et al., 2019; Tan et al., 2023). Amplified atmospheric moisture fuels storm systems, leading to the occurrence of more intensive storm events (Dong et al., 2021; Li et al., 2021). Concurrently, the increase in thermal energy under climate warming also contributes to an increase in evaporation rates, resulting in more frequent occurrences of droughts of higher severity (Dai, 2013). These changes lead to an intensification of the hydrologic cycle, which alters the spatial and temporal distributions of precipitation (Chou et al., 2009; Held & Soden, 2006). Such changes in the accumulation and spatiotemporal distributions of precipitation could significantly impact agriculture, water resources, biodiversity and ecosystems (Deng et al., 2020; Feng et al., 2013; Konapala et al., 2020). Therefore, it is essential to investigate the magnitude of changes to the spatiotemporal distributions of precipitation under the potential impact of global warming.

A simple metric called precipitation seasonality has been used to represent changes in the annual total precipitation and its interannual distribution. Several methodologies have been proposed to capture the characteristics of precipitation seasonality. Many studies have examined precipitation seasonality based on differences between the amount of precipitation over the traditional four seasons, for example, spring, summer, fall and winter. These studies found more severe precipitation events in high latitudes to occur during winter in recent years (Maussion et al., 2014; Stahle et al., 2020; Zhao et al., 2023). There have been studies conducted that found a growing contrast between wet and dry seasons at both regional and global scales (Chou et al., 2009, 2013; Pal et al., 2013). Walsh & Lawler (1981) first proposed a simple index to represent precipitation seasonality based on the monthly distribution of rainfall climatology, which they show to vary with respect to latitudes. However, the drawback of such simple approaches is that these methods predominantly focus on isolated aspects of precipitation characteristics in terms of either the precipitation depth or its temporal distribution. Feng et al. (2013) introduced a more comprehensive approach to develop rainfall metrics based on a probabilistic interpretation of rainfall fractions. By multiplying the mean annual total precipitation normalized by the maximum observed mean annual rainfall in the dataset with its relative entropy (RE), a dimensionless long-term precipitation seasonality index (SI) is developed. In other words, SI is a seasonality index that represent the precipitation depth integrated with its monthly distribution.

Changes in global and regional precipitation seasonality could depend on the dataset used in the analysis, for results obtained are not consistent, for different studies could report contrasting trends since the 20th century, depending on the dataset used in the studies (Feng et al., 2013; Tan et al., 2020). For example, more than 62% of terrestrial ecosystems are found to experience a reduced precipitation seasonality from 1950 to 2009, due to decreased regional

precipitation in the wet season but increased regional precipitation in the dry season (Murray-Tortarolo et al., 2017). In contrast, other studies found the precipitation seasonality to increase since the 1980s because of wetter wet seasons (Chou et al., 2013; Lan et al., 2019; Polson & Hegerl, 2017). The IPCC Sixth Assessment Report (AR6) explain that these conflicting results could be partly resolved by the dimming effect of anthropogenic aerosol forcing to the incoming solar radiation in the mid-20th century, followed by a partial recovery of the incoming solar radiation after the 1980s due to the enforcement of stricter environmental regulations (Douville et al., 2021; Wild, 2012). However, to what extent can changes to precipitation seasonality can be attributed to anthropogenic forcing remain largely unclear. The optimal fingerprint technique, a standard method for the detection and attribution (D&A) analysis, is often used to regress the observed changes in precipitation against expected response patterns to different external forcings (e.g., anthropogenic greenhouse gas forcing, anthropogenic aerosol forcing, natural external forcing, etc.) (Allen & Stott, 2003; Ribes et al., 2013). Past studies have successfully applied this method to investigate human-induced changes in the annual extreme and seasonal mean precipitation (Christidis & Stott, 2022; Paik et al., 2020; Sun et al., 2022; Xu et al., 2022; Zhang et al., 2013). Therefore, this fingerprint technique could also be used to assess the human influence on precipitation seasonality under a warming climate.

The amount of available water (AW) is approximately the difference between precipitation (P) and evaporation (E) (Konapala et al., 2020). Although changes in SI due to human-induced climate change impact since the mid-20th century may affect the mean annual AW (Haddeland et al., 2014; Schewe et al., 2014), there is a lack of studies exploring the relationship between SI and AW. The simple thermodynamic scaling, commonly known as "wet-get-wetter, dry-get-drier" mechanism, has been widely accepted by scientists to analyze global

and regional AW changes between wet and dry seasons, even though it is found to be not applicable over land in some regions (Greve et al., 2014; Held & Soden, 2006; Roderick et al., 2014). On the other hand, understanding combined changes in the annual mean AW and SI may provide a more comprehensive perspective on water availability at seasonal time scale. For example, AW changes could indicate a wetter or drier climatology pattern, while changes in SI could indicate an extended wet or dry season in regions of unimodal precipitation distribution (Pascale et al., 2015, 2016). Therefore, it is important to understand collective variations in AW and SI in both annual and seasonal time scales, which would help us to more comprehensively assess societal and ecological vulnerability to such changes and adaptation strategies that will be effective in minimizing the potential impact of such changes (Konapala et al., 2020).

In this chapter, we apply a non-parametric precipitation seasonality index (SI) based on four observational datasets and CMIP6 simulations to evaluate changes in the precipitation seasonality across the global land monsoon regions (GLM) and its subregions under a warming climate. By applying the optimal fingerprinting method, we detect and attribute changes in observed SI from 1950 to 2014 to different forcings, followed by plausible mechanistic explanations. We subsequently assess the impact of SI changes on AW under different future Shared Socioeconomic Pathways climate change scenarios of IPCC (2021) and different warming levels. This chapter is organized as follows: datasets and methods are described in Section 4.2, results are discussed in section 4.3, and conclusions and discussion are given in section 4.4.

4.2. Data and Methodology

4.2.1. Observed and Climate Model Data

In this chapter, four observed datasets are used to investigate changes to historical precipitation seasonality in the global land monsoon regions (GLM). The procedure is carefully selected to ensure the study's findings are valid and comprehensive. 1) First, regional datasets are not considered because the primary objective of this chapter is to assess the spatiotemporal patterns of precipitation seasonality on a global scale. Thus, only global datasets are considered for this chapter. 2) Second, to achieve a comprehensive comparison of precipitation seasonality longitudinally between data products, only datasets with records spanning no less than 60 years are selected. An adequate amount of data available is necessary to achieve a robust analysis that accurately capture variations and trends in precipitation seasonality over an extended period. 3) Lastly, datasets that have been widely used in previous studies and have demonstrated good performance in specific cases are preferred. This criterion is needed to enhance the reliability of the findings, to compare with results of past studies, as well as to build upon existing knowledge and related research in the field. Based on these considerations, four datasets are chosen for further analysis. These datasets are reanalysis datasets developed from gauge-based interpolations climate model simulations, as detailed in Table 4-1.

Table 4-1 List of four observed datasets used in this chapter.

Dataset	Category	Period	Resolution	Frequency	Coverage
CRU	Gauge-Base	1901-Present	0.5° × 0.5°	Monthly	Global Land
GPCC	Gauge-Base	1891-Present	1.0° × 1.0°	Daily	Global Land
ERA5	Reanalysis	1940-Present	0.25° ×0.25°	Monthly	Global Land & Ocean
NCEP-NCAR	Reanalysis	1948-Present	2.5° × 2.5°	Monthly	Global Land & Ocean

The Climatic Research Unit Time Series (CRU TS) version 4 dataset, that provides high-resolution, land-based (excluding Antarctica) gridded observations are obtained from the British Atmospheric Data Centre (BADC) at https://crudata.uea.ac.uk/cru/data/hrg/ (Harris et al., 2020). This dataset provides gridded global land data at a 0.5°×0.5° latitude/longitude resolution and spans temporally from 1901 to the present day. The CRU monthly climate data are taken from over 4000 individual weather station records, including the World Meteorological Organization (WMO) internationally exchanged stations (~2400 stations), National Climatic Data Center (NCDC) stations for WMO (~1500 stations) and the World Weather Records (WWR) decadal data publications (~1700 stations) (Harris et al., 2020; Tan et al., 2020). Different quality-control measures, such as removing outliers, omitting short records, and data that exceed anomaly values, were implemented by Ullah et al. (2022) in developing the latest CRU database. Monthly precipitation and temperature data from CRU are used in this chapter.

The Global Precipitation Climatology Centre (GPCC) Full Data Reanalysis Version 2020, based on in-situ measurements from about 67,200 stations worldwide, is provided by national meteorological and hydrological services, regional and global data collection centers as well as

WMO GTS-data. Meteorological stations worldwide, which are available at https://gpcc.dwd.de. GPCC provides a quality-controlled, homogenized dataset that effectively corrects for inhomogeneities, making it a reliable data source for examining precipitation seasonality on a global scale (Becker et al., 2013). With a monthly product resolution of 1.0°×1.0° latitude/longitude and that spans from 1891 to the present, this dataset enables us to conduct detailed analysis of long-term precipitation trends (Ziese et al., 2021). Monthly precipitation from GPCC is also used in this chapter.

The ERA5 Reanalysis Dataset developed by the European Centre for Medium-Range Weather Forecasts (ECMWF) that provides hourly and monthly estimates of a vast range of atmospheric, land, and oceanic climate variables (Hersbach et al., 2023), is available at https://cds.climate.copernicus.eu. The monthly precipitation data of ERA5 used in this chapter is reconstructed from both ground-based observations and satellite data at global coverage. This dataset at a high-resolution grid of 0.25°×0.25° latitude/longitude spans from 1940 to the present day. ERA5 utilizes a robust data assimilation system, combining millions of observational data points with climate model simulations to ensure an internally consistent dataset.

The National Centers for Environmental Prediction - National Center for Atmospheric Research (NCEP-NCAR) reanalysis dataset provides gridded climate records, at 4-times daily, daily and monthly averages at https://psl.noaa.gov. This dataset covers a long period, from 1948 to the present day, with a spatial resolution of 2.5°×2.5° latitude/longitude (Kalnay et al., 1996). The NCEP-NCAR dataset combines a diverse array of observational data with simulations of numerical weather prediction models to generate a temporally consistent climate dataset. While its spatial resolution is lower than other datasets used in this chapter, the long-term span of the data, along with the successful amalgamation of observational and modelled data, makes the

NCEP-NCAR reanalysis a valuable resource for examining long-term trends in precipitation seasonality.

4.2.2. CMIP6 Global Climate Model Data

Simulated monthly precipitation data are obtained from the Coupled Model Intercomparison Project Phase 6 (CMIP6) archive at the Earth System Grid data distribution porta (ESG, https://esgf-node.llnl.gov/search/cmip6/). Inner model uncertainties of past studies based on limited ensemble members are likely high, and comparisons can be "unfair" or non-representative when different ensemble members are used to detect climate model forcings (Xu et al., 2022; Zhang et al., 2013). To overcome these problems, this chapter selects CMIP6 global climate models (GCMs) with at least five ensemble members. These members in each of CMIP6 GCM are forced by historical forcings (ALL, both anthropogenic and natural external forcings), hist-GHG forcing (GHG, greenhouse gases forcing only), his-aer forcing (AER, anthropogenic aerosol forcing only) and hist-nat forcing (NAT, natural external forcing only) that are used for conducting the detection and attribution (D&A) analysis. In addition, a total of 91 chunks of non-overlapping 65-year simulations from the preindustrial control (CTL) experiment are applied to estimate the internal variability. Table 4-2 provides a detailed overview of the five selected CMIP6 GCMs used in this chapter. In total, there are 39 runs for ALL, GHG, AER, NAT forcings, and 91 chunks of preindustrial control experiments (CTL) shown in Table 4-2.

Table 4-2 List of CMIP6 model simulations used in this chapter.

No.	Model Name	ALL	NAT	GHG	AER	CTL	Institution	Resolution (Lon×Lat)
1	CanESM5	10	10	10	10	31	Canadian Centre for Climate Modelling and Analysis, Canada	128×64
2	HadGEM3-GC31-+LL	5	5	5	5	7	Met Office Hadley Centre, UK	192×144
3	IPSL-CM6A-LR	9	9	9	9	33	Institut Pierre-Simon Laplace, France	144×143
4	MIROC6	10	10	10	10	7	JAMSTEC, AORI, NIES, R-CCS, Japan	256×128
5	MRI-ESM2-0	5	5	5	5	13	Meteorological Research Institute, Japan	320×160
	Sum	39	39	39	39	91		

To assess projected changes in precipitation seasonality under three future Shared Socioeconomic Pathways (SSP1-2.6, SSP2-4.5 and SSP5-8.5) relative to 1961-1990, precipitation data from CMIP6 simulations under these three SSPs are obtained. Available runs of CMIP6 simulations under different scenarios are listed in Table A.4-1. We have also assessed projected changes in precipitation seasonality at specific warming levels (i.e., +1 ºC, +1.5 ºC, +2 ºC, +3 ºC and +4ºC) relative to pre-industrial levels (1850-1900), and precipitation data from CMIP6 simulations under SSP5-8.5 emissions scenarios are obtained. The 30-year average time period of different warming levels for CMIP6 data, generated by Mathias et al., are available at https://github.com/mathause/cmip_warming_levels. Corresponding runs of 5 models and their target year of different warming levels are shown in Table A.4-2. Moreover, precipitation (P) and evapotranspiration (E) data from three SSPs of CMIP6 GCMs between 2015 and 2100 are used to examine projected changes in water availability (P-E) under a warming climate.

Projected changes to selected CMIP6 GCMs runs are based on the concurrent precipitation and evaporation variables for historical and projected scenarios as list in Table A.4-1.

Our study primarily focuses on analyzing the precipitation seasonality under different forcings over the historical period of 1950 to 2014. This historical period was chosen because the three key considerations: 1) the global precipitation station coverage for the observed precipitation dataset was relatively sparse before 1950; 2) the common recording years for the four observations generally begin at the end of 1940s; and 3) historical simulations (ALL) of most CMIP6 GCMs do not go beyond 2014. We consider spatially averaged precipitation seasonality of three SSP scenarios till the end of the 21st century (2071-2100).

4.2.3. Seasonality Index

The precipitation seasonality index (SI), as proposed by Feng et al. (2013), is a crucial tool in understanding the distribution and variability of precipitation throughout the year. This method calculates the relative entropy (RE) of monthly precipitation, which is independent of specific locations or arbitrary thresholds. It has been developed in recent years for examining global and regional seasonality characteristics and changes (Deng et al., 2020; Konapala et al., 2020; Mao et al., 2022).

To estimate the RE in a grid cell over a year k, the aggregated annual quantities during the 12-month indices are computed by summing the monthly precipitation (x_i) over the k year as:

$$X_k = \sum_{i=1}^{12} x_{i,k} \qquad (4-1)$$

Where i is the month from 1 to 12 in a year k, X_k is the correspond annual total precipitation. Then the probability ($p_{i,k}$) of precipitation ($x_{i,k}$) in month i over a year k is estimated by a discrete a probability distribution:

$$p_{i,k} = \frac{x_{i,k}}{X_k} \qquad (4-2)$$

Subsequently, the RE_k, which estimates the uniformity of monthly precipitation distribution over year k by comparing the probability distribution ($p_{i,k}$) with a uniform distribution of precipitation in year k ($q_{i,k}$ = 1/12, i = 1, 2, …, 12), is calculated as shown in Eq. (3):

$$RE_k = \sum_{i=1}^{12} p_{i,k} \log_2 \left(\frac{p_{i,k}}{q_{i,k}}\right) \qquad (4-3)$$

Where i is the month from 1 to 12 in a year k, X_k is the correspond annual total precipitation.

By definition, when the amount of annual precipitation is quite evenly apportioned to each of the 12 months with the probability of 1/12, Eq. (4-3) assumes the minimum value of $RE_k = 0$. (Note that under an extremely dry condition, where the annual total precipitation $X_k = 0$, it becomes another form of evenly apportionment as $AE_k = 0$.) Conversely, the maximum value of $RE_k = \log_2 12$ occurs when the annual precipitation is concentrated in a single month. RE provides a quantitative measurement of the concentration of precipitation in the wet season.

The dimensionless long-term seasonality index (SI) in a grid cell for year k is then constructed by multiplying RE with its grided annual total precipitation normalized by the observed maximum annual total precipitation in the dataset (which is 9508 mm/year calculated from global land CRU dataset from 1950 to 2014) as shown in Eq. (4-4):

$$SI_k = RE_k \frac{X_k}{X_{max}} \quad (4-4)$$

We computed the annual RE and SI for observations and CMIP6 GCM simulations over the global land. To compare how representative are the precipitation seasonality estimated from these datasets, RE and SI are calculated at their original precipitation grid and then bilinearly interpolated into a common 1° × 1° resolution using the Climate Data Operators (CDO). The comparisons are conducted over the overlapping historical time period of 1950 to 2014, and the future time period from 2015 to 2100.

4.2.4. Global Land Monsoon Regions (GLM)

The global monsoon is recognized as the primary pattern in the annual cycle of global tropical circulation (Wang & Ding, 2008). This climate system is not only characterized by the annual reversal of surface winds but also by contrasting wet summers and dry winters (Liu et al., 2009). The domain of Global Land Monsoon (GLM) precipitation is characterized by the following two principal criteria and has been widely used in many previous studies (Cao et al., 2019; Lee & Wang, 2014; Lin et al., 2014; Liu et al., 2009; Wang et al., 2021).

1) The annual range of precipitation rate, calculated as the difference between the local summer total precipitation (STP) and the local winter total precipitation (WTP),

normalized by the total number of summer or winter days (D), should exceed a threshold of 2.0 mm/day:

$$\text{Region}_a = \frac{\text{STP}-\text{WTP}}{\text{D}} > 2.0\text{mm/day} \quad (4-5)$$

2) The local summer precipitation should exceed 55% of the annual total precipitation (ATP) as,

$$\text{Region}_b = \frac{\text{STP}}{\text{ATP}} \times 100\% > 55\% \quad (4-6)$$

A region is classified as part of the GLM if it satisfies both Eq. (4-5) and Eq. (4-6). The intersection of criteria can be represented as:

$$\text{GLM} = \text{Region}_a \cap \text{Region}_b \quad (4-7)$$

Here, summer refers to the period from May to September (MJJAS) in the Northern Hemisphere and from November to March (NDJFM) in the Southern Hemisphere. Conversely, winter is defined as NDJFM in the Northern Hemisphere and MJJAS in the Southern Hemisphere. The Annual Range of precipitation is defined as the difference between MJJAS precipitation and NDJFM precipitation in the respective hemispheres.

4.2.5. Detection and Attribution Analysis

In this chapter, we conduct detection and attribution (D&A) analysis for SI by using four observational datasets and CMIP6 simulations to focus on two historical periods: 1950-1979 and 1985-2014. SI anomalies are calculated as differences relative to the 1961-1990 mean at each grid point, and their areally averaged means are estimated. To reduce the dimensions and prevent too few constraints in the D&A analysis, a three-year non-overlapping mean was calculated

using these anomalies, producing 10 temporal points at each grid for each 30-year historical period.

The methodology for the D&A analysis is identical to that presented in Section 2.2.6 of Chapter 2. To avoid unnecessary redundancy, a detailed discussion of the D&A is omitted.

4.2.6. Available Water

The difference between monthly precipitation and evaporation variables from the CMIP6 climate models' simulations, (P-E), are applied approximately as the potentially available water for human and ecological consumption, assuming infiltration losses to be negligible. Here, we estimate the average net available water in mm/day for the two historical periods of 1950-1979 and 1985-2014 and for three SSPs of 2071–2100, which is expressed as:

$$AW_{i,k} = \frac{\sum_{k}^{k+30}(P_{i,k} - E_{i,k})}{30} \qquad (4-17)$$

Where $P_{i,k}$ and $E_{i,k}$ represent the monthly precipitation and evapotranspiration in a month i over the year k (k = 1950, 1985, 2071 corresponding to different time periods), respectively. The denominator 30 represents the total number of years taken into consideration for each time period. We further analyze the spatial-average distribution of monthly net available water in historical and future scenarios (SSP1-2.6, SSp2-4.5, SSP5-8.5) from CMIP6 GCMs over different subregions.

To understand the role of precipitation seasonality in the climatology of available water variability in a hydrologic year, we have extracted wet and dry available water data calculated by P-E from CMIP6 GCMs. We define the wet and dry seasons as three consecutive months with the highest and lowest climatological mean of P-E in a hydrologic year, respectively. The

difference in available water between the reference (1961-1990) and future (2071-2100) periods are calculated to assess the change of water availability under different SSP climate scenarios.

4.3. Results

4.3.1. Spatial Distribution between Observations and CMIP6 Models

Figure 4-1 compares spatial distributions and zonal means of ATP, RE and SI from the observed CRU dataset and the historical simulation of CMIP6 ensemble mean (CMIP6-EnM) over global land in 1950-2014. Spatial results of GPCC, ERA5 and NCEP-NCAR are shown in the Appendix Figure A.4-1. Results indicate that CMIP6-EnM could effectively reproduce the historical spatial patterns of observed ATP, RE and SI. However, it is important to note that CMIP6-EnM, being an interpolation of the simulations from 39 CMIP6 models' runs, could cancel some simulation errors, leading to relatively uniform precipitation compared to observations. Furthermore, as climate model-based data, CMIP6-EnM tends to over-simulate light rain events (e.g., drizzle), leading to overestimated precipitation, as reported by Zhao et al. (2023). Consequently, CMIP6-EnM is expected to yield a relatively higher SI than observed data.

The annual total precipitation (ATP), as represented by the CRU dataset (Figure 4-1a) and CMIP6-EnM (Figure 4-1b), is primarily higher in the tropics, where ATP tends to exceed 1500 mm/year. As shown in Figure 4-1c, the higher zonal mean precipitation lies between 20°S and 20°N. As expected, regions such as the polar areas, northern Africa, western India, and Middle Eastern countries receive less precipitation, generally with an ATP less than 300 mm/year. Elevated REs are predominantly observed within the tropical rain belt and the subtropical region (Figure 4-1f), consistent with the findings of Bal et al (2019) based on different dataset. In both the CRU and CMIP6-EnM datasets, the highest RE values (> 1.0) are

found in northern African and western Indian regions. These areas, characterized by a desert climate with relatively low ATP (Figure 4-1a, b), exhibit high REs because precipitation tends to occur within a short period. In contrast, regions such as the Arctic, sub-Arctic, or subpolar climatic regions, which even though have low ATP, have precipitation that occurs uniformly throughout the year, resulting in lower REs. This pattern is also observed in mid-latitude regions, such as the eastern United States and northwestern Europe with relatively higher ATP. SI is a composite result of the annual total precipitation (ATP) and precipitation discretion (RE) throughout the year, with the highest zonal mean observed in the subtropical region around 10°S and 10°N Figure 4-1f. High SIs are predominantly found in global land monsoon regions (GLM) (Figure 4-1g and Figure 4-1h), attributable to either high ATP or high RE. For example, in east-central South America, high SIs are embedded in the American monsoon systems, primarily resulting from high ATP. In contrast, in regions such as western sub-Saharan, central Africa, and South Asia, high SIs are a combination of relatively high ATP and high RE. However, in northern Australia, high SIs appear to be more attributed to high REs than ATP.

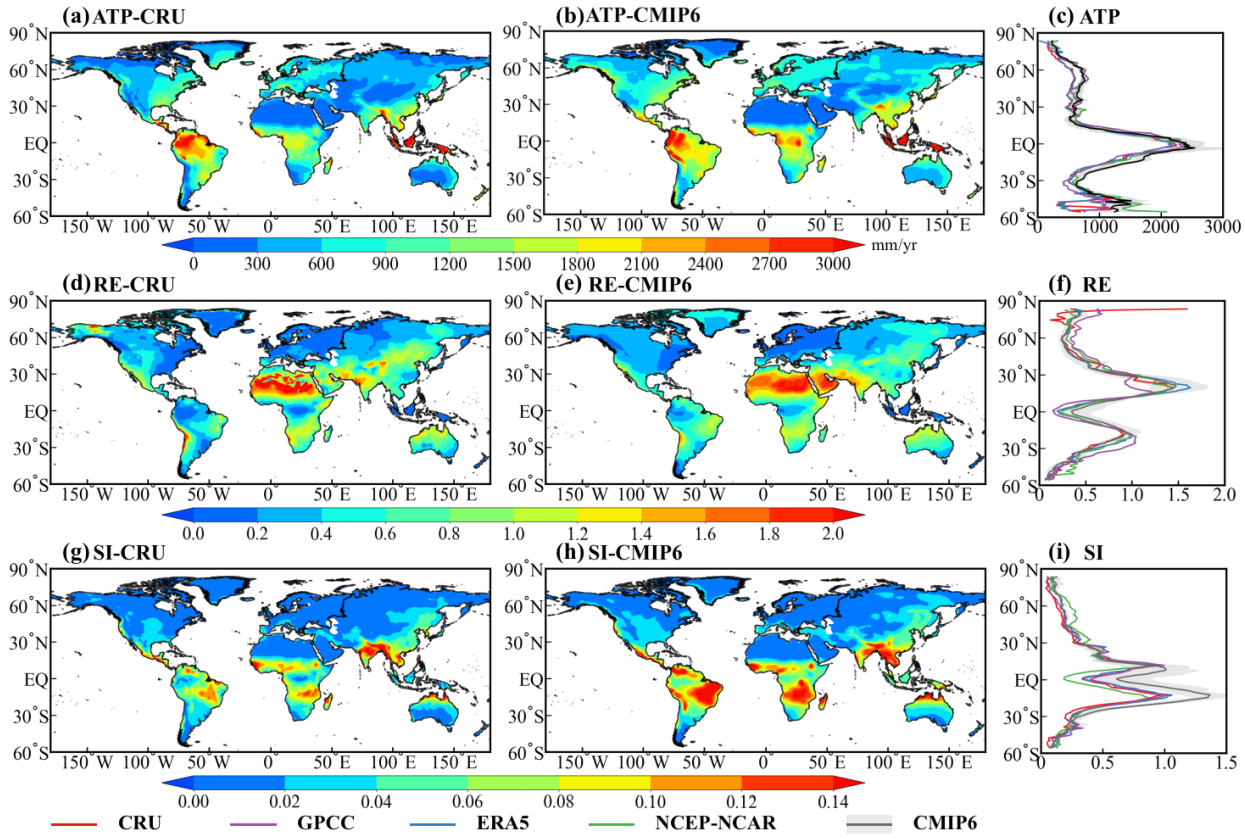

Figure 4-1 Geographical distribution of ATP (mm/yr), RE and SI in 1950–2014 for CRU (Figure 4-3a, d, g) and the ensemble mean of the CMIP6 historical simulations (Figure 4-3b, e, h). Zonal means (Figure 4-3c, f, i) for ATP (mm/yr), RE and SI among 4 observations (CRU, red; GPCC, purple; ERA5, blue; NCEP-NCAR, green) and CMIP6 ensemble mean (grey). Grey shadings are the interquartile spread of 39 model runs (10th and 90th quantiles).

4.3.2. Seasonality Index in Global Land Monsoon Regions

Based on the 1981-2010 monthly mean precipitation data of the CRU dataset, the global land monsoon regions (GLM) identified are shown in Figure 4-2a. This definition results in GLM that agree closely with the GLM given in Chapter 8 of the IPCC AR6 WG1 report (Douville et al., 2021). Notably, regions with high seasonality indices (SIs > 0.04) generally fall within the GLM, as illustrated in Figure 4-2b. A more detailed comparison between ATP, RE

and SI for both observational datasets and the CMIP6-EnM over the GLM is provided in the Appendix Figure A.4-2. The subsequent sections in this chapter will focus on analyzing precipitation seasonality over the GLM.

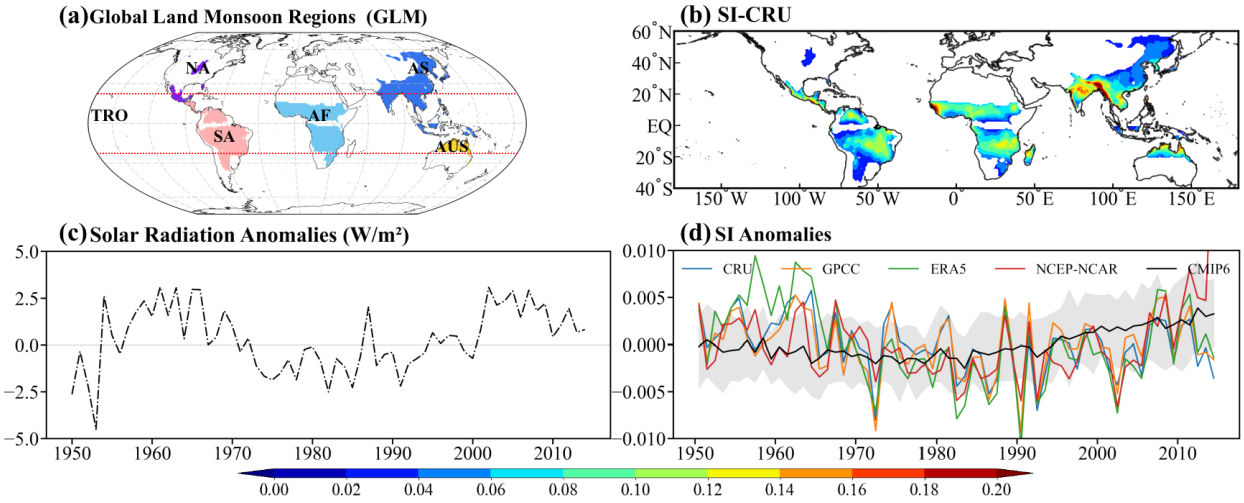

Figure 4-2 (a) Geographical distribution of global land monsoon regions defined by the 1981-2010 monthly precipitation data of CRU. GLM in different continents are shown in different colours, with North America (NA, purple), South America (SA, pink), Asia (AS, blue), Africa (AF, sky-blue) and Australia (AUS, yellow), respectively. Two red lines are 23.5°S and 23.5°N, respectively, which represent the tropical regions noted as TRO. (b) is the distribution of SI the same as Figure 4-1h, but for GLM. (c) is the 65-year surface downward solar radiation anomalies (Wm^{-2}) relative to 1961-1990 generated from CRU data set during 1950-2014. The solar radiation data is masked to the GLM. (d) is the 65-year SI anomalies relative to 1961-1990 for CRU (blue), GPCC (yellow), ERA5 (green), NCEP-NCAR (red) and CMIP6 ensemble mean (grey). Grey shadings are the interquartile spread of 39 model runs (10th and 90th quantiles). Observations and CMIP6 models are masked to the GLM.

Figure 4-2c shows the anomalies in solar radiation over the GLM, relative to the 1961-1990 baseline for the CRU dataset in 1950-2014. During the mid-20th century, specifically from the 1950s to the 1980s, anthropogenic aerosol emissions from North America and Europe were

significantly high, largely due to industrial activities and the burning of fossil fuels (Lamarque et al., 2010). These aerosol emissions potentially influence precipitation patterns by altering incoming shortwave and longwave radiation. The IPCC AR6 reported with high confidence that the observed recent downward trend in precipitation is attributed to the effects of anthropogenic aerosol emissions, which led to diminished incoming surface solar radiation (Douville et al., 2021). This dimming effect, which peaked in the late-1970s, has partially recovered, attributed to the implementation of stricter environmental regulations, advancements in cleaner technologies, and a shift in the global industrial landscape (Douville et al., 2021; Wild, 2012). This recovery trend in solar radiation since 1980s shown in Figure 4-2c is consistent with the findings of Bonfils et al. (2020), which indicate a decrease in the surface downward solar radiation before the 1980s and an increase thereafter. The dimming effect of aerosols weakens the monsoon precipitation (Ayantika et al., 2021), resulting in a decrease in SI anomalies between the 1950s and 1980s, as shown in Figure 4-2d. Based on results obtained from the four observational datasets, the CMIP6-EnM appear to show less fluctuation, suggesting that the CMIP6-EnM can effectively offset some under- or over-simulated errors of climate models. To further analyze the mechanism of changes in SI, the 65-year observation and CMIP6-model dataset are divided into two periods, 1950-1979 and 1985-2014, based on Figure 4-2c and Figure 4-2d, to investigate the decrease and increase patterns of SI, respectively.

4.3.3. Observed and Modeled Trends over the Global Land Monsoon Regions

Figure 4-3 shows the spatial patterns of observed and CMIP6 simulated trends for SI in 1950-1979 and 1985-2014. Results for GPCC, ERA5 and NCEP-NCAR are provided in Appendix Figure A.4-3. The CMIP6 ensemble means (CMIP6-EnM), driven by ALL forcings (Figure 4-2b, h), generally reproduce the observed trends of SI (Figure 4-2a, g), with pronounced

negative and positive trends detected across most GLM in 1950-1979 and 1985-2014, respectively. Simulated trends are generally less "noisy" than the observations because CMIP6-EnM filter out the internal variability of model simulations (Dong et al., 2021; Sun et al., 2022).

During the first 30-year period, seasonality decreased across nearly all GLM regions, particularly in western sub-Saharan, central Africa, east-central South America, and Southern Asia (Figure 4-3a, b). This general decrease in SI can be explained by the large aerosol (ARE) forcing in the mid-20th century (Figure 4-3d), which has been shown to decrease the contrast between the ATP of the wet (remains nearly constant) and dry seasons because the latter tends to increase (Kumar et al., 2015; Murray-Tortarolo et al., 2017). Interestingly, AER forcings tend to counteract or even relinquish the expected enhancement of SI due to increased GHG during 1950-1979 (Figure 4-3b) in regions such as east-central South America, eastern Asia and central Africa. This decrease in SI is found in more than 75% of the CMIP6 models' simulations, and in all four observational datasets (Figure 4-3f). Furthermore, over 90% of the CMIP6 models' simulations agree with the significant role of AER played in reducing the precipitation seasonality.

In the subsequent 30-year period, increasing trends of SI are found in most of the GLM regions (Figure 4-3g, h), with 100% of the CMIP6 models and all four observational datasets showing spatially averaged increasing trends in SI over all GLM regions (Figure 4-3l). This increased SI pattern dominated by wetter wet seasons is consistent with the trends simulated by CMIP3 and CMIP5 models (Chou et al., 2013). The contributions of GHG forcing are significant in both 1950-1979 and 1985-2014 periods, with nearly 75% of climate models simulated increasing trends in SI (Figure 4-3c and Figure 4-3i). However, the implementation of stricter environmental regulations after the 1980s led to a partial recovery of the cooling effect of AER

forcing across most GLM regions, thereby amplifying the impact of GHG forcings on the increased trends of SI, with greater amplitudes, larger impacted regions, and higher climate model agreements (> 75%). Moreover, the contribution of natural forcings (NAT) to the observed trends in SI is expected to be less significant in both periods compared with AER and GHG forcings.

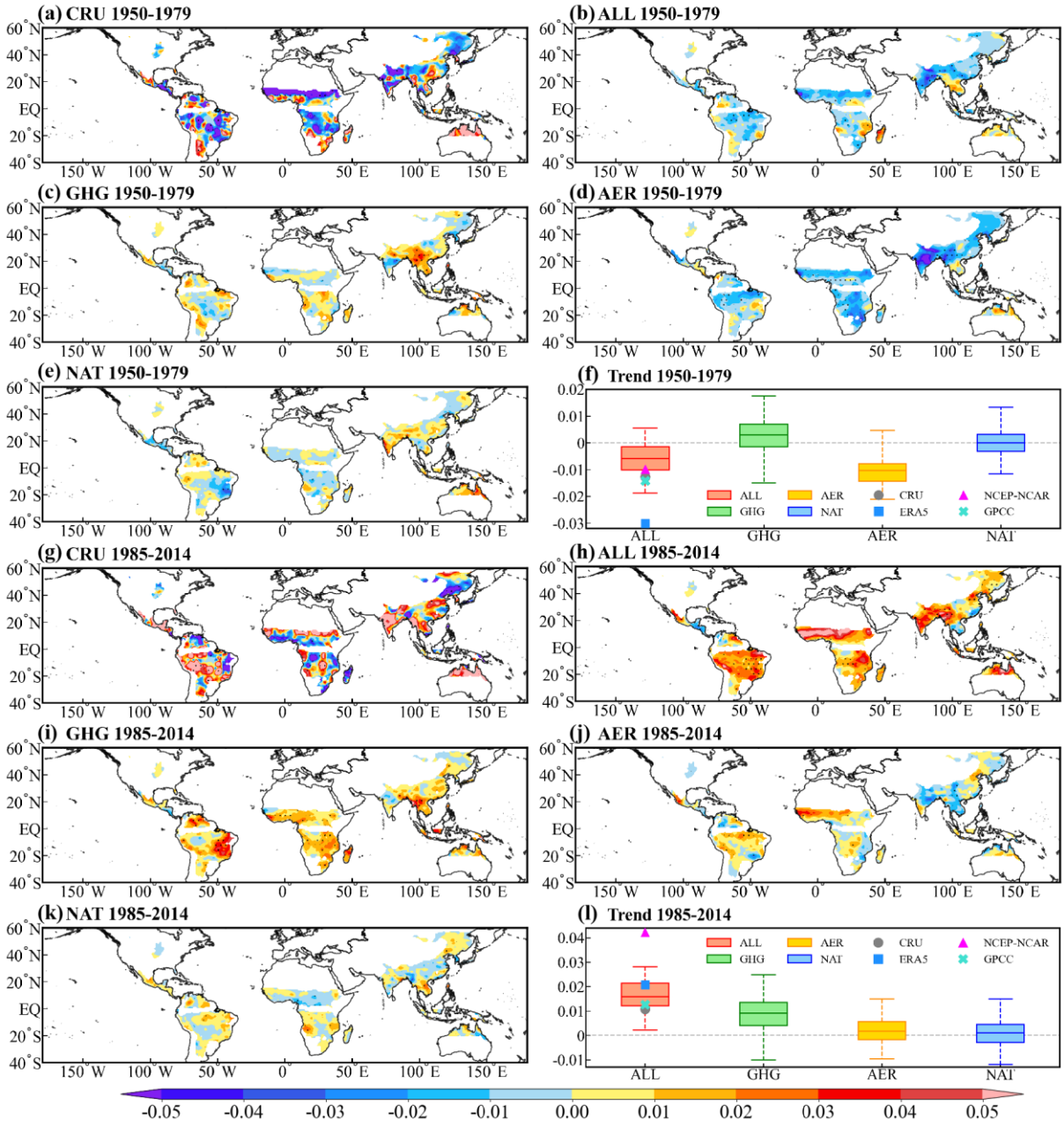

Figure 4-3 Geographical distribution of linear trends (×100/yr) in SI over 1950-1979 (Figure 4-3a-e) and 1985-2014 (Figure 4-3g-k) for CRU observation and CMIP6 model simulations (ALL, anthropogenic plus natural forcing; GHG, greenhouse gases forcing; AER, anthropogenic aerosol forcing; NAT, natural forcing). For models, ensemble means of trends from individual simulations are displayed. Black dots indicate grids with significant long-term trends at the 5% level. The spatially averaged trends of CMIP6's simulations under ALL (red), GHG (green), AER (yellow), and NAT (blue) forcings are presented as boxplots for 1950-1979 (Figure 4-3f) and 1985-2014 (Figure 4-3l), respectively.

Figure 4-4 shows the time series of SI anomalies over GLM and its subregions from 1950 to 2014, relative to the 1961-1990 baseline, based on both observation and CMIP6-EnM datasets. AER and GHG forcings during this period appear to exert contrasting influences on the changes of SI across five continents, except for Australia (AUS, Figure 4-4e). Specifically, AER forcings have led to a decrease in SI, while GHG forcings to an increase in SI over time. AER forcings, through their radiative and microphysical effects (Douville et al., 2021), contributed to a reduction in SI before the 1980s across GLM subregions. However, a rise in SI under AER forcings was found in North America (NA, Figure 4-4d), South America (SA, Figure 4-4f), and Africa (AF, Figure 4-4g) from 1985 to 2014. This trend of SI can be explained by less aerosol emissions after the 1980s, which accelerated the process of cloud droplet coalescence and ice precipitation (Liu et al., 2019; Rosenfeld, 2000). Notably, precipitation seasonality increases have been found in AUS monsoon regions since the 1950s, but there is low confidence in the anthropogenic (including AER and GHG) contributions to these changes as they are less evident in monsoon regions compared to other continents. In the AR6 report of IPCC, Douville et al. (2021) also concluded low confidence in the contributions of AER and GHG which may be partly due to the large interannual variability in AUS. However, an increase in SI in both periods

across five continents has been associated with enhanced moisture flux convergence due to the warming effect of GHG forcings (Tian et al., 2018), which has led to a significant increase of SI in Asia (AS, Figure 4-4c), SA, and AF in 1985-2014. NAT forcings, on the other hand, do not show statistically significant long-term trends in SI. However, they display mild decadal variations that may partly reflect the cooling effects of volcanic forcings, such as the Agung eruption in 1963 and the Pinatubo eruption in 1991 (Winter et al., 2015).

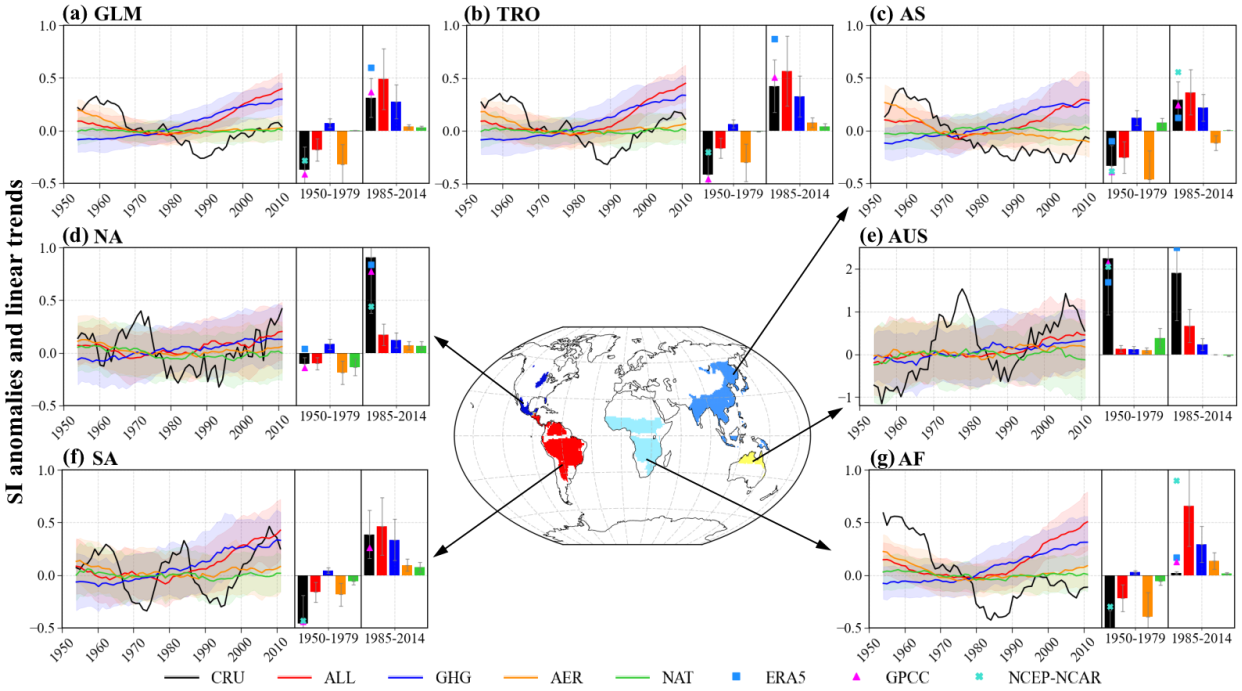

Figure 4-4 Time series of 65-year SI anomalies over GLM subregions from 1950 to 2014 relative to 1961-1990 and their linear trends (colored bars ×100/yr) with 5%–95% confidence intervals (gray error bars) for CRU(black) and the CMIP6 ensemble means of ALL forcing (red), GHG forcing (blue), AER forcing (orange) and NAT forcing (green) in 1950-1979 and 1985-2014. Coloured shadings in the time series indicate range of CMIP6 model simulations. Anomalies are averaged over the global land monsoon (GLM, Figure 4-5a), tropical regions (TRO, Figure 4-6b), North Asia (AS, Figure 4-7c), America (NA, Figure 4-8d), Australia (AUS, Figure 4-9e), South America (SA, Figure 4-10f) and Africa (AF, Figure 4-11g).

4.3.4. Detection and Attribution Analysis Results

The scaling factors of one-signal analysis (Figure 4-5a, d) show that AER and GHG forcings are easily detected in SI changes over GLM from 1950 to 2014. However, SI at regional scales is dominated by internal variability across much of the world (Knutson & Zeng, 2018). Specifically, SI changes before the 1980s are largely attributable to AER forcings because the 90% confidence intervals of scaling factors estimated by each of the four observation datasets are narrow and close to one. Moreover, there is high confidence that ARE-induced SI changes in 1950-1979 can be easily detected in all four observation datasets over TRO, AS and AF (see the Appendix Figure A.4-4 and Tab. S3). After the 1980s, results obtained from all four observation datasets show that GHG forcings are the primary drivers of SI changes. Furthermore, for the continental D&A analysis, the GHG fingerprints are detected in at least one or more observation datasets (see the Appendix Figure A.4-5), which increases the confidence that GHG forcings might be the main driver behind the increase in SI from 1985 to 2014. In the two-signal analysis (Figure 4-5b, e and Tab. S4), the scaling factor results obtained from the four observation datasets show that anthropogenic (ANT) forcings can be easily distinguished from NAT forcing in both periods. Moreover, ANT forcing is more detectable in 1985-2014 than in 1950-1979 which is expected. The attributable trends based on the estimated scaling factors in the two-signal analysis indicate that the observed decrease of SI over the GLM before the 1980s is primarily explained by the influence of ANT, which has contributed more than 80% of the observed SI trends in each of the four observation datasets. Notably, there is even an underestimation of ANT response in ERA5 ($\beta > 1$) in 1950-1979. The increased SI in 1985-2014 is attributable to ANT forcing with high confidence, as the attributable trends exceed 80% in

each of the observation datasets, except that of NCEP-NCAR of which the contribution of ANT forcing in 1985-2014 was slightly underestimated.

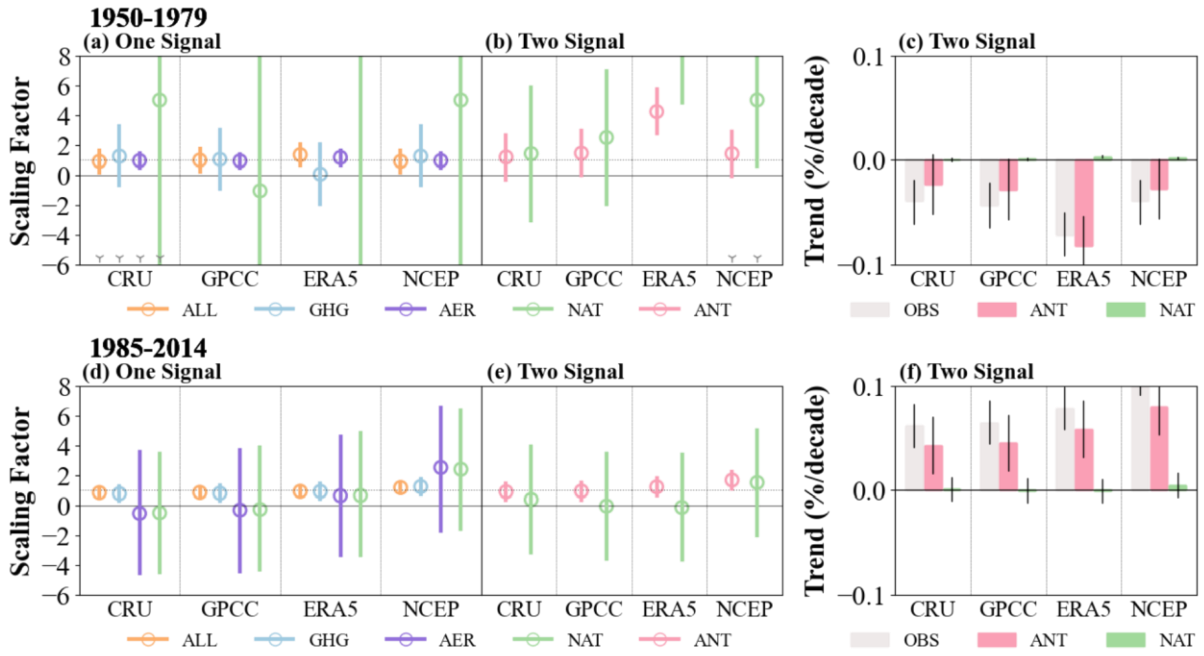

Figure 4-12 Results of the one- and two-signal analysis for SI anomalies over the global land monsoon are shown in (a), (b), (d) and (e). The circles and the vertical lines indicate the best estimates of scaling factors and their 10–90% confidence intervals, respectively. The two gray solid and dashed horizontal lines indicate zero and one, respectively. The gray triangles at the bottom of 5(a) show the failure of the residual consistency test due to too small model variability. The rightmost column in black solid frame is the attributable contribution from ANT and NAT forcings to observational SI anomalies trends during 1950-1979 and 1985-2014 and their 10–90% confidence interval (error bars).

Change in SI can be attributed to the variations in either the precipitation amount or its relative entropy (Eq. (4-4)). Given that precipitation amount generally intensifies with warming following the Clausius-Clapeyron relation (Douville et al., 2021), Figure 4-6 shows the relationship between changes in SI and the global mean surface air temperature (SAT) from

1950-2014. The 5-year mean SI changes under GHG forcing are regressed onto SAT of the CRU dataset. The regression results show a slope of 6.19%/K over the GLM with a robust correlation coefficient (R = 0.98) in 1950-2014. The TRO monsoon region, excluding mid-latitudes, exhibits marginally greater slopes (6.60%/K). In contrast, continental monsoon regions generally estimate slightly smaller regression slopes compared with GLM, with nearly 6%/K regression slopes in SA, AS and AF, with a high correlation coefficient (R > 0.85). The smallest regression slope is observed in NA (3.04%/K), which is consistent with the fact that NA monsoon regions are largely surrounded by oceans which have a lower warming rate compared to regions with extensive inland areas (Byrne & O'Gorman, 2018). AUS shows a relatively low correlation coefficient (R = 0.61), which could be attributed to its sparse grids which generally lead to a large interannual variability. Interestingly, the regression slopes after the 1980s are significantly larger than those in 1950-1979, a period dominated by AER forcing. This suggests an intensification of the impact of global warming on precipitation seasonality patterns in recent decades.

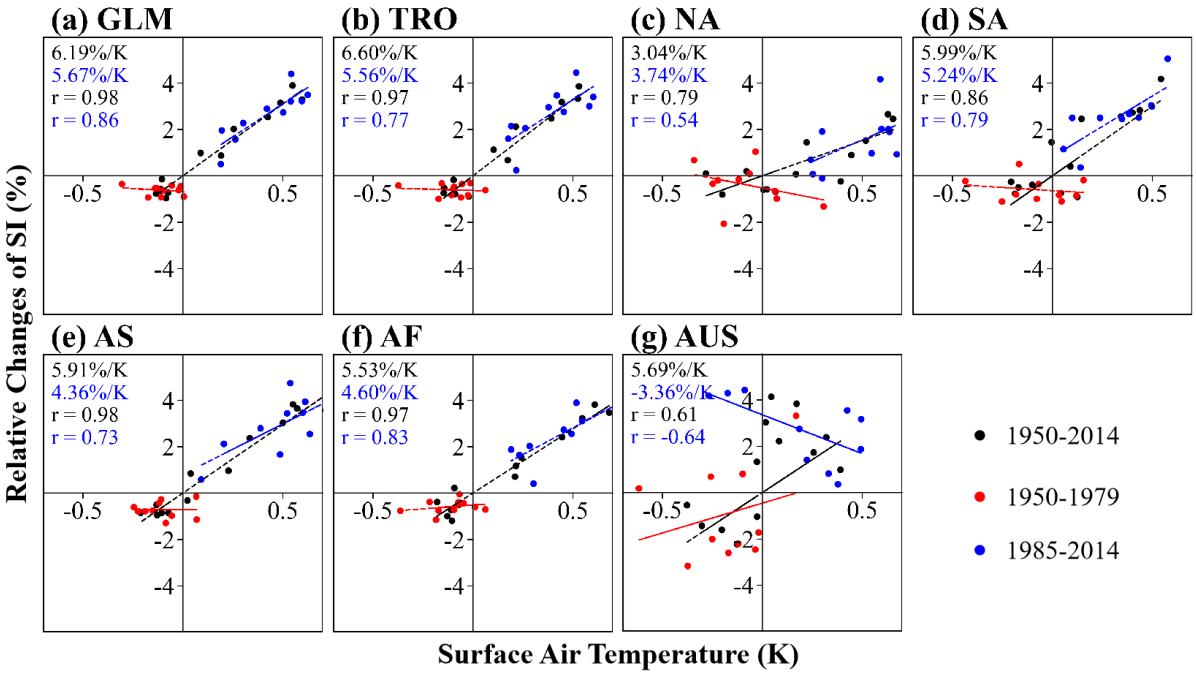

Figure 4-13 Scatter plots of SI anomalies (y-axis) in CMIP6 hist-GHG simulations and globally averaged surface air temperature (SAT) (x-axis) in the CRU dataset over 1950-2014 (black dots), 1950-1979 (red dots) and 1985-2014 (blue dots) relative to the baseline 1961-1990. Black dots represent the 5-year mean anomalous values obtained from SI of CMIP6 hist-GHG and SAT of CRU in 1950-2014. Red and blue dots represent the 3-year mean anomalies values obtained from SI of CMIP6 hist-GHG and SAT of CRU in 1950-1979 and 1985-2014, respectively. Trend lines of linear regression in 1950-1979, 1985-2014, and 1950-2014 are shown in red, blue, and black respectively. Corresponding values of regression slope (%/K) and correlation coefficient are listed in the top left for 1985-2014 (blue) and 1950-2014 (black).

4.3.5. Future Projections of Precipitation Seasonality over the Global Land Monsoon

The relative changes (%) of the spatially distributed SI (Figure 4-7a, b, c) and the continental averaged SI (Figure 4-7d) of the CMIP6 simulations under SSP1-2.6, SSP2-4.5, and SSP5-8.5 climate scenarios over the future period of 2071-2100 are shown in Figure 4-7. Precipitation seasonality is projected to increase with a relatively high model agreement (100 %) across most monsoon regions. Moreover, under higher emission scenarios, especially the SSP5-8.5 scenarios, SI is projected to increase in greater magnitude and over larger impacted regions progressively. The most significant increase in SI under SSP5-8.5 is projected in the Asia monsoon region (27% in CMIP6-EnM, Figure 4-7d) with 100% model agreement. This increase is primarily due to more than a 100% increase in India (Figure 4-7c). This result is consistent with the projected increase in the precipitation during the wet season for the South Asian monsoon domain, as documented in the AR6 report of IPCC. The African (AF) monsoon follows closely, with a projected 26% increase in SI, most notably over the Central Sahel (> 50%). NA is the only region where a lower SI is projected under higher SSPs due to a larger projected

decrease in precipitation during the wet season compared to the dry season, as reported by Zhao et al. (2023), indicating a uniform drier pattern over NA in the future throughout the year.

SI anomalies are projected to increase over time across the GLM and its subregions. However, these increases are indistinguishable among SSPs before the 2050s (see the Appendix Figure A.4-8). In the latter half of the 21st century, GLM, TRO, AS, and AF are projected to exhibit the highest increasing trends under SSP5-8.5 scenarios and the lowest increasing trends under SSP1-2.6, respectively, while SI is less sensitive to emission scenarios in NA, SA and AUS monsoon regions. We have also projected the relative changes of SI by the end of the 21st century under different warming levels (+1°C, +1.5°C, +2°C, +3°C, +4°C) relative to the period 1850-1900 (See Figure A.4-9). SI is projected to increase under higher warming levels due to thermodynamic increases in moisture (Douville et al., 2021).

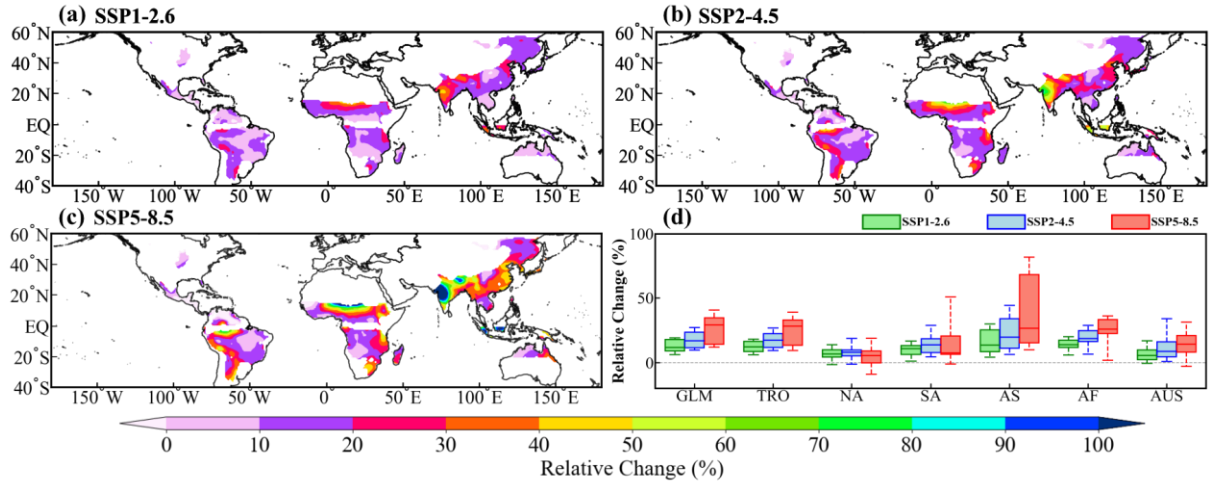

Figure 4-14 Temporally averaged changes in SI of CMIP6-EnM under SSP1−2.6 (Figure 4-7a), SSP2−4.5 (Figure 4-7b), and SSP5−8.5 scenarios (Figure 4-7c) in 2071-2100 (the 2080s) are displayed as differences (%) relative to the reference period (1961-1990). Figure 4-15d is the corresponding spatial averaged relative changes of SI (%) in the 2080s under SSP1-2.6 (green), SSP2-4.5 (blue) and SSP5-8.5 (red) over GLM and its subregions. Boxes indicate the model's spread

(25th and 75th interquartile), with the horizontal line inside indicating the ensemble mean of 39 CMIP6 model runs.

4.3.6. Influence of Precipitation Seasonality on Available Water

Figure 4-8 shows the historical distribution of monthly available water (AW) for the periods 1950-1979 and 1985-2014, in addition to future projections for 2071-2100 under three SSPs across GLM and its subregions. Results show that water supplies are generally prevalent between early March and late October across the GLM for both the historical period and the projected end of the 21st century. Specifically, the water supply period in the AS monsoon regions is approximately two months longer, with a more uniform distribution compared to the GLM. In contrast, AUS exhibits a relatively shorter supply period (< 5 months) with an uneven distribution. The projected monthly distribution of AW in the GLM shows a trend towards increased water availability in wet seasons (6th–9th month), particularly in AS and AF monsoon regions.

Although the precipitation seasonality in SA and AUS is becoming more variable under higher emission scenarios, the AW does not exhibit a similar trend, potentially due to the competing effects between evaporation and precipitation (Konapala et al., 2020). Interestingly, in the NA, there is an evident drying trend during the wet season and wetter conditions in the dry season, which may be associated with the decreased SI in summer shown in Figure 4-7. In addition, the high confidence in the delayed onsets and demises of the summer monsoon in NA, as reported in the IPCC AR6, leads to a rightward shift in the water supply as emissions increase. Although AW is sensitive to changes in radiative forcing, with higher emission scenarios corresponding to more variations, the range of the water supply period does not appear to be

significantly affected by radiative forcing. This could potentially result in a general increase in AW in the future over regions with higher precipitation seasonality.

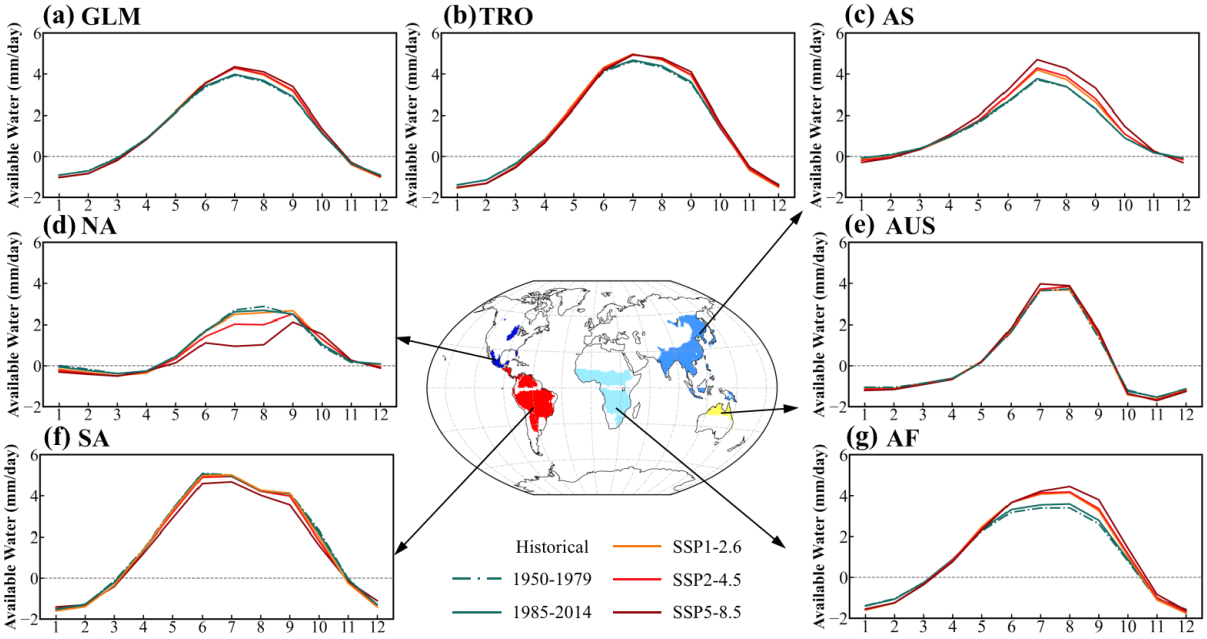

Figure 4-16 Monthly historical and projected available water (mm/day) in GLM and its subregions. The historical periods are 1950-1979 (green dashed line) and 1985-2014 (green solid line). The future period is 2071-2100 for SSP1−2.6 (orange solid line), SSP2−4.5 (red solid line), and SSP5−8.5 (dark red solid line).

The relative changes in available water during the wet and dry seasons for three future emission scenarios (SSP1-2.6, SSP2-4.5, SSP5-8.5) are shown in Figure 4-9, illustrating the relationship between water and energy balance at a seasonal scale (Konapala et al., 2020). Changes in AW are primarily dominated by the wet season, which is projected to undergo more pronounced changes compared to the dry season. Moreover, there is high confidence that the contrast in the inter-annual variability of AW between dry and wet seasons will likely increase across most of the global monsoon regions (> 75% model agreement), which is consistent with the "wet get wetter, dry get drier" hypothesis, which postulates that global warming intensifies

the hydrological cycle, leading to wetter wet seasons and drier dry seasons (Held & Soden, 2006). Specifically, 100% (>75%) of CMIP6 models agree with the projected increase (decrease) in AW over TRO, AS and AF under three SSPs during the wet (dry) season. The most significant increase of AW is projected in AS (3.84mm/day) and AF (3.52mm/day) monsoon during the wet season under SSP5-8.5 scenarios. Although more than 75% of climate models projected SI to increase under SSP2-4.5 and SSP5-8.5 scenarios, the projected annual change of AW of AUS from 2015 to 2100 is minimal (see the Appendix Figure A.4-10), because the projected increase in AW over AUS during the wet season is expected to offset the decrease during the dry season. For NA monsoon, there is high confidence (> 75% model agreement) in the projection of a decrease in AW, as reductions are anticipated in wet (0, -0.45 and -1.57mm/day) and dry (-0.50, -0.72 and -0.97mm/day) seasons under three SSPs. Conversely, there is only low confidence in the projected decrease in AW for the South American (SA) region, which means further investigation is necessary.

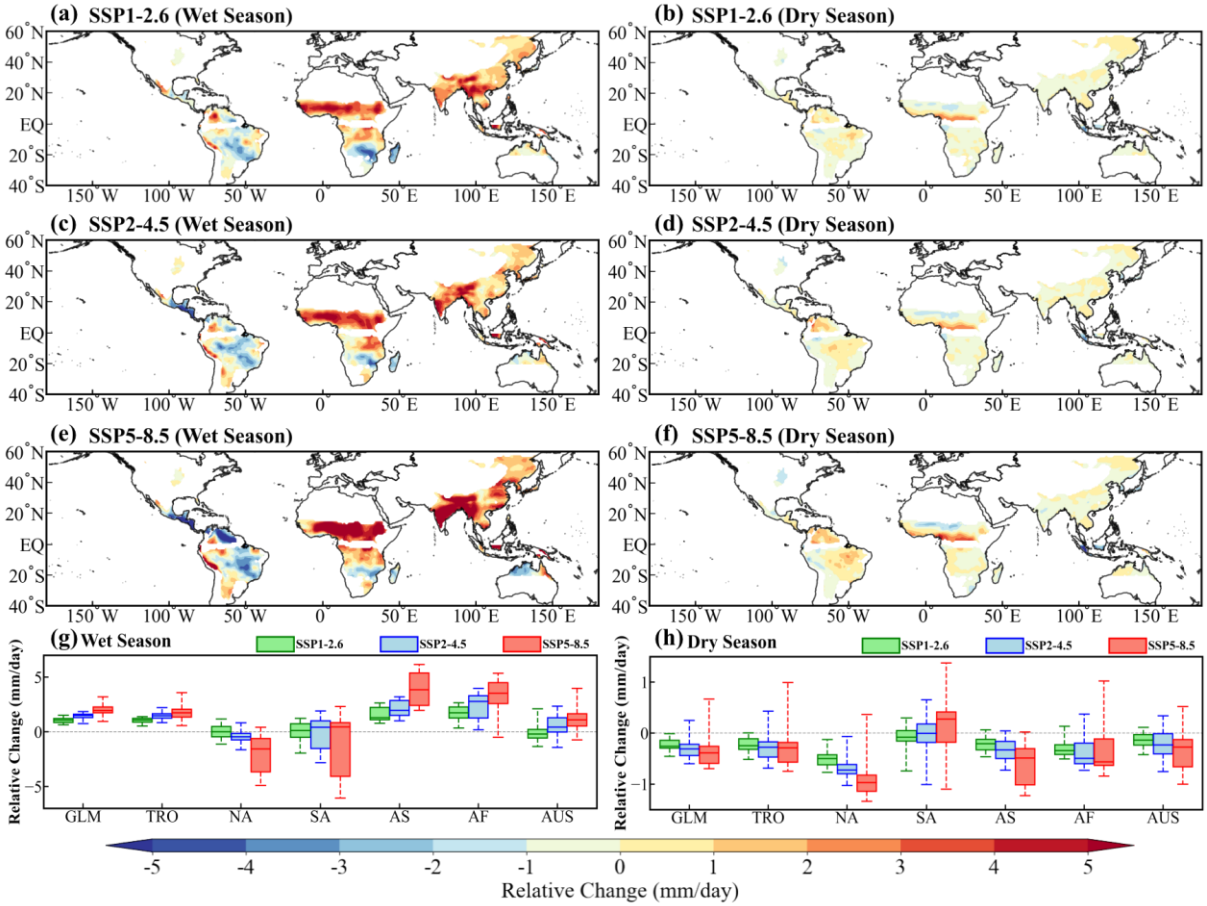

Figure 4-17 Temporally averaged changes in available water (AW) of CMIP6-EnM under SSP1−2.6 (Figure 4-9a, b), SSP2−4.5 (Figure 4-9c, d), and SSP5−8.5 (Figure 4-9e, f) for wet season (left column) and dry season (right column) in 2071-2100 (the 2080s) are presented as differences (mm/day) relative to the reference period (1961-1990). Figure 4-9g, h is the corresponding spatial averaged relative changes of AW (%) in the 2080s under SSP1-2.6 (green), SSP2-4.5 (blue) and SSP5-8.5 (red) for the wet season and dry season over GLM and its subregions. Box plots indicate the range of climate models' simulations (25th and 75th interquartile), with the horizontal line inside indicating the ensemble mean of 39 CMIP6 model runs.

4.4. Discuss and Conclusions

In this chapter, we investigated observed and projected changes in precipitation seasonality across global land monsoon regions under a warming climate and demonstrated the

importance of SI in modulating future seasonal water availability. We show that high SIs are the general characteristic of the global land monsoon regions due to their high values in either the precipitation amount (ATP) or its relative entropy (RE). In the NA and SA monsoon regions, high SIs mainly result from a substantial annual total precipitation. In contrast, relative entropy plays a more important role in the AUS monsoon region. However, high SIs are a combination of ATP and RE in the AS and AF monsoons. This chapter focuses on examining the precipitation seasonality over the GLM, which has experienced decreasing SI anomalies relative to the baseline before the 1980s, followed by a recovery. These changes in SI anomalies are consistent with the variation of the surface downward solar radiation anomalies, which was primarily caused by the dimming effect of large aerosol emissions before the 1980s, resulted in a decrease in the monsoon precipitation globally. However, due to the implementation of stricter environmental regulations, the dimming effect has partially recovered after the 1980s, which likely resulted in an increase in precipitation driven by warming (thermodynamic) (Paik et al., 2020).

Further analysis of precipitation seasonality show that over 75% of CMIP6 ALL simulations and four observational datasets show a reduction in SI over the 1950-1979 period, particularly in western sub-Saharan, central Africa, east-central South America, and Southern Asia. Increased AER emission scattered and absorbed more solar radiation, leading to a reduction in the energy available for surface evaporation and subsequently less monsoon precipitation (Chung & Soden, 2017). However, clouds formed under higher AER emissions (characterized by more numerous but smaller water droplets) need larger growth of water droplets to initiate rainfall, resulting in a delayed but more substantial rainfall (Abbott & Cronin, 2021; Konwar et al., 2012). Compared with the microphysical effect of AER, the reduction in

observed SI before the 1980s is more likely attributed to the radiative effects, as AER-induced SI shows an evident decreasing trend with high confidence (> 90% model agreement). Furthermore, by using the optimal fingerprinting method, we for the first time detected trends of SI under anthropogenic forcing across GLM in all four observational datasets from 1950 to 2014, with over 70% of observed changes in SI attributed to anthropogenic activities. There is high confidence that AER was the main driver behind decreased monsoon precipitation in GLM before the 1980s. In contrast, in 1985-2014, increasing trends of SI are detected almost everywhere in the GLM region with very high confidence (100% model agreement). Despite some European countries' success in reducing greenhouse gas emissions since the 1980s, global GHG levels continue to rise at about 1.5ppm/year due to deforestation, industrialization, fossil fuel consumption, and land use changes (Malik et al., 2016), leading to enhanced moisture flux convergence under the warming effect of GHG (Tian et al., 2018; Trenberth, 2011). Our results show that increased moisture within global land monsoon regions led to an increased SI at 6.19%/K (thermodynamic response) with high confidence (R = 0.98). Furthermore, all four observational datasets show an increase in SI after the1980s on a global scale with GHG forcing as the primary driver. Our study is one of the first to clearly demonstrate that changes in observed SI over global land monsoon regions are attributed to human influence with high confidence (medium confidence in IPCC AR6) (Douville et al., 2021; Marvel et al., 2017). However, even though we have detected the influence of ANT, AER and GHG on the SI of some regions, such as in AS and AF, confidence remains low in detecting changes to SI at regional scales partly because the interannual variability of SI is generally large. More study is needed to better understand possible changes to SI under the impact of climate warming.

The accessibility of local water resources (P-E) depends largely on the seasonality of precipitation which in this chapter is represented by the SI. At the end of the 21st century, SI is expected to increase over GLM with high confidence (100% model agreement) and appears to be sensitive to emission scenarios and warming levels, particularly in AS and AF monsoon regions. This enhancement of SI indicates a widening contrast in precipitation amounts between wet and dry seasons due to climate warming impact. This is consistent with the anticipated increase in the differences of inter-annual variability of AW between the dry and wet seasons across most global monsoon regions (> 75% model agreement). Changes in projected AW are largely attributed to changes in the wet season, as AW is projected to substantially increase in AS and AF monsoon regions but to substantially decrease in monsoon regions of NA and SA during the wet season. Apparently projected changes to AW have been mainly due to the increased in precipitation during the wet season than to the duration of the wet season. The increase in the inter-annual variation of AW is also reported by Douville et al. (2021), but only with medium confidence because the simple thermodynamic scaling, namely, "wet-get-wetter, dry-get-drier" mechanism, fails to clearly capture simulated changes in P − E over land (Greve et al., 2014; Held & Soden, 2006; Roderick et al., 2014). This mechanism is not always applicable because drylands may not always get drier under the impact of climate warming. However, our results offer a comprehensive perspective on seasonal water availability. While positive or negative AW changes means overall wetter or drier conditions, respectively, changes in SI further elucidate changes in the temporal distribution patterns of annual precipitation (see the Appendix Tab. S5). Regions such as AS and AF are projected with positive changes in both AW and SI, which means a higher availability of water in these regions, or the wet season becomes wetter ('wet get wetter). Conversely, for regions such as NA and SA, which are projected with less AW but

higher SI, it means the dry season becomes drier ('dry get drier'). Central American regions (Northern AS monsoon) is projected to become drier in the wet season ('wet get drier') as both AW and SI are projected to decrease. Amazon is projected to become wetter in its dry season ('dry get wetter'), it is characterized by higher projected AW but lower projected SI.

If we are not mistaken, for the first time, we have identified anthropogenic (AER and GHG) fingerprints on the precipitation seasonality index of GLM, reinforcing our confidence (high confidence) in the impact of human influence on precipitation seasonality. As an innovative approach based on the precipitation seasonality index, we have demonstrated a robust method in analyzing the seasonal patterns of future water availability, which is more comprehensive than the simple 'wet get wetter, dry get drier' mechanism (Greve et al., 2014; Held & Soden, 2006; Roderick et al., 2009). This chapter has contributed to our understanding of the water cycle change in the context of global warming impact. It enhances our ability to anticipate potential hydrological shifts, which are essential for us to develop effective global climate resilience and adaption strategies. Future research could apply these results to investigate the potential impact of water cycle changes in both wet and dry seasons over different regions across the world.

4.5. Notation

The following symbols are used in this chapter:

AER = His-aer forcing (anthropogenic aerosol forcing only)

ALL = Historical forcing (including both anthropogenic and natural external forcings)

ANT = Anthropogenic forcing, corresponding to ALL-NAT

AF = Africa Monsoon

AS = Asia Monsoon

ATP = Annual total precipitation

AUS = Australia Monsoon

AW = Available water

BADC = British Atmospheric Data Centre

CMIP6 = The Coupled Model Intercomparison Project Phase 6

CMIP6-EnM = CMIP6 ensemble mean

CRU TS = Climatic Research Unit Time Series

CTL = The preindustrial control experiment

D&A analysis = Detection and attribution analysis

E = Evaporation

ECMWF = The European Centre for Medium-Range Weather Forecasts

ESG = The Earth System Grid data distribution porta

GLM = Global Land Monsoon

GPCC = The Global Precipitation Climatology Centre

IPCC AR6 = IPCC Sixth Assessment Report

NA = North America Monsoon

NAT = Hist-nat forcing (natural external forcing only)

NCDC = National Climatic Data Center

NCEP-NCAR = The National Centers for Environmental Prediction - National Center for Atmospheric Research

OLS = Ordinary least square

P = Precipitation

R = Correlation coefficient

RE = Relative entropy

SA = South America Monsoon

SAT = Surface air temperature

SI = Precipitation seasonality index

STP = Summer total precipitation

WMO = World Meteorological Organization

WWR = World Weather Records

WTP = Winter total precipitation

TRO = Tropical Monsoon

Chapter 5 Conclusions and Future Work

5.1. Conclusions

Climate change is likely one of the most significant global-scale challenges to mankind in the 21st century, and the impact of global warming on the spatial and temporal changes of climate extremes has worsened, with devastating effects on agriculture, water resources, biodiversity, and overall ecosystems (Deng et al., 2020; Feng et al., 2013; Konapala et al., 2020). To mitigate the potential damage attributed to climate change, it is crucial to understand why and how high-impact precipitation events will develop, and to project future precipitation events under a changing climate and their potential societal impacts. These insights will provide the scientific basis for decision-makers to develop effective mitigation policies and adaptation strategies against the impacts of worsening extreme precipitation events under the impact of climate change.

This thesis focuses on investigating the influence of climate changes and anthropogenic activities on current and future extreme precipitation patterns. Chapter 1 provides a comprehensive understanding of how these factors shape the current precipitation patterns, thereby establishing the background, problem statement and objectives of this thesis. Chapter 2 specifically analyze the effects of anthropogenic activities in observed changes in precipitation extremes. This insight gained is critical in elucidating how climate warming has affected precipitation extremes, thereby enhancing our predictive ability on the hydroclimatic impact of climate change. In Chapter 3, the future characteristics of precipitation extremes under the influence of climate warming is projected. A realistic projection of future precipitation extreme is instrumental in developing effective mitigation policies and adaptation strategies. Chapter 4

provides a comprehensive perspective on future water availability based on the projections of future precipitation extremes. The insights derived from this chapter are summarized below which will contribute to water policymakers and engineers in developing water resource management and planning strategies to mitigate the potential impacts of water-related natural hazards such as floods and droughts.

5.1.1. Detection and Attribution of Observed Precipitation Extremes

Using an optimal fingerprinting method, we conducted a detection and attribution analysis in the change of seasonal extreme precipitation based on HadEX3 observations with CMIP6 simulations for 1950–2014 over low-risk (LR) region, high-risk (HR) region and 16 CMIP6 domains.

From the spatial patterns of the observed and CMIP6 simulated trends for PI, positive trends in the seasonal Rx1day have been detected across most of NHL since the mid-twentieth century. The increasing pattern is more significant and widespread in fall and winter but weaker in spring and summer. The influence of GHG forcing is similar in ALL forcings but with greater amplitudes and wider impacted regions, which shows the dominant impact of anthropogenic GHGs emissions. But the impact of GHG emission is reduced by the cooling effects of AER forcings, resulting in decreasing trends of ALL results over India and southern China in fall and winter.

From the temporal trend analysis, observed changes in Rx1day anomalies have generally decreased before the 1980s, followed by a rapid recovery, especially over Europe and Siberia. GHG-induced Rx1day has generally increased faster with statistical significance over most regions since the 1980s. On the other hand, the decreasing trends of AER-induced Rx1day have

generally slowed down over most regions with statistical significance since the 1980s. However, change points detected in the long-term trend of Rx1day under NAT forcings are mostly not statistically significant over the NHL and subregions.

From the detection and attribution analysis, anthropogenic forcing is detectable in at least one season over 80% of CMIP6 domains, with more than 60% attributable to anthropogenic forcing, especially in northern Eurasia. Long term increase in the seasonal Rx1day is generally attributed to GHG forcing with highly confidence, especially in the winter across northern Europe and northern Asia. Individual AER signal is most detectable in East Asia for their negative impact on Rx1day, particularly in JJA. Interestingly, although seasonal natural (NAT) forcings are undetectable in one-signal analysis, they are detectable in similar regions (e.g., WNA, SCA, MED, WCA and WAF) in the two- and three-signal analysis, suggesting that observed changes should not be solely attributed to anthropogenic forcings, because NATs could also contribute to the observed changes.

Our results on annual D&A analysis agree with findings of other results based on different indices, datasets, and study periods (Paik et al., 2020; Sun et al., 2022; Zhang et al., 2013). However, from what we know, our study in chapter 2 provides the first D&A analysis of seasonal precipitation changes on global and regional scales, providing valuable insight on why and how high-impact precipitation extremes have developed, which will provide the scientific basis for decision-makers to develop effective mitigation policies and adaptation planning against the impact of global warming to extreme precipitation events. Future research should focus on the combined impact of human influence and climate anomalies on both annual and seasonal precipitation extremes. New insight on extreme precipitation gained from such studies may give farmers and water resource managers more time to prepare against such major events.

5.1.2. Future Characteristics in Extreme Precipitation Indices

From a comprehensive evaluation of the performance of CMIP6 models against observed datasets, it shows that the CMIP6-EnM can reasonably reproduce the spatial patterns of observed precipitation events. Therefore, the projections of CMIP6-EnM should be representative for future periods because 10 ETCCDI extreme precipitation indices based on the simulations of CMIP6-EnM out-performs all 18 individual GCMs with negative $RMSE_{XY}$ over North America and its 8 subregions. The simulations of CMIP6-EnM also achieve a reasonable signal-to-noise ratio (SNR > 1) and higher R statistics (R > 0.8) in most sub-regions of North America.

The analysis of precipitation extreme indices computed from climate models' simulations generally project similar changes under climate warming scenarios of SSP1-2.6, SSP2-4.5 and SSP5-8.5 before the 2040s, particularly in high latitude regions. However, there is a growing divergence between the projections of different SSP scenarios by the late 21st century, with the most pronounced changes under SSP5-8.5 scenarios. There is high confidence that responses of extreme precipitation in North America to the impact of global warming will intensify throughout the 21st century, with projections of CMIP6 ensemble showing a greater magnitude of change than CMIP5 models (IPCC, 2021).

Spatial projections of extreme precipitation indices suggest a likelihood of heightened severity in extreme events throughout the 21st century, especially in latitudes above 55◦N of NA and coastal areas under the SSP5-8.5 climate scenarios. However, at middle latitudes, in-between WNA and southern NWN of NA (e.g., Oregon, Washington, and southern British Columbia), both extreme precipitation events and droughts are projected to become more severe. In lower latitudes such as Mexico and Texas, the precipitation indices of climate projections imply an

intensification of meteorological droughts in these regions. In addition, coastal regions are also projected to be more susceptible to severe extreme precipitation events.

From the projected changes in seasonal extreme precipitation, northern latitude and middle latitude regions are expected to experience more pronounced precipitation extremes in winter than in summer. On the other hand, changes between winter and summer in lower latitudes of North America (e.g., NCA and SCA) agree with the CMIP5 results that precipitation seasonality will decrease, with decreasing trends in both winter and summer, which means a more severe arid climate in the future (Sillmann et al., 2013b).

With regard to model agreement, CMIP6 climate models consistently project that precipitation extremes of NA will progressively become more severe towards the end of the Twenty-First century (the 2080s) with 100% agreement for all indices over high latitude regions. There is more than 80% agreement between CMIP6 GCMs' projections for all indices over middle latitude. However, there is low confidence (less than 60%) that lower latitudes of NA could become progressively wetter conditions over the 21st Century.

In conclusion, based on the projections of 18 GCMs of CMIP6, our analysis provides robust evidence supporting a likely increase in the frequency and intensity of extreme precipitation events, especially in the high latitudinal and coastal regions of North America. These results offer a critical information for developing adaptive strategies for these impending climatic changes. Stakeholders can work proactively toward implementing resilience-building measures by developing a clear understanding of the potential changes in precipitation extremes. This can range from updating infrastructure designs to withstand increased precipitation events,

optimizing water resource management systems for enhanced efficiency, to adopting sustainable agricultural practices that mitigate the impact of more variable climatic patterns in the future.

5.1.3. Impact of Precipitation Seasonality on Water Availability

Based on our analysis of observed datasets and simulations of CMIP6 climate models, the precipitation seasonality index (SI) that represent a composite result of precipitation amount (ATP) and precipitation uniformity (RE) annually show a noticeable change in Global Land Monsoon regions (GLM). To analyze climatic factors that contributed to detected changes in SI, we analyzed changes in incoming surface solar radiation over the GLM. The 1970s was a period of weakened monsoon precipitation due to reduced solar radiation caused by increased anthropogenic aerosol emissions (Ayantika et al., 2021). This decrease in monsoon precipitation resulted in lower SI anomalies between the 1950s and 1980s. However, the decades following the 1980s followed a reversed trend. Because of the implementation of more stringent environmental policies, the advent of cleaner technologies, and a transformation in the global industrial sector contributed to a recovery in the incoming surface solar radiation. This change was accompanied by a notable rise in the precipitation seasonality index. As such, we conjecture a relationship between anthropogenic activities and precipitation seasonality.

Our spatiotemporal analysis of precipitation seasonality reveals that over 75% of CMIP6 ALL simulations and four observational datasets agree on the reduction in SI during 1950-1979. Subsequently, the period spanning 1985-2014 show an increasing trend of SI almost everywhere in the GLM region, with very high confidence (100% model agreement). By using the optimal fingerprinting method, our study in chapter 4 is one of the first to clearly demonstrate changes in observed SI over global land monsoon regions are attributed to human influence with high

confidence (medium confidence in IPCC AR6). Specifically, anthropogenic (ANT) forcings are easily detected across GLM in all four observational datasets for both periods (1950-1979 and 1985-2014), with over 70% attributable contribution, indicating the significant impact of human influence on the variation of precipitation seasonality. As for the first 30-year period, there is high confidence that AER forcings are the main driver for the decreased SI in GLM. In contrast, the increase in SI during the subsequent 30-year period is largely attributable to GHG forcing. Furthermore, a strong correlation (R = 0.98) between changes in SI and global mean surface air temperature demonstrate the impact of global warming on precipitation seasonality patterns in recent decades, contributing to a 6.19%/K rise in SI, which is clearly a strong thermodynamic response.

The accessibility of local water resources (P-E) depends largely on the precipitation seasonality. At the end of the 21st century, there is a widening contrast in precipitation amounts between wet and dry seasons due to climate warming impact (> 75% model agreement). Notably, wet seasons are projected to experience significant changes. These changes coincide with the projected increase in SI over the GLM with high confidence (100% model agreement) which reveals an increasing disparity between wet and dry seasons. While conventional thermodynamic scaling, commonly known as “wet-get-wetter, dry-get-drier” mechanism, is generally used to model changes in P–E, these mechanisms do not invariably reflect reality. Our study amalgamates insights obtained from changes in AW and SI, thereby presenting a more holistic perspective on seasonal water availability, as AW changes could include shifts towards drier or wetter conditions, while SI elucidate distribution patterns and attributes these trends to wet or dry seasons. Results show that SI changes in the 2080s is expected to regulate seasonal water availability (AW) across GLM, with 'wet (dry) get wetter 'mechanism in regions projecting a

positive (negative) SI and higher AW, while with dry (wet) get drier' mechanism in regions projecting a positive (negative) SI and lower AW.

Overall, our findings, for the first time, identify the anthropogenic (AER and GHG) fingerprint on the precipitation seasonality index, strengthening the confidence (high) in the impact of human influence on precipitation seasonality. Also, based on insight gained using the precipitation seasonality index, we have demonstrated a robust method for analyzing the seasonal patterns of future water availability, which is more comprehensive than the traditional, 'wet get wetter, dry get drier' mechanisms. This finding has significant contribution to our understanding of the water cycle in the context of global climate change. It enhances our ability to anticipate potential hydrological shifts, fortifying global climate resilience and adaption strategies. Future research could apply the results to investigate water cycle changes in different regions and seasons.

5.2. Future Work

Given the research only provided limited analysis of changes in Precipitation Patterns under the impact of climate warming, accompanied by some qualitative discussions regarding the underlying physical mechanisms. Therefore, future work as a follow-up to this thesis will be:

Future Work 1 - The Impact of External Natural Forcing and Internal Variability on Precipitation Extremes

In Chapter 2, our findings present an overview of the detection and attribution analysis of changes in seasonal precipitation at global and regional scales. Results confirm that since the 1950s, external anthropogenic forcings have primarily influenced the observed changes across

hemispherical and regional scales. These insights will contribute to the scientific basis that decision-makers can use to implement effective mitigation policies and adaptation planning against the impact of global warming on extreme precipitation events. For future studies, exploring the impacts of external natural forcings and internal variability on precipitation extremes is imperative. This is because the sole influence of anthropogenic forcings cannot fully explain the observed changes. Interestingly, external natural forcings have been detected in several regions during both two- and three-signal analyses in Chapter 2, suggesting their potential role in driving climate changes - a contrast to prior studies that failed to detect the influence of NAT forcings. This prompts necessary further investigation to comprehensively understand observed changes, resulted from all external forcings. As for the internal variability of extreme weather, factors like the El Niño-Southern Oscillation (ENSO), the Pacific Decadal Oscillation (PDO), and the Atlantic Multidecadal Oscillation (AMO) also have significant impact on global extreme weather patterns. Through these investigations, gaining deeper insights into extreme precipitation could better equip farmers and water resource managers with enhanced preparedness for potential climatic adversities.

Future Work 2 - The Impact of Climate Anomalies on Precipitation Extremes in North America

In Chapter 3, it is with high confidence that extreme precipitation is projected to occur more frequently and in greater severity, especially in high latitudes and coastal regions of North America. These changes will contribute to more severe natural hazards such as floods, droughts, and wildfires, which may not only threaten water storage, conveyance and flood control infrastructure but also challenge the regional food supply, which will affect the social stability. CMIP6 results will help us to develop adaptive measures to mitigate the potential impact of these

changes in precipitation extremes to reduce the vulnerability of some parts of North America, such as the Canadian Prairies, against the impact of droughts and floods and possible structural and non-structural measures against future hazards in floods and droughts. Besides the impact of climate warming, the precipitation regime in terms of intensity, as well as the seasonality and spatiotemporal structure in some parts of North America has been shown to be related to the effect of climate anomalies such as El Niño Southern Oscillation, Pacific Decadal Oscillation, North Atlantic Oscillation, Arctic Oscillation and others (Agel et al. 2018; Deng et al. 2018; Innocenti et al. 2019; Mastrantonas et al. 2021; Gan et al. 2017). Future research should investigate the combined impact of climate warming and climate anomalies to the future precipitation extremes of North America.

Future Work 3 - Consider More Factors that Influence Water Availability

Chapter 4 for the first time identified anthropogenic (AER and GHG) fingerprints on the precipitation seasonality index over global land monsoon regions, reinforcing our confidence (high confidence) in the impact of human influence on precipitation seasonality. As an innovative approach based on the precipitation seasonality index, we have demonstrated a robust method in analyzing the seasonal patterns of future water availability, which is more comprehensive than the simple 'wet get wetter, dry get drier' mechanism (Greve et al., 2014; Held & Soden, 2006; Roderick et al., 2009). This chapter has contributed to our understanding of the water cycle change in the context of global warming impact. It enhances our ability to anticipate potential hydrological shifts, which are essential for us to develop effective global climate resilience and adaptation strategies. In this chapter, we have adopted a simplified approach to estimating water availability, approximated as the difference between monthly precipitation and potential evapotranspiration. It is acknowledged that the actual water

availability is more complex, encompassing factors such as runoff, infiltration, and transboundary inflows, among others. Future research can update findings in Chapter 4 by refining this calculation, thereby enabling a more precise examination of the potential ramifications of water cycle modifications during both wet and dry periods across diverse global regions.

Bibliography

Abbott, T. H., & Cronin, T. W. (2021). Aerosol invigoration of atmospheric convection through increases in humidity. *Science*, **371**(6524), 83–85. https://doi.org/10.1126/science.abc5181

Agel, L., & Barlow, M. (2020). How Well Do CMIP6 Historical Runs Match Observed Northeast U.S. Precipitation and Extreme Precipitation–Related Circulation? *Journal of Climate*, **33**(22), 9835–9848. https://doi.org/10.1175/JCLI-D-19-1025.1

Agel, L., Barlow, M., Feldstein, S. B., & Gutowski, W. J. (2018). Identification of large-scale meteorological patterns associated with extreme precipitation in the US northeast. *Climate Dynamics*, **50**, 1819–1839. https://doi.org/10.1007/s00382-017-3724-8

AghaKouchak, A., Chiang, F., Huning, L. S., Love, C. A., Mallakpour, I., Mazdiyasni, O., Moftakhari, H., Papalexiou, S. M., Ragno, E., & Sadegh, M. (2020). Climate Extremes and Compound Hazards in a Warming World. *Annual Review of Earth and Planetary Sciences*, **48**, 519–548. https://doi.org/10.1146/ANNUREV-EARTH-071719-055228

Akinsanola, A. A., Kooperman, G. J., Reed, K. A., Pendergrass, A. G., & Hannah, W. M. (2020a). Projected changes in seasonal precipitation extremes over the United States in CMIP6 simulations. Environmental Research Letters, **15**(10), 104078. https://doi.org/10.1088/1748-9326/ABB397

Akinsanola, A. A., Kooperman, G. J., Pendergrass, A. G., Hannah, W. H., & Reed, K. A. (2020b). Seasonal representation of extreme precipitation indices over the United States in CMIP6 present-day simulations. *Environmental Research Letters*, **15**(9), 094003. https://doi.org/10.1088/1748-9326/AB92C1

Allen, M., Abdul Halim, S., Antwi-Agyei, P., Aragón-Durand, F., Babiker, M., Bertoldi, P., Bindi, M., & Brown, S. (2019). Technical Summary: Global warming of 1.5°C. An IPCC Special Report on the impacts of global warming of 1.5°C above pre-industrial levels and related global greenhouse gas emission pathways, in the context of strengthening the global response to the threat of

climate change, sustainable development, and efforts to eradicate poverty. Intergovernmental Panel on Climate Change. *Keywan Riahi*. http://pure.iiasa.ac.at/id/eprint/15716/

Allen, M. R., & Stott, P. A. (2003). Estimating signal amplitudes in optimal fingerprinting, part I: Theory. *Climate Dynamics*, **21**, 477–491. https://doi.org/10.1007/S00382-003-0313-9

Almazroui, M., Islam, M. N., Saeed, F., Saeed, S., Ismail, M., Ehsan, M. A., Diallo, I., O'Brien, E., Ashfaq, M., Martínez-Castro, D., Cavazos, T., Cerezo-Mota, R., Tippett, M. K., Gutowski, W. J., Alfaro, E. J., Hidalgo, H. G., Vichot-Llano, A., Campbell, J. D., Kamil, S., … Barlow, M. (2021). Projected Changes in Temperature and Precipitation Over the United States, Central America, and the Caribbean in CMIP6 GCMs. *Earth Systems and Environment*, **5**(1), 1–24. https://doi.org/10.1007/S41748-021-00199-5

Argüeso, D., Evans, J. P., & Fita, L. (2013). Precipitation bias correction of very high resolution regional climate models. *Hydrology and Earth System Sciences*, **17**(11), 4379–4388. https://doi.org/10.5194/HESS-17-4379-2013

Ashfaq, M., Rastogi, D., Mei, R., Shih-Kao, C., Gangrade, S., Naz, B. S., & Touma, D. (2016). High-resolution ensemble projections of near-term regional climate over the continental United States. *Journal of Geophysical Research: Atmospheres*, **121**(17), 9943–9963. https://doi.org/10.1002/2016JD025285

Ayantika, D. C., Krishnan, R., Singh, M., Swapna, P., Sandeep, N., Prajeesh, A. G., & Vellore, R. (2021). Understanding the combined effects of global warming and anthropogenic aerosol forcing on the South Asian monsoon. *Climate Dynamics*, **56**, 1643–1662. https://doi.org/10.1007/s00382-020-05551-5

Bador, M., Boé, J., Terray, L., Alexander, L. V, Baker, A., Bellucci, A., Haarsma, R., Koenigk, T., Moine, M.-P., Lohmann, K., Putrasahan, D. A., Roberts, C., Roberts, M., Scoccimarro, E., Schiemann, R., Seddon, J., Senan, R., Valcke, S., & Vanniere, B. (2020). Impact of higher spatial atmospheric resolution on precipitation extremes over land in global climate models. *Journal of Geophysical Research: Atmospheres*, **125**(13), e2019JD032184. https://doi.org/10.1029/2019JD032184

Bai, H., Xiao, D., Wang, B., Liu, D. L., Feng, P., & Tang, J. (2021). Multi-model ensemble of CMIP6 projections for future extreme climate stress on wheat in the North China plain. *International Journal of Climatology*, **41**(S1), E171–E186. https://doi.org/10.1002/joc.6674

Bal, P. K., Pathak, R., Mishra, S. K., & Sahany, S. (2019). Effects of global warming and solar geoengineering on precipitation seasonality. *Environmental Research Letters*, **14**(3), 034011. https://doi.org/10.1088/1748-9326/aafc7d

Barcikowska, M. J., Kapnick, S. B., Krishnamurty, L., Russo, S., Cherchi, A., & Folland, C. K. (2020). Changes in the future summer Mediterranean climate: Contribution of teleconnections and local factors. *Earth System Dynamics*, **11**(1), 161–181. https://doi.org/10.5194/ESD-11-161-2020

Becker, A., Finger, P., Meyer-Christoffer, A., Rudolf, B., Schamm, K., Schneider, U., & Ziese, M. (2013). A description of the global land-surface precipitation data products of the Global Precipitation Climatology Centre with sample applications including centennial (trend) analysis from 1901-present. *Earth System Science Data*, **5**(1), 71–99. https://doi.org/10.5194/essd-5-71-2013

Berg, N., & Hall, A. (2015). Increased Interannual Precipitation Extremes over California under Climate Change. *Journal of Climate*, **28**(16), 6324–6334. https://doi.org/10.1175/JCLI-D-14-00624.1

Bishop, D. A., Williams, A. P., Seager, R., Fiore, A. M., Cook, B. I., Mankin, J. S., Singh, D., Smerdon, J. E., & Rao, M. P. (2019). Investigating the Causes of Increased Twentieth-Century Fall Precipitation over the Southeastern United States. *Journal of Climate*, **32**(2), 575–590. https://doi.org/10.1175/JCLI-D-18-0244.1

Bonfils, C. J. W., Santer, B. D., Fyfe, J. C., Marvel, K., Phillips, T. J., & Zimmerman, S. R. H. (2020). Human influence on joint changes in temperature, rainfall and continental aridity. *Nature Climate Change*, **10**, 726–731. https://doi.org/10.1038/s41558-020-0821-1

Boucher, O., Servonnat, J., Albright, A. L., Aumont, O., Balkanski, Y., Bastrikov, V., Bekki, S., Bonnet, R., Bony, S., Bopp, L., Braconnot, P., Brockmann, P., Cadule, P., Caubel, A., Cheruy, F.,

Codron, F., Cozic, A., Cugnet, D., D'Andrea, F., … Vuichard, N. (2020). Presentation and Evaluation of the IPSL-CM6A-LR Climate Model. *Journal of Advances in Modeling Earth Systems*, **12**(7), e2019MS002010. https://doi.org/10.1029/2019MS002010

Brogli, R., Sørland, S. L., Kröner, N., & Schär, C. (2019). Causes of future Mediterranean precipitation decline depend on the season. *Environmental Research Letters*, **14**(11), 114017. https://doi.org/10.1088/1748-9326/AB4438

Byrne, M. P., & O'Gorman, P. A. (2018). Trends in continental temperature and humidity directly linked to ocean warming. *Proceedings of the National Academy of Sciences of the United States of America*, **115**(19), 4863–4868. https://doi.org/10.1073/pnas.1722312115

Cao, J., Wang, B., & Ma, L. (2019). Attribution of global monsoon response to the last glacial maximum forcings. *Journal of Climate*, **32**(19), 6589-6605. https://doi.org/10.1175/JCLI-D-18-0871.1

Chen, H., Sun, J., Lin, W., & Xu, H. (2020). Comparison of CMIP6 and CMIP5 models in simulating climate extremes. *Science Bulletin*, **65**(17), 1415–1418. https://doi.org/10.1016/J.SCIB.2020.05.015

Chou, C., Chiang, J. C. H., Lan, C. W., Chung, C. H., Liao, Y. C., & Lee, C. J. (2013). Increase in the range between wet and dry season precipitation. *Nature Geoscience*, **6**(4), 263-267. https://doi.org/10.1038/ngeo1744

Chou, C., Neelin, J. D., Chen, C. A., & Tu, J. Y. (2009). Evaluating the "rich-get-richer" mechanism in tropical precipitation change under global warming. *Journal of Climate*, **22**(8), 1982-2005. https://doi.org/10.1175/2008JCLI2471.1

Christidis, N., & Stott, P. A. (2022). Human Influence on Seasonal Precipitation in Europe. *Journal of Climate*, **35**(15), 5215–5231. https://doi.org/10.1175/JCLI-D-21-0637.1

Chung, E. S., & Soden, B. J. (2017). Hemispheric climate shifts driven by anthropogenic aerosol-cloud interactions. *Nature Geoscience*, **10**(8), 566-571. https://doi.org/10.1038/NGEO2988

Cook, J., Nuccitelli, D., Green, S. A., Richardson, M., Winkler, B., Painting, R., Way, R., Jacobs, P., & Skuce, A. (2013). Quantifying the consensus on anthropogenic global warming in the scientific literature. *Environmental Research Letters*, **8**(2), 024024. https://doi.org/10.1088/1748-9326/8/2/024024

Dai, A. (2013). Increasing drought under global warming in observations and models. *Nature Climate Change*, **3**(1), 52-58. https://doi.org/10.1038/nclimate1633

de Abreu, R. C., Tett, S. F. B., Schurer, A., & Rocha, H. R. (2019). Attribution of Detected Temperature Trends in Southeast Brazil. *Geophysical Research Letters*, **46**(14), 8407–8414. https://doi.org/10.1029/2019GL083003

Deng, S., Sheng, C., Yang, N., Song, L., & Huang, Q. (2020). Anthropogenic forcing enhances rainfall seasonality in global land monsoon regions. *Environmental Research Letters*, **15**(10), 104057. https://doi.org/10.1088/1748-9326/abafd3

Deng, Y., Jiang, W., He, B., Chen, Z., & Jia, K. (2018). Change in Intensity and Frequency of Extreme Precipitation and its Possible Teleconnection With Large-Scale Climate Index Over the China From 1960 to 2015. *Journal of Geophysical Research: Atmospheres*, **123**(4), 2068-2081. https://doi.org/10.1002/2017JD027078

Donat, M. G., Lowry, A. L., Alexander, L. V., O'Gorman, P. A., & Maher, N. (2016). More extreme precipitation in the world's dry and wet regions. *Nature Climate Change*, **6**(5), 508–513. https://doi.org/10.1038/nclimate2941

Dong, L., Leung, L. R., Lu, J., & Gao, Y. (2019). Contributions of Extreme and Non-Extreme Precipitation to California Precipitation Seasonality Changes Under Warming. *Geophysical Research Letters*, **46**(22), 13470–13478. https://doi.org/10.1029/2019GL084225

Dong, L., Leung, L. R., & Song, F. (2018). Future Changes of Subseasonal Precipitation Variability in North America During Winter Under Global Warming. *Geophysical Research Letters*, **45**(22), 12,467-12,476. https://doi.org/10.1029/2018GL079900

Dong, S., Sun, Y., Li, C., Zhang, X., Min, S.-K., & Kim, Y.-H. (2021). Attribution of Extreme Precipitation with Updated Observations and CMIP6 Simulations. *Journal of Climate*, **34**(3), 871–881. https://doi.org/10.1175/JCLI-D-19-1017.1

Dong, T., Zhu, X., Deng, R., Ma, Y., & Dong, W. (2022). Detection and attribution of extreme precipitation events over the Asian monsoon region. *Weather and Climate Extremes*, **38**, 100497. https://doi.org/10.1016/J.WACE.2022.100497

Döscher, R., Acosta, M., Alessandri, A., Anthoni, P., Arsouze, T., Bergman, T., Bernardello, R., Boussetta, S., Caron, L.-P., Carver, G., Castrillo, M., Catalano, F., Cvijanovic, I., Davini, P., Dekker, E., Doblas-Reyes, F. J., Docquier, D., Echevarria, P., Fladrich, U., … Zhang, Q. (2022). The EC-Earth3 Earth system model for the Coupled Model Intercomparison Project 6. *Geoscientific Model Development*, **15**(7), 2973–3020. https://doi.org/10.5194/gmd-15-2973-2022

Dosio, A., Jones, R. G., Jack, C., Lennard, C., Nikulin, G., & Hewitson, B. (2019). What can we know about future precipitation in Africa? Robustness, significance and added value of projections from a large ensemble of regional climate models. *Climate Dynamics*, **53**, 5833–5858. https://doi.org/10.1007/s00382-019-04900-3

Douville, H., Raghavan, K., & Renwick, J. (2021). Chapter 8: Water Cycle Changes. In *Climate Change 2021: The Physical Science Basis. Contribution of Working Group I to the Sixth Assessment Report of the IPCC*.

Duan, J., Ma, Z., Wu, P., Xoplaki, E., Hegerl, G., Li, L., Schurer, A., Guan, D., Chen, L., Duan, Y., & Luterbacher, J. (2019a). Detection of human influences on temperature seasonality from the nineteenth century. *Nature Sustainability*, **2**(6), 484–490. https://doi.org/10.1038/s41893-019-0276-4

Duan, W., Hanasaki, N., Shiogama, H., Chen, Y., Zou, S., Nover, D., Zhou, B., & Wang, Y. (2019b). Evaluation and Future Projection of Chinese Precipitation Extremes Using Large Ensemble High-Resolution Climate Simulations. *Journal of Climate*, **32**(8), 2169–2183. https://doi.org/10.1175/JCLI-D-18-0465.1

Erler, A. R., & Richard Peltier, W. (2016). Projected Changes in Precipitation Extremes for Western Canada based on High-Resolution Regional Climate Simulations. *Journal of Climate*, **29**(24), 8841–8863. https://doi.org/10.1175/JCLI-D-15-0530.1

Eyring, V., Bony, S., Meehl, G. A., Senior, C. A., Stevens, B., Stouffer, R. J., & Taylor, K. E. (2016). Overview of the Coupled Model Intercomparison Project Phase 6 (CMIP6) experimental design and organization. *Geoscientific Model Development*, **9**(5), 1937–1958. https://doi.org/10.5194/gmd-9-1937-2016

Fan, X., Duan, Q., Shen, C., Wu, Y., & Xing, C. (2020a). Global surface air temperatures in CMIP6: historical performance and future changes. *Environmental Research Letters*, **15**(10), 104056. https://doi.org/10.1088/1748-9326/ABB051

Fan, X., Miao, C., Duan, Q., Shen, C., & Wu, Y. (2020b). The Performance of CMIP6 Versus CMIP5 in Simulating Temperature Extremes Over the Global Land Surface. *Journal of Geophysical Research: Atmospheres*, **125**(18), e2020JD033031. https://doi.org/10.1029/2020JD033031

Feng, X., Porporato, A., & Rodriguez-Iturbe, I. (2013). Changes in rainfall seasonality in the tropics. *Nature Climate Change*, ***3***(9), 811-815. https://doi.org/10.1038/nclimate1907

Gan, T. Y., Gobena, A. K., & Wang, Q. (2007). Precipitation of southwestern Canada: Wavelet, scaling, multifractal analysis, and teleconnection to climate anomalies. *Journal of Geophysical Research: Atmospheres*, **112**(D10), 10110. https://doi.org/10.1029/2006JD007157

Gaur, A., Bénichou, N., Armstrong, M., & Hill, F. (2021). Potential future changes in wildfire weather and behavior around 11 Canadian cities. *Urban Climate*, **35**, 100735. https://doi.org/10.1016/J.UCLIM.2020.100735

Ge, F., Zhu, S., Luo, H., Zhi, X., & Wang, H. (2021). Future changes in precipitation extremes over Southeast Asia: Insights from CMIP6 multi-model ensemble. *Environmental Research Letters*, **16**(2), 24013. https://doi.org/10.1088/1748-9326/abd7ad

Gibson, P. B., Waliser, D. E., Lee, H., Tian, B., & Massoud, E. (2019). Climate Model Evaluation in the Presence of Observational Uncertainty: Precipitation Indices over the Contiguous United

States. *Journal of Hydrometeorology*, **20**(7), 1339–1357. https://doi.org/10.1175/JHM-D-18-0230.1

Gidden, M. J., Riahi, K., Smith, S. J., Fujimori, S., Luderer, G., Kriegler, E., Van Vuuren, D. P., Van Den Berg, M., Feng, L., Klein, D., Calvin, K., Doelman, J. C., Frank, S., Fricko, O., Harmsen, M., Hasegawa, T., Havlik, P., Hilaire, J., Hoesly, R., … Takahashi, K. (2019). Global emissions pathways under different socioeconomic scenarios for use in CMIP6: A dataset of harmonized emissions trajectories through the end of the century. *Geoscientific Model Development*, **12**(4), 1443–1475. https://doi.org/10.5194/GMD-12-1443-2019

Giorgi, F., Im, E. S., Coppola, E., Diffenbaugh, N. S., Gao, X. J., Mariotti, L., & Shi, Y. (2011). Higher hydroclimatic intensity with global warming. *Journal of Climate*, **24**(20), 5309-5324. https://doi.org/10.1175/2011JCLI3979.1

Greve, P., Orlowsky, B., Mueller, B., Sheffield, J., Reichstein, M., & Seneviratne, S. I. (2014). Global assessment of trends in wetting and drying over land. *Nature Geoscience*, **7**(10), 716-721. https://doi.org/10.1038/NGEO2247

Haddeland, I., Heinke, J., Biemans, H., Eisner, S., Flörke, M., Hanasaki, N., Konzmann, M., Ludwig, F., Masaki, Y., Schewe, J., Stacke, T., Tessler, Z. D., Wada, Y., & Wisser, D. (2014). Global water resources affected by human interventions and climate change. *Proceedings of the National Academy of Sciences of the United States of America*, **111**(9), 3251-3256. https://doi.org/10.1073/pnas.1222475110

Harris, I., Osborn, T. J., Jones, P., & Lister, D. (2020). Version 4 of the CRU TS monthly high-resolution gridded multivariate climate dataset. *Scientific Data*, **7**(1), 1–18. https://doi.org/10.1038/s41597-020-0453-3

Held, I. M., & Soden, B. J. (2006). Robust responses of the hydrological cycle to global warming. *Journal of Climate*, **19**(21), 5686–5699. https://doi.org/10.1175/JCLI3990.1

Herold, N., Behrangi, A., & Alexander, L. v. (2017). Large uncertainties in observed daily precipitation extremes over land. *Journal of Geophysical Research: Atmospheres*, **122**(2), 668–681. https://doi.org/10.1002/2016JD025842

Huang, X., Stevenson, S., & Hall, A. D. (2020). Future Warming and Intensification of Precipitation Extremes: A "Double Whammy" Leading to Increasing Flood Risk in California. *Geophysical Research Letters*, **47**(16), e2020GL088679. https://doi.org/10.1029/2020GL088679

Innocenti, S., Mailhot, A., Leduc, M., Cannon, A. J., & Frigon, A. (2019). Projected Changes in the Probability Distributions, Seasonality, and Spatiotemporal Scaling of Daily and Subdaily Extreme Precipitation Simulated by a 50-Member Ensemble Over Northeastern North America. *Journal of Geophysical Research: Atmospheres*, **124**(19), 10427–10449. https://doi.org/10.1029/2019JD031210

IPCC. (2022). IPCC, 2022: Summary for Policy Makers. In *Climate Change 2022: Impacts, Adaptation and Vulnerability*. https://doi.org/10.1017/9781009157926.001

Islam, Z., & Gan, T. Y. (2015). Future Irrigation Demand of South Saskatchewan River Basin under the Combined Impacts of Climate Change and El Niño Southern Oscillation. *Water Resources Management*, **29**(6), 2091–2105. https://doi.org/10.1007/S11269-015-0930-1/FIGURES/5

Iturbide, M., Gutiérrez, J., … L. A.-E. S., & 2020, U. (2021). An update of IPCC climate reference regions for subcontinental analysis of climate model data: definition and aggregated datasets. *Earth System Science Data Discussions,* 1–16. https://doi.org/10.5194/essd-12-2959-2020

Iturbide, M., Gutiérrez, J. M., Alves, L. M., Bedia, J., Cerezo-Mota, R., Cimadevilla, E., Cofiño, A. S., Luca, A. Di, Faria, S. H., Gorodetskaya, I. V., Hauser, M., Herrera, S., Hennessy, K., Hewitt, H. T., Jones, R. G., Krakovska, S., Manzanas, R., Martínez-Castro, D., Narisma, G. T., … Vera, C. S. (2020a). An update of IPCC climate reference regions for subcontinental analysis of climate model data: definition and aggregated datasets. *Earth System Science Data*, **12**(4), 2959–2970. https://doi.org/10.5194/essd-12-2959-2020

Iturbide, M., Gutiérrez, J. M., Alves, L. M., Bedia, J., Cerezo-Mota, R., Cimadevilla, E., Cofiño, A. S., Luca, A. Di, Faria, S. H., Gorodetskaya, I. V., Hauser, M., Herrera, S., Hennessy, K., Hewitt, H. T., Jones, R. G., Krakovska, S., Manzanas, R., Martínez-Castro, D., Narisma, G. T., … Vera, C. S. (2020b). An update of IPCC climate reference regions for subcontinental analysis of climate model data: definition and aggregated datasets. *Earth System Science Data*, **12**(4), 2959–2970. https://doi.org/10.5194/ESSD-12-2959-2020

Jones, G. S., Stott, P. A., & Christidis, N. (2013). Attribution of observed historical near-surface temperature variations to anthropogenic and natural causes using CMIP5 simulations. *Journal of Geophysical Research Atmospheres*, **118**(10), 4001-4024. https://doi.org/10.1002/jgrd.50239

Kalnay, E., Kanamitsu, M., Kistler, R., Collins, W., Deaven, D., Gandin, L., Iredell, M., Saha, S., White, G., Woollen, J., Zhu, Y., Chelliah, M., Ebisuzaki, W., Higgins, W., Janowiak, J., Mo, K. C., Ropelewski, C., Wang, J., Leetmaa, A., … Joseph, D. (1996). The NCEP/NCAR 40-year reanalysis project. *Bulletin of the American Meteorological Society*, **77**, 437-471. https://doi.org/10.1175/1520-0477(1996)077<0437:TNYRP>2.0.CO;2

Kharin, V. V., & Zwiers, F. W. (2005). Estimating Extremes in Transient Climate Change Simulations. *Journal of Climate*, **18**(8), 1156–1173. https://doi.org/10.1175/JCLI3320.1

Kim, Y.-H., Min, S.-K., Zhang, X., Sillmann, J., & Sandstad, M. (2020). Evaluation of the CMIP6 multi-model ensemble for climate extreme indices. *Weather and Climate Extremes*, **29**, 100269. https://doi.org/10.1016/j.wace.2020.100269

Kirchmeier-Young, M. C., & Zhang, X. (2020). Human influence has intensified extreme precipitation in North America. *Proceedings of the National Academy of Sciences*, **117**(24), 13308–13313. https://doi.org/10.1073/pnas.1921628117

Knutson, T. R., & Zeng, F. (2018). Model assessment of observed precipitation trends over land regions: Detectable human influences and possible low bias in model trends. *Journal of Climate*, **31**(12), 4617-4637. https://doi.org/10.1175/JCLI-D-17-0672.1

Knutti, R., Allen, M. R., Friedlingstein, P., Gregory, J. M., Hegerl, G. C., Meehl, G. A., Meinshausen, M., Murphy, J. M., Plattner, G.-K., Raper, S. C. B., Stocker, T. F., Stott, P. A., Teng, H., & Wigley, T. M. L. (2008). A Review of Uncertainties in Global Temperature Projections over the Twenty-First Century. *Journal of Climate*, **21**(11), 2651–2663. https://doi.org/10.1175/2007JCLI2119.1

Konapala, G., Mishra, A. K., Wada, Y., & Mann, M. E. (2020). Climate change will affect global water availability through compounding changes in seasonal precipitation and evaporation. *Nature Communications*, **11**(1). https://doi.org/10.1038/s41467-020-16757-w

Konwar, M., Maheskumar, R. S., Kulkarni, J. R., Freud, E., Goswami, B. N., & Rosenfeld, D. (2012). Aerosol control on depth of warm rain in convective clouds. *Journal of Geophysical Research Atmospheres*, **117**(13), 3044. https://doi.org/10.1029/2012JD017585

Kumar, S., Allan, R. P., Zwiers, F., Lawrence, D. M., & Dirmeyer, P. A. (2015). Revisiting trends in wetness and dryness in the presence of internal climate variability and water limitations over land. *Geophysical Research Letters*, **42**(24), 10-867. https://doi.org/10.1002/2015GL066858

Lamarque, J. F., Bond, T. C., Eyring, V., Granier, C., Heil, A., Klimont, Z., Lee, D., Liousse, C., Mieville, A., Owen, B., Schultz, M. G., Shindell, D., Smith, S. J., Stehfest, E., Van Aardenne, J., Cooper, O. R., Kainuma, M., Mahowald, N., McConnell, J. R., … Van Vuuren, D. P. (2010). Historical (1850-2000) gridded anthropogenic and biomass burning emissions of reactive gases and aerosols: Methodology and application. *Atmospheric Chemistry and Physics*, **10**(15), 7017-7039. https://doi.org/10.5194/acp-10-7017-2010

Lan, C. W., Lo, M. H., Chen, C. A., & Yu, J. Y. (2019). The mechanisms behind changes in the seasonality of global precipitation found in reanalysis products and CMIP5 simulations. *Climate Dynamics*, **53**, 4173-4187. https://doi.org/10.1007/s00382-019-04781-6

Lee, J. Y., & Wang, B. (2014). Future change of global monsoon in the CMIP5. *Climate Dynamics*, **42**, 101-119. https://doi.org/10.1007/s00382-012-1564-0

Lee, J.-Y., J. Marotzke, G. Bala, L. Cao, S. Corti, J.P. Dunne, F. Engelbrecht, E. Fischer, J.C. Fyfe, C. Jones, A.Maycock, J. Mutemi, O. Ndiaye, S. Panickal, and T. Z. (2021). Chapter 4: Future global climate: scenario-based projections and near-term information. In *In Climate Change 2021: The Physical Science Basis. Contribution of Working Group I to the Sixth Assessment Report of the Intergovernmental Panel on Climate Change*, 553-672. Cambridge University Press. https://doi.org/10.1017/9781009157896.006.

Li, C., Zwiers, F., Zhang, X., Li, G., Sun, Y., & Wehner, M. (2021). Changes in Annual Extremes of Daily Temperature and Precipitation in CMIP6 Models. *Journal of Climate*, **34**(9), 3441–3460. https://doi.org/10.1175/JCLI-D-19-1013.1

Lin, R., Zhou, T., & Qian, Y. (2014). Evaluation of global monsoon precipitation changes based on five reanalysis datasets. *Journal of Climate*, **27**(3), 1271-1289. https://doi.org/10.1175/JCLI-D-13-00215.1

Liu, C., Ikeda, K., Rasmussen, R., Barlage, M., Newman, A. J., Prein, A. F., Chen, F., Chen, L., Clark, M., Dai, A., Dudhia, J., Eidhammer, T., Gochis, D., Gutmann, E., Kurkute, S., Li, Y., Thompson, G., & Yates, D. (2017). Continental-scale convection-permitting modeling of the current and future climate of North America. *Climate Dynamics*, **49**, 71–95. https://doi.org/10.1007/s00382-016-3327-9

Liu, H., Guo, J., Koren, I., Altaratz, O., Dagan, G., Wang, Y., Jiang, J. H., Zhai, P., & Yung, Y. L. (2019). Non-Monotonic Aerosol Effect on Precipitation in Convective Clouds over Tropical Oceans. *Scientific Reports*, **9**(1), 7809. https://doi.org/10.1038/s41598-019-44284-2

Liu, J., Wang, B., Ding, Q., Kuang, X., Soon, W., & Zorita, E. (2009). Centennial variations of the global monsoon precipitation in the last millennium: Results from ECHO-G model. *Journal of Climate*, **22**(9), 2356-2371. https://doi.org/10.1175/2008JCLI2353.1

Liu, J., Wu, D., Xu, X., Ji, M., Chen, Q., & Wang, X. (2021a). Projection of extreme precipitation induced by Arctic amplification over the Northern Hemisphere. *Environmental Research Letters*, **16**(7), 074012. https://doi.org/10.1088/1748-9326/AC0ACC

Liu, X., Ma, X., Chang, P., Jia, Y., Fu, D., Xu, G., Wu, L., Saravanan, R., & Patricola, C. M. (2021b). Ocean fronts and eddies force atmospheric rivers and heavy precipitation in western North America. *Nature Communications*, **12**(1), 1268. https://doi.org/10.1038/s41467-021-21504-w

Lora, J. M., Mitchell, J. L., Risi, C., & Tripati, A. E. (2017). North Pacific atmospheric rivers and their influence on western North America at the Last Glacial Maximum. *Geophysical Research Letters*, **44**(2), 1051–1059. https://doi.org/10.1002/2016GL071541

Ma, W., Norris, J., & Chen, G. (2020). Projected Changes to Extreme Precipitation Along North American West Coast From the CESM Large Ensemble. *Geophysical Research Letters*, **47**(1), e2019GL086038. https://doi.org/10.1029/2019GL086038

Malik, A., Lan, J., & Lenzen, M. (2016). Trends in Global Greenhouse Gas Emissions from 1990 to 2010. *Environmental Science and Technology*, **50**(9), 4722-4730. https://doi.org/10.1021/acs.est.5b06162

Maloney, E. D., Camargo, S. J., Chang, E., Colle, B., Fu, R., Geil, K. L., Hu, Q., Jiang, X., Johnson, N., Karnauskas, K. B., Kinter, J., Kirtman, B., Kumar, S., Langenbrunner, B., Lombardo, K., Long, L. N., Mariotti, A., Meyerson, J. E., Mo, K. C., … Zhao, M. (2014). North American Climate in CMIP5 Experiments: Part III: Assessment of Twenty-First-Century Projections. *Journal of Climate*, **27**(6), 2230–2270. https://doi.org/10.1175/JCLI-D-13-00273.1

Mao, Y., Wu, G., Xu, G., & Wang, K. (2022). Reduction in Precipitation Seasonality in China from 1960 to 2018. *Journal of Climate*, **35**(1), 227-248. https://doi.org/10.1175/JCLI-D-21-0324.1

Marvel, K., & Bonfils, C. (2013). Identifying external influences on global precipitation. *Proceedings of the National Academy of Sciences of the United States of America*, **110**(48), 19301–19306. https://doi.org/10.1073/pnas.1314382110

Mastrantonas, N., Herrera-Lormendez, P., Magnusson, L., Pappenberger, F., & Matschullat, J. (2021). Extreme precipitation events in the Mediterranean: Spatiotemporal characteristics and connection to large-scale atmospheric flow patterns. *International Journal of Climatology*, **41**(4), 2710-2728. https://doi.org/10.1002/joc.6985

Maussion, F., Scherer, D., Mölg, T., Collier, E., Curio, J., & Finkelnburg, R. (2014). Precipitation seasonality and variability over the Tibetan Plateau as resolved by the high Asia reanalysis. *Journal of Climate*, **27**(5), 1910-1927. https://doi.org/10.1175/JCLI-D-13-00282.1

McAfee, S. A., Russell, J. L., & Goodman, P. J. (2011). Evaluating IPCC AR4 cool-season precipitation simulations and projections for impacts assessment over North America. *Climate Dynamics*, **37**(11–12), 2271–2287. https://doi.org/10.1007/s00382-011-1136-8

Mesinger, F., DiMego, G., Kalnay, E., Mitchell, K., Shafran, P. C., Ebisuzaki, W., Jović, D., Woollen, J., Rogers, E., Berbery, E. H., Ek, M. B., Fan, Y., Grumbine, R., Higgins, W., Li, H., Lin, Y., Manikin, G., Parrish, D., & Shi, W. (2006). North American Regional Reanalysis. *Bulletin of the American Meteorological Society*, **87**(3), 343–360. https://doi.org/10.1175/BAMS-87-3-343

Min, S. K., Zhang, X., Zwiers, F., Shiogama, H., Tung, Y. S., & Wehner, M. (2013). Multimodel Detection and Attribution of Extreme Temperature Changes. *Journal of Climate*, **26**(19), 7430–7451. https://doi.org/10.1175/JCLI-D-12-00551.1

Min, S. K., Zhang, X., Zwiers, F. W., & Hegerl, G. C. (2011). Human contribution to more-intense precipitation extremes. *Nature*, **470**(7334), 378–381. https://doi.org/10.1038/nature09763

Mukherjee, S., Aadhar, S., Stone, D., & Mishra, V. (2018). Increase in extreme precipitation events under anthropogenic warming in India. *Weather and Climate Extremes*, **20**, 45–53. https://doi.org/10.1016/J.WACE.2018.03.005

Murray-Tortarolo, G., Jaramillo, V. J., Maass, M., Friedlingstein, P., & Sitch, S. (2017). The decreasing range between dry- and wet-season precipitation over land and its effect on vegetation primary productivity. *PLoS ONE*, **12**(12), e0190304. https://doi.org/10.1371/journal.pone.0190304

Nanditha, J. S., Kushwaha, A. P., Singh, R., Malik, I., Solanki, H., Chuphal, D. S., Dangar, S., Mahto, S. S., Vegad, U., & Mishra, V. (2023). The Pakistan Flood of August 2022: Causes and Implications. *Earth's Future*, **11**(3), e2022EF003230. https://doi.org/10.1029/2022EF003230

Ning, L., & Bradley, R. S. (2016). NAO and PNA influences on winter temperature and precipitation over the eastern United States in CMIP5 GCMs. *Climate Dynamics*, **46**, 1257–1276. https://doi.org/10.1007/s00382-015-2643-9

Ogungbenro, S. B., & Morakinyo, T. E. (2014). Rainfall distribution and change detection across climatic zones in Nigeria. *Weather and Climate Extremes*, **5**, 1-6. https://doi.org/10.1016/j.wace.2014.10.002

O'Neill, B. C., Kriegler, E., Riahi, K., Ebi, K. L., Hallegatte, S., Carter, T. R., Mathur, R., & van Vuuren, D. P. (2014). A new scenario framework for climate change research: the concept of shared socioeconomic pathways. *Climatic Change*, **122**(3), 387–400. https://doi.org/10.1007/s10584-013-0905-2

O'Neill, B. C., Tebaldi, C., Van Vuuren, D. P., Eyring, V., Friedlingstein, P., Hurtt, G., Knutti, R., Kriegler, E., Lamarque, J. F., Lowe, J., Meehl, G. A., Moss, R., Riahi, K., & Sanderson, B. M. (2016). The Scenario Model Intercomparison Project (ScenarioMIP) for CMIP6. *Geoscientific Model Development*, **9**(9), 3461–3482. https://doi.org/10.5194/GMD-9-3461-2016

Oubeidillah, A. A., Kao, S. C., Ashfaq, M., Naz, B. S., & Tootle, G. (2014). A large-scale, high-resolution hydrological model parameter data set for climate change impact assessment for the conterminous US. *Hydrology and Earth System Sciences*, **18**(1), 67–84. https://doi.org/10.5194/HESS-18-67-2014

Paik, S., Min, S. K., Zhang, X., Donat, M. G., King, A. D., & Sun, Q. (2020). Determining the Anthropogenic Greenhouse Gas Contribution to the Observed Intensification of Extreme Precipitation. *Geophysical Research Letters*, **47**(12), e2019GL086875. https://doi.org/10.1029/2019GL086875

Pal, I., Anderson, B. T., Salvucci, G. D., & Gianotti, D. J. (2013). Shifting seasonality and increasing frequency of precipitation in wet and dry seasons across the U.S. *Geophysical Research Letters*, **40**(15), 4030–4035. https://doi.org/10.1002/GRL.50760

Pascale, S., Boos, W. R., Bordoni, S., Delworth, T. L., Kapnick, S. B., Murakami, H., Vecchi, G. A., & Zhang, W. (2017). Weakening of the North American monsoon with global warming. *Nature Climate Change*, **7**(11), 806-812. https://doi.org/10.1038/nclimate3412

Pascale, S., Lucarini, V., Feng, X., Porporato, A., & Hasson, S. ul. (2015). Analysis of rainfall seasonality from observations and climate models. *Climate Dynamics*, **44**, 3281-3301. https://doi.org/10.1007/s00382-014-2278-2

Pascale, S., Lucarini, V., Feng, X., Porporato, A., & ul Hasson, S. (2016). Projected changes of rainfall seasonality and dry spells in a high greenhouse gas emissions scenario. *Climate Dynamics*, **46**, 1331-1350. https://doi.org/10.1007/s00382-015-2648-4

Pettitt, A. N. (1979). A Non-Parametric Approach to the Change-Point Problem. *Applied Statistics*, **28**(2), 126-135. https://doi.org/10.2307/2346729

Polson, D., & Hegerl, G. C. (2017). Strengthening contrast between precipitation in tropical wet and dry regions. *Geophysical Research Letters*, **44**(1), 365-373. https://doi.org/10.1002/2016GL071194

Pörtner, H. O., Roberts, D. C., Poloczanska, E. S., Mintenbeck, K., Tignor, M., Alegría, A., Craig, M., Langsdorf, S., Löschke, S., Möller, V., & Okem, A. (2022). IPCC, 2022: Summary for Policymakers. In H.O. Pörtner, D.C. Roberts, M. Tignor, E.S. Poloczanska, K. Mintenbeck, A. Alegría, M. Craig, S. Langsdorf, S. Löschke, V. Möller, A. Okem, B. Rama (Eds.), IPCC, 2022: Climate Change 2022: Impacts, Adaptation, and Vulnerability. Contribution of Working Group II to the Sixth Assessment Report of the Intergovernmental Panel on Climate Change. In *Ipcc*. Cambridge University Press. https://doi.org/10.1017/9781009325844.001

Priestley, M. D. K., Ackerley, D., Catto, J. L., Hodges, K. I., McDonald, R. E., & Lee, R. W. (2020). An Overview of the Extratropical Storm Tracks in CMIP6 Historical Simulations. *Journal of Climate*, **33**(15), 6315–6343. https://doi.org/10.1175/JCLI-D-19-0928.1

Rantanen, M., Karpechko, A. Y., Lipponen, A., Nordling, K., Hyvärinen, O., Ruosteenoja, K., Vihma, T., & Laaksonen, A. (2022). The Arctic has warmed nearly four times faster than the globe since 1979. *Communications Earth & Environment*, **3**(1), 1–10. https://doi.org/10.1038/s43247-022-00498-3

Rao, K. K., Kulkarni, A., Patwardhan, S., Kumar, B. V., & Kumar, T. V. L. (2020). Future changes in precipitation extremes during northeast monsoon over south peninsular India. *Theoretical and Applied Climatology*, **142**(1–2), 205–217. https://doi.org/10.1007/s00704-020-03308-y

Riahi, K., van Vuuren, D. P., Kriegler, E., Edmonds, J., O'Neill, B. C., Fujimori, S., Bauer, N., Calvin, K., Dellink, R., Fricko, O., Lutz, W., Popp, A., Cuaresma, J. C., KC, S., Leimbach, M., Jiang, L., Kram, T., Rao, S., Emmerling, J., … Tavoni, M. (2017). The Shared Socioeconomic Pathways and their energy, land use, and greenhouse gas emissions implications: An overview. *Global Environmental Change*, **42***,* 153-168. https://doi.org/10.1016/j.gloenvcha.2016.05.009

Ribes, A., Planton, S., & Terray, L. (2013). Application of regularised optimal fingerprinting to attribution. Part I: Method, properties and idealised analysis. *Climate Dynamics*, **41**(11–12), 2817–2836. https://doi.org/10.1007/s00382-013-1735-7

Ribes, A., Zwiers, F. W., Azaïs, J. M., & Naveau, P. (2017). A new statistical approach to climate change detection and attribution. *Climate Dynamics*, **48**(1–2), 367–386. https://doi.org/10.1007/s00382-016-3079-6

Roberts, M. J., Vidale, P. L., Senior, C., Hewitt, H. T., Bates, C., Berthou, S., Chang, P., Christensen, H. M., Danilov, S., Demory, M. E., Griffies, S. M., Haarsma, R., Jung, T., Martin, G., Minobe, S., Ringler, T., Satoh, M., Schiemann, R., Scoccimarro, E., … Wehner, M. F. (2018). The benefits of global high resolution for climate simulation process understanding and the enabling of stakeholder decisions at the regional scale. *Bulletin of the American Meteorological Society*, **99**(11), 2341-2359. https://doi.org/10.1175/BAMS-D-15-00320.1

Robock, A. (2000). Volcanic eruptions and climate. *Reviews of Geophysics*, **38**(2), 191-219. https://doi.org/10.1029/1998RG000054

Roderick, M. L., Hobbins, M. T., & Farquhar, G. D. (2009). Pan evaporation trends and the terrestrial water balance. II. Energy balance and interpretation. *Geography Compass*, **3**(2), 761-78. https://doi.org/10.1111/j.1749-8198.2008.00214.x

Roderick, M. L., Sun, F., Lim, W. H., & Farquhar, G. D. (2014). A general framework for understanding the response of the water cycle to global warming over land and ocean. *Hydrology and Earth System Sciences*, **18**(5), 1575-1589. https://doi.org/10.5194/hess-18-1575-2014

Rosenfeld, D. (2000). Suppression of rain and snow by urban and industrial air pollution. *Science*, **287**(5459), 1793-1796. https://doi.org/10.1126/science.287.5459.1793

Rosenfeld, D., Lohmann, U., Raga, G. B., O'Dowd, C. D., Kulmala, M., Fuzzi, S., Reissell, A., & Andreae, M. O. (2008). Flood or drought: How do aerosols affect precipitation? *Science*, **321**(5894), 1309–1313. https://doi.org/10.1126/science.1160606

Rowell, D. P. (2009). Projected midlatitude continental summer drying: North America versus Europe. *Journal of Climate*, **22**(11), 2813-2833. https://doi.org/10.1175/2008JCLI2713.1

Ryberg, K. R., Hodgkins, G. A., & Dudley, R. W. (2020). Change points in annual peak streamflows: Method comparisons and historical change points in the United States. *Journal of Hydrology*, **583**, 124307. https://doi.org/10.1016/j.jhydrol.2019.124307

Sarojini, B. B., Stott, P. A., & Black, E. (2016). Detection and attribution of human influence on regional precipitation. *Nature Climate Change*, **6**(7), 669–675. https://doi.org/10.1038/nclimate2976

Schewe, J., Heinke, J., Gerten, D., Haddeland, I., Arnell, N. W., Clark, D. B., Dankers, R., Eisner, S., Fekete, B. M., Colón-González, F. J., Gosling, S. N., Kim, H., Liu, X., Masaki, Y., Portmann, F. T., Satoh, Y., Stacke, T., Tang, Q., Wada, Y., … Kabat, P. (2014). Multimodel assessment of water scarcity under climate change. *Proceedings of the National Academy of Sciences of the United States of America*, **111**(9), 3245-3250. https://doi.org/10.1073/pnas.1222460110

Seong, M. G., Min, S. K., Kim, Y. H., Zhang, X., & Sun, Y. (2021). Anthropogenic Greenhouse Gas and Aerosol Contributions to Extreme Temperature Changes during 1951–2015. *Journal of Climate*, **34**(3), 857–870. https://doi.org/10.1175/JCLI-D-19-1023.1

Sillmann, J., Kharin, V. V., Zhang, X., Zwiers, F. W., & Bronaugh, D. (2013a). Climate extremes indices in the CMIP5 multimodel ensemble: Part 1. Model evaluation in the present climate. *Journal of Geophysical Research Atmospheres*, **118**(4), 1716–1733. https://doi.org/10.1002/jgrd.50203

Sillmann, J., Kharin, V. V, Zwiers, F. W., Zhang, X., & Bronaugh, D. (2013b). Climate extremes indices in the CMIP5 multimodel ensemble: Part 2. Future climate projections. *Journal of Geophysical Research: Atmospheres*, **118**(6), 2473–2493. https://doi.org/10.1002/jgrd.50188

Spinoni, J., Vogt, J. V., Barbosa, P., Dosio, A., McCormick, N., Bigano, A., & Füssel, H. M. (2018). Changes of heating and cooling degree-days in Europe from 1981 to 2100. *International Journal of Climatology*, **38**, e191–e208. https://doi.org/10.1002/JOC.5362

Srivastava, A., Grotjahn, R., & Ullrich, P. A. (2020). Evaluation of historical CMIP6 model simulations of extreme precipitation over contiguous US regions. *Weather and Climate Extremes*, **29**, 100268. https://doi.org/10.1016/j.wace.2020.100268

Srivastava, A. K., Grotjahn, R., Ullrich, P. A., & Zarzycki, C. (2022). Evaluation of precipitation indices in suites of dynamically and statistically downscaled regional climate models over Florida. *Climate Dynamics*, **58**(5–6), 1587–1611. https://doi.org/10.1007/s00382-021-05980-w

Stahle, D. W., Cook, E. R., Burnette, D. J., Torbenson, M. C. A., Howard, I. M., Griffin, D., Villanueva Diaz, J., Cook, B. I., Williams, A. P., Watson, E., Sauchyn, D. J., Pederson, N., Woodhouse, C. A., Pederson, G. T., Meko, D., Coulthard, B., & Crawford, C. J. (2020). Dynamics, Variability, and Change in Seasonal Precipitation Reconstructions for North America. *Journal of Climate*, **33**(8), 3173-3195. https://doi.org/10.1175/JCLI-D-19-0270.1

Stenchikov, G., Robock, A., Ramaswamy, V., Schwarzkopf, M. D., Hamilton, K., & Ramachandran, S. (2002). Arctic Oscillation response to the 1991 Mount Pinatubo eruption: Effects of volcanic aerosols and ozone depletion. *Journal of Geophysical Research Atmospheres*, **107**(D24), ACL-28. https://doi.org/10.1029/2002JD002090

Stephens, G. L., L'Ecuyer, T., Forbes, R., Gettlemen, A., Golaz, J. C., Bodas-Salcedo, A., Suzuki, K., Gabriel, P., & Haynes, J. (2010). Dreary state of precipitation in global models. *Journal of Geophysical Research: Atmospheres*, **115**(D24), 24211. https://doi.org/10.1029/2010JD014532

Stjern, C. W., Lund, M. T., Samset, B. H., Myhre, G., Forster, P. M., Andrews, T., Boucher, O., Faluvegi, G., Fläschner, D., Iversen, T., Kasoar, M., Kharin, V., Kirkevåg, A., Lamarque, J. F., Olivié, D., Richardson, T., Sand, M., Shawki, D., Shindell, D., … Voulgarakis, A. (2019). Arctic Amplification Response to Individual Climate Drivers. *Journal of Geophysical Research: Atmospheres*, **124**(13), 6698–6717. https://doi.org/10.1029/2018JD029726

Stocker, T. F., Qin, D., Plattner, G.-K., Tignor, M., Allen, S. K., Boschung, J., Nauels, A., Xia, Y., Bex, V., & Midgley, P. M. (2013). IPCC, 2013: Climate Change 2013: The Physical Science Basis. Contribution of Working Group I to the Fifth Assessment Report of the Intergovernmental Panel on Climate Change. *IPCC*, *AR5*.

Stouffer, R. J., Eyring, V., Meehl, G. A., Bony, S., Senior, C., Stevens, B., & Taylor, K. E. (2017a). CMIP5 Scientific Gaps and Recommendations for CMIP6. *Bulletin of the American Meteorological Society*, **98**(1), 95–105. https://doi.org/10.1175/BAMS-D-15-00013.1

Stouffer, R. J., Eyring, V., Meehl, G. A., Bony, S., Senior, C., Stevens, B., & Taylor, K. E. (2017b). CMIP5 Scientific Gaps and Recommendations for CMIP6. *Bulletin of the American Meteorological Society*, **98**(1), 95–105. https://doi.org/10.1175/BAMS-D-15-00013.1

Sun, F., Berg, N., Hall, A., Schwartz, M., & Walton, D. (2019). Understanding End-of-Century Snowpack Changes Over California's Sierra Nevada. *Geophysical Research Letters*, **46**(2), 933–943. https://doi.org/10.1029/2018GL080362

Sun, Q., Zwiers, F., Zhang, X., & Yan, J. (2022). Quantifying the Human Influence on the Intensity of Extreme 1- and 5-Day Precipitation Amounts at Global, Continental, and Regional Scales. *Journal of Climate*, **35**(1), 195–210. https://doi.org/10.1175/JCLI-D-21-0028.1

Tabari, H. (2020). Climate change impact on flood and extreme precipitation increases with water availability. *Scientific Reports*, **10**(1), 13768. https://doi.org/10.1038/s41598-020-70816-2

Tan, X., & Gan, T. Y. (2017). Non-stationary analysis of the frequency and intensity of heavy precipitation over Canada and their relations to large-scale climate patterns. *Climate Dynamics*, **48**(9), 2983–3001. https://doi.org/10.1007/s00382-016-3246-9

Tan, X., Gan, T. Y., Chen, S., & Liu, B. (2019). Modeling distributional changes in winter precipitation of Canada using Bayesian spatiotemporal quantile regression subjected to different teleconnections. *Climate Dynamics*, **52**(3), 2105–2124. https://doi.org/10.1007/s00382-018-4241-0

Tan, X., Gan, T. Y., & Shao, D. (2017). Effects of persistence and large-scale climate anomalies on trends and change points in extreme precipitation of Canada. *Journal of Hydrology*, **550**, 453–465. https://doi.org/10.1016/J.JHYDROL.2017.05.028

Tan, X., Wu, X., Huang, Z., Deng, S., Hu, M., & Yew Gan, T. (2022). Detection and attribution of the decreasing precipitation and extreme drought 2020 in southeastern China. *Journal of Hydrology*, **610**, 127996. https://doi.org/10.1016/J.JHYDROL.2022.127996

Tan, X., Wu, X., Huang, Z., Fu, J., Tan, X., Deng, S., Liu, Y., Gan, T. Y., & Liu, B. (2023). Increasing global precipitation whiplash due to anthropogenic greenhouse gas emissions. *Nature Communications*, **14**(1), 2796. https://doi.org/10.1038/s41467-023-38510-9

Tan, X., Wu, Y., Liu, B., & Chen, S. (2020). Inconsistent changes in global precipitation seasonality in seven precipitation datasets. *Climate Dynamics*, **54**, 3091-3108. https://doi.org/10.1007/s00382-020-05158-w

Tang, J., Xu, X., Cai, W., & Wang, C. (2023). Water vapour multi-vortex structure under the interactions of typhoons and mid-low latitude systems during extreme precipitation in North China. *Advances in Climate Change Research*, **14**(1), 116–125. https://doi.org/10.1016/J.ACCRE.2023.01.006

Thornton, P. E., Shrestha, R., Thornton, M., Kao, S.-C., Wei, Y., & Wilson, B. E. (2021). Gridded daily weather data for North America with comprehensive uncertainty quantification. *Scientific Data*, **8**(1), 190. https://doi.org/10.1038/s41597-021-00973-0

Tian, F., Dong, B., Robson, J., & Sutton, R. (2018). Forced decadal changes in the East Asian summer monsoon: the roles of greenhouse gases and anthropogenic aerosols. *Climate Dynamics*, **51**(9–10), 3699–3715. https://doi.org/10.1007/s00382-018-4105-7

Trenberth, K. (2011). Changes in precipitation with climate change. *Climate Research*, **47**(1), 123–138. https://doi.org/10.3354/cr00953

Ullah, S., You, Q., Sachindra, D. A., Nowosad, M., Ullah, W., Bhatti, A. S., Jin, Z., & Ali, A. (2022). Spatiotemporal changes in global aridity in terms of multiple aridity indices: An assessment based on the CRU data. *Atmospheric Research*, **268**, 105998. https://doi.org/10.1016/J.ATMOSRES.2021.105998

Undorf, S., Bollasina, M. A., & Hegerl, G. C. (2018a). Impacts of the 1900–74 Increase in Anthropogenic Aerosol Emissions from North America and Europe on Eurasian Summer Climate. *Journal of Climate*, **31**(20), 8381–8399. https://doi.org/10.1175/JCLI-D-17-0850.1

Undorf, S., Polson, D., Bollasina, M. A., Ming, Y., Schurer, A., & Hegerl, G. C. (2018b). Detectable Impact of Local and Remote Anthropogenic Aerosols on the 20th Century Changes of West African and South Asian Monsoon Precipitation. *Journal of Geophysical Research: Atmospheres*, **123**(10), 4871-4889. https://doi.org/10.1029/2017JD027711

van Vuuren, D. P., Kriegler, E., O'Neill, B. C., Ebi, K. L., Riahi, K., Carter, T. R., Edmonds, J., Hallegatte, S., Kram, T., Mathur, R., & Winkler, H. (2014). A new scenario framework for Climate Change Research: Scenario matrix architecture. *Climatic Change*, **122**, 373-386. https://doi.org/10.1007/s10584-013-0906-1

Walsh, R. P. D., & Lawler, D. M. (1981). Rainfall seasonality: description, spatial patterns and change through time. *Weather*, **36**(7), 201-208. https://doi.org/10.1002/j.1477-8696.1981.tb05400.x

Wang, B., Biasutti, M., Byrne, M. P., Castro, C., Chang, C. P., Cook, K., Fu, R., Grimm, A. M., Ha, K. J., Hendon, H., Kitoh, A., Krishnan, R., Lee, J. Y., Li, J., Liu, J., Moise, A., Pascale, S., Roxy, M. K., Seth, A., … Zhou, T. (2021). Monsoons climate change assessment. *Bulletin of the American Meteorological Society*, **102**(1), E1-E19. https://doi.org/10.1175/BAMS-D-19-0335.1

Wang, B., & Ding, Q. (2008). Global monsoon: Dominant mode of annual variation in the tropics. *Dynamics of Atmospheres and Oceans*, **44**(3–4), 165-183. https://doi.org/10.1016/j.dynatmoce.2007.05.002

Weber B. (2023). 'Something's changed': Summer 2023 is screaming climate change, scientists say. *CBC*. https://www.cbc.ca/news/canada/calgary/climate-change-something-changed-summer-2023-canada-1.692927

Wehner, M. F. (2020). Characterization of long period return values of extreme daily temperature and precipitation in the CMIP6 models: Part 2, projections of future change. *Weather and Climate Extremes*, **30**, 100284. https://doi.org/10.1016/j.wace.2020.100284

Westra, S., Alexander, L. V., & Zwiers, F. W. (2013). Global increasing trends in annual maximum daily precipitation. *Journal of Climate*, **26**(11), 3904-3918. https://doi.org/10.1175/JCLI-D-12-00502.1

Wild, M. (2012). Enlightening global dimming and brightening. *Bulletin of the American Meteorological Society*, **93**(1), 27-37. https://doi.org/10.1175/BAMS-D-11-00074.1

Winter, A., Zanchettin, D., Miller, T., Kushnir, Y., Black, D., Lohmann, G., Burnett, A., Haug, G. H., Estrella-Martinez, J., Breitenbach, S. F. M., Beaufort, L., Rubino, A., & Cheng, H. (2015).

Persistent drying in the tropics linked to natural forcing. *Nature Communications*, **6**(1), 7627. https://doi.org/10.1038/ncomms8627

Xu, H., Chen, H., & Wang, H. (2022). Detectable Human Influence on Changes in Precipitation Extremes Across China. *Earth's Future*, **10**(2), e2021EF002409. https://doi.org/10.1029/2021EF002409

Xu, K., Xu, B., Ju, J., Wu, C., Dai, H., & Hu, B. X. (2019). Projection and uncertainty of precipitation extremes in the CMIP5 multimodel ensembles over nine major basins in China. *Atmospheric Research*, **226**, 122–137. https://doi.org/10.1016/j.atmosres.2019.04.018

Zelinka, M. D., Myers, T. A., McCoy, D. T., Po-Chedley, S., Caldwell, P. M., Ceppi, P., Klein, S. A., & Taylor, K. E. (2020). Causes of Higher Climate Sensitivity in CMIP6 Models. *Geophysical Research Letters*, **47**(1), e2019GL085782. https://doi.org/10.1029/2019GL085782

Zhan, W., He, X., Sheffield, J., & Wood, E. F. (2020). Projected Seasonal Changes in Large-Scale Global Precipitation and Temperature Extremes Based on the CMIP5 Ensemble. *Journal of Climate*, **33**(13), 5651–5671. https://doi.org/10.1175/JCLI-D-19-0311.1

Zhang, W., & Zhou, T. (2020). Increasing impacts from extreme precipitation on population over China with global warming. *Science Bulletin*, **65**(3), 243–252. https://doi.org/10.1016/J.SCIB.2019.12.002

Zhang, X., Alexander, L., Hegerl, G. C., Jones, P., Tank, A. K., Peterson, T. C., Trewin, B., & Zwiers, F. W. (2011). Indices for monitoring changes in extremes based on daily temperature and precipitation data. *WIREs Climate Change*, **2**(6), 851–870. https://doi.org/10.1002/wcc.147

Zhang, X., He, J., Zhang, J., Polyakov, I., Gerdes, R., Inoue, J., & Wu, P. (2012). Enhanced poleward moisture transport and amplified northern high-latitude wetting trend. *Nature Climate Change*, **3**(1), 47–51. https://doi.org/10.1038/nclimate1631

Zhang, X., Wan, H., Zwiers, F. W., Hegerl, G. C., & Min, S. K. (2013). Attributing intensification of precipitation extremes to human influence. *Geophysical Research Letters*, **40**(19), 5252–5257. https://doi.org/10.1002/GRL.51010

Zhang, X., Zwiers, F. W., Hegerl, G. C., Lambert, F. H., Gillett, N. P., Solomon, S., Stott, P. A., & Nozawa, T. (2007). Detection of human influence on twentieth-century precipitation trends. *Nature*, **448**(7152), 461–465. https://doi.org/10.1038/nature06025

Zhang, Z., & Colle, B. A. (2017). Changes in Extratropical Cyclone Precipitation and Associated Processes during the Twenty-First Century over Eastern North America and the Western Atlantic Using a Cyclone-Relative Approach. *Journal of Climate*, **30**(21), 8633–8656. https://doi.org/10.1175/JCLI-D-16-0906.1

Zhao, J., Gan, T. Y., Zhang, G., & Zhang, S. (2023). Projected changes of precipitation extremes in North America using CMIP6 multi-climate model ensembles. *Journal of Hydrology*, **621**, 129598. https://doi.org/10.1016/J.JHYDROL.2023.129598

Zhou, W., Leung, L. R., & Lu, J. (2022). Seasonally Dependent Future Changes in the U.S. Midwest Hydroclimate and Extremes. *Journal of Climate*, **35**(1), 17–27. https://doi.org/10.1175/JCLI-D-21-0012.1

Zhou, X., Huang, G., Wang, X., & Cheng, G. (2018). Future Changes in Precipitation Extremes Over Canada: Driving Factors and Inherent Mechanism. *Journal of Geophysical Research: Atmospheres*, **123**(11), 5783–5803. https://doi.org/10.1029/2017JD027735

Zhu, Y. Y., & Yang, S. (2020). Evaluation of CMIP6 for historical temperature and precipitation over the Tibetan Plateau and its comparison with CMIP5. *Advances in Climate Change Research*, **11**(3), 239–251. https://doi.org/10.1016/J.ACCRE.2020.08.001

Ziese, M., Rauthe-Schöch, A., Becker, A., Finger, P., Rustemeier, E., & Schneider, U. (2021). GPCC Full Data Daily Version 2020 at 1.0°: Daily Land-Surface Precipitation from Rain-Gauges built on GTS-based and Historic Data. *Global Precipitation Climatology Centre (GPCC, Http://Gpcc.Dwd.de/) at Deutscher Wetterdienst*.

Appendix

Appendix for Chapter 2

Table A.2-1 List of CMIP6 model simulations used in this chapter.

No.	Model Name	ALL	NAT	GHG	AER	CTL	Institution	Resolution (Lon×Lat)
1	CanESM5	10	10	10	10	15	Canadian Centre for Climate Modelling and Analysis, Canada	128×64
2	HadGEM3-GC31-LL	5	5	5	5	7	Met Office Hadley Centre, UK	192×144
3	IPSL-CM6A-LR	9	9	9	9	30	Institut Pierre-Simon Laplace, France	144×143
4	MIROC6	10	10	10	10	7	JAMSTEC, AORI, NIES, R-CCS, Japan	256×128
5	MRI-ESM2-0	5	5	5	5	3	Meteorological Research Institute, Japan	320×160
	Sum	39	39	39	39	62		

Table A.2-2 List of the HadEX3 data coverage (%) for 20 CMIP6 domains in NHL. Only the subregions with more than 30% spatial coverage are analyzed in this chapter.

No.	Continent	Acronym	Subregion	Spatial coverage (%)
1	North America	NWN	northwestern North America	20.76
2		WNA	western North America	94.07
3		CNA	central North America	98.41
4		ENA	eastern North America	94.67
5		NCA	north Central America	100
6		SCA	southern Central America	60
7	Europe	NEU	North Europe	97.47
8		WCE	Western & Central Europe	94.68
9		MED	Mediterranean	35.96
10		EEU	eastern Europe	92.02
11	Asia	RAR	Russian Arctic	20.7
12		WSB	West Siberia	51.17
13		ESB	eastern Siberia	67.56
14		RFE	Russian Far East	61.8
15		WCA	western central Asia	31.28
16		ECA	Eastern Central Asia	21.85
17		TIB	Tibetan Plateau	19.19
18		EAS	East Asia	90.61
19		SAS	South Asia	68.39
20	Africa	WAF	Western Africa	79.65

Table A.2-3 D&A results of one-signal analysis for Rx1day

No.	Regions	ANN				MAM				JJA				SON				DJF			
		ALL	GHG	AER	NAT	ALL	GHG	AER	NAT	ALL	GHG	AER	NAT	ALL	GHG	AER	NAT	ALL	GHG	AER	NAT
1	NHL	A	A	A		A	A	A		A	A	A		A	A	A		A	A	A	
2	LR	A	A	A		A	A			A	A	A		A	A	A		A	A	A	
3	HR	A	A	A		A	A	A		A	A	A		A	A	A		A	A	A	
4	WNA	A	A				A								A				A		
5	CNA	A	A				A							A	A			A	A		
6	ENA	A	A	A		A	A	A			A			A	A			A	A		
7	NCA	A	A												A						
8	SCA		A																		
9	NEU	A	A			A	A			A	A			A	A			A	A		
10	WCE	A	A	A		A	A							A	A			A	A		
11	MED									A	A										
12	EEU	A	A	A		A	A			A	A	A		A	A			A	A	A	
13	WSB	A	A	A		A	A			A	A			A	A			A	A		
14	ESB	A	A	A		A	A	A		A	A	A		A	A	A		A	A		
15	RFE	A	A	A		A	A	A		A	A	A		A	A	A		A	A		
16	WCA																				
17	EAS	A	A	A		A	A	A			A	A			A	A			A	A	
18	SAS	A	A								A				A						
19	WAF	A								A				A							

Table A.2-4 D&A results of two-signal analysis for Rx1day

No.	Regions	ANN		MAM		JJA		SON		DJF	
		ANT	NAT	ANT	NAT	ANT	NAT	ANT	NAT	ANT	NAT
1	NHL	A		A		A		A		A	
2	LR	A		A		A		A		A	
3	HR	A		A		A		A	A	A	
4	WNA								D		
5	CNA									D	
6	ENA	A		A				D	D		
7	NCA			A	A						
8	SCA	D	D						D		
9	NEU	D		A		A				D	
10	WCE	A		A				D			
11	MED						D				
12	EEU			A				A		D	A
13	WSB							A		D	
14	ESB	A		D		A	A			A	
15	RFE	A						A			
16	WCA								A		A
17	EAS	A		A		A					A
18	SAS	A						A			
19	WAF	A	D				D		D		

Table A.2-5 D&A results of three-signal analysis for Rx1day

No.	Regions	ANN			MAM			JJA			SON			DJF		
		GHG	AER	NAT	GHG	AER	NAT	GHG	AER	NAT	GHG	AER	NAT	GHG	AER	NAT
1	NHL	A			A			A			D			A		
2	LR	A			D			A			D			A		
3	HR	D						A		A	D		A			
4	WNA								D				A			
5	CNA	A									D			D		
6	ENA	A									D			A		
7	NCA							D						A	D	
8	SCA	D	A										A			
9	NEU	D			A			D		D				A		
10	WCE	D			D						D			A		
11	MED		A			A		A		D		D				
12	EEU	A			A	A					A			A		
13	WSB				A						A			A		
14	ESB	A			D			A	A		A			A		
15	RFE													A		
16	WCA															D
17	EAS												D			A
18	SAS	A			D											
19	WAF		D			D			D	D		D	A			

Table A.2-6 D&A results of one-signal analysis for Rx5day

No.	Regions	ANN				MAM				JJA				SON				DJF			
		ALL	GHG	AER	NAT	ALL	GHG	AER	NAT	ALL	GHG	AER	NAT	ALL	GHG	AER	NAT	ALL	GHG	AER	NAT
1	NHL	A	A	A		A	A	A		A	A	A		A	A	A		A	A	A	
2	LR	A	A	A		A	A			A	A	A		A	A	A		A	A	A	
3	HR	A	A	A		A	A	A			A	A			A			A	A	A	
4	WNA		A																A		
5	CNA		A				A											A	A		
6	ENA	A	A	A		A	A			A	A			A	A			A	A		
7	NCA		A												A						
8	SCA																				
9	NEU	A	A			A	A			A	A			A	A			A	A		
10	WCE	A	A			A	A							A	A			A	A		
11	MED									A	A										
12	EEU	A	A	A		A	A				A			A	A			A	A		
13	WSB	A	A	A		A	A				A			A	A			A	A		
14	ESB	A	A	A		A	A	A		A	A	A		A	A	A		A	A		
15	RFE	A	A	A		A	A			A	A	A			A	A		A	A		
16	WCA																				
17	EAS		A	A			A	A			A	A		A	A	A			A	A	
18	SAS		A								A				A	A					
19	WAF	A												A							

Table A.2-7 D&A results of two-signal analysis for Rx5day

No.	Regions	ANN		MAM		JJA		SON		DJF	
		ANT	NAT	ANT	NAT	ANT	NAT	ANT	NAT	ANT	NAT
1	NHL	A		A				A		A	
2	LR	A		A				A		A	
3	HR	D		A					A		A
4	WNA								A		
5	CNA									D	
6	ENA	D		A				A	A		
7	NCA				D						
8	SCA							A	D		
9	NEU	D		D		A	D			D	
10	WCE	A						D			
11	MED										
12	EEU			A	A					A	
13	WSB							A		A	
14	ESB			D		A	A			A	
15	RFE		A					A			
16	WCA								A		A
17	EAS		A			A	D				D
18	SAS										
19	WAF	A	D				A		D		

Table A.2-8 D&A results of three-signal analysis for Rx5day

No.	Regions	ANN			MAM			JJA			SON			DJF		
		GHG	AER	NAT	GHG	AER	NAT	GHG	AER	NAT	GHG	AER	NAT	GHG	AER	NAT
1	NHL	A			A			A			A					
2	LR	A			D						A			A		
3	HR	D	D		D						D			A		D
4	WNA	A														
5	CNA	A									D			A		
6	ENA	D						D			D			A		
7	NCA						D				A			A	A	
8	SCA	D											A			D
9	NEU	D			D					D				A		
10	WCE	D			A						D			A		
11	MED		A			A			A							
12	EEU				A		A							A		
13	WSB				A						A					
14	ESB	A			D			A	A		A			A		
15	RFE			D						D						
16	WCA												A			D
17	EAS			D			A						A			D
18	SAS	A			A											
19	WAF		D	D					D	D		D			A	

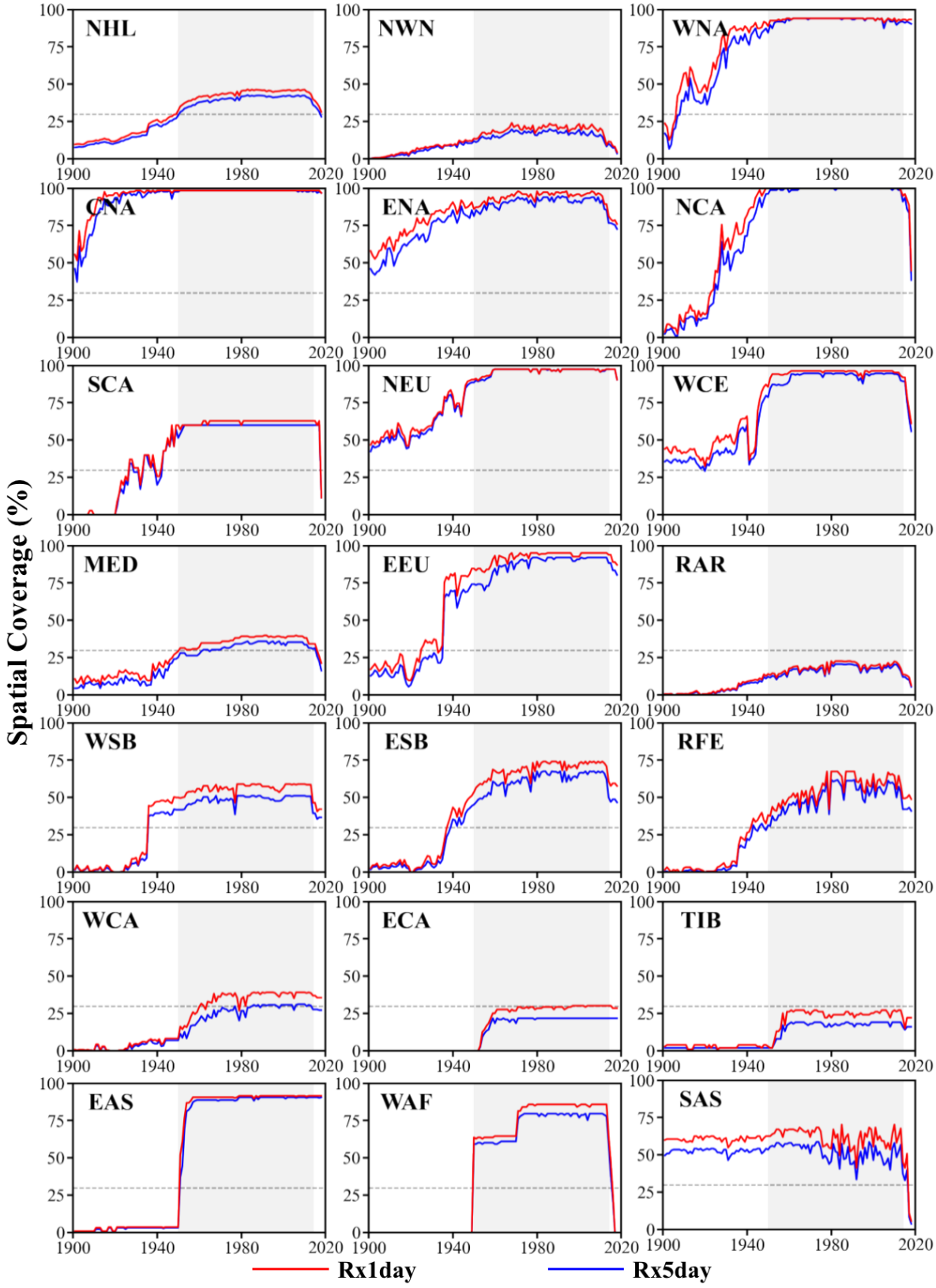

Figure A.2-1 Percentage change of spatial coverage for Rx1day (green) and Rx5day (red) in HadEx3 datasets from 1900 to 2020. Grey rectangle in each subplot is the study period, 1950-2014.

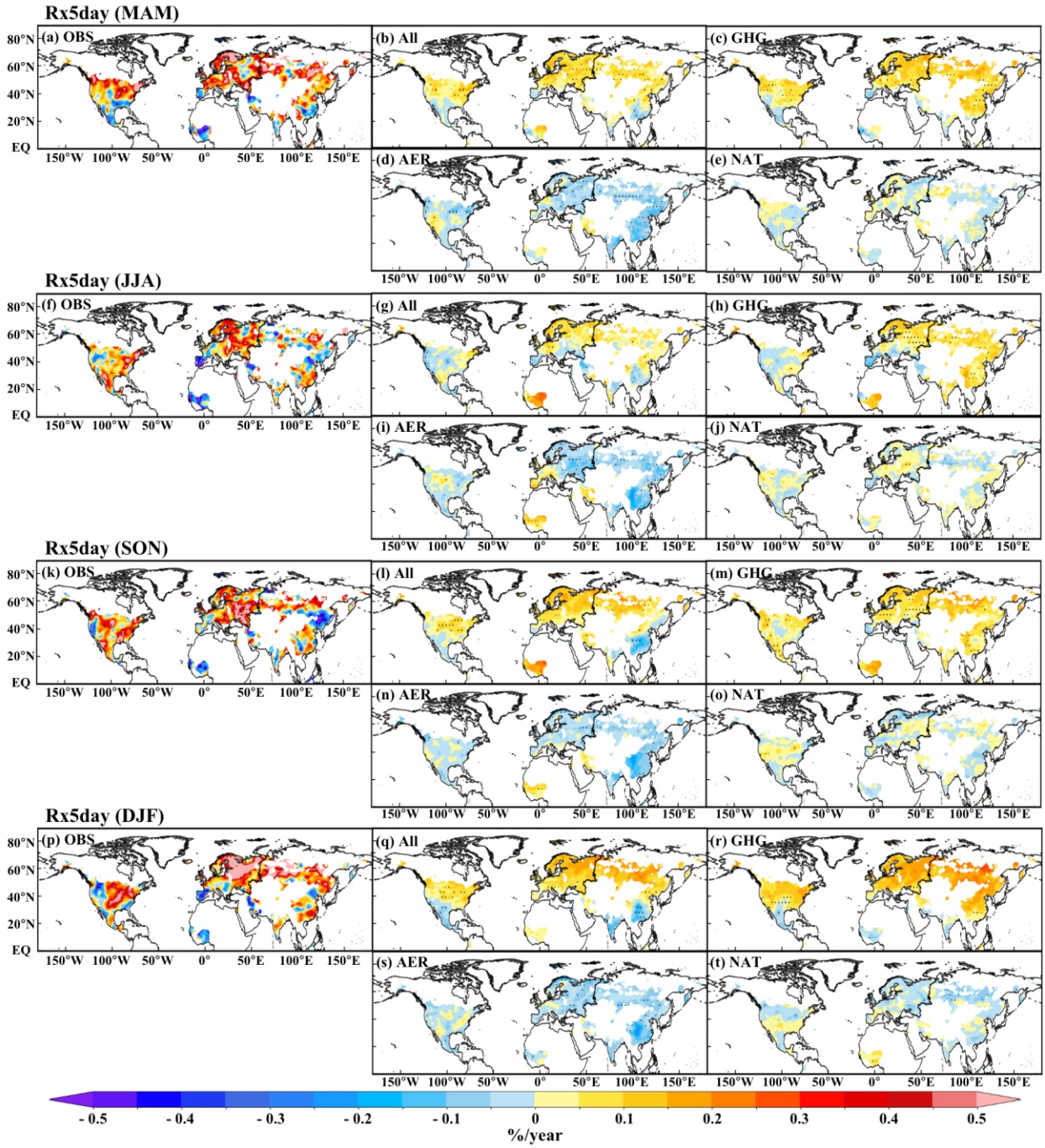

Figure A.2-2 Same as Figure 2-2, but for Rx5day.

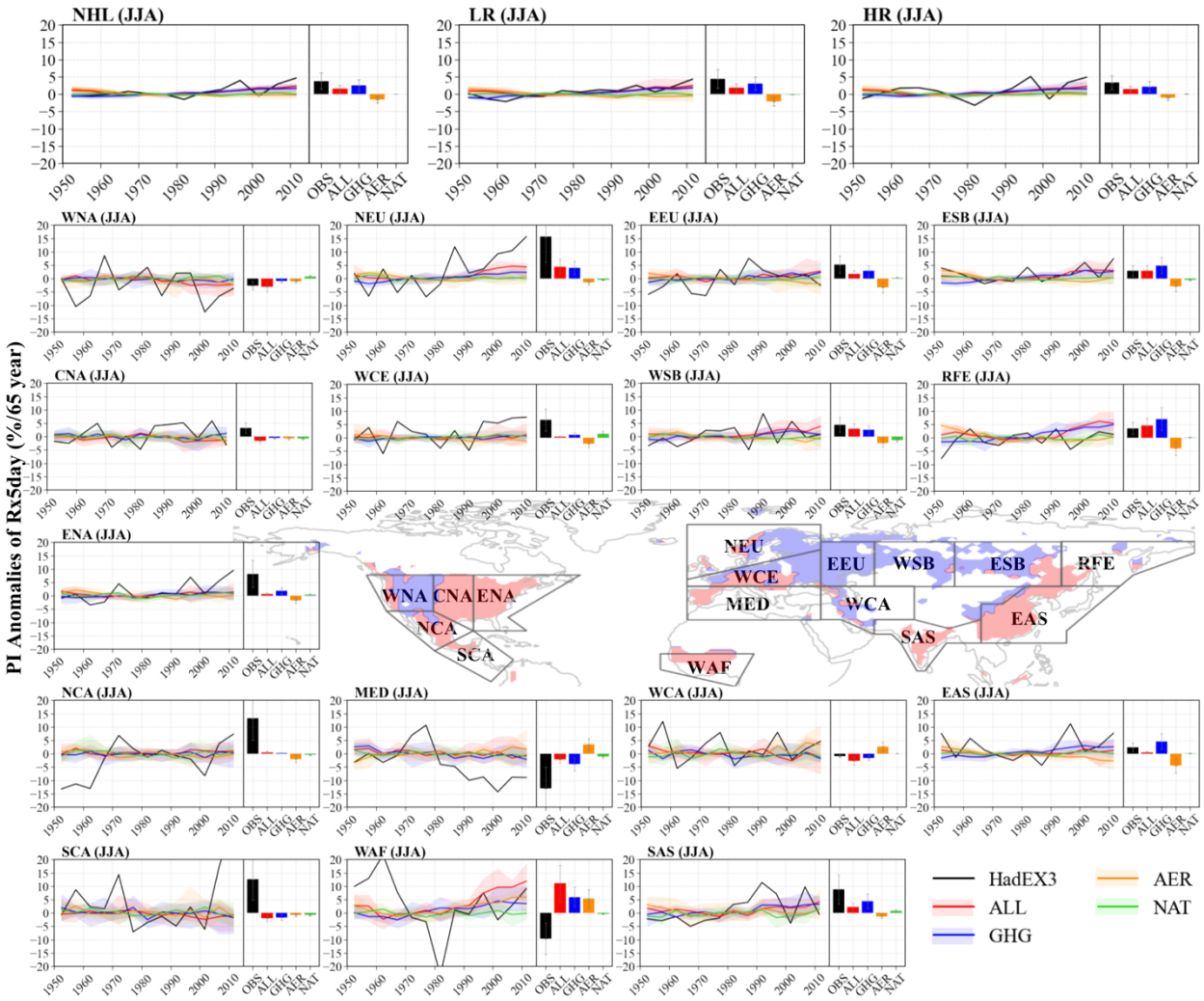

Figure A.2-3 Same as Figure 2-3, but for Rx5day in JJA.

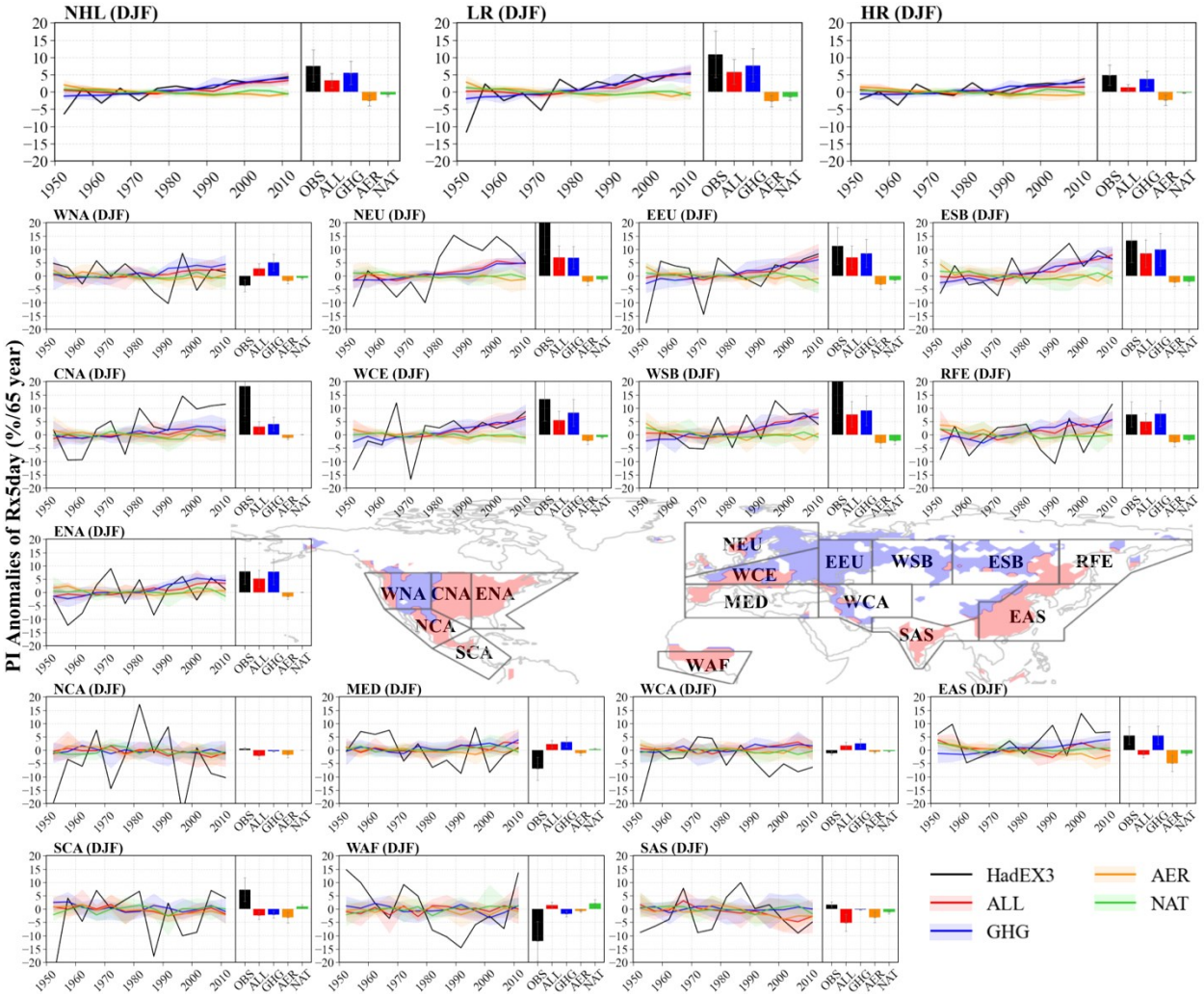

Figure A.2-4 Same as Figure 2-3, but for Rx5day in DJF.

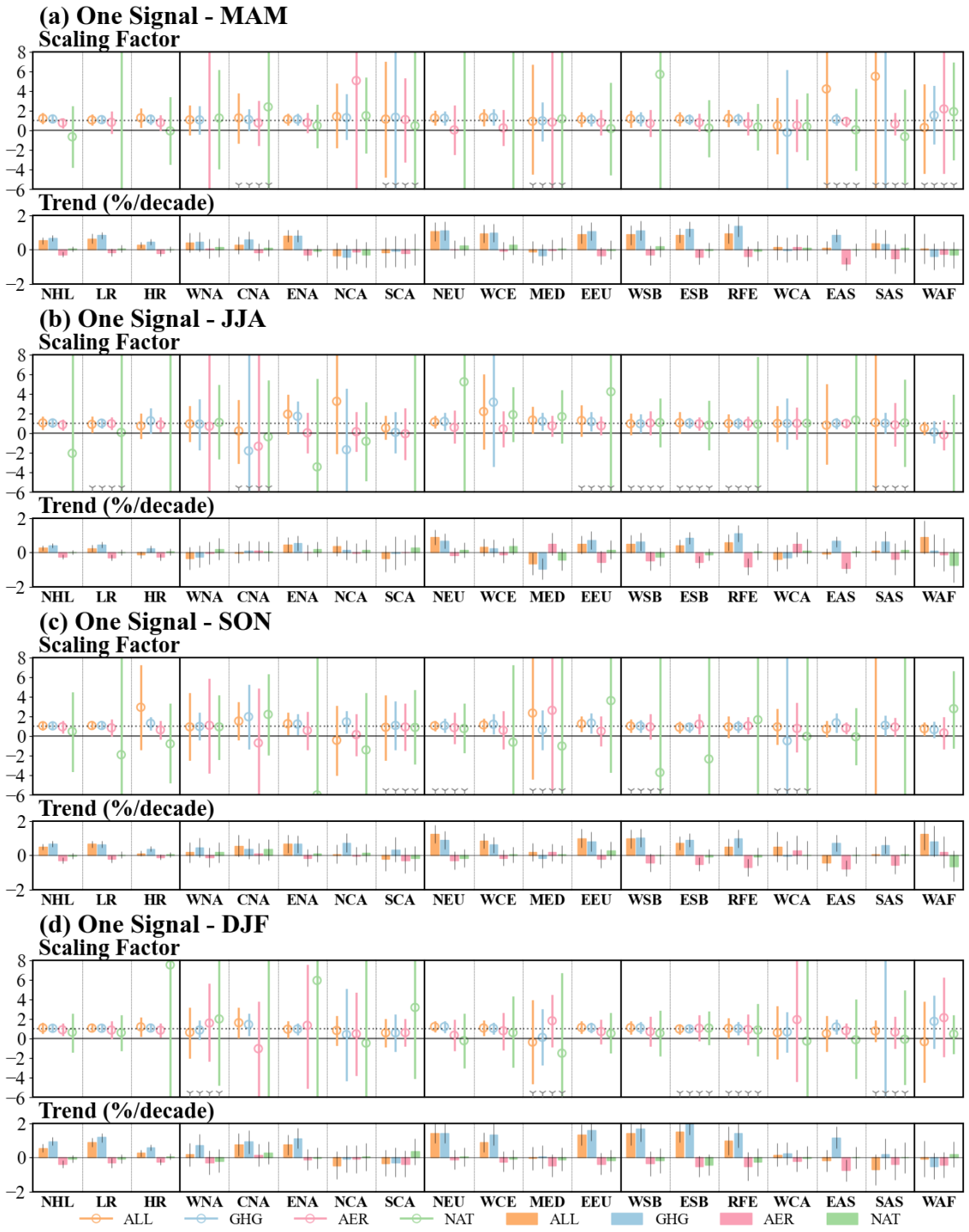

Figure A.2-5 a–e, scaling factors (upper subplots) and attributable contribution (lower subplots) derived from one-signal analysis (ALL (orange), GHG (blue), ARE (pink) and NAT (green)) in MAM (a), JJA (b), SON (c) and DJF (d) for Rx5day. The confidence intervals for the scaling factors and attributable contribution are 10–90%.

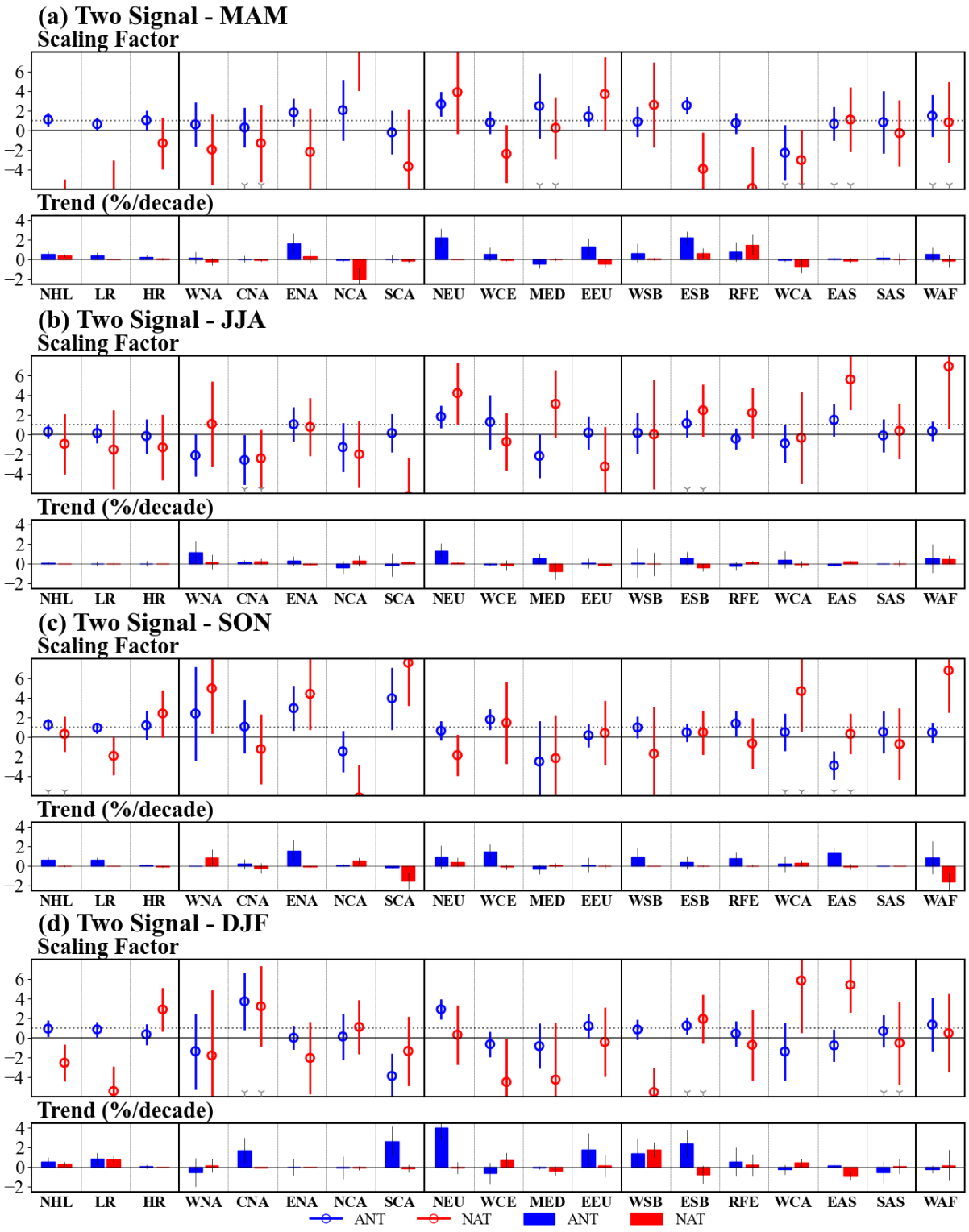

Figure A.2-6 Same as Figure A.2-5, but for two-signal analysis, ANT (blue) and NAT (red).

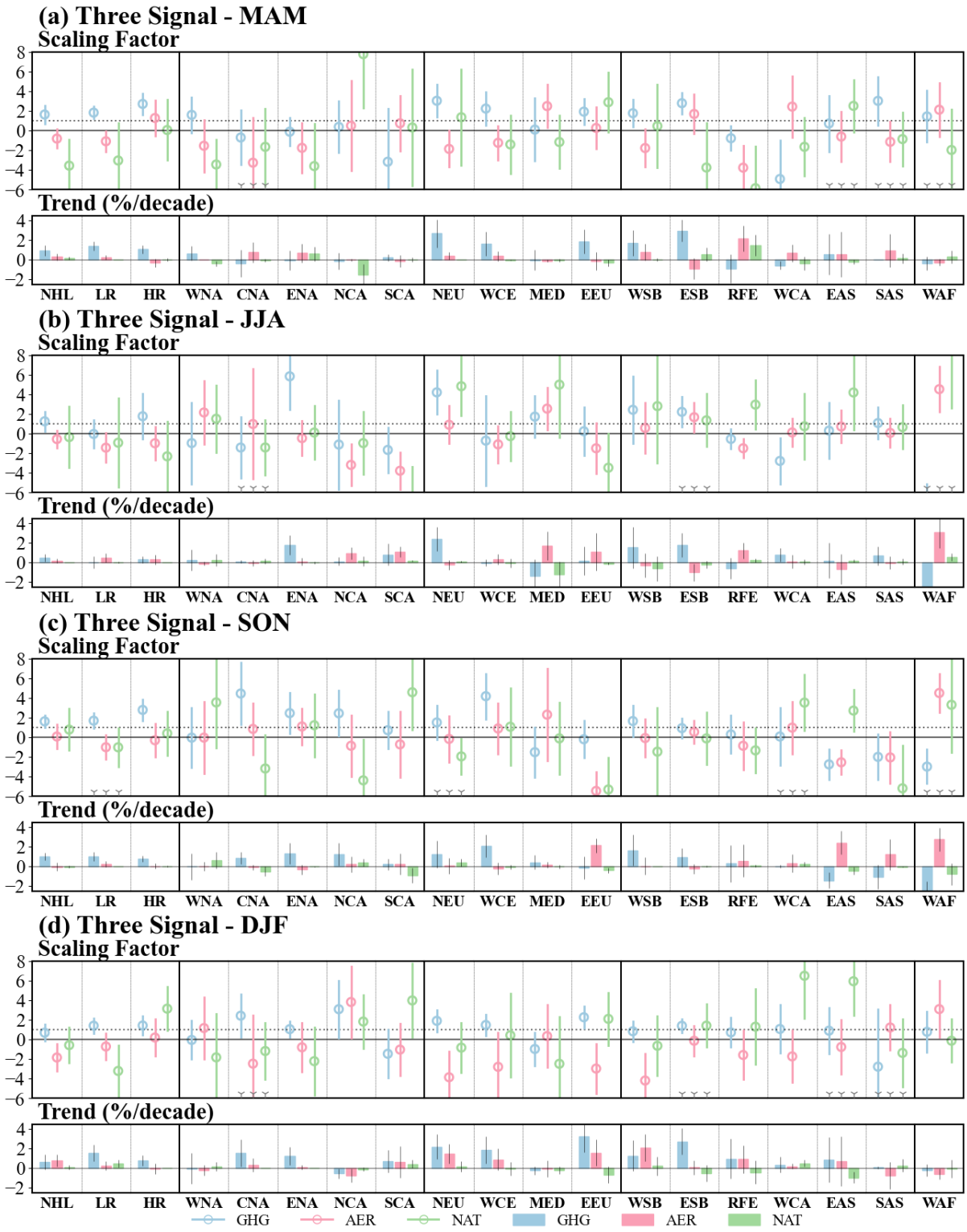

Figure A.2-7 Same as Figure A.2-5, but for three-signal analysis, GHG (blue), AER (pink) and NAT (green).

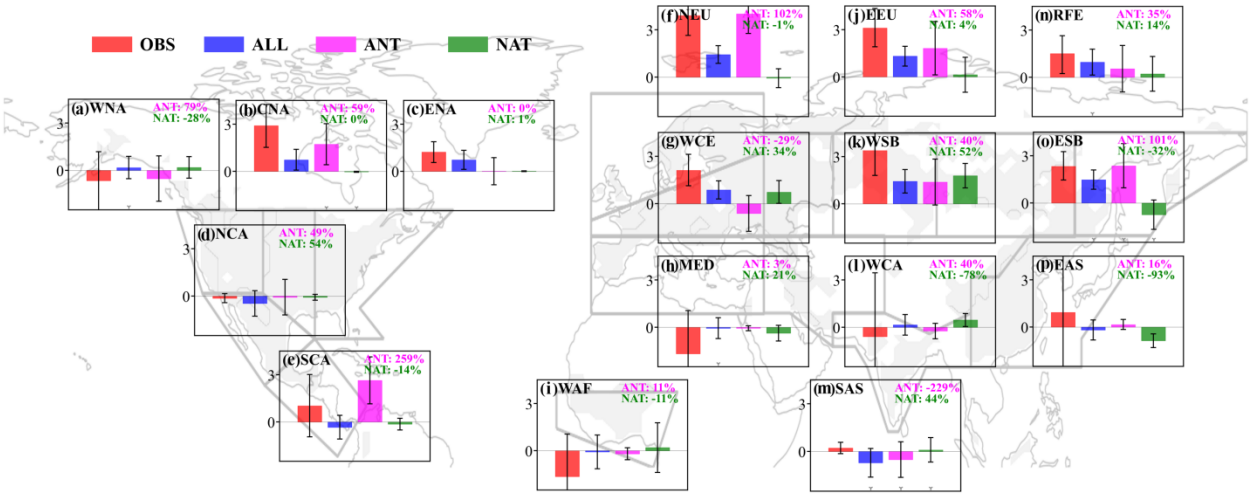

Figure A.2-8. Same as Figure 2-10, but for Rx5day.

Below is the Results of the annual analysis for chapter 2:

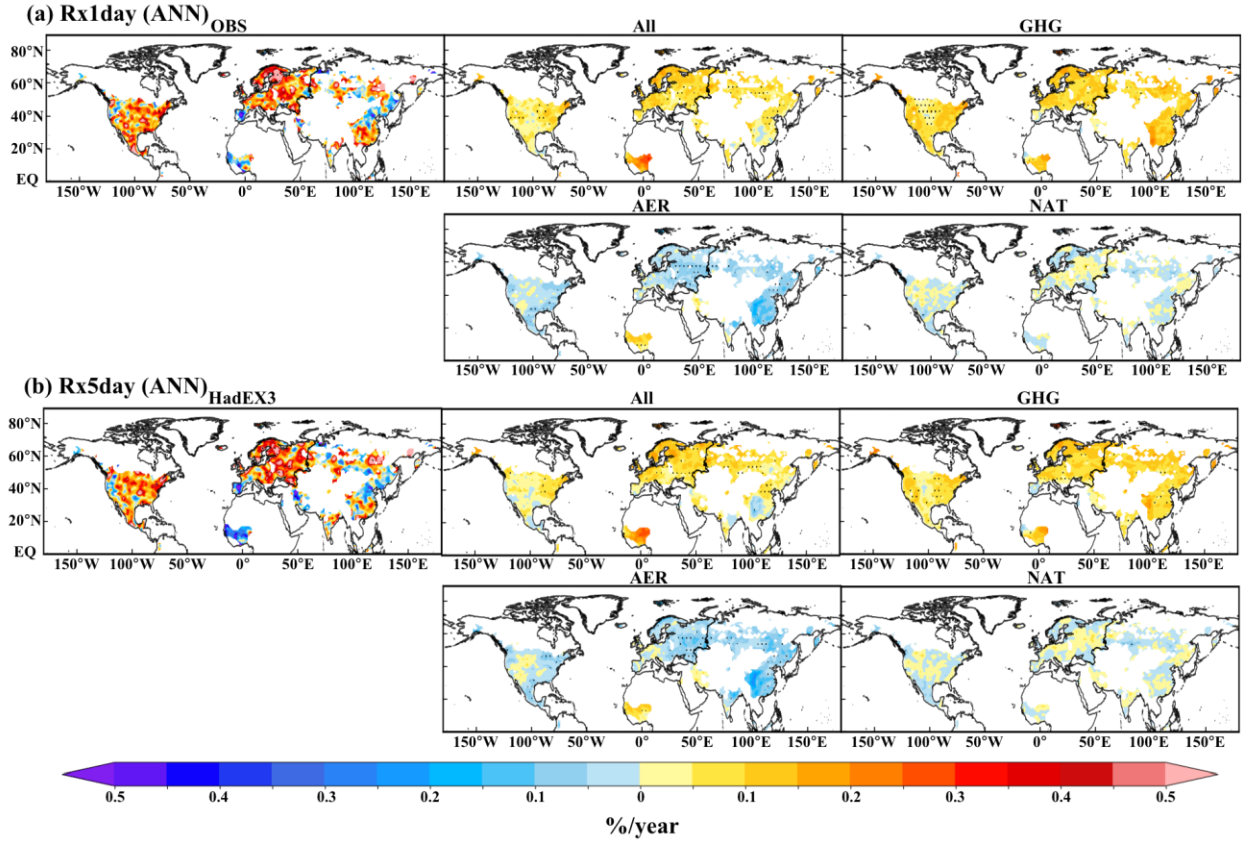

Figure A.2-9 Same as Figure 2-2, but for Rx1day and Rx5day in ANN.

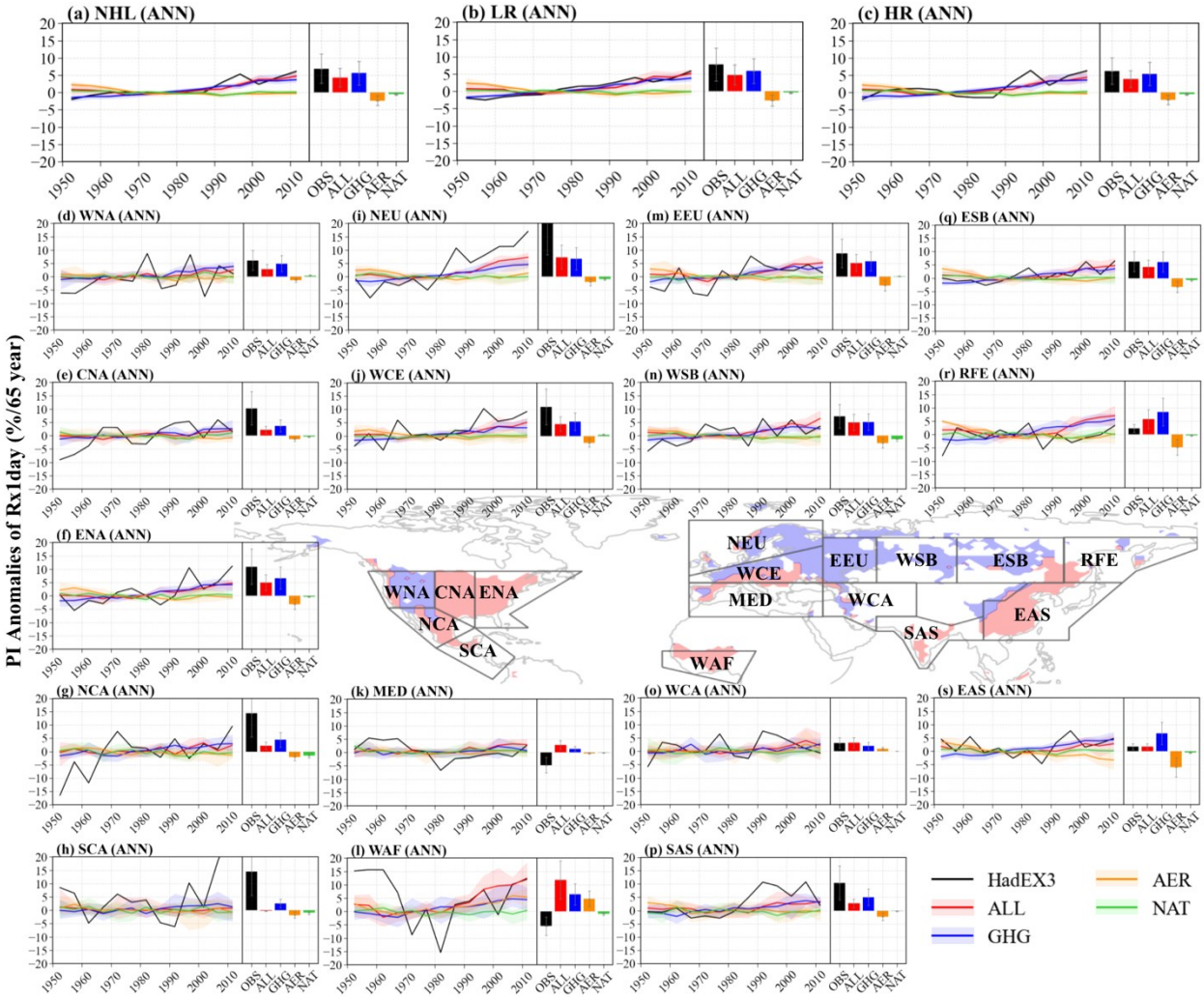

Figure A.2-10 Same as Figure 2-3, but for Rx1day in ANN.

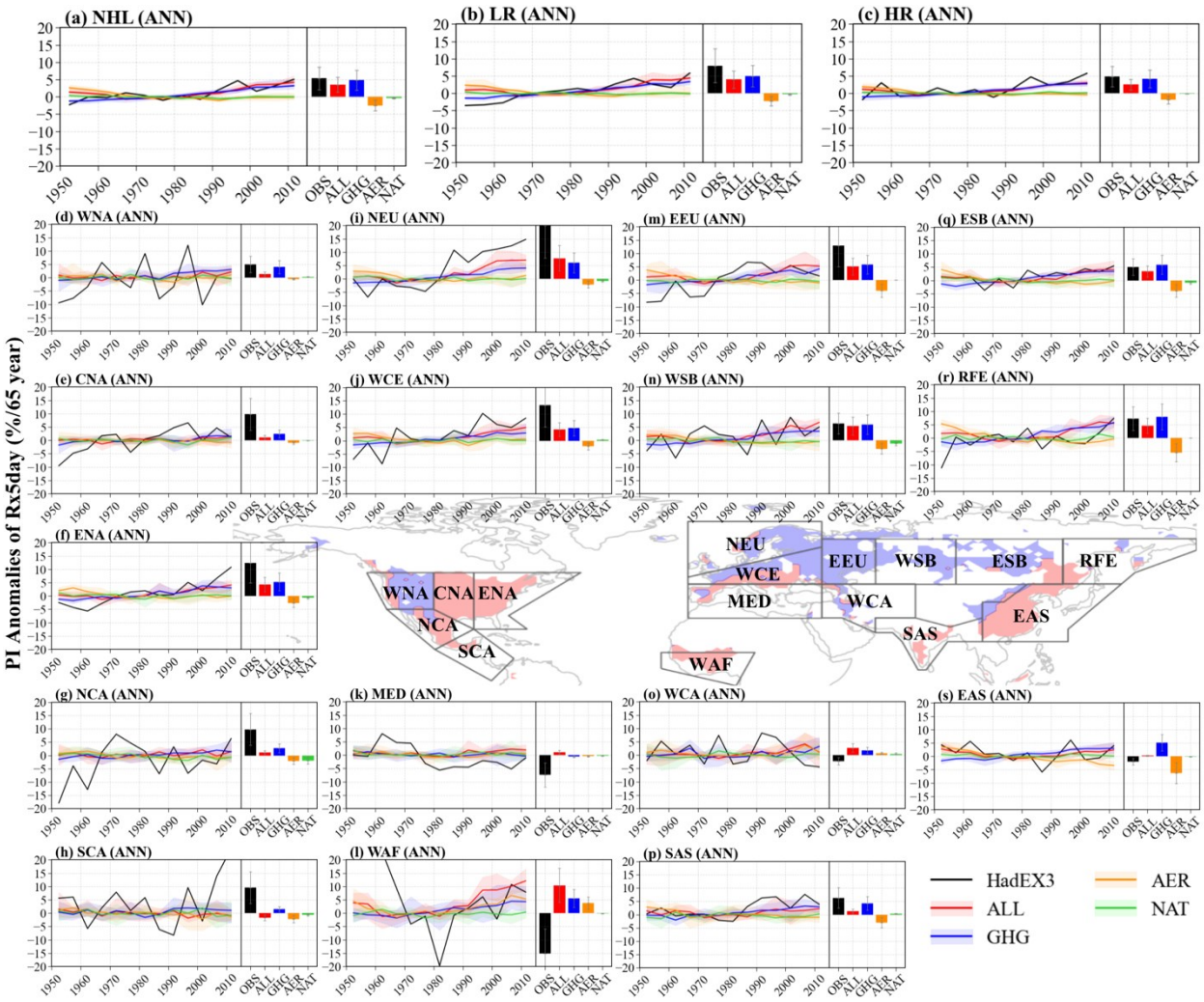

Figure A.2-11 Same as Figure 2-3, but for Rx5day in ANN.

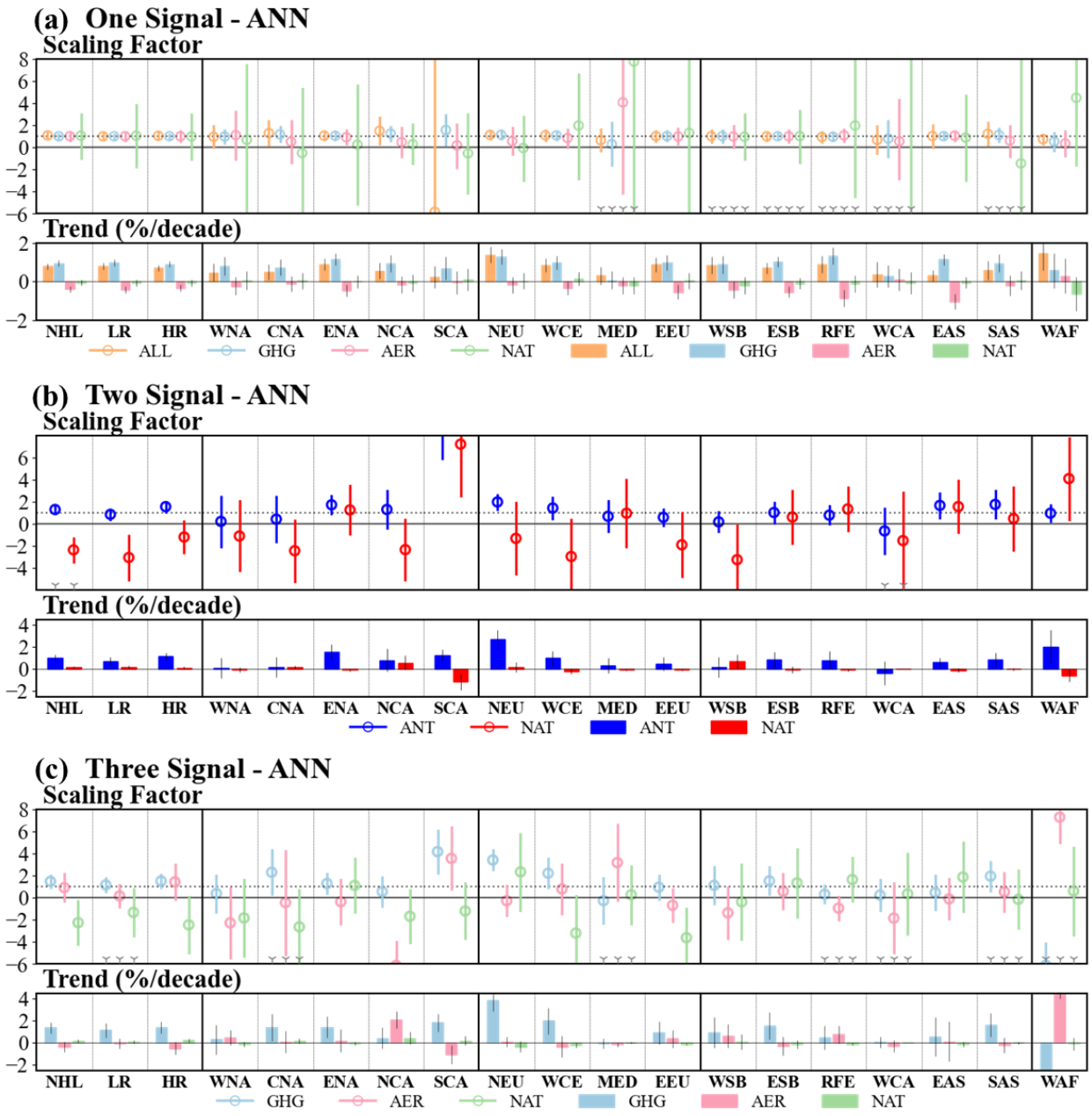

Figure A.2-12 (a) is same as Figure A.2-5, (b) is same as Figure A.2-6, (c) is same as Figure A.2-7, but for Rx1day in ANN.

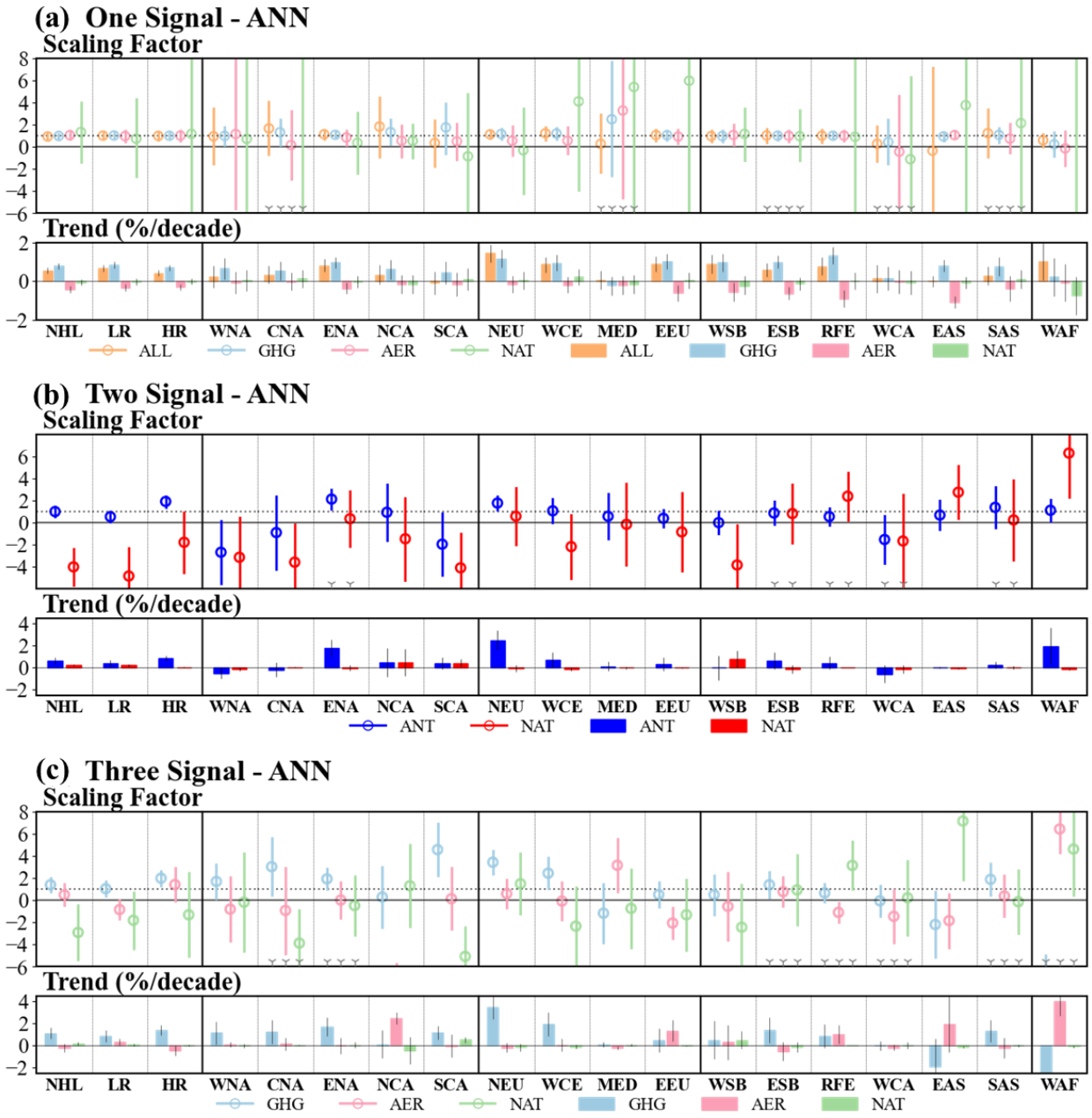

Figure A.2-13 (a) is same as Figure A.2-5, (b) is same as Figure A.2-6, (c) is same as Figure A.2-7, but for Rx5day in ANN.

Appendix for Chapter 3

Table A.3-1 Information of the eighteen Global Climate Models of CMIP6 used in this chapter

S/N	Model	Organization	Horizontal Resolution (km)	Nominal Resolution (Lon×Lat)	Run
1	ACCESS-CM2	Commonwealth Scientific and Industrial	250km	192×144	r1i1p1f1
2	ACCESS-ESM1-5	Research Organisation and Australian Research Council Centre of Excellence for Climate System Science, Australia	250km	192×145	r1i1p1f1
3	BCC-CSM2-MR	Beijing Climate Center, China Meteorological Administration, China	100km	320×160	r1i1p1f1
4	EC-Earth3	EC-Earth-Consortium	100km	512×256	r1i1p1f1
5	FGOALS-g3	Chines Academy of Sciences, China	250km	180×80	r1i1p1f1
6	GFDL-ESM4	Geophysical Fluid Dynamics Laboratory, USA	100km	288×180	r1i1p1f1
7	INM-CM4-8	nstitute for Numerical Mathematics,	100km	180×120	r1i1p1f1
8	INM-CM5-0	Russia	100km	180×120	r1i1p1f1
9	IPSL-CM6A-LR	Institut Pierre-Simon Laplace, France	250km	144×143	r1i1p1f1
10	KACE-1-0-G	National Institute of Meteorological Science/Korea Meteorological Administration, Korea	250km	192×144	r1i1p1f1
11	MIROC6	JAMSTEC, AORI, NIES, R-CCS, Japan	250km	256×128	r1i1p1f1
12	MPI-ESM1-2-HR	Max Planck Institute for Meteorology, Germany	100km	384×192	r1i1p1f1
13	MPI-ESM1-2-LR		250km	192×96	r1i1p1f1
14	MRI-ESM2-0	Meteorological Research Institute, Japan	100km	320×160	r1i1p1f1
15	NESM3	Nanjing University of Information Science and Technology, China	250km	192×96	r1i1p1f1
16	NorESM2-LM	NorESM climate modeling Consortium of CICERO, MET-Norway, NERSC, NILU, UiB, UiO and UNI, Norway	250km	144×96	r1i1p1f1
17	NorESM2-MM		100km	288×192	r1i1p1f1
18	UKESM1-0-LL		100km		r1i1p1f1

Table A.3-2 Ten extreme precipitation indices used in this chapter

NO.	Label	Index Name	Index Definition	Units
1	Rx1day	Max 1 day precipitation	Let RR_{ij} be the daily precipitation amount on day i in period j. The maximum 1 day value for period j are: $Rx1day_j = \max(RR_{ij})$	mm
2	Rx5day	Max consecutive 5-day precipitation	Let RR_{kj} be the precipitation amount for the 5 day interval ending k, period j. Then maximum 5 day values for period j are: $Rx5day_j = \max(RR_{kj})$	mm
3	R10mm	Heavy precipitation days	Let RR_{ij} be the daily precipitation amount on day i in period j. Count the number of days where $RR_{ij} > 10$ mm	days
4	R20mm	Very heavy precipitation days	Let RR_{ij} be the daily precipitation amount on day i in period j. Count the number of days where $RR_{ij} > 20$ mm	days
5	CDD	Consecutive dry days	Let RR_{ij} be the daily precipitation amount on day i in period j. Count the largest number of consecutive days where $RR_{ij} < 1$ mm	days
6	CWD	Consecutive wet days	Let RR_{ij} be the daily precipitation amount on day i in period j. Count the largest number of consecutive days where $RR_{ij} > 1$ mm	days
7	R95p	Very wet days	Let RR_{wj} be the daily precipitation amount on a wet day w ($RR \geq 1$ mm) in period i and let $RR_{wn}95$ be the 95th percentile of precipitation on wet days in the 1981–2010 period. If W represents the number of wet days in the period, then: $R95p_j = \sum_{w=1}^{W} RR_{wj}$, where $RR_{wj} > RR_{wn}95$	mm
8	R99p	Extremely wet days	Let RR_{wj} be the daily precipitation amount on a wet day w ($RR \geq 1$ mm) in period i and let $RR_{wn}99$ be the 99th percentile of precipitation on wet days in the 1981–2010 period. If W represents the number of wet days in the period, then: $R99pj = \sum_{w=1}^{W} RR_{wj}$, where $RR_{wj} > RR_{wn}99$	mm
9	SDII	Simple daily intensity	Let RR_{wj} be the daily precipitation amount on wet days, w($RR \geq 1$ mm) in period j. If W represents number of wet days in j, then: $SDII_j = \frac{\sum_{w=1}^{W} RR_{wj}}{W}$	mm
10	PRCPTOT	Total wet-day precipitation	Let RRij be the daily precipitation amount on day i in period j. If I represents the number of days in j, then: $PRCPTOTj = \sum_{i=1}^{I} RR_{ij}$	mm

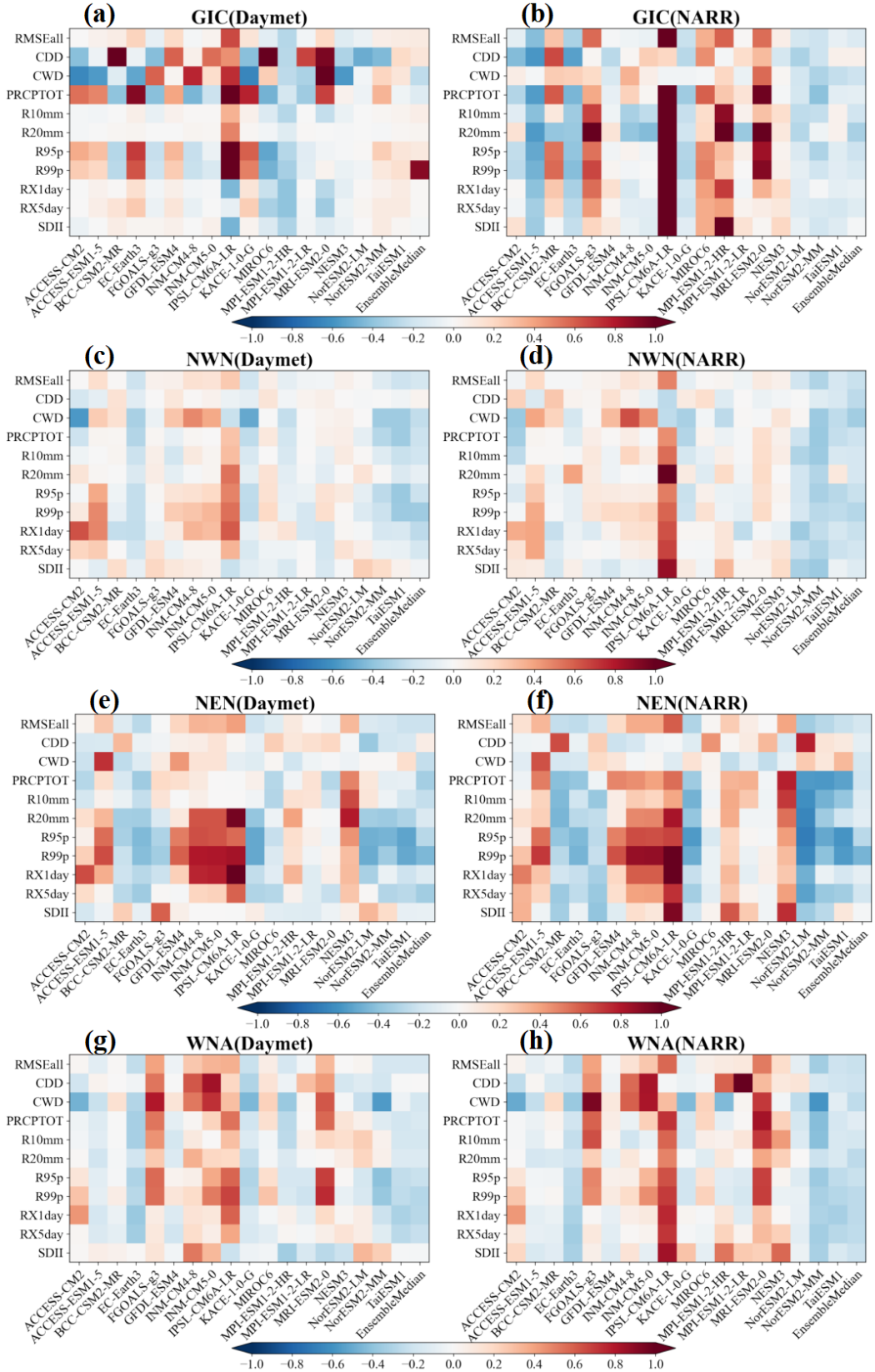
(a) GIC(Daymet)
(b) GIC(NARR)
(c) NWN(Daymet)
(d) NWN(NARR)
(e) NEN(Daymet)
(f) NEN(NARR)
(g) WNA(Daymet)
(h) WNA(NARR)
RMSEall
CDD
CWD
PRCPTOT
R10mm
R20mm
R95p
R99p
RX1day
RX5day
SDII
ACCESS-CM2
ACCESS-ESM1-5
BCC-CSM2-MR
EC-Earth3
FGOALS-g3
GFDL-ESM4
INM-CM4-8
INM-CM5-0
IPSL-CM6A-LR
KACE-1-0-G
MIROC6
MPI-ESM1-2-HR
MPI-ESM1-2-LR
MRI-ESM2-0
NESM3
NorESM2-LM
NorESM2-MM
TaiESM1
EnsembleMedian
−1.0 −0.8 −0.6 −0.4 −0.2 0.0 0.2 0.4 0.6 0.8 1.0

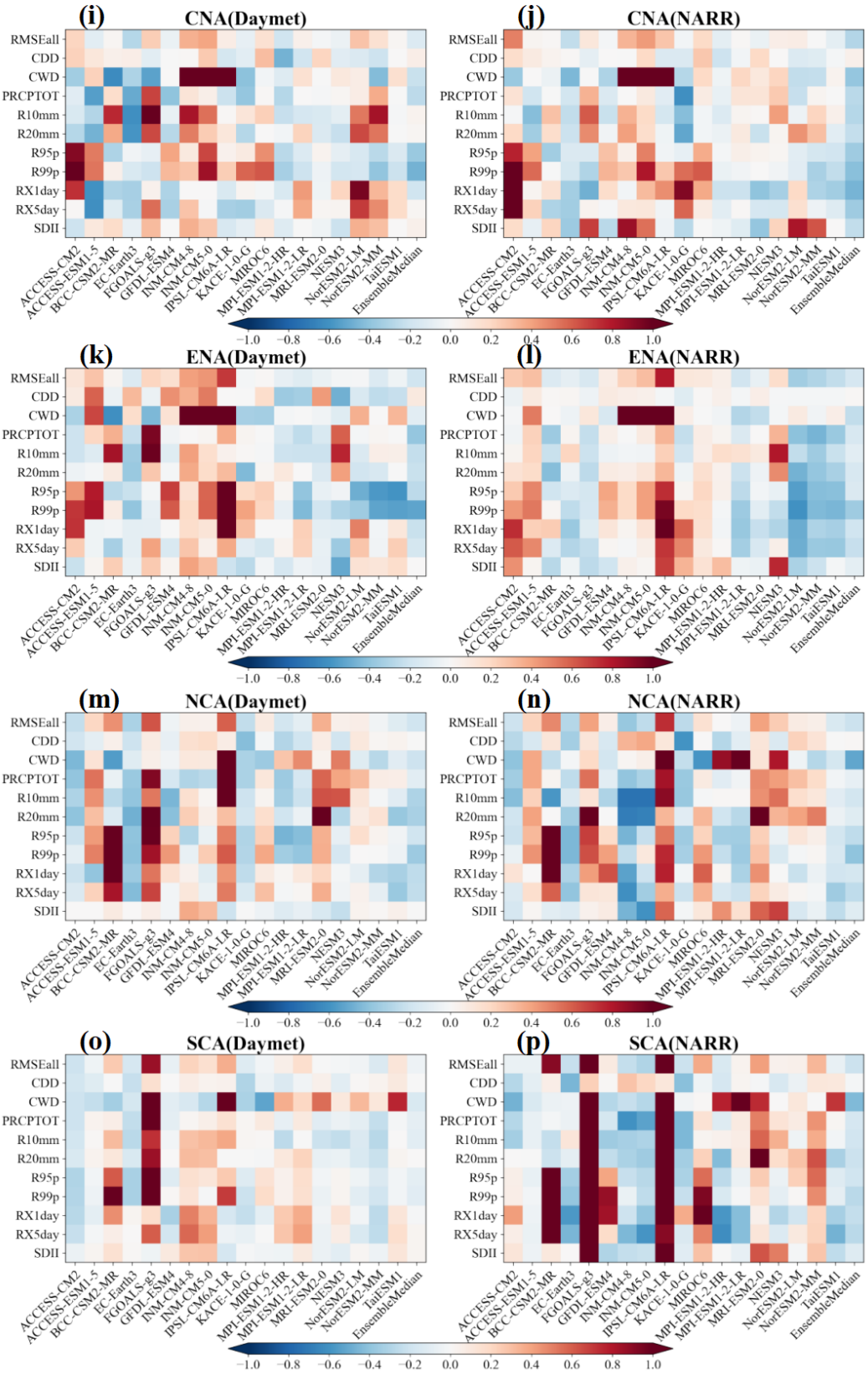

Figure A.3-1 Same as Figure 3-2, but for eight subregions of NA.

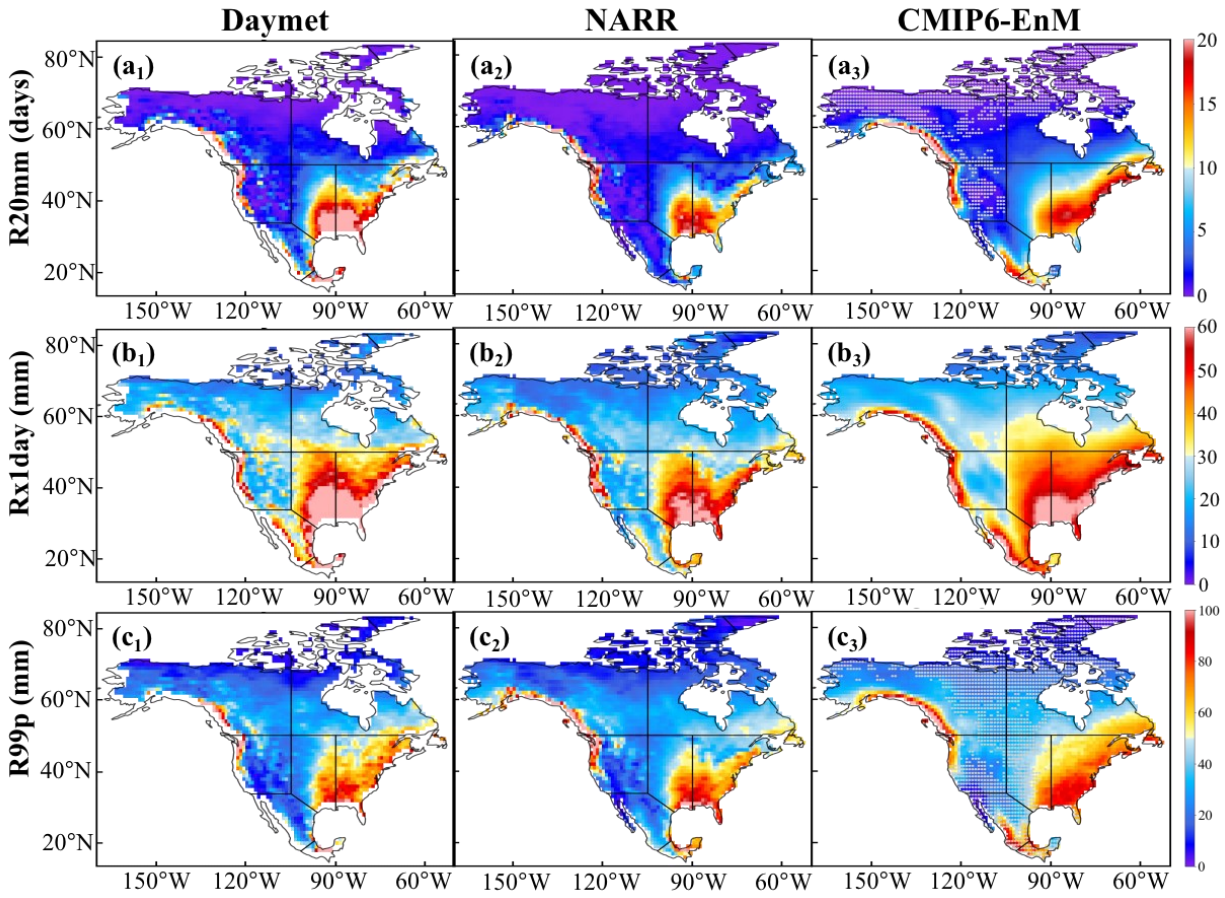

Figure A.3-2 Same as Figure 3-3, but for R20mm, Rx1day and R99p.

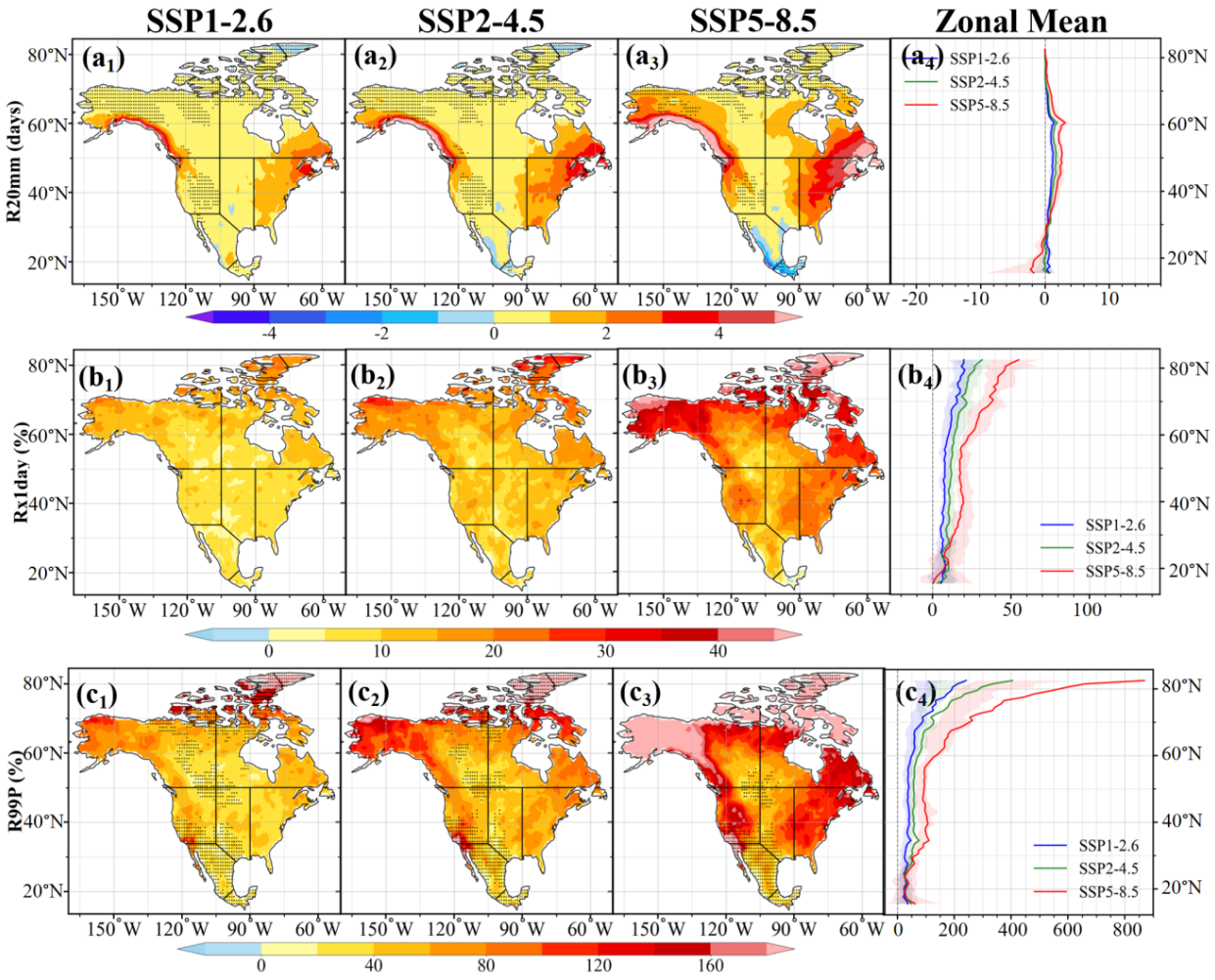

Figure A.3-3 Same as Figure 3-7, but for R20mm, Rx1day and R99p.

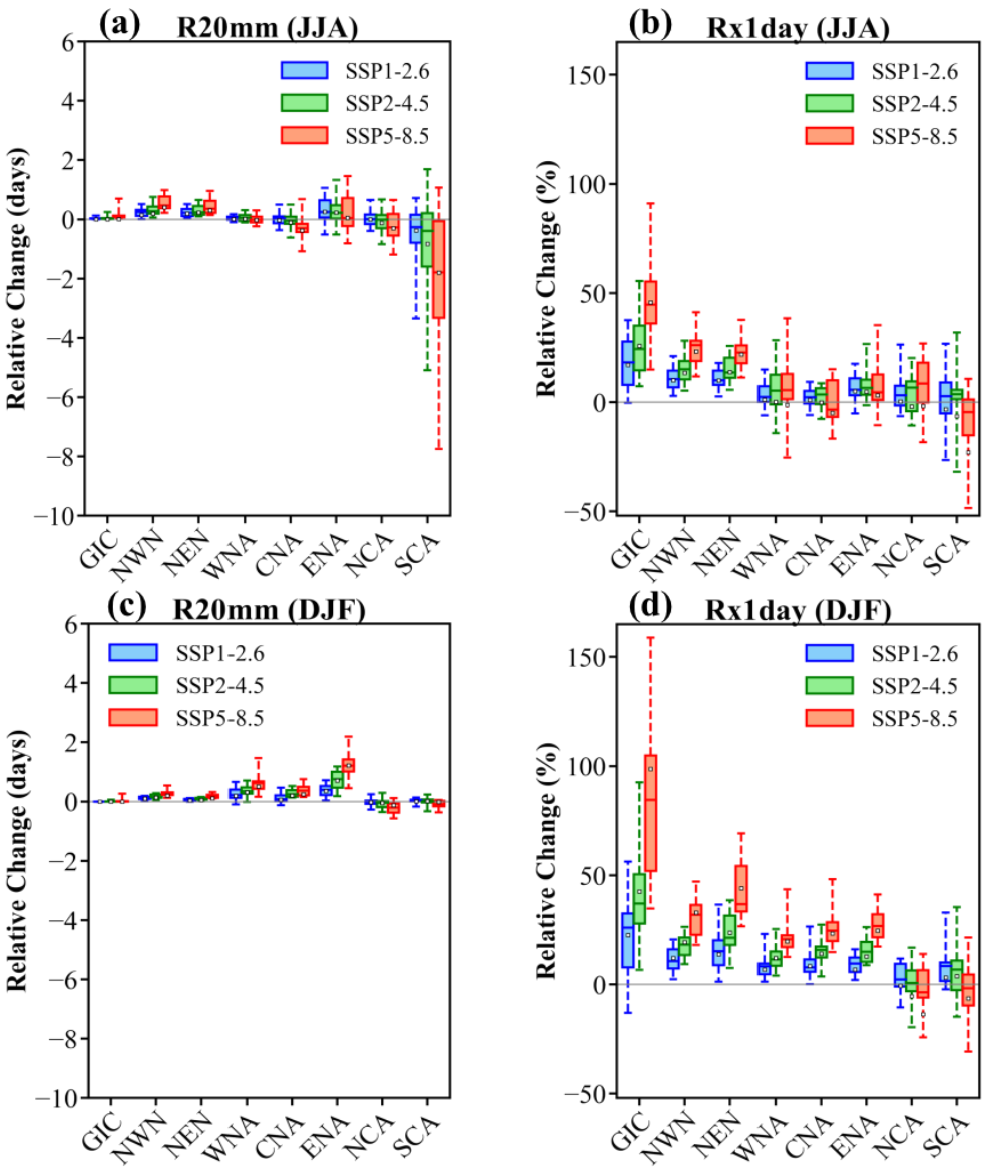

Figure A.3-4 Same as Figure 3-8, but for R20mm and Rx1day.

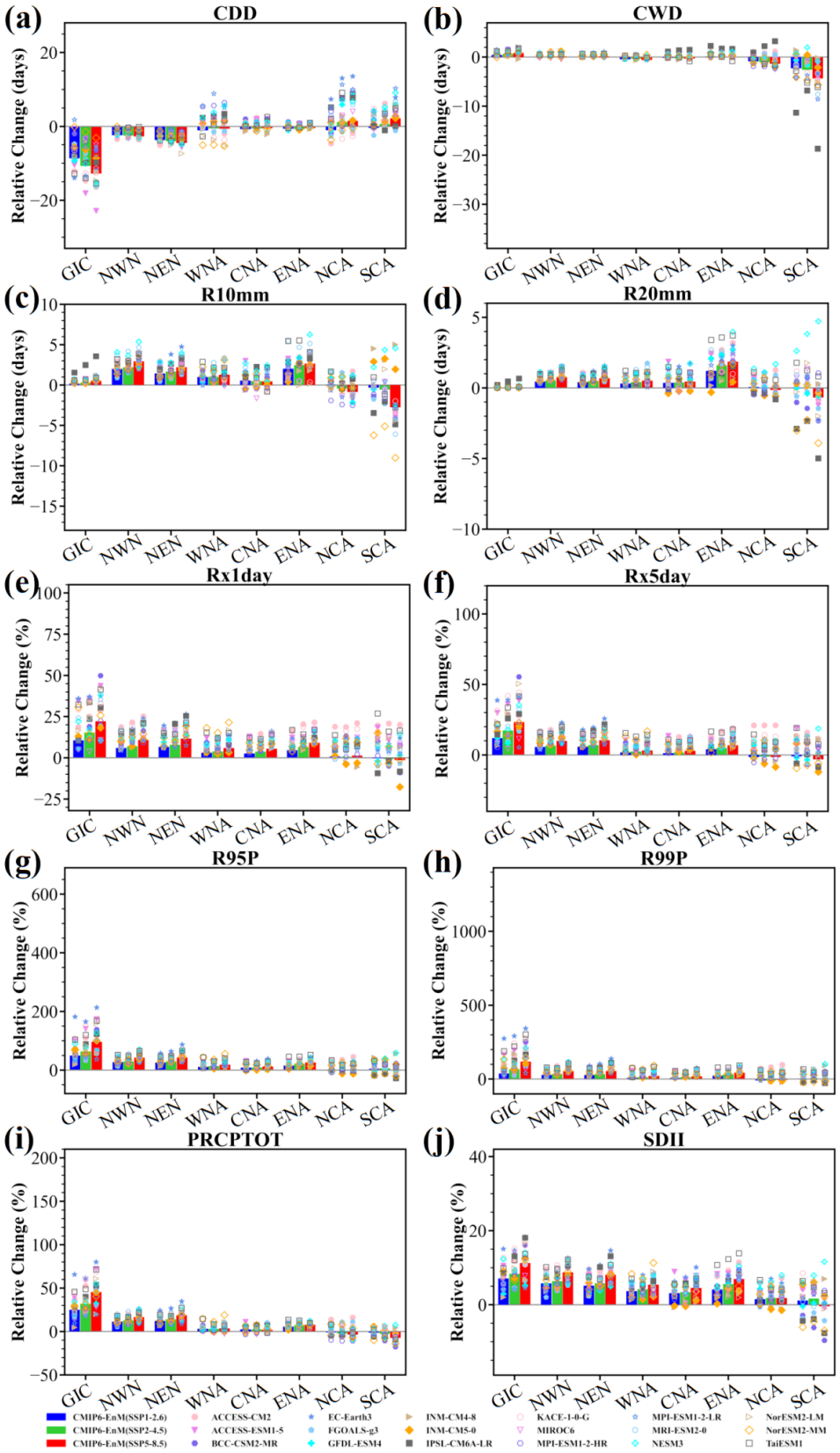

Figure A.3-5 Same as Figure 3-9, but for the period 2041-2070.

Appendix for Chapter 4

Table A.4-1 List of CMIP6 model simulations used in this chapter under different scenarios

No.	Model	Run	CMIP6 Experiment ID							
			historical	hist-ghg	hist-aer	hist-nat	piControl	SSP1-2.6	SSP2-4.5	SSP5-8.5
1	CanESM5	r1i1p1f1	√	√	√	√	√	√	√	√
2		r2i1p1f1	√	√	√	√	√	√	√	√
3		r3i1p1f1	√	√	√	√	√	√	√	√
4		r4i1p1f1	√	√	√	√	√	√	√	√
5		r5i1p1f1	√	√	√	√	√	√	√	√
6		r6i1p1f1	√	√	√	√	√	√	√	√
7		r7i1p1f1	√	√	√	√	√	√	√	√
8		r8i1p1f1	√	√	√	√	√	√	√	√
9		r9i1p1f1	√	√	√	√	√	√	√	√
10		r10i1p1f1	√	√	√	√	√	√	√	√
11	HadGEM3-GC31-LL	r1i1p1f3	√	√	√	√	√	√	√	√
12		r2i1p1f3	√	√	√	√	√		√	√
13		r3i1p1f3	√	√	√	√	√		√	√
14		r4i1p1f3	√	√	√	√	√		√	√
15		r5i1p1f3	√	√	√	√	√			
16	IPSL-CM6A-LR	r1i1p1f1	√	√	√	√	√	√	√	√
17		r2i1p1f1	√	√	√	√	√	√	√	√
18		r3i1p1f1	√	√	√	√	√			
19		r4i1p1f1	√	√	√	√	√	√	√	√
20		r6i1p1f1	√	√	√	√	√	√	√	√
21		r7i1p1f1	√	√	√	√	√			
22		r8i1p1f1	√	√	√	√	√			
23		r9i1p1f1	√	√	√	√	√			
24		r10i1p1f1	√	√	√	√	√			
25	MIROC6	r1i1p1f1	√	√	√	√	√	√	√	√
26		r2i1p1f1	√	√	√	√	√	√	√	√
27		r3i1p1f1	√	√	√	√	√	√	√	√
28		r4i1p1f1	√	√	√	√	√	√	√	√
29		r5i1p1f1	√	√	√	√	√	√	√	√
30		r6i1p1f1	√	√	√	√	√	√	√	√
31		r7i1p1f1	√	√	√	√	√	√	√	√
32		r8i1p1f1	√	√	√	√	√	√	√	√
33		r9i1p1f1	√	√	√	√	√	√	√	√
34		r10i1p1f1	√	√	√	√	√	√	√	√
35	MRI-ESM2-0	r1i1p1f1	√	√	√	√	√	√	√	√
36		r2i1p1f1	√	√	√	√	√	√	√	√
37		r3i1p1f1	√	√	√	√	√	√	√	√
38		r4i1p1f1	√	√	√	√	√	√	√	√
39		r5i1p1f1	√	√	√	√	√	√	√	√

Table A.4-2 List of CMIP6 model simulations and corresponding time period for different warming levels under SSP5-8.5

No.	Model Name	Run	Warming Level (+1 ℃)	Warming Level (+1.5 ℃)	Warming Level (+2 ℃)	Warming Level (+3 ℃)	Warming Level (+4 ℃)
1	CanESM5	r1i1p1f1	1990/2009	2003/2022	2013/2032	2031/2050	2045/2064
2		r2i1p1f1	1991/2010	2002/2021	2011/2030	2029/2048	2044/2063
3		r3i1p1f1	1991/2010	2002/2021	2011/2030	2030/2049	2044/2063
4		r4i1p1f1	1988/2007	1998/2017	2010/2029	2030/2049	2045/2064
5		r5i1p1f1	1992/2011	2003/2022	2013/2032	2030/2049	2045/2064
6		r6i1p1f1	1986/2005	1999/2018	2011/2030	2030/2049	2045/2064
7		r7i1p1f1	1989/2008	2001/2020	2012/2031	2030/2049	2044/2063
8		r8i1p1f1	1988/2007	1999/2018	2012/2031	2031/2050	2046/2065
9		r9i1p1f1	1991/2010	2001/2020	2011/2030	2030/2049	2045/2064
10		r10i1p1f1	1991/2010	2000/2019	2011/2030	2032/2051	2045/2064
11	HadGEM3-GC31-LL	r1i1p1f3	2000/2019	2011/2030	2021/2040	2038/2057	2054/2073
12		r2i1p1f3	1998/2017	2009/2028	2021/2040	2038/2057	2053/2072
13		r3i1p1f3	2005/2024	2014/2033	2024/2043	2042/2061	2055/2074
14		r4i1p1f3	2007/2026	2017/2036	2025/2044	2041/2060	2057/2076
15		r5i1p1f3	/	/	/	/	/
16	IPSL-CM6A-LR	r1i1p1f1	1993/2012	2009/2028	2025/2044	2041/2060	2057/2076
17		r2i1p1f1	1991/2010	2009/2028	2021/2040	2042/2061	2058/2077
18		r3i1p1f1	1991/2010	2008/2027	2024/2043	2042/2061	2056/2075
19		r4i1p1f1	1994/2013	2008/2027	2020/2039	2041/2060	2056/2075
20		r6i1p1f1	1998/2017	2013/2032	2024/2043	2044/2063	2058/2077
21		r7i1p1f1	/	/	/	/	/
22		r8i1p1f1	/	/	/	/	/
23		r9i1p1f1	/	/	/	/	/
24		r10i1p1f1	/	/	/	/	/
25	MIROC6	r1i1p1f1	2013/2032	2031/2050	2044/2063	2067/2086	2056/2075
26		r2i1p1f1	2016/2035	2031/2050	2045/2064	2067/2086	/
27		r3i1p1f1	2015/2034	2030/2049	2043/2062	2065/2084	/
28		r4i1p1f1	2013/2032	2028/2047	2042/2061	2066/2085	/
29		r5i1p1f1	2015/2034	2029/2048	2042/2061	2066/2085	/
30		r6i1p1f1	2011/2030	2029/2048	2042/2061	2064/2083	/
31		r7i1p1f1	2013/2032	2029/2048	2042/2061	2065/2084	/
32		r8i1p1f1	2015/2034	2030/2049	2044/2063	2068/2087	/
33		r9i1p1f1	2012/2031	2026/2045	2040/2059	2065/2084	/
34		r10i1p1f1	2013/2032	2031/2050	2043/2062	2068/2087	/
35	MRI-ESM2-0	r1i1p1f1	2004/2023	2017/2036	2029/2048	2055/2074	2074/2093
36		r1i2p1f1	2004/2023	2018/2037	2032/2051	2056/2075	2076/2095
37		r3i1p1f1	/	/	/	/	/
38		r4i1p1f1	/	/	/	/	/
39		r5i1p1f1	/	/	/	/	/

Table A.4-3 Detection and attribution results for one-signal analysis

Region	Period	CRU				GPCC				ERA5				NCEP-NCAR			
		ALL	GHG	AER	NAT	ALL	GHG	AER	NAT	ALL	GHG	AER	NAT	ALL	GHG	AER	NAT
GLM	1950-1979	A		A		A		A		A		A		A		A	
	1985-2015	A	A			A	A			A	A			A	A		
TRO	1950-1979	A		A		A		A		A		A		A		A	
	1985-2015	A	A			A	A			A	A			A	A		
NA	1950-1979																
	1985-2015																
SA	1950-1979																
	1985-2015																
AS	1950-1979	A		A		A		A		A		A		A		A	
	1985-2015	A	A			A	A			A	A			A	A		
AF	1950-1979	A		A		A		A		A		A		A		A	
	1985-2015	A	A			A	A			A	A			A	A		
AUS	1950-1979																
	1985-2015	A				A				A				A			

Table A.4-4 Detection and attribution results for two-signal analysis

Region	Period	CRU		GPCC		ERA5		NCEP-NCAR	
		ANT	NAT	ANT	NAT	ANT	NAT	ANT	NAT
GLM	1950-1979			A		D		A	
	1985-2015	A		A		A		D	
TRO	1950-1979					D			
	1985-2015	A		A		A		D	
NA	1950-1979							A	
	1985-2015					A			
SA	1950-1979							A	
	1985-2015	A				A		D	
AS	1950-1979							A	
	1985-2015								
AF	1950-1979					A			
	1985-2015							A	
AUS	1950-1979								
	1985-2015			D		A		D	

Table A.4-5 seasonal changes according to the variation in annual total precipitation (ATP) and precipitation seasonality index (SI)

No.	ATP	SI	seasonal chanegs
1	increase (+)	increase (+)	wet get wetter
2	increase (+)	decrease (-)	dry get wetter
3	decrease (-)	decrease (-)	wet get drier
4	decrease (-)	increase (+)	dry get drier

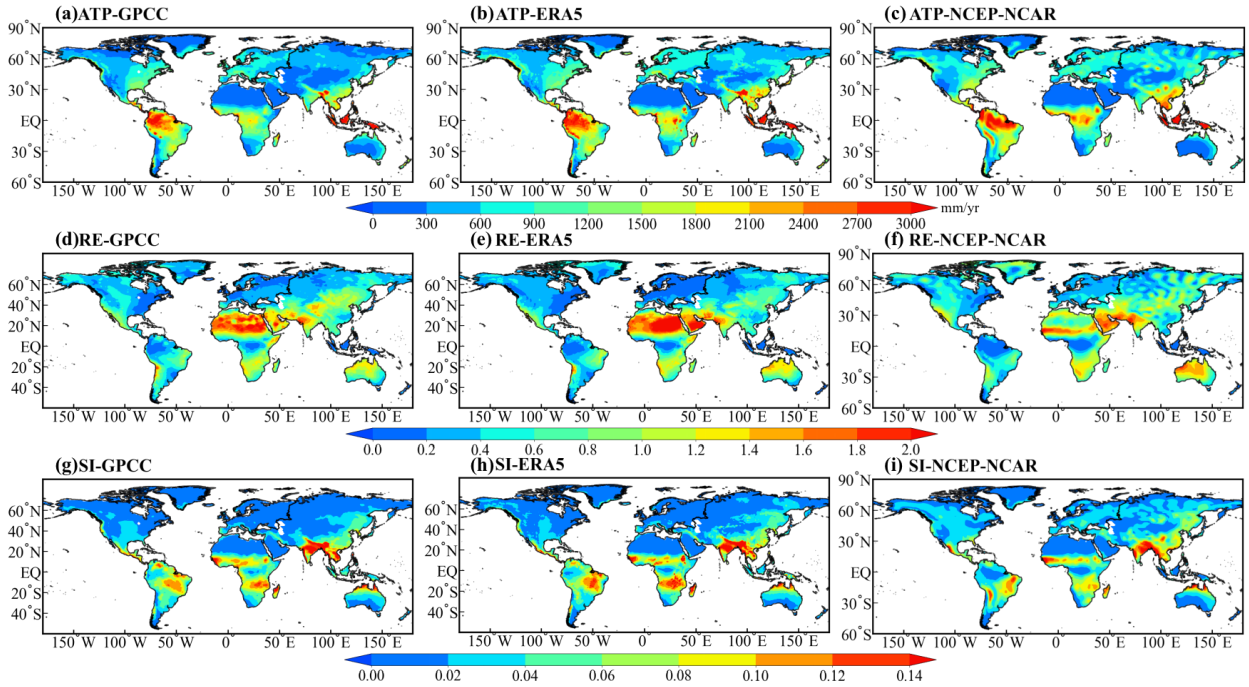

Figure A.4-1 Geographical distribution of ATP (mm/yr), RE and SI in 1950–2014 for ERA5 (Figure A.4-1a, d, g), GPCC (Figure A.4-1b, e, h) and NCEP-NCAR (Figure A.4-1c, f, i).

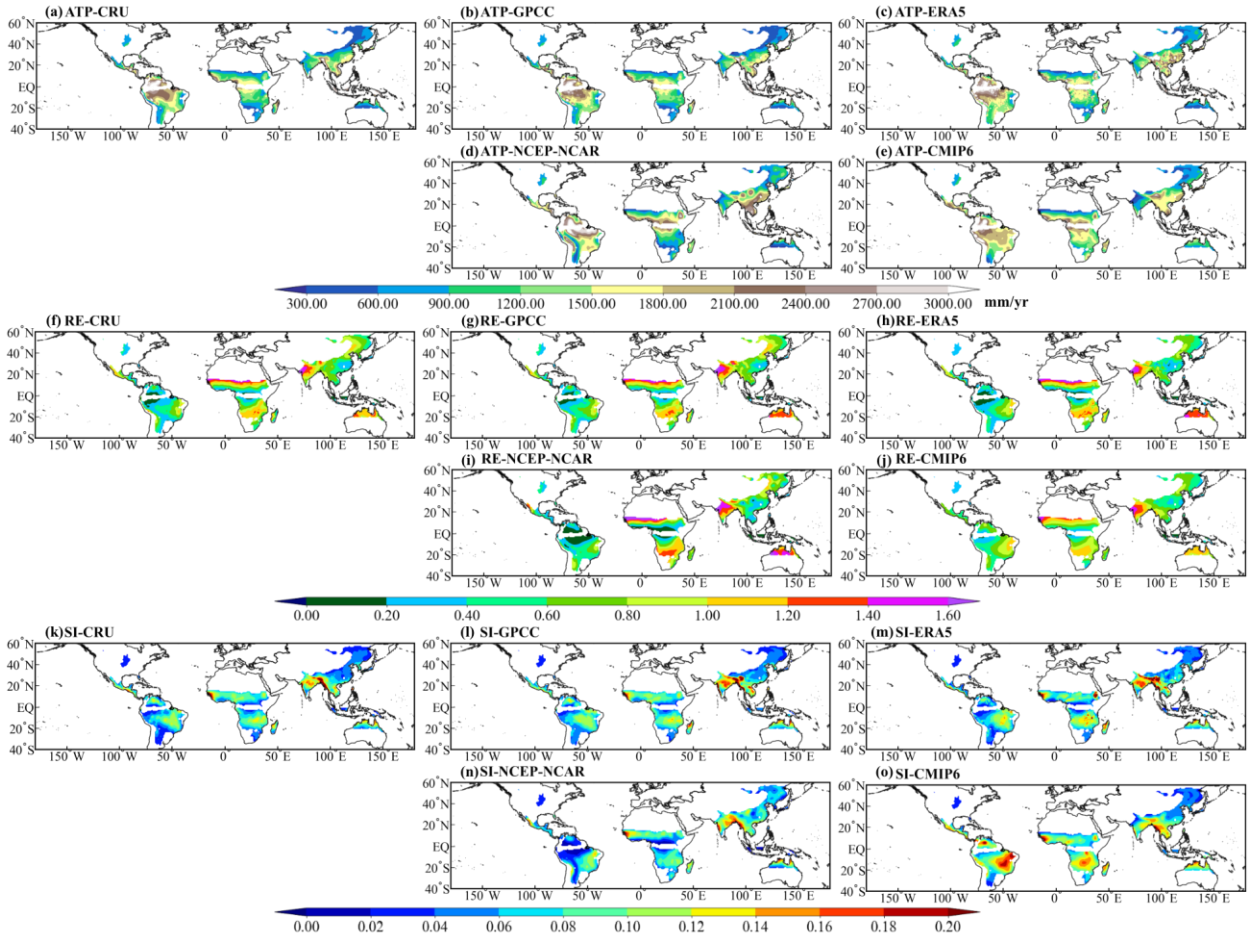

Figure A.4-2 Geographical distribution of ATP (mm/yr), RE and SI in 1950–2014 for CRU (Figure A.4-2a, f, k), GPCC (Figure A.4-2b, g, l), ERA5(Figure A.4-2c, h, m), and NCEP-NCAR (Figure A.4-2d, i, n) and CMIP6-EnM (Figure A.4-2e, j, o).

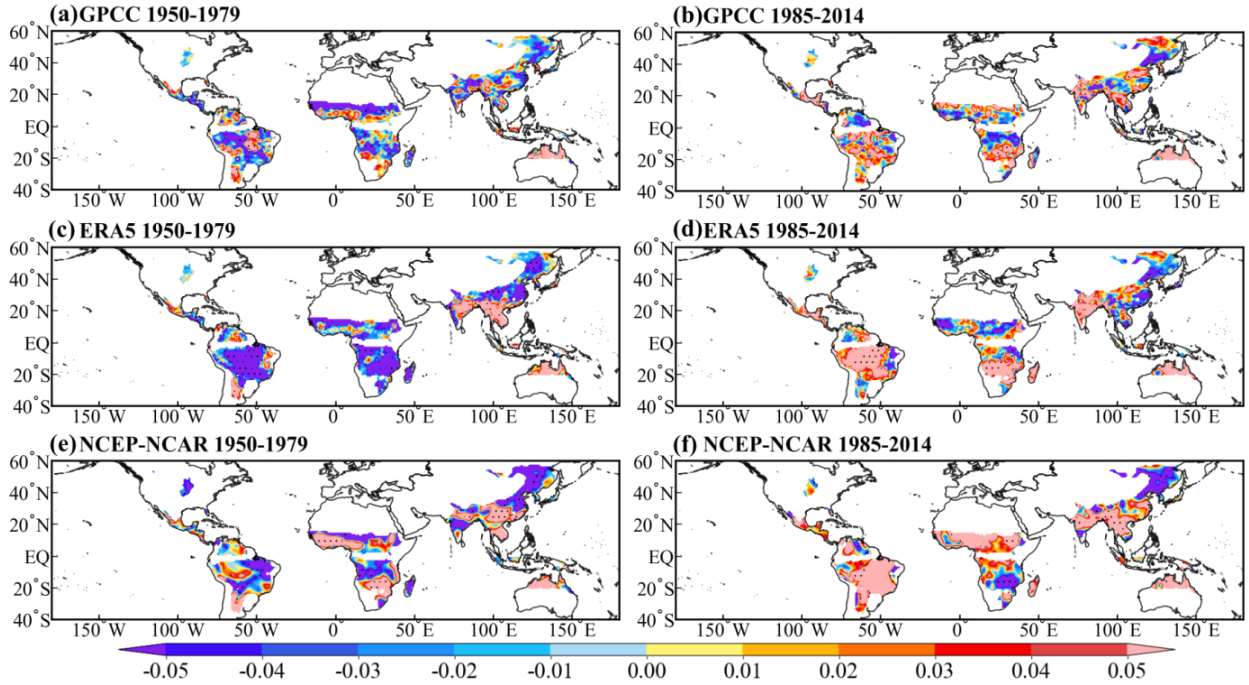

Figure A.4-3 Geographical distribution of linear trends (×100/yr) in SI during 1950-1979 (Figure A.4-3a, c, e) and 1985-2014 (Figure A.4-3b, d, f) for GPCC, ERA5 and NCEP-NCAR observations. Black dots indicate grids with significant long-term trends at the 5% level.

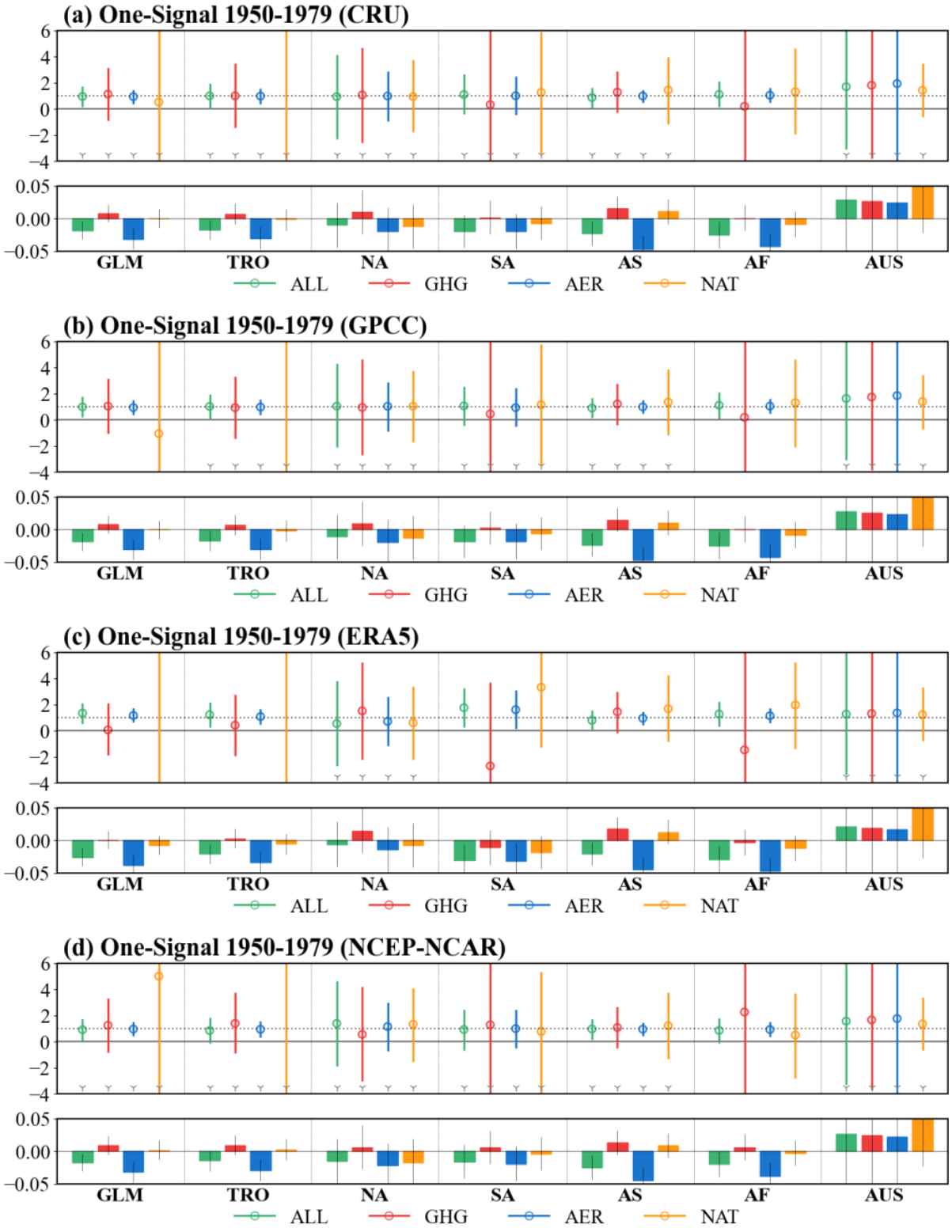

Figure A.4-4 Results of the one-signal analysis for SI anomalies over global land monsoon and its subregions in 1950-1979. The cycle and vertical line indicate the best estimates of scaling factors and their 10–90% confidence intervals, respectively. The two gray solid and dashed horizontal lines

indicate zero and one, respectively. The gray triangles at the bottom show the failure of the residual consistency test due to too small model variability.

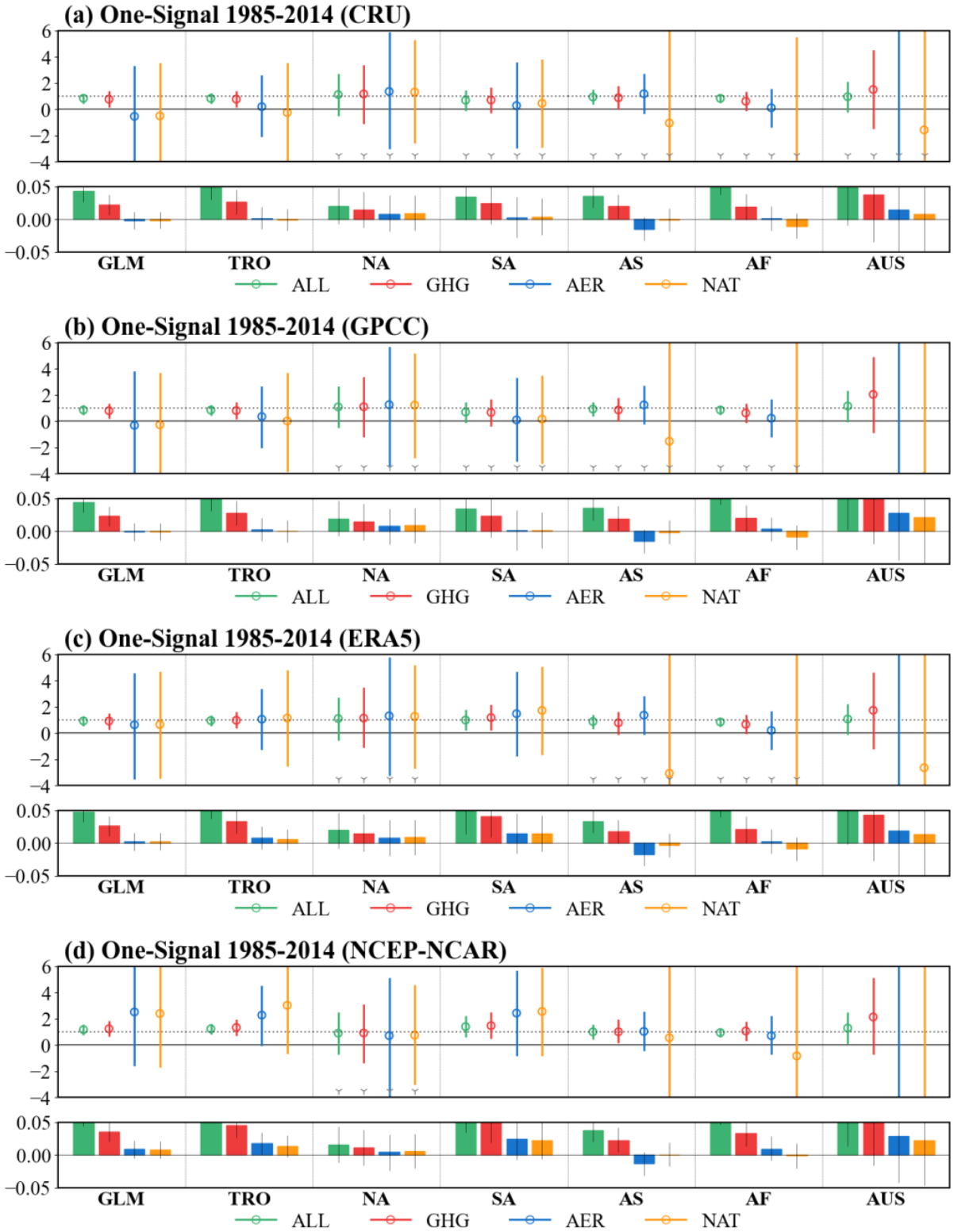

Figure A.4-5 Same as Figure A.4-4, but for one-signal analysis in 1985-2014

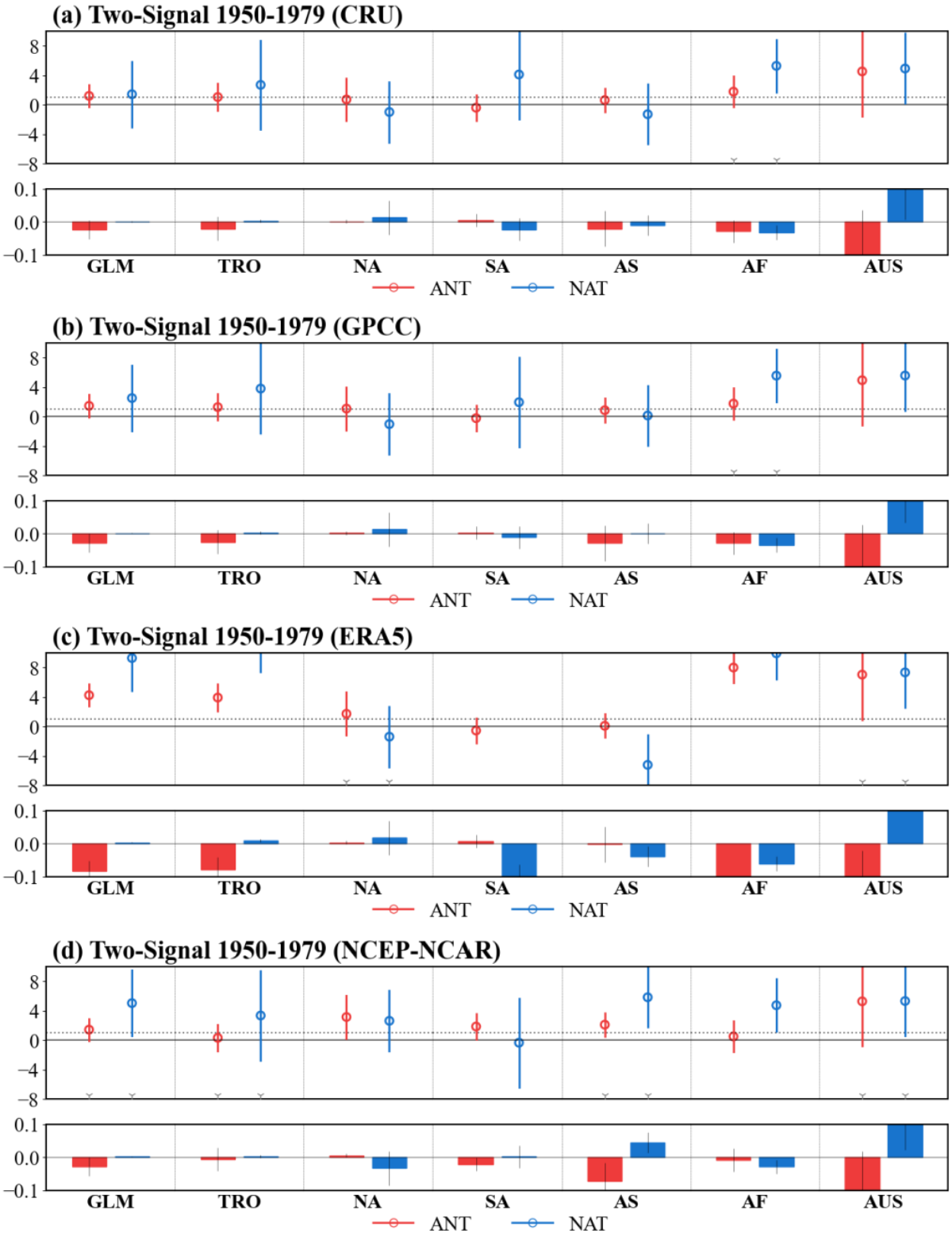

Figure A.4-6 Same as Figure A.4-4, but for two-signal analysis in 1950-1979

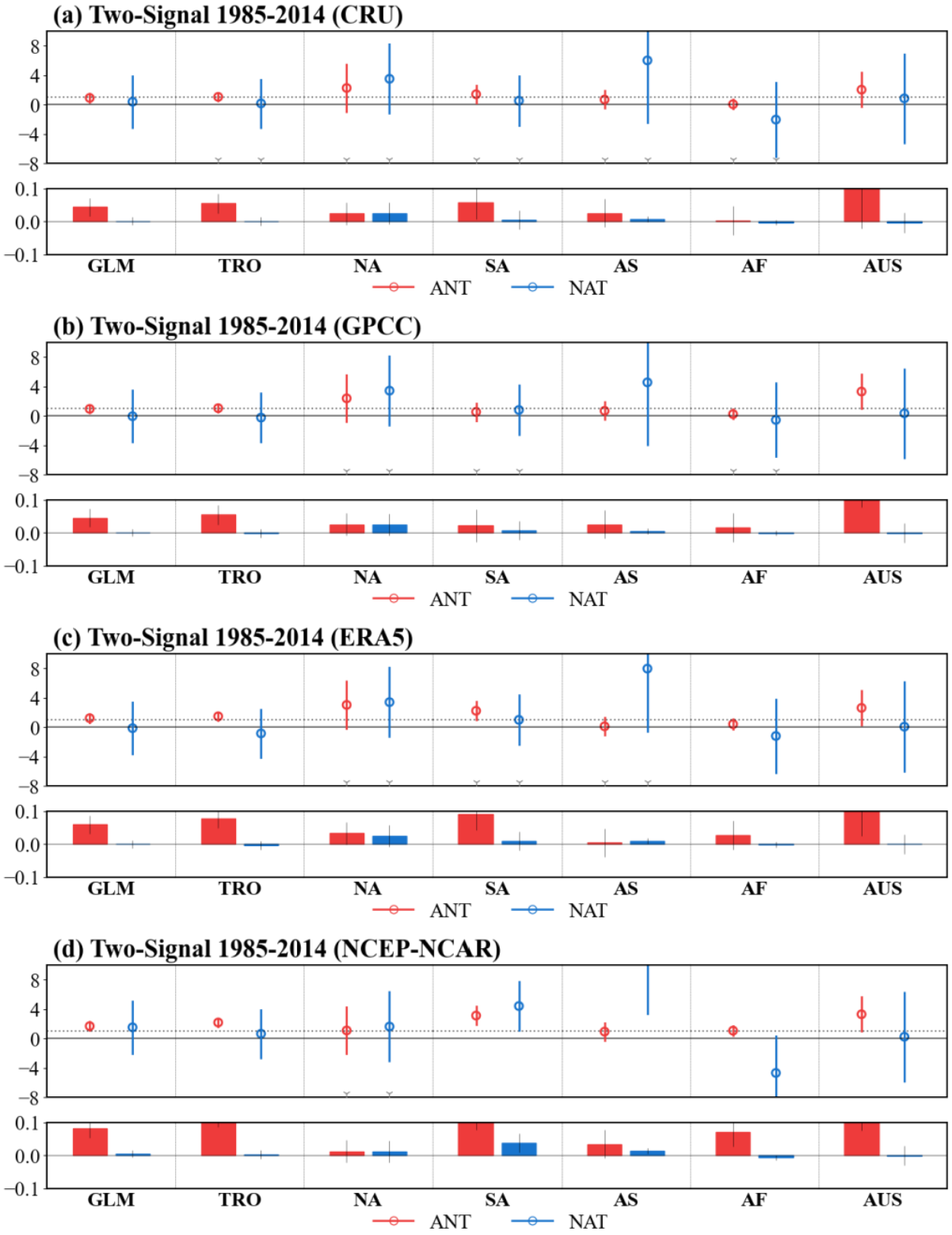

Figure A.4-7 Same as Figure A.4-4, but for two-signal analysis in 1985-2014.

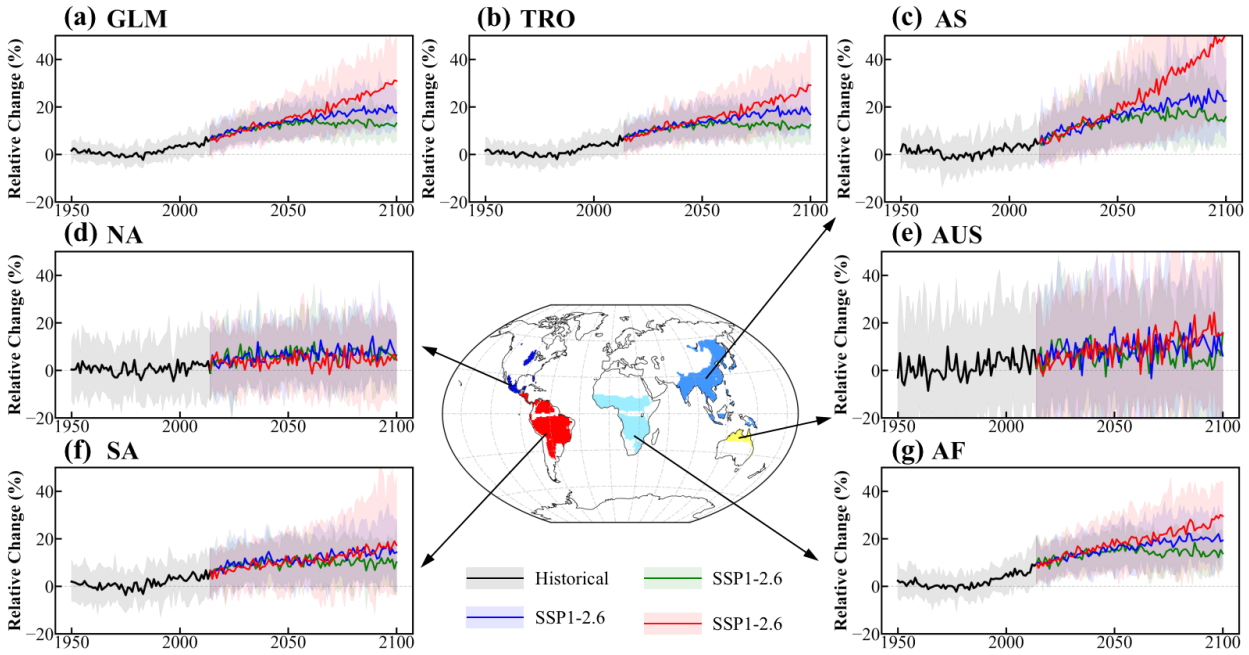

Figure A.4-8 Spatial average of SI anomalies over the GLM and its subregions as simulated by the CMIP6 models for historical (black), SSP1−2.6 (green), SSP2−4.5 (blue) and SSP5−8.5 (red) relative to the reference period 1961-1990. Solid lines indicate the results of CMIP6-EnM, shadings show the interquartile spread of 39 CMIP6 model runs (10th and 90th quantiles).

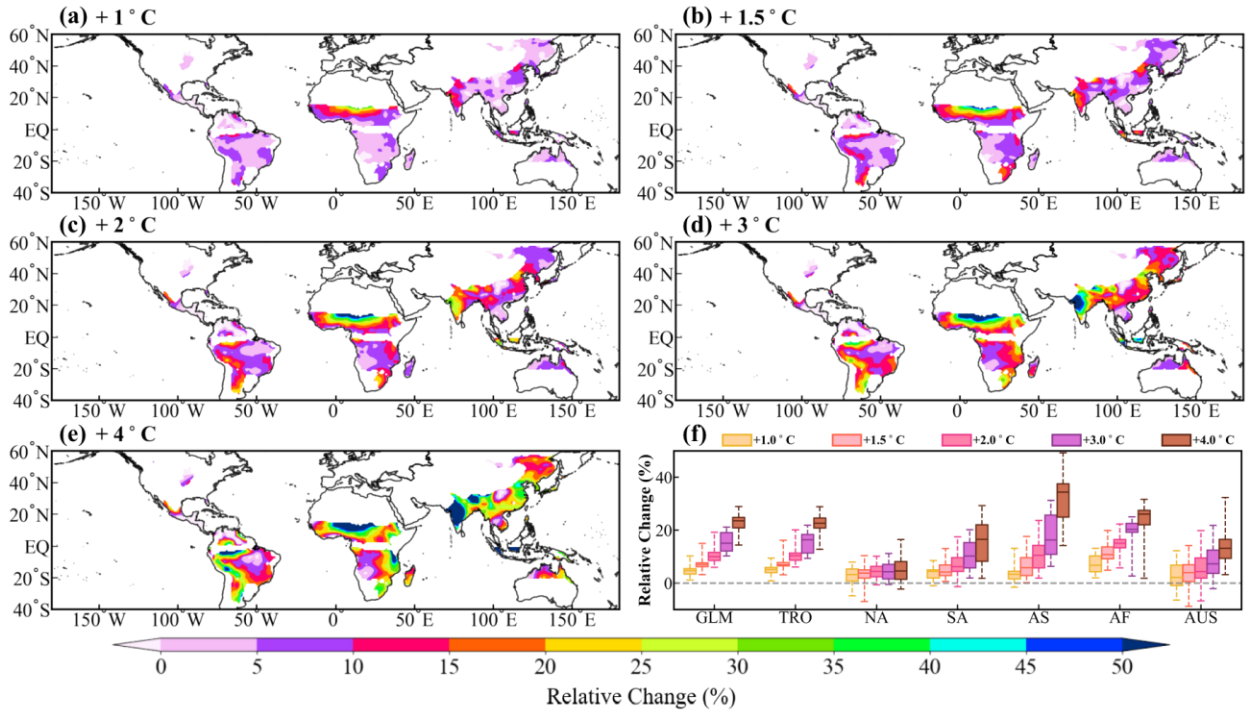

Figure A.4-9 Same as Figure 4-7 but for different warming levels relative to 1850-1900.

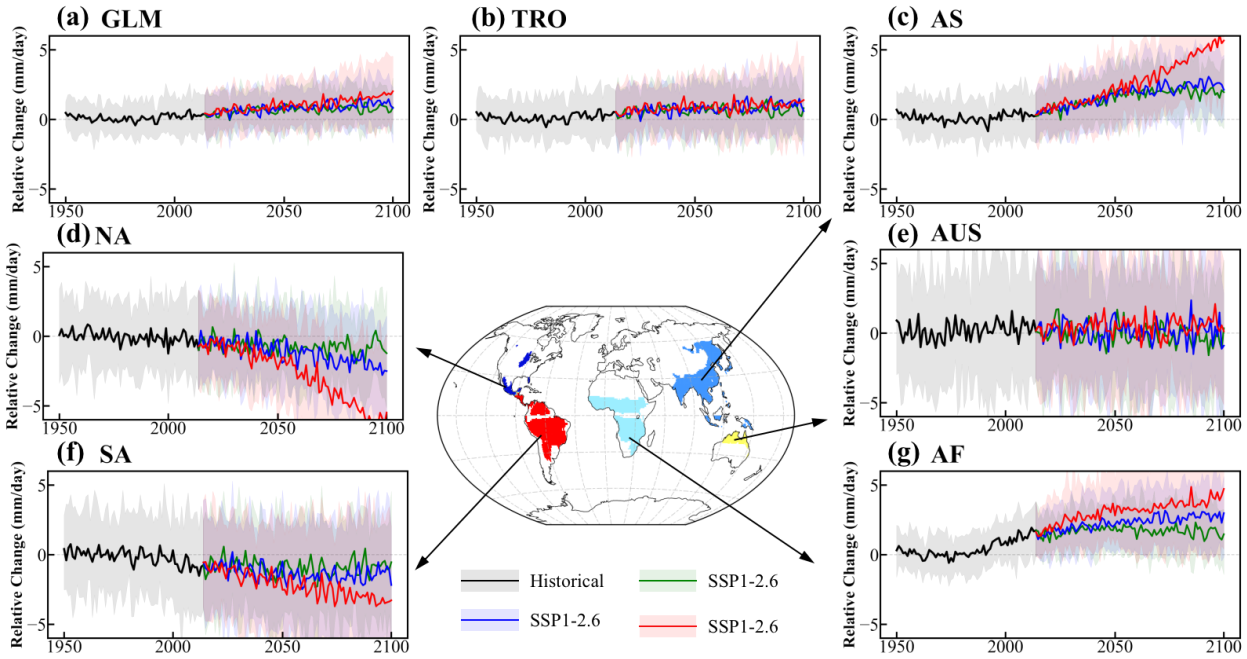

Figure A.4-10 Spatial average of AW anomalies over the GLM and its subregions as simulated by the CMIP6 models for historical (black), SSP1−2.6 (green), SSP2−4.5 (blue) and SSP5−8.5 (red) relative to the reference period 1961-1990. Solid lines indicate the results of CMIP6-EnM, shadings show the interquartile spread of 39 CMIP6 model runs (10th and 90th quantiles.